

Numerical Analysis of Fluid-Structure Interactions
in an Air- or Helium-filled Hard Disk Drive

A Dissertation

Presented to
the faculty of the School of Engineering and Applied Science
University of Virginia

in partial fulfillment
of the requirements for the degree

Doctor of Philosophy

by

Sae Woong Kil

August

2014

APPROVAL SHEET

The dissertation
is submitted in partial fulfillment of the requirements
for the degree of
Doctor of Philosophy



AUTHOR

The dissertation has been read and approved by the examining committee:

Hossein Haj-Hariri

Advisor

Robert Ribando

Matthew Reidenbach

Houston Wood

Haibo Dong

Accepted for the School of Engineering and Applied Science:



Dean, School of Engineering and Applied Science

August
2014

Abstract

From the advent, the HDD has been the most effective and important medium of data storage. To satisfy trends of the data storage industry, the design of the HDD has continued to evolve. The modern trend in the HDD tries to minimize the dimensions for better portability, and to maximize the data density on the disk surface for enhanced capacity. These trends require quite high positioning accuracy of Slider Suspension Units (SSU), which support the magnetic head. Another important demand is faster rotating speeds so that the data transfer time of the HDD can remain competitive with other storage devices such as flash memory. However, the increased rotating speed of the disk induces turbulent flow in the HDD and deteriorates the positioning accuracy of the SSU. Many investigations have tried to reduce the turbulent flow and the magnitude of the flow-induced vibration on the SSU by installing blockages upstream of the SSU to decrease the local turbulent flow. However, such geometrical modifications are ad hoc and have little basis in the underlying physics.

The goal of the present research is to reduce the flow-induced vibration of the SSU by changing the fluid medium inside the HDD. The fundamental nature of the flow field between the co-rotating disks is investigated in the presence of the actuator arm and the SSU. Helium is chosen as an alternative medium inside the HDD. The physical properties of helium decrease the fluid forces on the SSU and the turbulent kinetic energy around the SSU by stabilizing the flow field. To analyze the flow field in the space between the disks, numerical calculations were executed by employing commercial software ANSYS-

CFX. To find a fundamental correlation between the flow oscillation and the vibration of the SSU at high rotating speeds, a FEM code (ANSYS) was fully coupled with ANSYS/CFX. By employing the coupled calculation technique, the underpinning physics of the SSU vibration is exposed. Also, it is demonstrated that the magnitude of the vibration is reduced substantially by using helium instead of air in the HDD.

Acknowledgements

I would like to thank to my advisor Dr. Hossein Haj-Hariri. He advised me until I completed all the numerical calculations with a great patience and sincere discussions to find underpinning physics of the present investigations. I also thank to all committee members. Their efforts made huge contributions to elevate the quality of my dissertation. Thank my parents and my friends. Your love and friendships always cheered me up. I would like to thank Information Storage Industry Consortium (INSIC). They gave us motivations of this problem and technical supports at the beginning of our research. My lovely wife, Yun Kyoung Kim, was the most supportive during my Ph.D. and you are the biggest present in my life, Brandon Hyunsuh Kil, my son.

Contents

1	Introduction to the problem	
1.1	Introduction	1
1.2	Hard Disk Drive components	2
1.3	Motivations	4
2	Prior works	
2.1	Unobstructed flow	6
2.1.1	Experiment in unobstructed flow	6
2.1.2	Numerical calculations in unobstructed flow	11
2.2	Obstructed flow	15
2.2.1	Experiment with obstructed flow	15
2.2.2	Numerical calculations with obstructed flow	20
3	Problem Model	
3.1	Geometry generation	27
3.1.1	Actuator arm and Slider Suspension Unit	27
3.1.2	Disk	29
3.1.3	Fluid domain	30
3.1.4	Inner and Outer Configuration	32
3.2	Governing equations	33
3.3	Material properties	33
3.4	Initial conditions	34
3.5	Boundary conditions	34
3.6	Introduction of ANSYS/CFX and ANSYS code	36
3.7	Grid generation	38
3.7.1	Kolmogorov and Taylor microscales	38
3.7.2	Boundary layers	41
3.7.3	Solid domain	43
3.7.4	Numerical result validation	44
3.8	Time step calculation	47
4	Results of numerical calculation	
4.1	Inner configuration	53
4.1.1	Mean velocity magnitude	53
4.1.2	Vorticity	70
4.1.3	Turbulence Intensity (TI)	81
4.1.4	Displacement and Frequency Analyses of the Slider Suspension Unit	90
4.2	Outer configuration	101

4.2.1	Mean velocity magnitude	101
4.2.2	Vorticity	115
4.2.3	Turbulence Intensity (TI)	126
4.2.4	Displacement and Frequency Analyses of the Slider Suspension Unit	135
5	Conclusions and future work	
5.1	Conclusions	144
5.1.1	Findings of the fluid domain	144
5.1.2	Findings of the solid domain	146
5.2	Future work	147
	Appendix	
A	Inner configuration	149
A.1	Velocity with vectors	150
A.1.1	Air flow at 5400 rpm	150
A.1.2	Helium flow at 5400 rpm	152
A.1.3	Air flow at 15000 rpm	154
A.1.4	Helium flow at 15000 rpm	156
A.2	Z-axial vorticity	158
A.2.1	Air flow at 5400 rpm	158
A.2.2	Helium flow at 5400 rpm	160
A.2.3	Air flow at 15000 rpm	162
A.2.4	Helium flow at 15000 rpm	164
B	Inner configuration	166
B.1	Velocity with vectors	167
B.1.1	Air flow at 5400 rpm	167
B.1.2	Helium flow at 5400 rpm	169
B.1.3	Air flow at 15000 rpm	171
B.1.4	Helium flow at 15000 rpm	173
B.2	Z-axial vorticity	175
B.2.1	Air flow at 5400 rpm	175
B.2.2	Helium flow at 5400 rpm	177
B.2.3	Air flow at 15000 rpm	179
B.2.4	Helium flow at 15000 rpm	181
C	Derivation of Taylor-Proudman theorem	186
D	Introduction of Taylor microscale	188
	Reference	192

List of Figures

1.1	Picture of components of HDD (The first Terabyte capacity HDD shipped by Hitachi GST with five 95 mm disks). [1]	3
3.1	(a) Top view and (b) side view of the actuator arm with dimensions.	28
3.2	(a) Top view of the magnetic tip, (b) Top view of and (c) side view of the SSU with dimensions.	29
3.3	(a) Top view and side view (b) of the disk with dimensions.	30
3.4	Schematic of the fluid domain.	31
3.5	Top view of the Inner Configuration (a) and the Outer Configuration (b) with a distance between the rotating axis and the center of the magnetic tip.	32
3.6	(a) Top view and (b) Iso view of the fluid domain with boundary conditions. ..	36
3.7	Flow chart of the FSI [34].	37
3.8	Snapshot of the grid domain for the fluid.	40
3.9	Snapshot of packed number of grid around the arm and the SSU.	42
3.10	(a) Top view of the grid domain for the SSU and (b) Iso-view of the grid domain for the SSU.	44
3.11	Mean velocity magnitude with streamlines at 5400 rpm on the inter-disk mid-plane from (a) the experiment and (b) the numerical calculation.	45
3.12	(a) The location of the line A-B where the mean velocity profile is measured. Mean velocity profiles of the experiment and the numerical calculation (b) for the inner configuration at 5,400 rpm and (c) for the outer configuration at 15,000 rpm.	47
4.1	Planes perpendicular to the rotating axis where the contour plots are plotted. ..	50
4.2	Planes perpendicular to the disk surface where the contour plots are plotted for (a) the IC and (b) the OC.	51
4.3	Contour plots of mean velocity of (a) air and (b) helium at the inter-disk mid-plane ($Z=0$ mm) at 5400 rpm.	57
4.4	Contour plots of mean velocity of (a) air and (b) helium at the inter-disk mid-plane ($Z=0$ mm) at 15000 rpm.	57
4.5	Schematic drawing of the trejectories of the incoming flow upstream of the arm (a) and the stagnation point displacement for the helium at 5400 and 15000 rpm (b).	58
4.6	Contour plots of mean velocity of (a) air and (b) helium at the plane across the flanges ($Z= 0.355$ mm) at 5400 rpm.	61
4.7	Contour plots of mean velocity of (a) air and (b) helium at the plane across the flanges ($Z= 0.355$ mm) at 15000 rpm.	62

4.8	Contour plots of mean velocity of (a) air and (b) helium at the plane between the arm and the disk ($Z = 0.8$ mm) at 5400 rpm.	64
4.9	Contour plots of mean velocity of (a) air and (b) helium at the plane between the arm and the disk ($Z = 0.8$ mm) at 15000 rpm.	65
4.10	Contour plots of mean velocity on three plange across the stiffening; (a) near the arm. (b) middle of the flanges. (c) the end of the flanges in air at 5400 rpm. ...	67
4.11	Contour plots of mean velocity on three plange across the stiffening; (a) near the arm. (b) middle of the flanges. (c) the end of the flanges in helium at 5400 rpm.	68
4.12	Contour plots of mean velocity on three plange across the stiffening; (a) near the arm. (b) middle of the flanges. (c) the end of the flanges in air at 15000 rpm.	68
4.13	Contour plots of mean velocity on three plange across the stiffening; (a) near the arm. (b) middle of the flanges. (c) the end of the flanges in helium at 15000 rpm.	69
4.14	Contour plots of Z - axial vorticity of (a) air and (b) helium at the inter-disk mid-plane ($Z=0$ mm) at 5400 rpm.	72
4.15	Contour plots of Z - axial vorticity of (a) air and (b) helium at the inter-disk mid-plane ($Z=0$ mm) at 15000 rpm.	73
4.16	Contour plots of Z - axial vorticity of of (a) air and (b) helium at the plane across the flanges ($Z= 0.355$ mm) at 5400 rpm.	74
4.17	Contour plots of Z - axial vorticity of of (a) air and (b) helium at the plane across the flanges ($Z= 0.355$ mm) at 15000 rpm.	75
4.18	Contour plots of Z - axial vorticity of of (a) air and (b) helium at the plane between the arm and the disk ($Z = 0.8$ mm) at 5400 rpm.	76
4.19	Contour plots of Z - axial vorticity of of (a) air and (b) helium at the plane between the arm and the disk ($Z = 0.8$ mm) at 15000 rpm.	77
4.20	Contour plots of Y - axial vorticity of on three plange across the stiffening; (a) near the arm. (b) middle of the flanges. (c) the end of the flanges in air at 5400 rpm.	79
4.21	Contour plots of Y - axial vorticity of on three plange across the stiffening; (a) near the arm. (b) middle of the flanges. (c) the end of the flanges in helium at 5400 rpm.	79
4.22	Contour plots of Y - axial vorticity on three plange across the stiffening; (a) near the arm. (b) middle of the flanges. (c) the end of the flanges in air at 15000 rpm.	80
4.23	Contour plots of Y - axial vorticity on three plange across the stiffening; (a) near the arm. (b) middle of the flanges. (c) the end of the flanges in helium at 15000 rpm.	80

4.24	Contour plots of TI^* of (a) air and (b) helium at the inter-disk mid-plane ($Z=0$ mm) at 5400 rpm.	84
4.25	Contour plots of TI^* of (a) air and (b) helium at the inter-disk mid-plane ($Z=0$ mm) at 15000 rpm.	85
4.26	Contour plots of TI^* of (a) air and (b) helium at the plane across the flanges ($Z= 0.355$ mm) at 5400 rpm.	86
4.27	Contour plots of TI^* of (a) air and (b) helium at the plane across the flanges ($Z= 0.355$ mm) at 15000 rpm.	87
4.28	Contour plots of TI^* of (a) air and (b) helium at the plane between the arm and the disk ($Z = 0.8$ mm) at 5400 rpm.	88
4.29	Contour plots of TI^* of (a) air and (b) helium at the plane between the arm and the disk ($Z = 0.8$ mm) at 15000 rpm.	89
4.30	Displacement in X – axis on the center of the magnetic tips at 5400 rpm.	91
4.31	Displacement in Y – axis on the center of the magnetic tips at 5400 rpm.	92
4.32	Displacement in Z – axis on the center of the magnetic tips at 5400 rpm.	92
4.33	Displacement in X – axis on the center of the magnetic tips at 15000 rpm.	93
4.34	Displacement in Y – axis on the center of the magnetic tips at 15000 rpm.	93
4.35	Displacement in Z – axis on the center of the magnetic tips at 15000 rpm.	94
4.36	Power Spectral Density of the in-plane displacement at 5400 rpm.	97
4.37	Power Spectral Density of the axial displacement at 5400 rpm.	97
4.38	Power Spectral Density of the velocity fluctuation downstream of the SSU at 5400 rpm.	98
4.39	Power Spectral Density of the in-plane displacement at 15000 rpm.	99
4.40	Power Spectral Density of the axial displacement at 15000 rpm.	99
4.41	Power Spectral Density of the velocity fluctuation downstream of the SSU at 15000 rpm.	100
4.42	Contour plots of mean velocity of (a) air and (b) helium at the inter-disk mid-plane ($Z=0$ mm) at 5400 rpm.	103
4.43	Contour plots of mean velocity of (a) air and (b) helium at the inter-disk mid-plane ($Z=0$ mm) at 15000 rpm.	104
4.44	Contour plots of mean velocity of (a) air and (b) helium at the plane across the flanges ($Z= 0.355$ mm) at 5400 rpm.	107
4.45	Contour plots of mean velocity of (a) air and (b) helium at the plane across the flanges ($Z= 0.355$ mm) at 15000 rpm.	107
4.46	Contour plots of mean velocity of (a) air and (b) helium at the mid-plane between the arm and the upper disk ($Z= 0.8$ mm) at 5400 rpm.	109
4.47	Contour plots of mean velocity of (a) air and (b) helium at the mid-plane between the arm and the upper disk ($Z= 0.8$ mm) at 15000 rpm.	110

4.48	Contour plots of mean velocity on three plane across the stiffening; (a) near the arm. (b) middle of the flanges. (c) the end of the flanges in air at 5400 rpm. · ·	113
4.49	Contour plots of mean velocity on three plane across the stiffening; (a) near the arm. (b) middle of the flanges. (c) the end of the flanges in helium at 5400 rpm. ······	113
4.50	Contour plots of mean velocity on three plane across the stiffening; (a) near the arm. (b) middle of the flanges. (c) the end of the flanges in air at 15000 rpm. ······	114
4.51	Contour plots of mean velocity on three plane across the stiffening; (a) near the arm. (b) middle of the flanges. (c) the end of the flanges in helium at 5000 rpm. ······	114
4.52	Contour plots of Z - axial vorticity of (a) air and (b) helium at the inter-disk mid-plane ($Z=0$ mm) at 5400 rpm. ······	117
4.53	Contour plots of Z - axial vorticity of (a) air and (b) helium at the inter-disk mid-plane ($Z=0$ mm) at 15000 rpm. ······	118
4.54	Contour plots of Z - axial vorticity of (a) air and (b) helium at the plane across the flanges ($Z=0.355$ mm) at 5400 rpm. ······	119
4.55	Contour plots of Z - axial vorticity of (a) air and (b) helium at the plane across the flanges ($Z=0.355$ mm) at 15000 rpm. ······	120
4.56	Contour plots of Z - axial vorticity of (a) air and (b) helium at the plane between the arm and the disk ($Z=0.8$ mm) at 5400 rpm. ······	121
4.57	Contour plots of Z - axial vorticity of (a) air and (b) helium at the plane between the arm and the disk ($Z=0.8$ mm) at 15000 rpm. ······	122
4.58	Contour plots of X - axial vorticity of on three plane across the stiffening; (a) near the arm. (b) middle of the flanges. (c) the end of the flanges in air at 5400 rpm. ······	124
4.59	Contour plots of X - axial vorticity of on three plane across the stiffening; (a) near the arm. (b) middle of the flanges. (c) the end of the flanges in helium at 5400 rpm. ······	124
4.60	Contour plots of X - axial vorticity on three plane across the stiffening; (a) near the arm. (b) middle of the flanges. (c) the end of the flanges in air at 15000 rpm. ······	125
4.61	Contour plots of X - axial vorticity on three plane across the stiffening; (a) near the arm. (b) middle of the flanges. (c) the end of the flanges in helium at 15000 rpm. ······	125
4.62	Contour plots of TI^* of (a) air and (b) helium at the inter-disk mid-plane ($Z=0$ mm) at 5400 rpm. ······	129
4.63	Contour plots of TI^* of (a) air and (b) helium at the inter-disk mid-plane ($Z=0$ mm) at 15000 rpm. ······	130

4.64	Contour plots of TI^* of (a) air and (b) helium at the plane across the flanges ($Z= 0.355$ mm) at 5400 rpm.	131
4.65	Contour plots of TI^* of (a) air and (b) helium at the plane across the flanges ($Z= 0.355$ mm) at 15000 rpm.	132
4.66	Contour plots of TI^* of (a) air and (b) helium at the plane between the arm and the disk ($Z = 0.8$ mm) at 5400 rpm.	133
4.67	Contour plots of TI^* of (a) air and (b) helium at the plane between the arm and the disk ($Z = 0.8$ mm) at 15000 rpm.	134
4.68	Displacement in X – axis on the center of the magnetic tips at 5400 rpm.	136
4.69	Displacement in Y – axis on the center of the magnetic tips at 5400 rpm.	137
4.70	Displacement in Z – axis on the center of the magnetic tips at 5400 rpm.	137
4.71	Displacement in X – axis on the center of the magnetic tips at 15000 rpm. ...	138
4.72	Displacement in Y – axis on the center of the magnetic tips at 15000 rpm. ...	138
4.73	Displacement in Z – axis on the center of the magnetic tips at 15000 rpm.	139
4.74	Power Spectral Density of the in-plane displacement at 5400 rpm.	141
4.75	Power Spectral Density of the axial displacement at 5400 rpm.	141
4.76	Power Spectral Density of the velocity fluctuation downstream of the SSU at 5400 rpm.	142
4.77	Power Spectral Density of the in-plane displacement at 15000 rpm.	142
4.78	Power Spectral Density of the axial displacement at 15000 rpm.	143
4.79	Power Spectral Density of the velocity fluctuation downstream of the SSU at 15000 rpm.	143
A.1	Contour plot of velocity with vectors of air at 5400 rpm.	151
A.2	Contour plot of velocity with vectors of helium at 5400 rpm.	153
A.3	Contour plot of velocity with vectors of air at 15000 rpm.	155
A.4	Contour plot of velocity with vectors of helium at 15000 rpm.	157
A.5	Contour plot of Z-axial vorticity for the air flow at 5400 rpm.	159
A.6	Contour plot of Z-axial vorticity for the helium flow at 5400 rpm.	161
A.7	Contour plot of Z-axial vorticity for the air flow at 15000 rpm.	163
A.8	Contour plot of Z-axial vorticity for the helium flow at 15000 rpm.	165
B.1	Contour plot of velocity with vectors of air at 5400 rpm.	168
B.2	Contour plot of velocity with vectors of helium at 5400 rpm.	170
B.3	Contour plot of velocity with vectors of air at 15000 rpm.	172
B.4	Contour plot of velocity with vectors of helium at 15000 rpm.	174
B.5	Contour plot of Z-axial vorticity for the air flow at 5400 rpm.	176
B.6	Contour plot of Z-axial vorticity for the helium flow at 5400 rpm.	178
B.7	Contour plot of Z-axial vorticity for the air flow at 15000 rpm.	180
B.8	Contour plot of Z-axial vorticity for the helium flow at 15000 rpm.	182

List of Tables

3.1	Table 3.1: Physical properties of air and helium at 20 °C.	33
3.2	Table 3.2: Material properties for the structural analysis.	34
4.1	Table 4.1: Natural frequency of the lower Slider Suspension Unit.	95

Symbols

r : Radius of the disk

r_c : Critical radius

r^* : Non-dimensionalized radius

Re : Reynolds Number

z^* : Non-dimensionalized height in the axial direction

Ω : Disk tip rotating speed

ρ : Density

ν : Kinematic viscosity of the fluid

S : Ratio of inter-disk spacing to disk radius

Δt : Time step

P : Pressure

η : Smallest eddy length scale of the Kolmogorov microscale

u_η : Velocity scale of the smallest eddy of the Kolmogorov microscale

t : Time

l_0 : Largest eddy length scale

u_0 : Velocity scale of the largest eddy

λ : Smallest eddy length scale of the Taylor microscale

δ : Thickness of the boundary layer

δ_E : Thickness of the Ekman layer

- ω : Rotating speed of the disk
- τ_0 : Timescale of the largest eddy
- τ_η : Timescale of the smallest eddy
- N: Number of samples
- U_r : Mean circumferential velocity component
- U_θ : Mean radial velocity component
- U_z : Mean axial velocity component
- V_{mag} : Normalized mean velocity magnitude
- ω_x^* : Normalized mean X-axial vorticity
- ω_y^* : Normalized mean Y-axial vorticity
- ω_z^* : Normalized mean Z-axial vorticity
- t^* : Non-dimensionalized time by one cycle duration of the disk
- x: Characteristic length

Abbreviations

- DNS: Direct Numerical Simulation
- ECM: Electronically Commutated Motor
- FVM: Finite Volume Method
- HDD: Hard Disk Drive
- IC: Inner Configuration
- LES: Large Eddy Simulation
- OC: Outer Configuration
- PES: Positioning Error Signal
- PIV: Particle Image Velocimetry

RMS: Root Mean Square

RPM: Revolutions Per Minute

SSU: Slider Suspension Unit

TI: Turbulence Intensity

VCM: Voice Coil Motor

CPU: Central Processing Unit

RAM: Random Access Memory

LDV: Laser Doppler Velocimeter

RMS: Root Mean Square

LDA: Laser Doppler Anemometer

SBR: Solid Body Rotation

TCV: Taylor Couette Vortices

HWA: Hot Wire Anemometer

TEV: Trailing Edge Vortex

LEV: Leading Edge Vortex

TV1: Tip Vortex 1

TV2: Tip Vortex 2

FEA: Finite Element Analysis

HGA: Head Gimbal Assembly

GUI: Graphic User Interface

FEM: Finite Element Method

FSI: Fluid-Structure Interaction

TI: Turbulence Intensity

Chapter 1

Introduction to the problem

1. Problem Description

1.1 Introduction

Information technology has become an essential part of our lives. Advances in this field have enabled many conveniences, as well as new fields of technology. Examples of such advances are the development of the Internet, user-friendly software and interfaces as well as ever-increasing applications of big data. An implicit requirement has been the advancement of data storage.

Despite the invention of many other storage devices, the Hard Disk Drive (HDD) has retained its dominant position and the largest market share of the data storage field. It is anticipated that the HDD will continue to play the main role for the foreseeable future.

The HDD has many superior features compared with other storage devices. In particular, it is very portable. Today's HDDs in laptops are normally 2.5 inches or less and the trend

is towards even smaller sizes. HDD's are also quite durable. Except for a few extreme cases (i.e. water leakage, collision and contact with a strong magnetic field), the HDD can function semi-permanently. Also, HDD's have the cheapest cost per unit storage capacity compared with other devices. For these reasons, much research is done in the data storage industry and academic institutions to develop new technologies to improve the mechanical and electrical efficiency of the HDD. The future trend of the commercial drive points towards continued enhanced portability, manufacturability, reduction of noise and heat from the spindle, decreased power consumption, prompt data seeking, and increased data capacity. To this end, the size of the disk is getting smaller, and the rotating speed is getting faster.

1.2 Hard Disk Drive components

Commercial HDDs are equipped with at least four stacks of concentric and equally-spaced disks. All the disks are rotated by the spindle at the center. Between each stack of disks, a hub is inserted. The hub co-rotates with the disk and has a radius 30 or 40 % of the disk. Since both the upper and the lower surfaces of the disk are capable of storing data, two Slider Suspension Units (SSU) are mounted on the upper and the lower surface of the actuator arm, which is inserted between neighboring disks. On the SSU, a magnetic tip is mounted. This magnetic tip actually writes and loads data from the disk surface. Since the SSU is stamped of very thin steel alloy, two stiffening flanges are added on the SSU perpendicular to the circumferential direction of the disk. Outside the disk domain, a Voice Coil Motor (VCM) is installed (Figure 1.1). This VCM supports the actuator arm so that the stroke of the arm can rotate along the axis parallel to the rotating axis to cover

the whole surface of the disk. In the middle of the actuator arm, one or two perforations exist to save electrical power consumption and moment of inertia for the stroke of the arm by reducing the weight of the arm. In the region upstream of the arm, an air dam, an air spoiler or other types of blockage may be installed. The role of these components is to decrease turbulent kinetic energy of the fluid approaching the SSU. A sealed enclosure surrounds all of these components. Particularly, the enclosure is designed with a small clearance between its wall and the edge of the disk stack. However, in the region upstream and downstream of the actuator arm, the disk domain is not surrounded by the enclosure to accommodate the stroke of the arm and the SSU. The top and the bottom surface of the enclosure are covered with a steel alloy plate which enables the space inside the enclosure to be sealed from the outside.

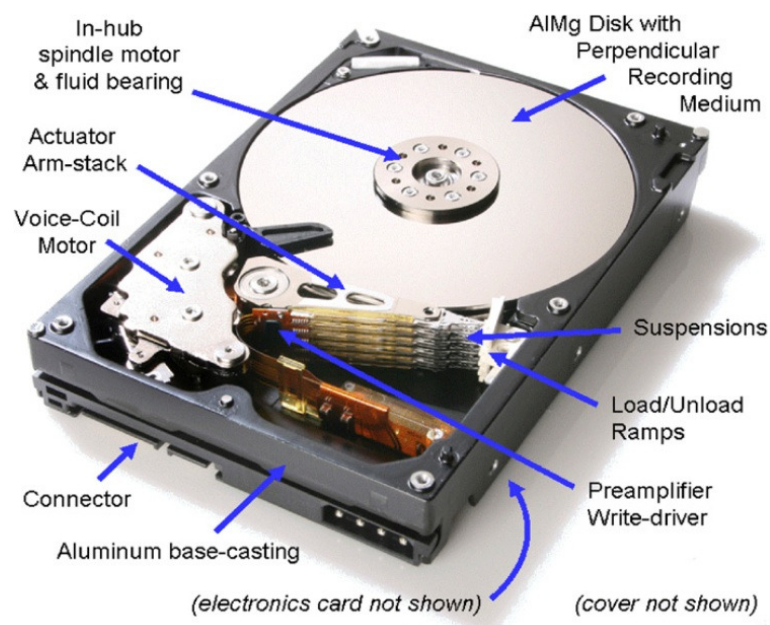


Figure 1.1: Picture of components of HDD (The first Terabyte capacity HDD shipped by Hitachi GST with five 95 mm disks). [1]

1.3. Motivation

The performance of the HDD needs to improve continually so that it can keep pace with the increasing performance of other pieces of hardware (i.e. Central Processing Unit (CPU) and Random Access Memory (RAM)). The improvement of the HDD performance doesn't simply imply an increment of the HDD capacity. To improve the performance of the HDD, the rotating speed of the disk has to increase. When the first HDD was invented by IBM, it rotated at 1,200 rpm so that the space between a pair of disks showed a laminar and stable flow. Today, most commercial HDD's currently on the market have rotation speeds from 5,400 rpm to 7,200 rpm. However, the rotating speed of the disk needs to increase even further to improve the data transfer speed and seek time. The industries in this field are aiming at rotating speeds higher than 15,000 rpm [3]. Corresponding to the elevated rotating speed, the flow field between each pair of disks is highly turbulent and unsteady. Particularly, this turbulent flow and the complicated geometries of the actuator arm and the SSU induce an intensified fluid-structure interaction phenomenon upstream and downstream of the arm. On the other hand, the size of the disk needs to be smaller to decrease the total size and the weight of the HDD. Since the HDD needs to store more data on the smaller disk surface, the aerial density of data has to be increased. The aerial density on the disk of the first HDD was merely 2 Kbits/in². An aerial density of 100 Gbits/in² was achieved in 2005 [2]. Researchers are still trying to increase the data density up to Tbits/in² scale. Therefore, the positioning accuracy of the SSU which actually reads and writes data on the disk surface also has to be improved to decrease the size of the disk and seek time of data. However, the turbulent flow induced by the rotation of the disk generates a flow-induced vibration on the SSU

which deteriorates data seek time or leads to the failure of the HDD. Many different solutions have been explored and applied in commercial drives. The most common method is installing a blockage upstream of the actuator arm. The role of the blockage is to decelerate the flow field and reduce the turbulent kinetic energy around the actuator arm and the SSU. However, these methods are not fundamental solutions to eliminate the flow-induced vibration of the SSU. For this reason, helium is chosen as an alternative working fluid in the HDD due to its high kinematic viscosity.

In the present investigation, one of the main purposes is the reduction of the flow-induced vibration in the SSU at fast rotating speeds of the disk. As the flow velocity distribution developed by the rotation of the disk becomes faster, the flow field becomes more susceptible to change by small perturbations. It means that flow characteristics can possibly be altered by the deformations in the SSU, and correspondingly new fluid forces are induced on the SSU surfaces which further lead to a modified deformation. Therefore, it is imperative to include these instantaneous flow/structure interactions. For this reason, a coupled Fluid-Structure Interaction (FSI) algorithm of ANSYS package is employed to compute more realistic frequencies of the flow-induced vibration by accounting for the mutual influences of the flow field and the SSU deformation. Adding to this, the flow field around the SSU and the arm where the most turbulent flow arises is expected to be stabilized favorably by the higher viscous force of helium than air without the need for any flow blockages. As a result, helium is estimated to decrease the flow excitation on the SSU and stabilize the turbulent flow around the arm and the SSU, and lower the power consumption for the disk drive operation so that much improved positioning accuracy of the magnetic tip can be achieved efficiently.

Chapter 2

Literature review

2.1 Unobstructed flow

2.1.1 Experimental results in unobstructed flow

In 1974, Lennemann [4] visualized the flow field between a pair of co-rotating disks experimentally. His setup consisted of two co-rotating disks. To measure the flow pattern between the two disks, the upper disk was made of transparent glass, and brass was used for the lower disk. Both disks were clamped onto the same shaft and submerged in a water tank. The rotating speed of the disk was controlled by a motor installed at the bottom of the water tank, and a camera was suspended on the tip of the experimental apparatus. To visualize the flow field, hydrogen bubble, neutral-density beads, or suspended aluminum powder particles were used.

At the onset of the rotation, a laminar flow was obtained. However, as the rotating speed increased, the flow field experienced a transition from laminar flow to turbulent and unsteady flow near the water tank wall while the inner region still showed solid body rotation. The shape of the inner region was dependent on the clearance between the edge of the disk and the shroud. With the clearance of 8 mm, the inner region induced a hexagonal shape. As the clearance increased, the number of sides in the inner region decreased. For the case of the experiment without the shroud around the disks, an oval shape was achieved in the inner region.

In 1985, Mochizuki and Yang visualized flow the field between parallel disks using the method of dye injection, hydrogen-bubble generation and paraffin mist to investigate radial flows [5]. The experimental setup they used was equipped with a steady influx through the hole at the center of the disks. Their results revealed that a uniform velocity profile was formed in the region near the center of the disk. As the flow approached to the outer radius position, the flow field started oscillating with respect to the inter-disk mid-plane, and in the region further downstream near the edge of the disk, vortices started arising near both disks surfaces.

In 1988, Abrahamson et al. [6] investigated large scale motions and developed a detailed description of the flow structure between shrouded co-rotating disks. Four stacks of disks were submerged in a water tank enclosed by a plexiglass case. The flow structure was visualized by using the method of a “Bromothymol blue technique”, and velocity was measured using a particle tracking technique. Time-exposed photos were captured over a time period so that the displacements of the particles could be shown as streaks. As a result, the velocity was estimated by the length of the streaks. They observed the presence

of the inner region with a polygonal shape and a low mixing rate. The outer region was more turbulent and the corresponding mixing rate was higher than the inner region. Particularly, the same number of vortical structures as the number of side of the polygonal shaped-inner region arose around the outer region, and a precession rate of these vortical structures was estimated about 25 % of the disk rotation speed. On the plane perpendicular to the disk surface, a pair of counter rotating Taylor-Couette type vortices was observed. Near the shroud wall, a difference of the rotation rate between the region near the disk surface and the inter-disk mid-plane induced boundary layers (Ekman layer) on the upper and the lower disk surfaces. In these boundary layers, the fluid was driven radially outward direction toward the shroud wall. On the shroud wall, the fluid was redirected in the axial direction of the disk rotation toward the inter-disk mid-plane. Around the inter-disk mid-plane, corresponding radially inward flow existed to satisfy continuity. As a consequence, a pair of vortices was formed in the outer region in the r - z plane of the cylindrical coordinate system.

In 1990, Schuler et al. [7] performed a Laser Doppler Velocimeter (LDV) to measure a circumferential velocity component and its Root Mean Square (RMS) at four radial positions for three rotational rates ($\Omega = 300, 1200, \text{ and } 3600 \text{ rpm}$). Four disks were clamped by a single axle and enclosed by a fixed plexiglass shroud. Mineral oil droplets ranging from 0.5 to $2 \mu\text{m}$ were used for the LDV measurements. At each position, 2,500 samples were captured to compute accurate values of a mean velocity and a RMS. The velocity profile showed that the flow field departed from the motion of solid body rotation due to no-slip boundary condition on the shroud wall roughly at $r = 0.75$ at 300 rpm and $r = 0.65$ at 1,200 rpm where r indicates a dimensionless radial location. The

RMS profile indicated that maxima were observed at radial locations $r > 0.8$, and $r < 0.75$ where a boundary existed between the solid body rotation region and the outer region. Minima were found at approximately $r = 0.75$ where the mean velocity profile showed a maximum value.

In 1991, Tzeng and Humphrey [8] measured velocity profiles at the inter-disk mid-plane between a pair of co-rotating disks using the method of a Laser Doppler Anemometer (LDA). They used atomized silicon oils with a nominal diameter of $1 \mu\text{m}$ as a particle in an aerosol generator. They investigated five different rotating speeds (586, 1171, 1757, 3513, and 5269 rpm), and the measured data were non-dimensionalized by a local disk surface velocity. They observed two different regions distinguished by the critical radius $r_c = 34 \text{ mm}$. In the inner region ($r < r_c$), the velocity profile of air showed the value of the disk rotating velocity within 10 % of fluctuations. However, in the outer region ($r > r_c$), the velocity showed a linear deceleration up to 63 % of disk rotating speed.

In 2003, Soong et al. [15] performed experiments to investigate the nature of three-dimensional flow structures between a pair of co-rotating disks. They visualized a flow pattern between two disks by injecting paraffin mist through a hole in the middle of the rotating axis. Then, a laser light sheet with a thickness of approximately 2 mm illuminated the region of interest. They compared results of three different conditions; i) co-rotating disks, ii) one rotating (rotor) and one stationary (stator) disks, iii) counter rotating disks at various Reynolds numbers.

Their experiments proved that the case of co-rotating disks formed a radially stationary region called a Solid Body Rotation (SBR) region near the rotating axis. In the outer region, the Ekman layers developed on both the upper and the lower surfaces on the disks.

In the Ekman layer, the fluid was pumped radially outward direction, and external air was redirected into the rotating frame around the inter-disk mid-plane so that a pair of counter rotating vortices appeared at the outer region of the disk. Additionally, as the Reynolds number and the rotating speed increased, the size of the SBR region decreased. For the case of the rotor-stator disks, the Ekman layer only arose on the rotor disk surface, and the external air was absorbed from the outside the rotating domain near the stator disk surface. This process created a single vortex near the outer edge of the disk. Similar to the case of the co-rotating disks, the thickness of the Ekman layer became thinner and the vortex lost its generation regularity as the Reynolds number increased. The flow field between the counter-rotating disks showed more turbulent and chaotic flow near the edge of the disks. The SBR region was less obvious and smaller than that of the co-rotating disks. Therefore, the radially inward flow around the inter-disk mid-plane reached deeper than that of the co-rotating disks case toward the rotating axis. A pair of counter rotating vortices in the outer region was also observed. However, the increased level of turbulence induced a higher mixing rate in the outer region so that the presence of the vortices was observed with more diluted smoke than that of the co-rotating disks.

In 2007, Tsai et al. [9] performed a time-resolved Particle Image Velocimeter (PIV) and Laser Doppler Velocimeter (LDV) between a pair of co-rotating disks. They visualized flow field on the r - θ plane of the cylindrical coordinate system. Results revealed the presence of the inner region with a low mixing rate. Therefore, the inner region retained particles so that the inner region reflected illumination strongly whereas the outer region lost most of the particles. The inner region developed a triangular shape, and vortical structures with equal spacing were observed in the outer region. The number of the

vortical structures was equal to the number of polygonal sides in the inner region. The boundary between the inner and the outer region was clearly noticeable due to the particle accumulation in the inner region. The non-dimensional radius of the inscribed circle for the inner region was approximately $r^* = 0.4$, and the radius of the circumscribed circle was estimated as $r^* = 0.6$. The vortical structures in the outer region decided the shape of the polygonal inner region. As one vortical structure approached to a sample axis ($\theta = 0^\circ$), the vortical structure started pressurizing the inner region so that the area shrank gradually toward the rotating axis. However, when the vortical structure left the sample axis, the vortical structure stretched the inner region to the radially outward direction. No velocity fluctuation was found at the center of the vortical structure, and the maximum of the mean circumferential velocity was observed at the same position.

2.1.2 Numerical results in unobstructed flow

Dijkstra and Van Heijst [10] solved full Navier-Stokes equations numerically in 1983 with single disk rotating and two counter-rotating disks. The flow with single disk showed all the features from other works. It completed a single vortex cell in the r - z plane of the cylindrical coordinate system. They arbitrarily imposed two different angular velocity conditions on each disk. The flow field between two disks which were counter-rotating generated two cell structures on the r - z plane. A new finding was the presence of stagnation point on the disk surface with the lower rotating speed. On the both disk surfaces, the fluid was redirected toward radially outward direction to the enclosure. On the enclosure wall, the driven flow was carried vertically upward and experienced one more flow path change to the radially inward direction near the slower-rotating disk.

Since the higher-rotating disk generated more radial momentum, the size of vortex induced by the disk rotation with the higher velocity needed to show a larger size. As a result, the stagnation point was formed by an impingement between the inward flow of the larger vortex and the outward flow of the smaller size vortex in the radial axis.

Humphrey et al. [11] investigated the structure and dynamics of air flow between a pair of co-rotating disks. They performed two- and three-dimensional calculations with a range of Reynolds numbers ($Re = r\Omega^2/\nu$) (4,400, 7,400, 14,800, 22,000 and 48,000). Results reported that Ekman layers with thickness of the order of $(\nu/\Omega)^{1/2}$, where ν is the kinematic viscosity of air and Ω is the rotating speed of the disk, developed on both disk surfaces near the outer region. In this Ekman layer, the fluid was driven radially outward and forced to the rotating axial direction of the disk on the enclosure wall. Corresponding to this radially outward flow, a radially inward flow was observed near the inter-disk mid-plane. As a result, a pair of counter rotating vortices was completed maintaining symmetry with respect to the inter-disk mid-plane when the Reynolds number was less than 22,000. However, for the flow with $Re > 22,000$, the symmetry of the vortices was broken and they started oscillating with respect to the inter-disk mid-plane due to an intensified radially inward flow. After the oscillation, the radial inward flow showed periodic motion in the axial direction.

In 1998, the effect of the clearance between the tip of a disk and the enclosure wall on flow field was investigated by Iglesias and Humphrey [12]. In their study, two different distances were tested, $T = 0.186$ and 279 (with $T = H / R_2 + a - R$ where H is the axial distance between two disks, R_2 is the disk radius, a is the disk tip-enclosure wall clearance, and the R is the hub radius). The results of the numerical work indicated that

the threshold Reynolds number for transition to unsteady motion tended to decrease corresponding to an increase of the disk rim-enclosure clearance. The flow field was able to stabilize itself with an arbitrary perturbation at a low Reynolds number. However, for each configuration, above the critical Reynolds number (23,150 for $T = 0.186$ and 15,430 for $T = 0.279$), the flow field experienced transition from a stable flow to an unsteady three-dimensional flow without any perturbations.

Various configurations and Reynolds number of flow were tested numerically by Herrero et al. [13] in 1999. They investigated flow pattern changes corresponding to the change of the Reynolds number from 0 to 82,380 and a ratio of inter-disk spacing to disk radius, S , in the range between 0.05 and 0.2. They presented a bifurcation diagram for the flow between a pair of disks. This diagram showed three regions for different values of S , Re .

- i) Two-dimensional steady flow with inter-disk mid-plane symmetry.
- ii) Three-dimensional unsteady flow with shift-and-reflect symmetry.
- iii) Three-dimensional unsteady flow with symmetry breaking about the inter-disk mid-plane.

A full three-dimensional analysis was performed by Tatewaki et al. [14] in 2001 employing a Large Eddy Simulation (LES) of turbulence model. Their physical model consisted of three stacks of disks rotating at 10,000 rpm and surrounded by an enclosure wall. What they have observed was a presence of the secondary flow through a clearance between the tip of the disk and the enclosure wall. This secondary flow induced a phase

difference of spatial pressure patterns between the top surface and bottom, and created a disk flutter.

Ferdinand [16] performed numerical calculations to find a correlation between velocity fluctuations and disk vibrations in 2010. The fluid domain in his model was coupled with disks using commercial aerodynamics/structural code. Due to a presence of Ekman layers on the disk surfaces, there were corresponding radially inward flows at the inter-disk mid-plane region and completed Taylor Couette Vortices (TCV) near the edge of the disks. Also, this radially inward flow induced an unstable wake which moved in the axial direction toward each disk surfaces. The occurrence of this unstable wake was highly related with the deflection of the disk. The direction of the deflection was clearly inverted between two disks, and a sudden deflection with a high magnitude was observed when the unstable wake was redirected toward each disk.

2.2 Obstructed flow

2.2.1 Experimental results for obstructed flow

Lennemann [4] tested the effect of the slider arm on the flow field between a pair of co-rotating disks. Observations from experiments showed that the arm changed the flow pattern completely for each radial and circumferential position. He characterized four different regions in the flow field with the slider arm in the middle of the flow field [4].

- a) Turbulent wake region behind the arm.
- b) Flow re-stabilized to the solid body rotation downstream of the arm.
- c) Turbulent region upstream of the arm due to direction change of flow.
- d) Vortex sheet shed from the arm tip.

Important findings from the experiments were the presence of vortex sheet and the disappearance of the rotating central core.

Abrahamson et al. [17] described modifications of flow pattern caused by an insertion of a read arm blockage on flow field. The arm was occupying approximately 90 % of the disk radius and 57 % of an axial separation of the disks. They reported that a primary difference was three-dimensional turbulent region downstream of the arm where the inner region still showed relatively two dimensional solid body rotation. Through a clearance between the tip of the arm and a co-rotating hub, the flow field near the inner region was accelerated due to strain. However, the inner region was decelerated abruptly 170° downstream of the arm and such a decelerating trend lasted to 190° downstream of the arm. Around the vicinity of the arm, the flow field had several features. One of them was the presence of a stagnation point on the upstream surface of the arm. The incoming flow

upstream of the arm at the inter-disk mid-plane radii smaller than the stagnation point was redirected toward the co-rotating hub and accelerated through the clearance in the circumferential direction. At the tip of the arm, flow separation was observed and generated strong re-circulations in the region downstream of the arm. The flow at radii larger than the stagnation point climbed up the arm or was driven to the outside of the rotating frame. The flow across the arm was also characterized by the location of the stagnation point. The portion at radii smaller than the stagnation point was drawn radially inward whereas the flow over the arm maintained constant radius at radii larger than the stagnation point.

Tzeng and Humphrey [8] compared results from experiments with and without an obstruction in the middle of flow field. They measured the radial distribution of the average circumferential velocity component at 68° , 180° and 292° downstream of the arm at 3,513 rpm. What they observed was the presence of an acceleration region between the obstruction and the co-rotating hub so that the average circumferential velocity showed a higher magnitude than that the local disk velocity. Moreover, the presence of the obstruction revealed that most of turbulent flow was concentrated around the region downstream of the blockage while the unobstructed flow induced most of its turbulent flow near the outer disk region where the flow field was highly sheared.

Tzeng and Chang [18] performed Time-resolved Laser Doppler Anemometry (LDA) measurements in 1991. They collected data at the inter-disk mid-plane. Their results supported that an arm blockage caused an accelerated mean flow which exceeded the local disk velocity in the inner radii region, and this high velocity flow gradually relaxed

from 50° to 180° downstream of the arm blockage. After the dissipation of the sudden velocity increase, the flow field showed very little variation from 180° to 310° .

In 1993, Usry et al. [19] measured time-resolved circumferential velocity component using a Laser Doppler Velocimeter (LDV) and a Hot Wire Anemometer (HWA) technique with two different lengths of obstructions (15.9 mm and 31.8 mm). They reported that both lengths of the obstructions could alter the mean velocity and RMS profiles. In particular, the short obstruction generates clear two peaks which is estimated to be frequencies of shedding from the obstruction. The most dominant frequency was found at 132 Hz where the long obstruction showed three relative weak peaks at 93, 137, 183 Hz. The region upstream of the obstructions was also measured. Those results revealed that the same dominant frequencies existed as observed downstream of the obstructions. However, the amount of energy was quite much higher than that of the region upstream of the obstructions. These results supported that the oscillating motion of the flow field could be reestablished to the state of unobstructed flow condition within one revolution of the disk.

Girard et al. [20] investigated the impact of a rotary style arm on flow field between co-rotating disks with an enclosure. They recorded the entire fluid motion in the domain between two disks, and found tangential slip of the fluid to the disk surfaces with a low velocity magnitude upstream of the arm and a high velocity downstream of the arm. Corresponding to this velocity difference at two different azimuthal locations, an azimuthal pressure gradient was observed. The highest pressure gradient was found at the region upstream of the arm and it induced a strong shear at the arm tip where a mixing layer-like structure was formed. Since not all the incoming flow upstream of the arm was

redirected toward the space between the arm and the hub, the portion near the outer region passed across the clearance between the arm and the disks.

Barbier et al. [21] reported a flow pattern change depending on the position of the Slider Suspension Unit (SSU). They designed a tapered arm and SSU with one square and two circular weight saving holes in the middle. Two configurations of the arm and the SSU were tested at several rotating speeds (250, 500, 1000, 1500, 2000, and 3000 rpm) using Particle Image Velocimetry (PIV) technique. For the inner configuration, the incoming flow upstream of the arm was sharply redirected toward the clearance between the SSU and the hub. This redirected flow induced unsteady toroidal vortices from the tip of the SSU. Adding to these findings, a three-dimensional reversed flow was found upstream of the arm and the SSU to satisfy fluid continuity, and a large amount of air was driven into the rotating frame from outside of the disk domain downstream of the arm. For the outer configuration, since the space between the SSU and the hub was wide enough to allow a smooth flow redirection so that the reversed flow upstream of the arm observed for the inner configuration was absent. The redirected flow generated a boundary layer flow on the upstream lateral surface of the arm and was highly sheared at the tip of the arm.

In 2007, Aruga et al. [22] conducted experiments in helium- and air-filled chambers to measure Positioning Error Signals (PES) at the tip of magnetic heads. To maintain constant material properties, they fixed temperature of a chamber at 20°C. Their experimental apparatus consisted of four stacks of disks with diameters of 3.5 inches rotating at 15,000 rpm with an enclosure which enabled the chamber to prevent a leakage of helium and air. The conclusions of the experiment were:

a) The helium-filled drive's positioning error was less than half of that in the air-filled

drive.

- b) In the helium-filled drive, low frequency windage, disk flutter, and suspension resonance were reduced by around 10 dB or more.

Kaneko et al. [23] studied effects of the weight saving hole in the middle of an arm on flow field between disks. They submerged the arm in a water channel to lower the inlet flow velocity at a desired Reynolds number by using fluid with a higher kinematic viscosity. They summarized their new findings:

- (a) Trailing edge vortex (TEV): alternating vortices in the wake of the carriage arm (St is about 0.24)
- (b) Leading edge vortex (LEV): small scale vortices shed from the leading edges of the carriage arm due to shear flow instability,
- (c) Tip vortex 1(TV1): disturbance due to the flow wrapping around the tip of the carriage arm,
- (d) Tip vortex 2(TV2): small scale vortices in the shear flow separated from the arm tip in the cases that the installation angle is not zero.

Kil et al. [24] visualized flow field with air and helium with a 2.5-times expanded geometry between a pair of co-rotating disks in 2012 using the PIV technique. Their designs of the experiment were based on Seagate cheetah 2.5 inch drive. They also investigated two different configuration of the arm and the SSU like Barbier's work; i) inner configuration and ii) outer configuration. They hypothesized the helium flow could successfully reduce turbulent flows due to its inertial properties. At 20° C, the kinematic viscosity of helium is approximately 10.2 times higher than that of air which can lead to a higher viscous force, and the density of helium is merely 1/7 than that of air so that

inertial fluid forces from helium are always lower than that of air under the same velocity. Results proved that the helium flow was more affected by the rotation of the disk and the presence of the arm and the SSU than the air flow. Since the kinematic viscosity of helium is higher than that of air, more momentum from the disks was transported into the fluid region. For this reason, the flow field showed a higher velocity magnitude in most of regions and more decelerated by the presence of the arm and the SSU than the air flow. The higher kinematic viscosity of helium also decreased a level of turbulence intensity downstream of the arm and the SSU so that a reduced level of flow induced vibrations was expected on the magnetic head.

2.2.2 Numerical results for obstructed flow

Tatewaki et al. [14] compared results with and without an arm in the middle of flow field. Due to the presence of the arm, the secondary flow observed in the unobstructed condition was removed for this condition. Adding to this finding, the radial velocity distribution showed an abrupt increase in the vicinity of upstream and downstream of the arm. Corresponding to the increment of the radial velocity near the arm, considerable excitation forces were found at the same regions.

Hayato et al. [25] performed numerical simulations to find a correlation between aerodynamics forces and amplitude of disk vibration by employing the Large Eddy Simulation (LES) technique. The disk vibration was estimated to be highly related with positioning error of a read/write head. Their results revealed that the presence of the arm caused intensified pressure fluctuations on the disk surface where the arm was located. Additionally, the presence of the arm also induced steep velocity gradients between the

top and the bottom surfaces of the arm and the upper and the lower disks. This steep velocity gradient led to shear stress increase and created more disk vibration.

In 2002, Kubotera et al. [26] tested the effect of the weight-saving hole in the middle of the arm on flow field. They created geometries based on an actual 3.5 inch disk drive rotating at 10,000 rpm. They observed three-dimensional Karman-type periodic vortices with a frequency of 4 kHz downstream of the arm. The flow with the weight-saving hole generated relatively larger scale of vortex shedding than those of the arm without the hole. In particular, an incoming flow upstream of the arm climbed up the upstream rib and induced a pair of counter-rotating vortices inside the weight-saving hole which had the same frequency as the shedding downstream of the arm. These vortices inside the hole showed growth in a size gradually. After those vortices completely filled the height of the hole near the downstream rib, they escaped the hole and created the vortex shedding downstream of the arm.

Kirpekar and Bogy [27] reported changes of flow field in presence of various flow stabilizers upstream of the arm. The tested installations were M0; original flow, M1; a blocking plate placed upstream between co-rotating disks, M2; a spoiler located downstream of the arm, and M3; a spoiler installed upstream of the arm. They investigated the influence of those blockages upstream of the arm. A reduction of the local velocity near the SSU and the actuator arm could be achieved, which eventually lead to a decrease of the windage-disturbance around the region of interest. Their results described that flow stabilizers were not fundamental solutions. For the case of M1, M2 and M3, those components upstream of the arm caused a decreased velocity in all regions of the fluid domain. Corresponding to the velocity reductions, a decreased kinetic energy

of the air flow was observed around the SSU. The case of M3 showed the most reduction of flow oscillations compared to other modifications. At the same time, those components generated vorticity streams in the region upstream and downstream of the arm, and these vorticity streaks could possibly induce another frequency of flow oscillation near the SSU. Kazemi M. [28] performed a numerical calculation with a simplified model of an actuator arm and SSU. Since a full three dimensional simulation requires much computing power, a wedge-like domain was isolated in the region upstream and downstream of the arm. To mitigate uncertainties of this flow domain simplification, steady-state velocity conditions acquired from an experiment by Schuler et al. [7] were imposed on ends of the extended upstream and downstream domain. New findings from this work were an observation of sudden pressure increase around the SSU. The leading surface of the slider induces higher pressure. Corresponding to this pressure increase by the slider, results of a Finite Element Analysis (FEA) for the slider revealed that the presence of the slider caused more intensified off-track vibration than the case without the slider. The FEA performed using commercial software (ANSYS) showed the magnetic tip oscillation in the off-track direction with the slider to be 6.35 nm whereas the flow without the slider merely generated an off-track vibration of 3.57 nm. The vibration of the slider was peaked at 2.05, 2.95, and 4.10 kHz which were frequencies of vortex shedding around the region of interest.

Most of investigations to reduce the flow-induced vibration on the SSU were focused on modifying the components or geometries inside the rotating frame (space between the disks). However, Zhang et al. [29] investigated effects of changes outside the rotating domain on the flow field. In particular, they hypothesized that an increased clearance

between the enclosure wall and the Voice Coil Motor (VCM) could decrease the velocity magnitude and the flow-induced vibration on the SSU by using the flow stabilizers between the disks at the same time. Three different conditions were modeled using the Large Eddy Simulation (LES) technique at 10,000 rpm; a) Model 1 (Original HDD), b) Model 2 (Modification 1). c) Model 3 (Modification 2). Model 2 was equipped with (1) a flow diverter upstream of the arm, (2) the increased bypass upstream of the flow diverter and (3) blocking the flow at vertical flex cable area to reduce the pressure fluctuation caused by vibration of the flex cable. In Model 3, Additional downstream flow spoilers were installed with the thickness of 0.3 mm. Large amount of velocity reduction was found by implementing flow diverters and making the bypass larger than the original model. Thus, a smaller magnitude of the flow-induced vibration was expected. From this result, FEA analyses were conducted with a solid model including an actuator arm and the SSU, and the transient data of each time step from the fluid calculations were used as boundary conditions. As expected, noticeable magnitude reductions were found from the FEA result. In particular, approximately 50 % vibration reduction was measured at the suspension tip for the case of M2 compared with the original case, and M3 showed more reduction than M2.

Liu et al. [30] studied the coupling effect of the fluid domain and the solid domain for high frequencies and small displacements. They hypothesized that the solid part would be vibrated by fluid forces, and the movement of the solid could influence the fluid flow around itself. In their results, the low velocity flow region increased than that of the flow with a fixed arm. The axial vibration of the arm reduced the flow rate over the arm which led to the growth of the region with the low velocity, and the flow rate to the space

between the arm tip and the hub increased. From this flow field change, the amplitude of the arm vibration changed in both the in-plane and the out-of-plane direction. The fluid-structure coupling effect decreased the vibration amplitude of the out-of-plane direction due to the growth of the low velocity region downstream of the arm. However, the increased flow rate at the tip of the arm strengthened the amplitude of the in-plane vibration.

A full three-dimensional model was built by Kil et al. [31] in 2012 using commercial software (ANSYS/CFX). Their model resolved the Taylor microscale and was based on a 2.5 times-time scale of an actual commercial disk drive (Cheetah drive from Seagate). Helium was selected as an alternative medium to air due to its inertial properties. The fluid domain between a pair of disks was modeled. In their observation, helium induced more accelerated velocity magnitude than air. Since the kinematic viscosity of helium is approximately ten times higher than that of air, helium transported more momentum into the fluid domain from the rotation of the disks than air. At the same time, strong shear layers arose around all solid surfaces caused by no-slip boundary conditions. In particular, the complexity of the SSU design triggered several streaks of shear layers in the downstream region. Since the velocity magnitude was higher in helium than air, more intensified shear layers were generated in helium than in air along the direction the disk rotation. However, this same higher kinematic viscosity of helium successfully lowered the level of turbulence intensity around the SSU. As a result, they estimated that using helium could make substantial contributions to the reduction of the flow induced vibration of the SSU, and improve the positioning accuracy of the magnetic tip.

Kil et al. [32] also investigated the effect of a weight-saving hole in the middle of an arm

on flow field numerically for air and helium. The weight-saving hole is perforated to make a stroke of the arm swift and to lower power consumption. However, the weight-saving hole perturbs the flow field downstream of the arm. They hypothesized helium to be a good working medium for reducing the unsteady flow downstream of the hole as it did downstream of the SSU. At low rotating speeds of the disk, helium flow successfully stabilized the turbulent flow downstream of the weight-saving hole compared with the air flow. As the rotating rate of the disk accelerated, the turbulence intensity of helium flow became more intensified than that of air. This turbulence intensity inversion between 1000 and 3000 rpm was induced by a stagnation point displacement. The incoming flow upstream of the arm made an impingement on the lateral surface on the arm and redirected toward a space between the co-rotating hub and the SSU or climbed up the arm and generated the unsteady vortex shedding downstream of the arm. These two streams of the incoming flow were distinguished by a stagnation point. At 1000 rpm, the stagnation point was observed near the outer end of the weight-saving hole in the helium flow, whereas in air the stagnation point was located in the middle of the arm. Therefore, vortex shedding downstream of the arm was weak in helium at 1000 rpm. However, the stagnation point was displaced radially inward direction in helium at 3000 rpm. Corresponding to this relocation, the helium flow started generating vortex shedding. Since the velocity magnitude of helium was higher than that of air due to more momentum transport by the higher kinematic viscosity, the vortex shedding downstream of the arm was more rigorous in helium than in air. As a result, increased level of turbulence intensity was found in the helium flow compared with air at 3000 rpm.

Sundaravadivelu et al. [33] measured aerodynamic forces on each component such as a

VCM, arm, slider and suspension. Their results suggested that the greatest aerodynamic force was found on the arm whereas the slider experienced the smallest force. As the frequency became higher, the off-track force tended to decrease gradually. However, the arm still showed the highest windage perturbation, and the lowest force was exerted on the slider. They also tested various ratio of helium-air mixture in the disk drive geometry at different positions of the SSU. With the low portion of helium under 40 percent, the flow didn't showed drastic change of the aerodynamics force compared with pure air. Nevertheless, corresponding to an increase of helium percentage, a reduction of the force was noticeable. In particular, the maximum decrease was observed when the SSU was positioned at the outer radius of the disk. As a result, a higher percentage of helium always guaranteed lower aerodynamic forces on the SSU.

Chapter 3

Problem Model

Full three-dimensional calculations have been conducted using a commercial code. All details regarding grid generations, time steps, calculation durations, governing equations, material properties, and boundary conditions are specified below.

3.1 Geometry generation

3.1.1 Actuator arm and Slider Suspension Unit

The actuator arm and the SSU were modeled based on a commercial drive (Cheetah Seagate drive) from Seagate. The arm had the shape of a tapered quadrangle with two weight-saving holes in the middle. The larger weight-saving hole had an elliptical configuration which was also tapered toward a smaller hole (Figure 3.1 (a)). The arm was inserted between two disks and occupies approximately a half of the clearance between the upper and the lower disk (Figure 3.1 (b)). All dimensions are shown below in the figures.

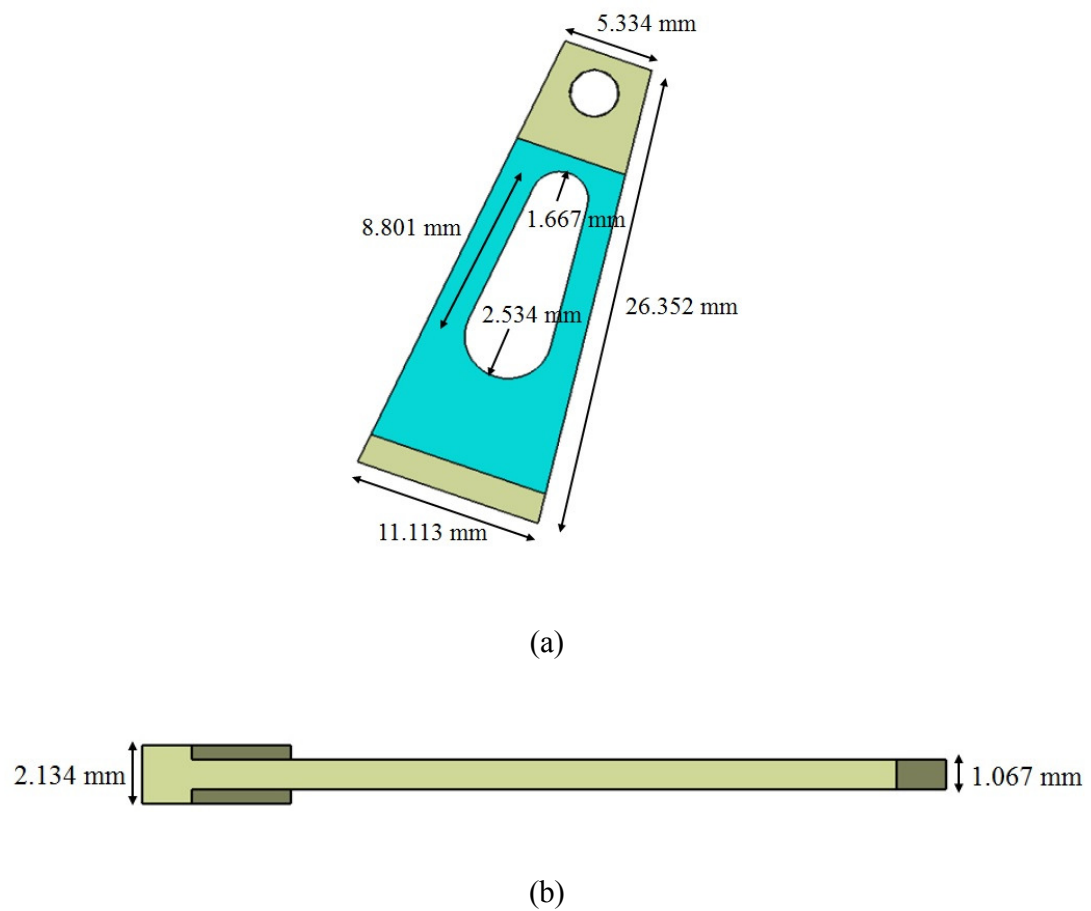


Figure 3.1: (a) Top view and (b) side view of the actuator arm with dimensions.

Two SSU's were mounted and made a perfect contact with the upper and the lower surface of the arm. Each SSU had a uniform thickness of 0.2 mm across the length and the largest hole among three perforations was concentric with the hole in the arm. One triangular hole was located in the middle of the SSU, and an elliptical hole was placed near a quadrangle tip which mimics the magnetic tip (Figure 3.2 (b)). One magnetic tip was attached on each SSU in the surface facing the disk (Figure 3.2 (a)), and One SSU had two stiffening flanges extruded in the rotating axial direction to reinforce a strength of the structure (Figure 3.2 (c)).

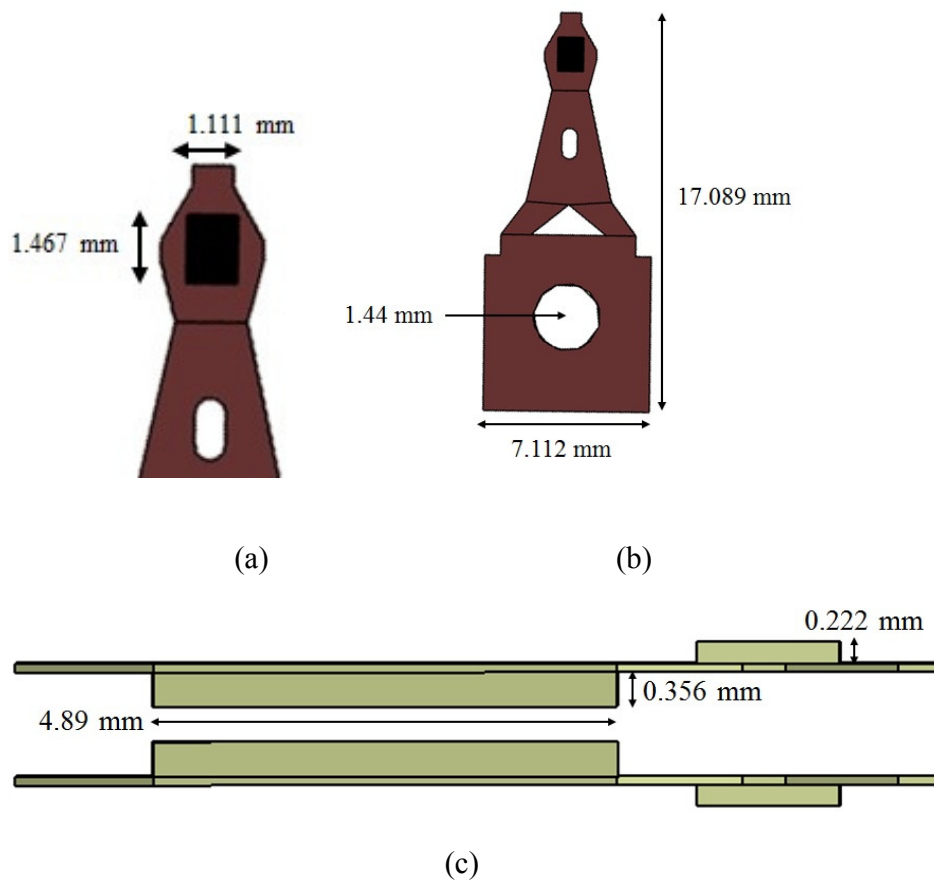


Figure 3.2: (a) Top view of the magnetic tip, (b) Top view of and (c) side view of the SSU with dimensions.

3.1.2 Disk

The disk was a perfect circular shape with a radius of 44.45 mm. Since the fluid domain was extracted between a pair of disks, two disks were modeled in the present investigation. Those two disks had the same dimensions and were spaced by a hub which rotates at the same rate of the disk. In the space between the disks, the actuator arm and the SSU's were inserted in the middle. The upper SSU faced the lower surface of the

upper disk, and the lower SSU was installed parallel to the upper surface of the lower disk (Figure 3.3).

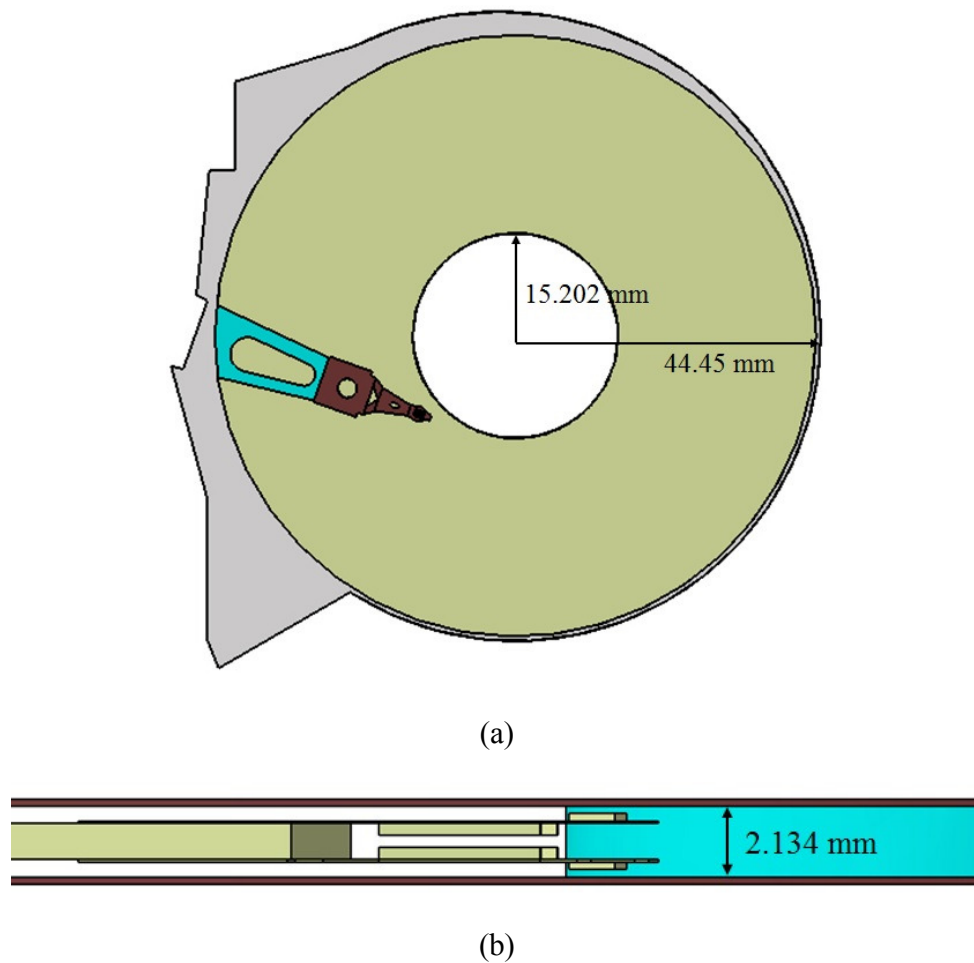


Figure 3.3: (a) Top view and side view (b) of the disk with dimensions.

3.1.3 Fluid domain

In general, the actual commercial HDD's are operated with three or four stacks of disks in the enclosure. Since there is a clearance between edges of the disks and the enclosure wall to prevent the disk surfaces and maintains a stability of the disk rotation from

collisions with the enclosure wall, the secondary flow exists through the gap. However, Tatewaki et al. [14] visualized the flow field inside the enclosure with three stacks of disks and found the secondary flow in the axial direction which showed interactions between layers of the disks. They also proved that the presence of the obstruction in the middle of the flow field was able to remove those interactions through the clearance between the edge of the disks and the enclosure wall so that the secondary flows were not observed in the obstructed condition. In the present research, the actuator arm and the SSU were able to perform a role of the obstruction. Therefore, the secondary flow in the direction of the rotating axis was assumed not to exist. As a result, the domain between a pair of disks was extracted for the numerical calculations. Also, from the investigation of Kil et al. [31], interactions between the inside and the outside of the rotating domain only existed with relatively steady and low velocities in small bypasses where the disk is not affected by the enclosure. Thus, the region outside of the rotating frame was not modeled and was captured by imposing an opening boundary condition on those bypasses (Figure 3.4).

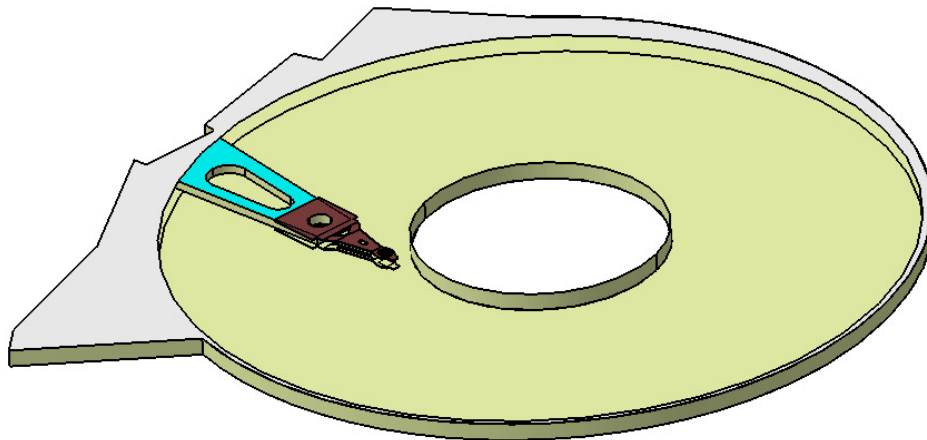


Figure 3.4: Schematic of the fluid domain.

3.1.4 Inner and Outer Configuration

Data is saved across the entire surface of the disk. This means a stroke of the actuator arm has to cover all area of the disk surface in the radial direction. Since high Reynolds number flows are susceptible to a small geometry change, different locations of the arm will generate quite different flow patterns. For this reason, two different positions of the arm and the SSU were simulated; i) Inner Configuration (IC), ii) Outer Configuration (OC). The IC was the case where the arm was located near the co-rotating hub (Figure 3.6 (a)). The OC was where the arm and the SSU were inserted with an alignment of the magnetic tip near the outer edge of the disk (Figure 3.5 (b)).

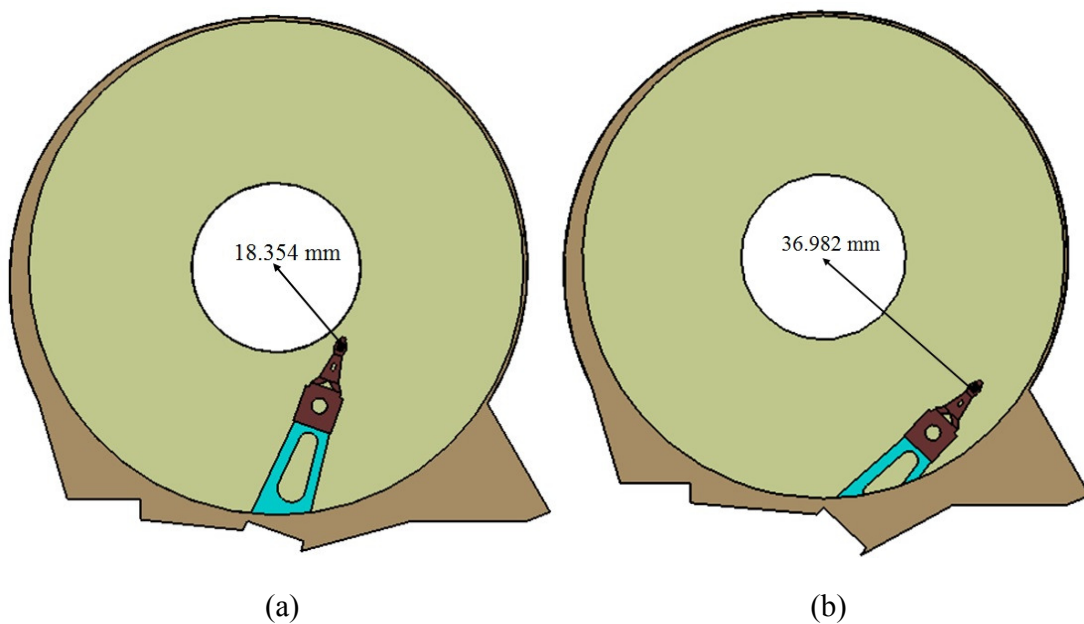


Figure 3.5: Top view of the Inner Configuration (a) and the Outer Configuration (b) with a distance between the rotating axis and the center of the magnetic tip.

3.2 Governing equations

The fluids were assumed to be Newtonian, incompressible and constant property. Mass and momentum conservation equations are given below:

$$\nabla \cdot \mathbf{U} = 0 \quad (5.1)$$

$$\frac{\partial \mathbf{U}}{\partial t} + \mathbf{U} \cdot \nabla \mathbf{U} = -\frac{1}{\rho} \nabla P + \nu \nabla^2 \mathbf{U} \quad (5.2)$$

where \mathbf{U} indicates velocity (vector), t is time, ρ is the density of the fluid, P is the pressure and ν is the kinematic viscosity.

3.3 Material property

The fluid domain in the present investigation was filled with air or helium. Material properties of both gases were selected under three assumptions; i) Air and helium are Newtonian fluids, ii) The flow field is incompressible, iii) Heat distribution inside the disk drive is small enough for the physical properties to be assumed constant. Temperature inside the HDD was assumed to be 20 °C (Ambient temperature). Overall, material properties used in the calculations are shown in Table 3.1

	Air	He	Ratio (He/Air)
Density (kg/m ³)	1.205	0.1667	0.138
Kinematic viscosity (m ² /s)	1.511 × 10 ⁻⁵	1.173 × 10 ⁻⁴	10.2

Table 3.1: Physical properties of air and helium at 20 °C.

Prior literatures suggest that the magnitude of the flow-induced vibration is of the order of nano-meters. Compared to the length of the Slider Suspension Unit (SSU) specified in section 3.1, the scale of the deformation is much less than 1 percent. Therefore, constant physical properties were assumed to be sufficient in an absence of non-linear and visco-elastic effects. Since an actual SSU consists of steel alloy, material properties of steel alloy in Table 3.2 were used

Young's modulus	210 GPa
Density	8,700 kg/m ³
Poisson's ratio	0.30

Table 3.2: Material properties for the structural analysis.

3.4 Initial conditions

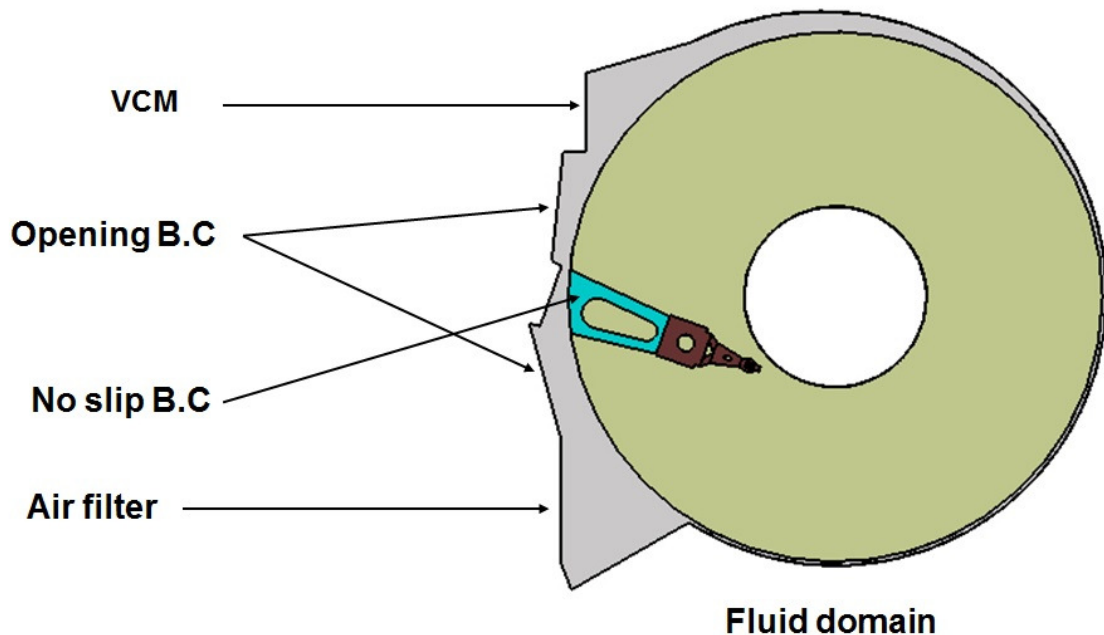
To obtain more realistic calculation results, an initial condition for the present study was the fully developed flow. For achieving this condition, a steady state analysis was performed first. A transient flow calculation was conducted with the initial condition from the above steady state analysis obtained in the absence of the coupling algorithm. All these calculations were completed using the same grid domain specified in Chapter 3.8.

3.5 Boundary conditions

Boundary conditions were imposed to simulate the operating state of the commercial drive. As mentioned above in Chapter 3.1, an opening boundary condition was imposed

on the surface where the rotating region was opened to the outside region (Figure 3.6). All surfaces of the solid domain were given no-slip condition, and on the SSU, the boundary condition was one of fluid-solid interaction except where the SSU's were mounted on the actuator arm. In summary:

- Disk surfaces and hub: $U_r = 0$, $U_\theta = r \times \Omega$, $U_z = 0$
- Arm: No-slip boundary condition
- SSU: Fluid structure interactions
- VCM walls: No-slip boundary condition
- Enclosure walls: No-slip boundary condition
- Mid-disk gap space to the outer enclosure: symmetry boundary condition



(a)

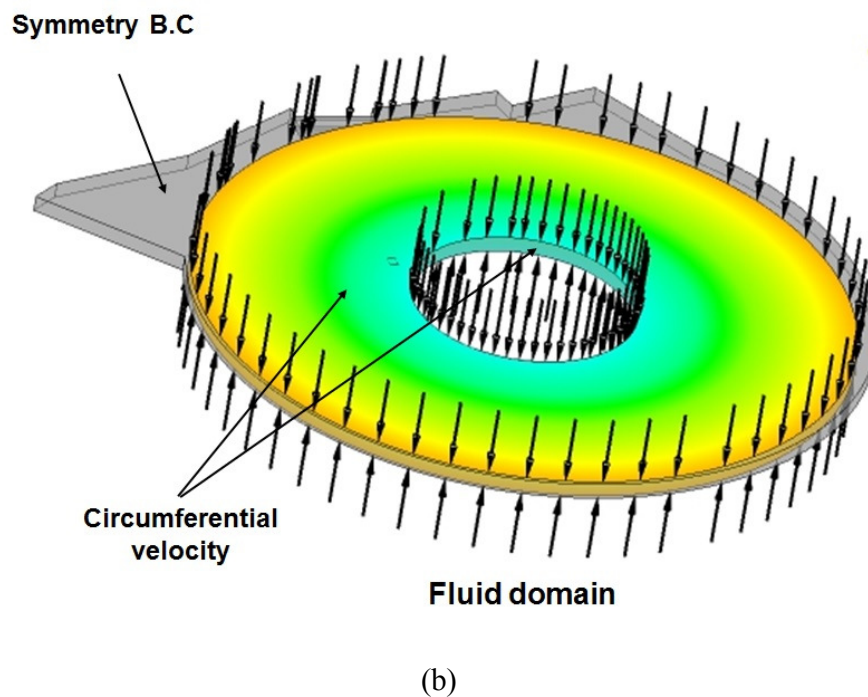


Figure 3.6: (a) Top view and (b) Iso view of the fluid domain with boundary conditions.

3.6 Introduction of ANSYS/CFX and ANSYS code.

ANSYS/CFX is extensively used commercial software based on the Finite Volume Method (FVM). It has capabilities to address fluid flow, heat transfer, multi-phase flow and fluid-structure interaction, and is equipped with well-designed Graphic User Interface (GUI) and a number of turbulence models. ANSYS - Mechanical is the Finite Element Method (FEM) code and is capable of solving a wide range of problems in linear and non-linear solid mechanics. In this study, the calculations of fluid flow were performed using ANSYS/CFX code, while ANSYS - Mechanical code is employed to solve solid domain problems. Since the present research is aiming at including instantaneous correlations between the solid and the fluid domain in each time step, a code-coupling Fluid-Structure Interaction (FSI) algorithm was used (Figure 3.7). In each

time step, fluid forces (pressure and shear stresses) were calculated by ANSYS/CFX. Since the prior works proved that the flow field experiences the strong velocity oscillation with respect to the inter-disk mid-plane. Moreover, the accelerated flow around the SSU will generate boundary layers and flow separations. For this reason, the fluid domain is calculated by employing Large Eddy Simulation (LES) which is estimated to be appropriate to calculate the unsteady flow field in the rotating frame [34]. Adding to this, the advection scheme is discretized with central difference scheme which shows quite robust iterations and requires small computing powers. As a result, the fluid forces from the calculations were imposed on surfaces where FSI was active in the solid domain. With boundary conditions from the fluid flow, deformations in the solid part was computed and returned to the fluid region as velocities. As a result, the deformations of the solid domain induced a change of the fluid flow.

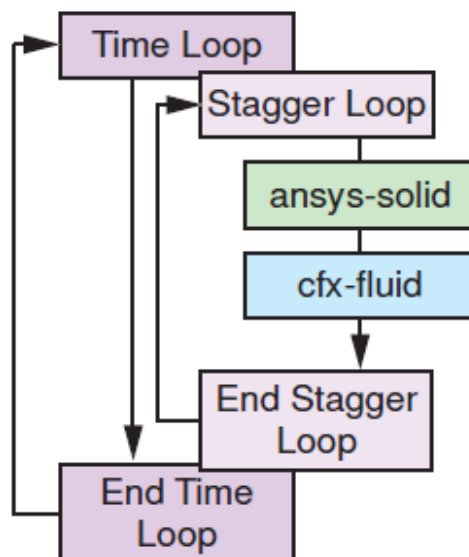


Figure 3.7: Flow chart of the FSI [34].

3.7 Grid generation

For grid generation, ICEM-CFD, a commercial code in ANSYS package, was used for both the solid and the fluid domain. All grid generation consisted of hexahedral elements. All details related to a grid size and criteria are specified.

3.7.1 Kolmogorov and Taylor microscales

For grid generation, the smallest eddy size had to be estimated to resolve all length scales of flow motions. These were Kolmogorov and Taylor microscales. Kolmogorov scale is obtained based on the following hypotheses [35].

1. At sufficiently high Reynolds number, the small scale turbulent motions are statistically isotropic.
2. The statistics of the small length scales, η , has a universal form that is uniquely determined by the viscosity and the dissipation rate.

Under assumptions of those hypotheses, Kolmogorov microscales were calculated by definitions below [36].

$$\eta / l_0 \sim \text{Re}^{-3/4} \quad (5.3)$$

$$u_\eta / u_0 \sim \text{Re}^{-1/4} \quad (5.4)$$

where η and u_η indicate the length and the velocity scale of the smallest eddy, l_0 and u_0 mean the length and the velocity scale of the largest eddy. As higher rotating speeds of

the disk are achieved, smaller scales of eddies are generated in the flow field. Therefore, the speed of the disk edge at 15,000 rpm (69.82 m/s at the edge of the disk) was used for the estimation of Reynolds number and the material properties of air were used. The spacing between the disks was used for l_0 .

$$\text{Re} \sim l_0 r \Omega / \nu \approx 9861 \quad (5.5)$$

$$\eta \approx 2.15652 \times 10^{-6} \text{ m} \quad (5.6)$$

$$u_\eta \approx 7.01 \text{ m/s} \quad (5.7)$$

The Taylor microscale is also used for the scale estimation. The smallest eddy size from Taylor microscale, λ , can be determined by following equations [36]. l_0 was also the value of the disk-to-disk clearance. Reynolds number was calculated at 15,000 rpm based on the material properties of air.

$$\lambda \sim l_0 \sqrt{15} \text{Re}^{-1/2} \quad (5.8)$$

$$\lambda \approx 8.33 \times 10^{-5} \text{ m} \quad (5.9)$$

From prior work, the highest turbulent flow was observed around the SSU and the region downstream of the actuator arm due to sources of unsteady flow such as the stiffening flanges and the weight-saving hole. Moreover, the coupled Fluid-Structure Interaction (FSI) algorithm requires tremendous Random Access Memory (RAM) and data storage spaces. Thus, the grid size by the Taylor microscale was selected to generate the grid domain and this smallest eddy size was only resolved around the SSU and the arm. Other

fluid regions were built by the eddy size, λ_d , from Taylor micro scale based on the radius of the disk.

$$\lambda_d \approx 3.8 \times 10^{-4} \text{ m} \quad (5.9)$$

As a result, in total 5.3 million hexahedral elements were used, and a snapshot of the grid domain for the fluid is show in Figure 3.8.

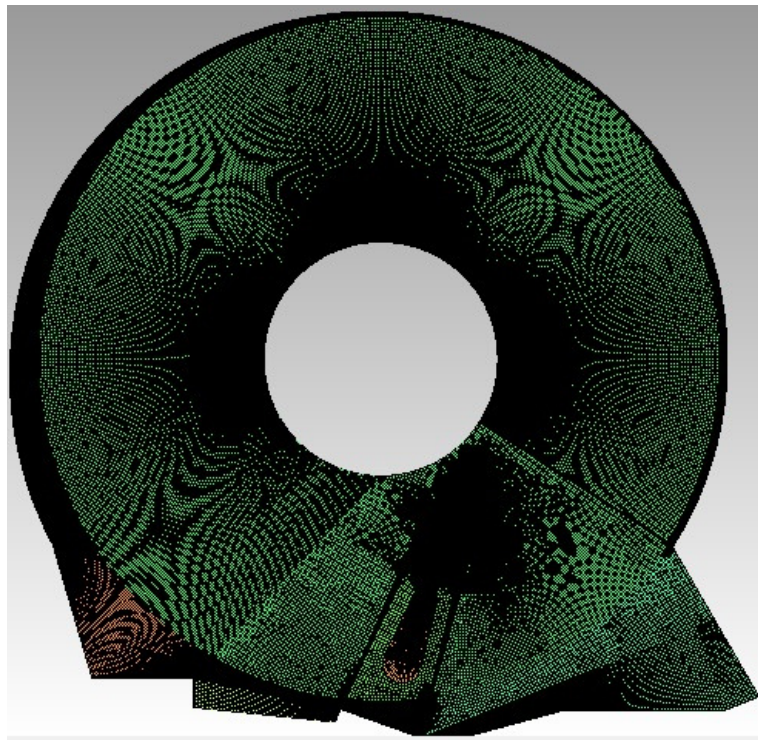


Figure 3.8: Snapshot of the grid domain for the fluid.

3.7.2 Boundary layers

Solid surfaces are always sources of boundary layers. Since the arm and the SSU were located in the direction blocking the incoming flow and the rotation of the disk was entirely governed by the circumferential motion, a strong boundary layer arises on a lateral surface of the arm. In this region, a condensed number of grids were used to capture vigorously sheared velocity region. The thickness of the boundary layer, δ , can be estimated by the solution of the Blasius equation [37]. Blasius equation is one of classical method to estimate the thickness of the boundary layer. The flow with a uniform directional inlet flow direction on a semi-infinite flat plate will induce the boundary layer. In the region far downstream where the boundary layer is assumed to be fully developed, the thickness of this boundary layer can be calculated using the solution of Blasius equation. As mentioned above, the flow field in the region upstream of the arm and the SSU shows the dominant motion in the azimuthal axis. Therefore, the solution of Blasius equation is reasonable method to estimate the thickness of the boundary layer induced on the surfaces of the arm and the SSU. The solution of the Blasius equation can be defined by

$$\delta = 4.96 \sqrt{\frac{\nu x}{U}} \quad (5.10)$$

where x is the characteristic length and U is the inlet velocity profile. In this research, the length of the actuator arm was used as the characteristic length, and the rotating speed at the edge of the disk at 5,400 rpm was inserted in the inlet velocity. From this calculation,

the boundary layer thickness, δ , was estimated by 1.7 mm, and eighteen layers of grid were used near the arm and the SSU to describe the boundary layer (Figure 3.9). The first grid was located 7.9×10^{-6} m away from the surface of the arm with no-slip boundary condition. This distance corresponds to $y^+ \sim 2$ using the length of the arm as the boundary layer length and the rotating speed at the edge of the disk as the free-stream velocity.

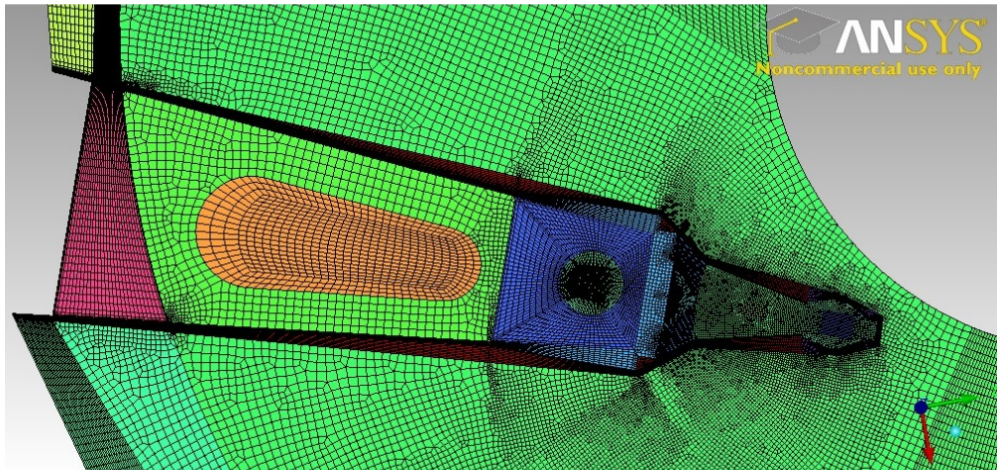


Figure 3.9: Snapshot of packed number of grid around the arm and the SSU.

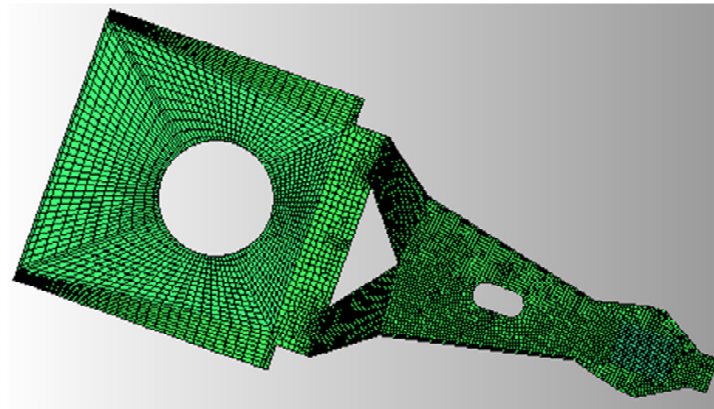
The other source of boundary layer was the enclosed condition of the disk drive. The inter-disk mid-plane region experiences a velocity reduction by no-slip boundary condition imposed on the enclosure wall, and corresponding velocity difference is introduced between the flow field near the disk surface and the mid-disk regions. Therefore, a boundary layer is developed near the disk surface. This is Ekman layer found in rotating fluid flows. In this region, the fluid is driven radially outward and corresponding radially inward flow is created by the enclosure wall near the inter-disk mid-plane. The thickness of Ekman layer, δ_E , can be scaled [39]

$$\delta_E = \left(\frac{\nu}{\omega}\right)^{1/2} \quad (5.11)$$

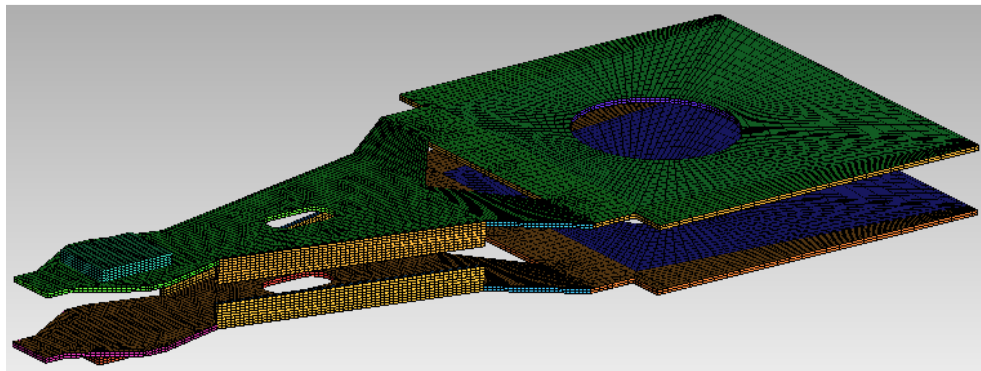
where ω is the rotating speed of the disk. For this thickness estimation, the kinematic viscosity of helium at 20 °C and the rotating speed of 5,400 rpm were used. By doing this, the thickness of Ekman layer was estimated as 2.16 mm. However, the clearance between two disks was already 2.134 mm, and a collision of two Ekman layers developed by each disk is expected. It means a condensed number of grids were required in the axial direction. As a result, totally 46 grids were used across the entire fluid domain, and the size was 0.0464 mm.

3.7.3 Solid domain

The solid domain basically had the same grid size as the fluid domain. The grid size on all the surfaces of the SSU except the surface meeting the actuator arm was 0.083 mm which was the Taylor microscale at 15,000 rpm (Figure 3.10). The surface where the SSU made a contact with the arm was given a fixed boundary condition (Chapter 3.6). Therefore, an infinitesimal displacement is expected around that surface. As a result, those surfaces had the grid size of 0.2 mm.



(a)



(b)

Figure 3.10: (a) Top view of the grid domain for the SSU and (b) Iso-view of the grid domain for the SSU.

3.7.4 Numerical result validation

For validation of the current numerical investigation, the results are compared with the experimental results performed by Kil et al. [34]. These features from their work are noted: 1) presence of three-dimensional inversed flow (Box A in Figure 1), 2) flow acceleration between the tip of the arm and the co-rotating hub (Box B in Figure 1) and, 3) fluid entrainment from outside of the rotating frame (Box C in Figure 1). As observed in

the contour plots of the experiment and the numerical calculation in Figure 1 (a) and (b), all the features found in the experiment are also observed in the result of the numerical work.

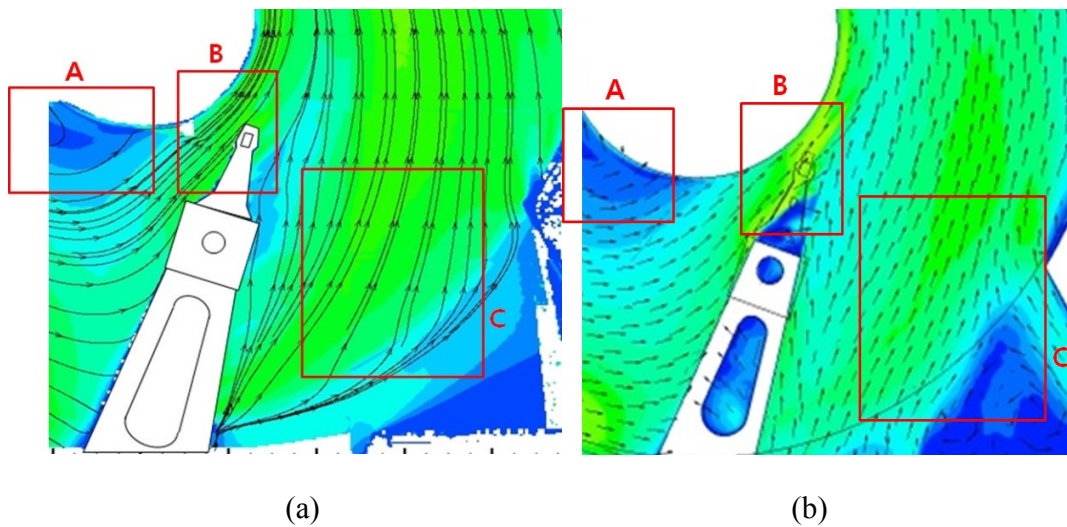
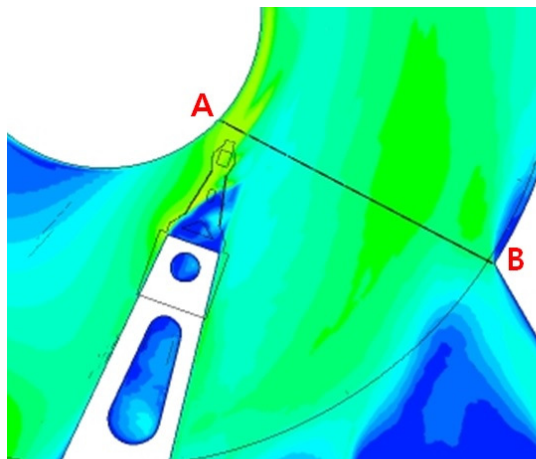


Figure 3.11: Mean velocity magnitude with streamlines at 5400 rpm on the inter-disk mid-plane from (a) the experiment and (b) the numerical calculation.

For more quantitative comparison, the mean velocity magnitude profile is plotted for the line A-B in Figure 2(a). The mean velocity magnitude profiles shown in Figure 2(b) and (c) reveal acceptable match of trends between the experiment and the current numerical work. The horizontal axis is non-dimensionalized radius. The increase of the mean velocity magnitude is observed in both the experiment and the numerical calculation, and is due to the acceleration through the clearance between the arm and the hub. Also, a velocity magnitude decrease is induced by the flow blockage of the actuator arm in the range of the normalized radius between 0.4 and 0.5. Farther out, the velocity magnitude

profile in both cases tends to show an increase as it recovers from the flow deficit caused by the SSU and the arm (Figure 2(b)). For the outer configuration, the flow field doesn't experience the severe blockage of the inner configuration. The incoming flow upstream of the arm is accelerated in the space between the tip of the arm and the co-rotating hub ($0.4 < R < 0.65$ in Figure 2(c)). The region where the arm and the SSU are located shows a velocity magnitude decrease in both numerical calculation and experiment ($0.65 < R < 0.8$ in Figure 2 (c)). In the region downstream of the arm, the flow redirection from outside of the rotating domain exists, resulting in a slight velocity magnitude increase. Overall, the result of the numerical work follows the trend of the flow field measured by the experiment in the region of interest. The ratio between the maximum values of the experiment and the numerical result is 77.8 percent for the inner configuration at 5,400 rpm, and is 89 percent for the outer configuration at 15,000 rpm.



(a)

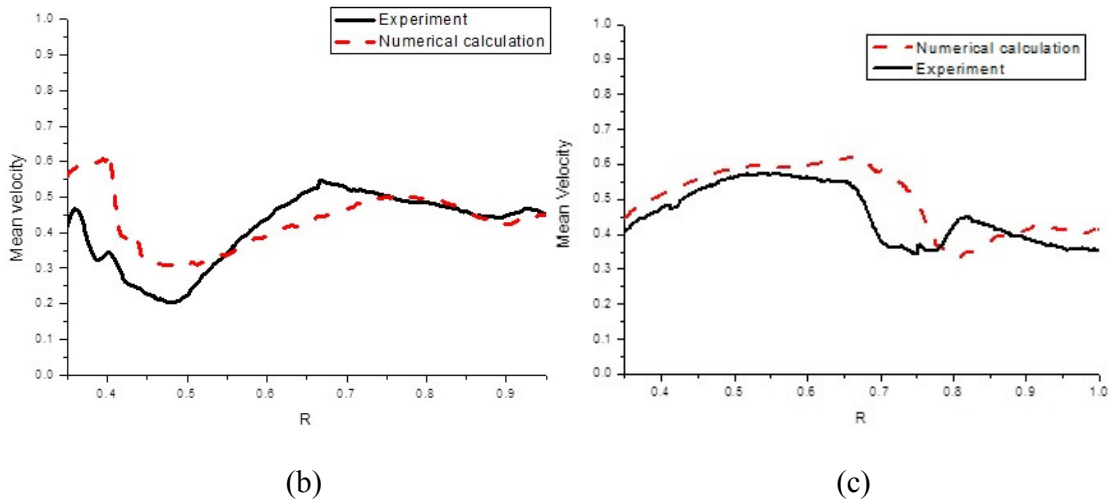


Figure 3.12: (a) The location of the line A-B where the mean velocity profile is measured. Mean velocity profiles of the experiment and the numerical calculation (b) for the inner configuration at 5,400 rpm and (c) for the outer configuration at 15,000 rpm.

3.8 Time step calculation

Time steps for the numerical works were also calculated by Kolmogorov microscales [36]. Kolmogorov time scale can be defined by

$$\tau_{\eta} \sim \tau_0 \text{Re}^{-1/2} \quad (5.12)$$

where τ_{η} is the time scale of the smallest eddy and τ_0 can be estimated by l_0 / u_0 . A small time step is needed to obtain physically accurate results. Therefore, Reynolds numbers were calculated using the rotating speed at the tip of the disk which was 25.136 m/s at

5,400 rpm and 69.822 m/s at 15,000 rpm. Then, the radius of the disk was plugged in τ_0 .

Time steps from these processes were

$$\tau_{\eta}^{1000} \approx 6.5032 \times 10^{-6} \text{ s} \quad (5.13)$$

$$\tau_{\eta}^{3000} \approx 1.4047 \times 10^{-6} \text{ s} \quad (5.14)$$

All simulations were conducted for one cycle of the disk rotation. At 5,400 rpm, one cycle consisted of 1709 time steps, and there were 2848 time steps at 15,000 rpm. Velocity magnitudes and fluctuating components of the velocity were calculated over one cycle. Errors from the number of the time steps are estimated for 95 % confidence interval. By taking the mean velocity and the fluctuating component on the mean and the standard deviation of a normal distribution, the $100(1 - \alpha)$ % confidence interval with an unknown standard deviation is given by [38]

$$U \pm \frac{t_{\frac{\alpha}{2}} S}{\sqrt{N}} \quad (5.15)$$

where $t_{\frac{\alpha}{2}}$ is the $\frac{\alpha}{2}$ percentage point of the Student's t distribution with $N - 1$ degrees of freedom. With 1000 samples, the confidence interval of 95 % and using the equation (5.15), the error range of the mean velocity can be estimated

$$U \pm 0.062 u' \quad (5.16)$$

where u' is the fluctuating component of the velocity. At 5,400 rpm, 1709 samples were considered for the mean and the fluctuation of the velocity. Therefore, the error range of the mean velocity is expected to be less than 5 %.

An error range of the velocity fluctuation is determined by the upper and the lower bound of the standard deviation with the $100(1 - \alpha)$ % confidence interval. The equations for the upper and the lower bound of the standard deviation are given by [38]

$$\frac{(N - 1)u'^2}{\chi_{\frac{\alpha}{2}}^2} < u'^2 < \frac{(N - 1)u'^2}{\chi_{1-\frac{\alpha}{2}}^2} \quad (5.17)$$

where $\chi_{\frac{\alpha}{2}}^2$ is the $\frac{\alpha}{2}$ points of the chi-square distribution with N-1 degrees of freedom. With the 95 percent confidence interval and 1000 degrees of freedom, the error range of the velocity fluctuation is estimated

$$0.96 u' < u' < 1.05 u' \quad (5.18)$$

As mentioned above, the sample number is larger than 1000. As a result, the error of the velocity fluctuation can be expected to be within $\pm 5\%$.

Chapter 4

Results of the numerical calculations

Contour plots from the results of the numerical calculations are presented and supported by physical explanations. Plotted variables are mean velocity magnitude with vectors, Turbulence Intensity (TI) and x, y and z - axial vorticity on planes perpendicular to the rotating axis and the surface of the disk. The planes parallel to the disk surface are located at the inter-disk mid-plane ($z = 0\text{mm}$), the mid-height of the stiffening flange ($z = 0.355\text{mm}$) and the mid-plane between the top surface of the arm and the lower surface of the upper disk ($z = 0.8\text{mm}$) (Figure 4.1).

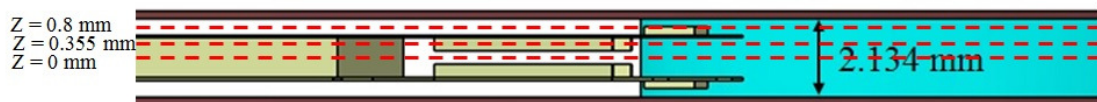


Figure 4.1: Planes perpendicular to the rotating axis where the contour plots are plotted.

Additional plots are obtained at three different planes normal to the disk and the Slider Suspension Unit (SSU), and shown in Figure 4.2 for both the Inner Configuration (IC) and the Outer Configuration (OC).

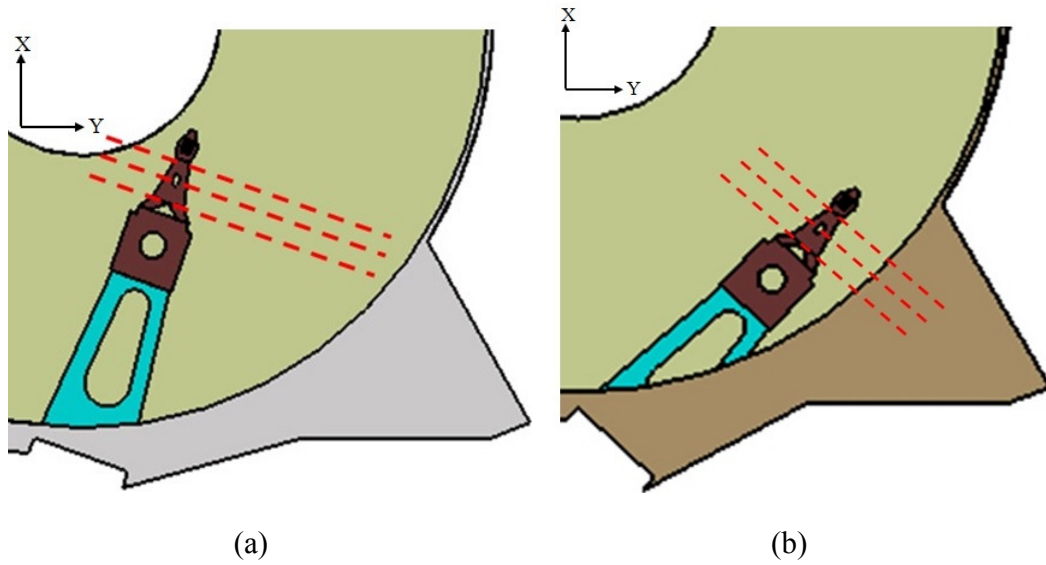


Figure 4.2: Planes perpendicular to the disk surface where the contour plots are plotted for (a) the IC and (b) the OC.

All variables are non-dimensionalized by the rotating speed at the edge of the disk.

$$V_{\text{mag}}^* = \frac{\sqrt{U_r^2 + U_\theta^2 + U_z^2}}{R\Omega} \quad (4.1)$$

$$\omega_x^* = \frac{1}{\Omega} \left(\frac{\partial U_z}{\partial y} - \frac{\partial U_y}{\partial z} \right) \quad (4.2)$$

$$\omega_y^* = \frac{1}{\Omega} \left(\frac{\partial U_x}{\partial z} - \frac{\partial U_z}{\partial x} \right) \quad (4.3)$$

$$\omega_z^* = \frac{1}{\Omega} \left(\frac{\partial U_y}{\partial x} - \frac{\partial U_x}{\partial y} \right) \quad (4.4)$$

$$TI^* = \frac{\sqrt{u_r^2 + u_\theta^2 + u_z^2}}{\sqrt{U_r^2 + U_\theta^2 + U_z^2}} \quad (4.5)$$

where R is the radius of the disk, Ω is the rotating rate of the disk, * indicates the non-dimensionalization, U_x , U_y , U_z , U_r and U_θ are velocity components in x , y , z , radial and circumferential axes, u_x , u_y , u_z , u_r and u_θ fluctuating velocity components in those axes, ω_x , ω_y and ω_z are the mean vorticity in x , y and z axes.

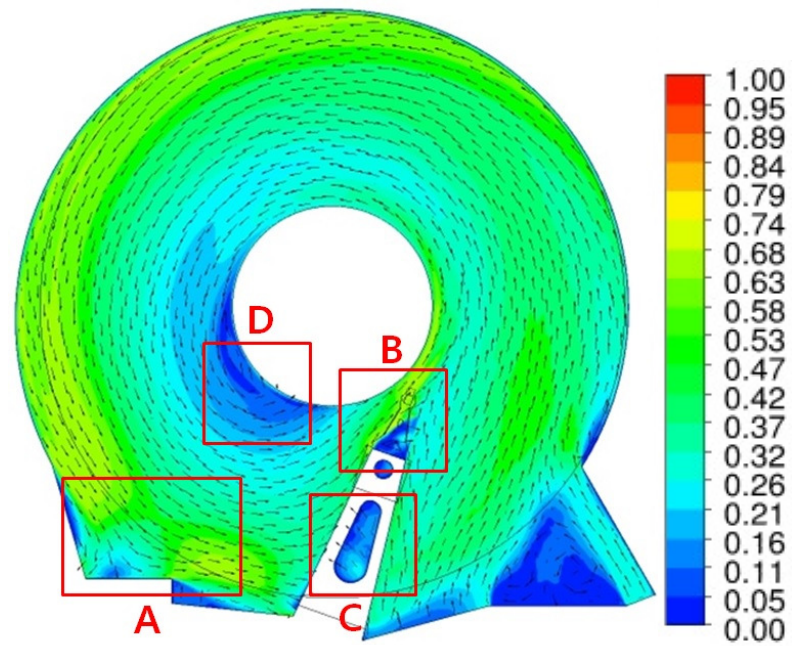
4.1 Inner configuration.

4.1.1 Mean velocity magnitude

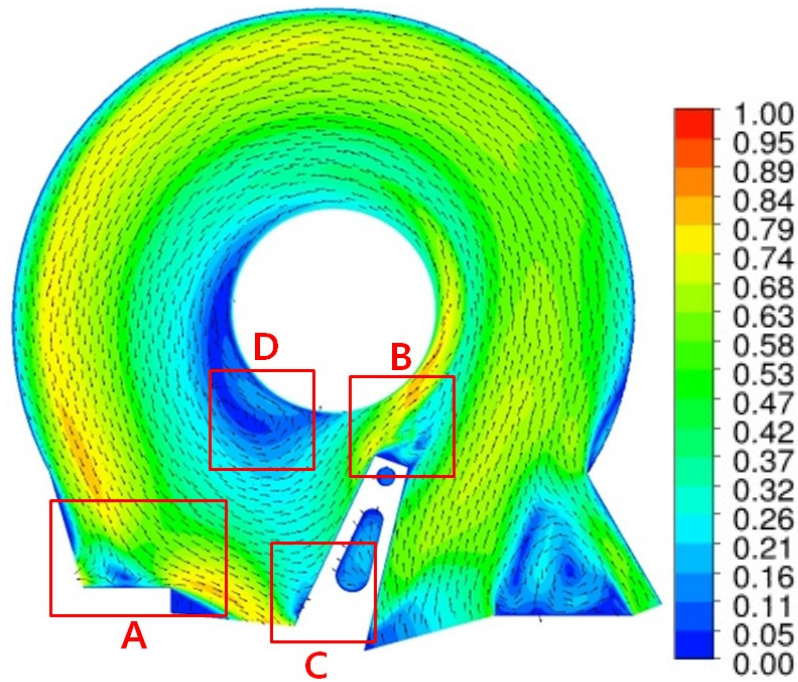
Contour plots are presented for the inter-disk mid-plane, the middle of the stiffening flanges and the mid-plane between the upper surface of the arm and the lower surface of the upper disk (Figures 4.3, 4.4, 4.6, 4.7, 4.8 and 4.9). Vectors imposed on the plots reveal that the flow field is governed by motions in the circumferential direction in both the air and the helium flow except the region around the actuator arm and the SSU. At the inter-disk mid-plane, as the incoming flow upstream of the arm approaches toward the arm, it experiences a transition from a shrouded condition to an open condition where the flow is opened to the outside of the rotating disk (Box A in Figures 4.3 and 4.4). Due to this pressure relief, the incoming flow tries to escape the disk domain. However, most of that flow is redirected into the rotating region by the presence of the outer walls in the Voice Coil Motor (VCM). This redirected flow impinges on a lateral surface of the arm and generates a stagnation point. The stagnation point on the arm induces a unique feature found in rotating flows with an obstruction in the middle of the flow field. In the region radially smaller than the stagnation point, the incoming flow is smoothly redirected toward the space between the arm and the hub. On the other hand, the incoming flow at radii larger than the stagnation point climbs up the arm and induces vortex shedding downstream of the weight saving hole (Box C in Figures 4.3 and 4.4). The location of the stagnation point which divides the incoming flow into two streams is decided by a size of the vortical structures in the outer region of the disk. In the inner region near the co-rotating hub, the flow field exhibits solid body rotation where the fluid has the same rotating speed as the disk. The outer region of the disk starts showing a

deviation from the solid body rotation due to the viscous effect from the enclosure wall. Therefore, a velocity difference is induced between the disk surface and the inter-disk mid-plane region, and a boundary layer develops on the disk surface (Ekman layer). In the boundary layer, the fluid is driven radially outward direction and redirected toward the inter-disk mid-plane by the enclosure wall. To satisfy the fluid continuity, corresponding radially inward flow is generated around the mid-plane region. As a result, a pair of counter-rotating vortices is completed on the plane perpendicular to the disk surface. The maximum velocity is found at the boundary between the inner region and the outer region. Since the velocity distribution is converted to the pressure distribution on the solid surface, the stagnation point is estimated to be observed at the region where the maximum velocity is generated. Moreover, Soong et al. [15] reported that the size of the vortical structure (non-solid-body) in the outer region becomes larger as the Reynolds number increases. Due to the lower Reynolds number in helium than in air by the higher kinematic viscosity at the same rotating speed of the disk, the size of the vortical structure is always smaller in the helium flow than in the air flow, and the maximum velocity is induced at a larger radial location in helium than in air (Figure 4.3 (a) and (b)). By the difference of the stagnation point location in air and helium, the incoming flow is more redirected toward the Slider Suspension Unit (SSU) in the helium flow than the air flow. Due to a narrow space between the arm and the SSU, the velocity in the clearance needs to be accelerated to satisfy the fluid continuity in both air and helium flow (Box B in Figures 4.3 and 4.4). Therefore, a larger driven flow in helium toward this space causes a higher velocity magnitude than in air. Adding to this, the higher kinematic viscosity of helium contributes to the infusion of more momentum into the fluid region by the disk so

that the helium flow shows higher magnitudes of velocity than the air flow. At the same time, a region with a low velocity magnitude is induced near the hub where a three-dimensional inversed flow exists upstream of the arm and a large amount of fluid is driven from the outside of the rotating frame to the region downstream of the arm to satisfy the fluid continuity (Box D in Figure 4.3). At 15000 rpm, the stagnation point is still located at the radially smaller point in air than in helium. However, an increased rotating speed relocates the stagnation point by making the size of the vortical structure larger than those at 5400 rpm in both air and helium. In particular, the air flow moves the stagnation point to smaller radius than that at 5400 rpm. Thus, most of the incoming flows directly impinge on the arm. As a result, the inversed three-dimensional flow doesn't need to be generated to satisfy the fluid continuity where the helium flow still induces the inversed flow upstream of the arm (Figure 4.4 (a) and (b)). The helium flow also moves the stagnation point radially inward direction at 15,000 rpm. Thus, the flow acceleration in the space between the arm and the SSU doesn't need to be as high as the intensity at 5400 rpm.

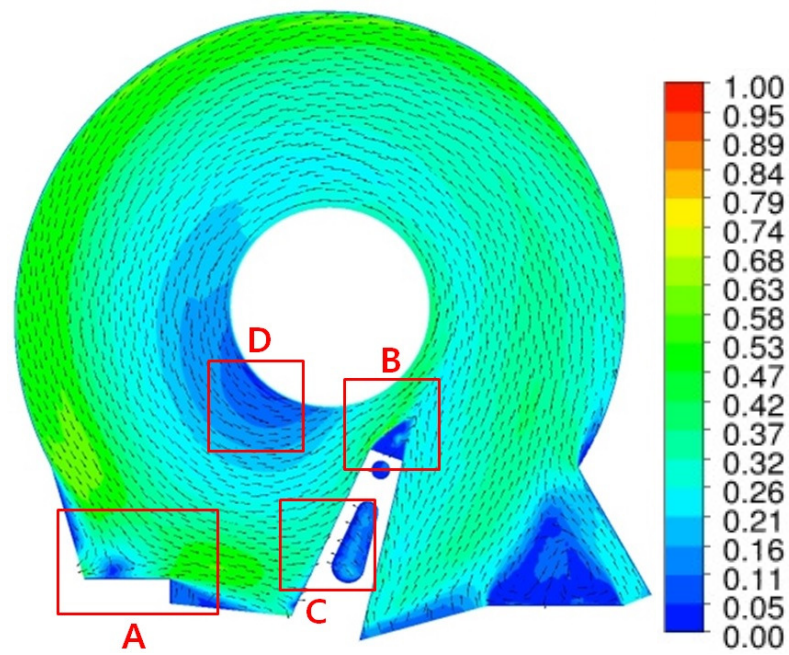


(a)

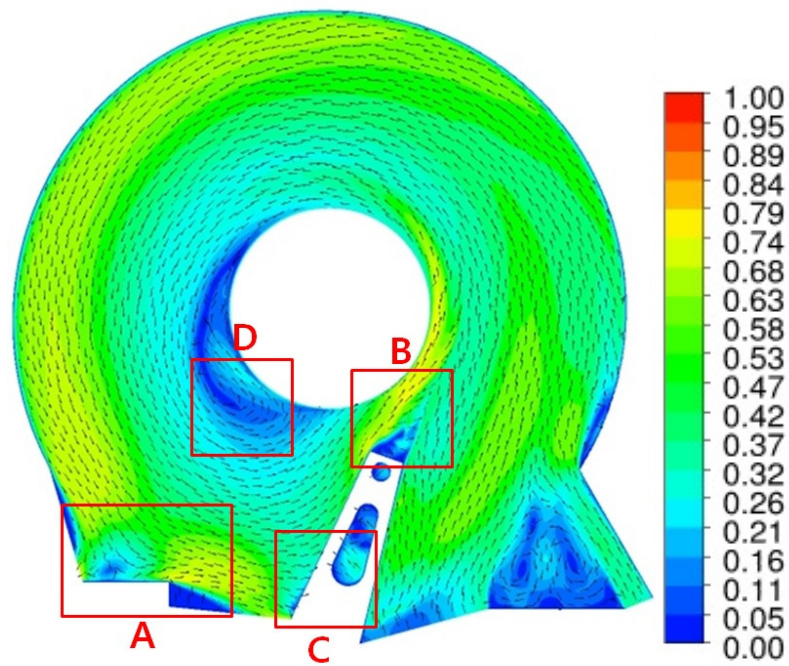


(b)

Figure 4.3: Contour plots of mean velocity of (a) air and (b) helium at the inter-disk mid-plane ($z = 0$ mm) at 5400 rpm.

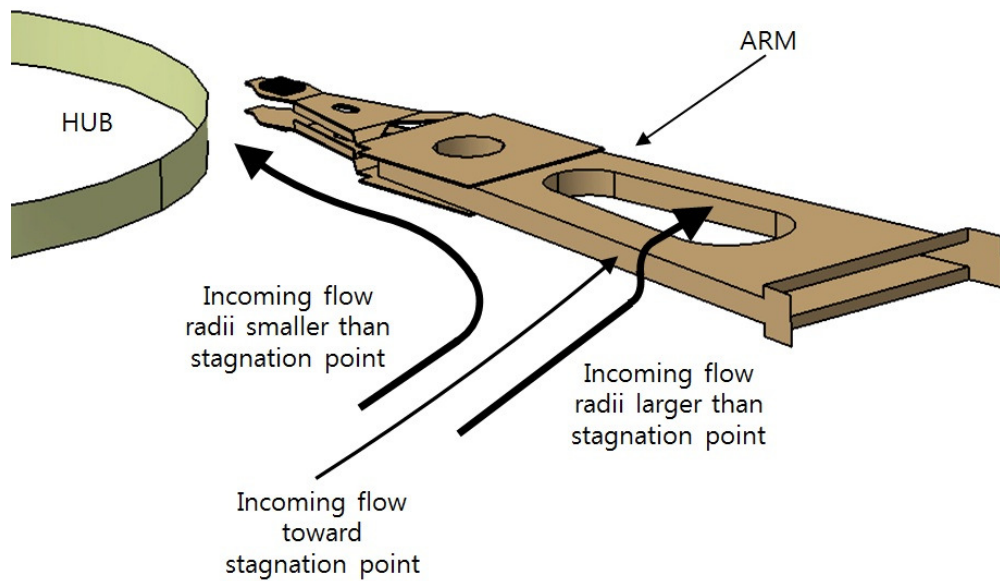


(a)

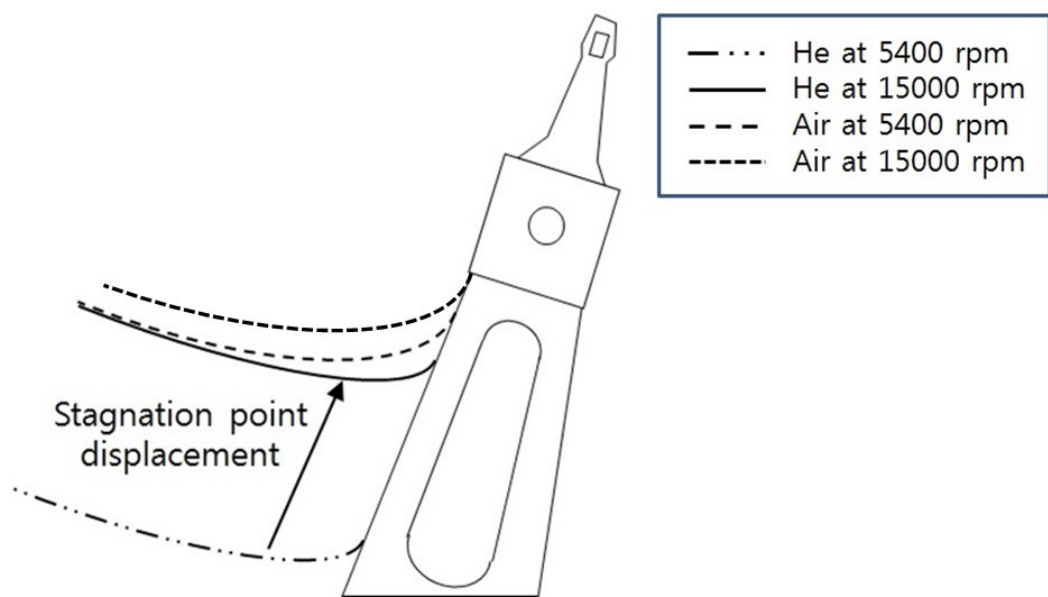


(b)

Figure 4.4: Contour plots of mean velocity of (a) air and (b) helium at the inter-disk mid-plane ($z = 0$ mm) at 15000 rpm.



(a)

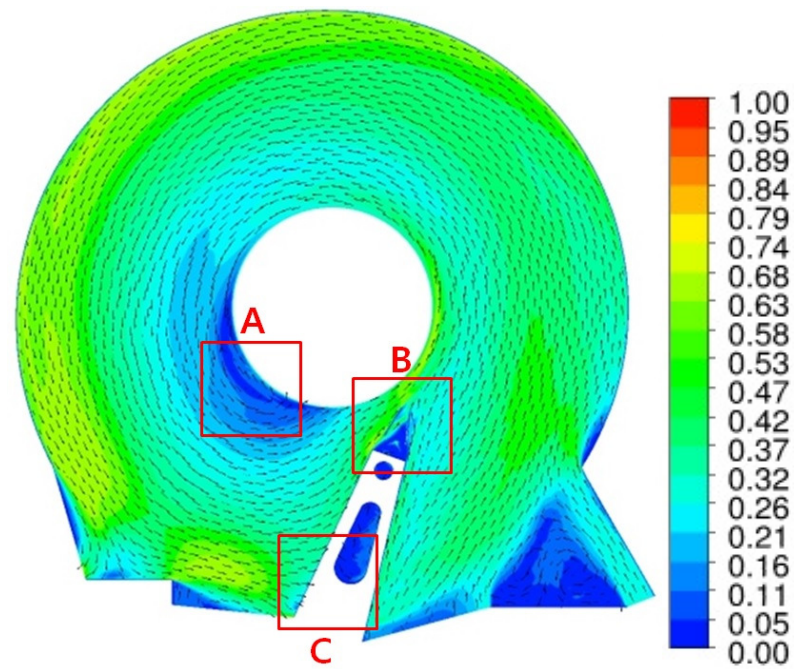


(b)

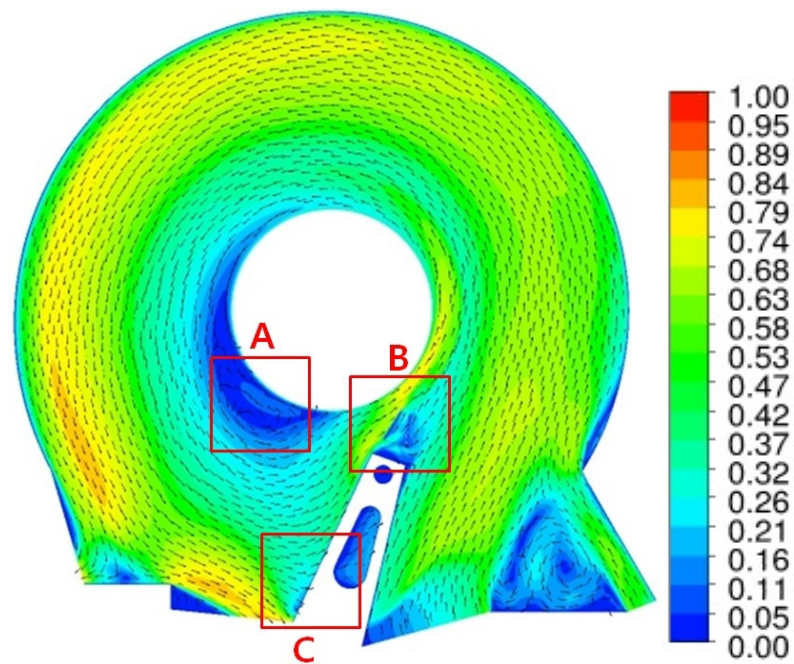
Figure 4.5: Schematic drawing of the trajectories of the incoming flow upstream of the arm (a) and the stagnation point displacement for the helium at 5400 and 15000 rpm (b).

At the height of the middle of the stiffening flanges ($Z = 0.355$ mm), flow patterns seem to be almost similar to the flow field at the inter-disk mid-plane (Figures 4.6 and 4.7). The inversed three-dimensional flow is still clearly observed in the region upstream of the arm in both air and helium at 5400 rpm (Box A in Figure 4.6 (a) and (b)). It is clearly proved that the inversed flow upstream of the arm is three-dimensional. Also, the inversed flow is no longer found in the air flow at 15000 rpm where the helium flow still retains it (Box A in Figure 4.7 (a) and (b)). In addition, the stagnation point is also still valid at this height. The locations of the stagnation points in both gases at two different rotating speeds are almost identical to those at inter-disk mid-plane (Box C In Figures 4.6 and 4.7). This is induced by Taylor–Proudman theorem (Appendix C). One unique character of the rotating flow is a tendency to diminish velocity gradients in the axial direction. In other words, if flow field experiences an obstruction at one height, velocity distributions and flow patterns generated at that height tend to persist for all planes along the axis of rotation. Thus, the flow pattern at the inter-disk mid-plane is maintained at the current plane (Box B in Figures 4.6 and 4.7). However, the flow around the SSU shows differences compared to that at the mid-plane. At the mid-plane, the flow field doesn't meet any blockages except the actuator arm so that the redirected flow toward the SSU only experiences the acceleration through the gap between the upper and the lower SSU's. At this height, two stiffening flanges are working as a blocking wall in the middle of the flow field. As a result, the redirected flow by the arm diverges into two streams by the leading stiffening flange. The first stream is guided to the co-rotating hub and accelerated through the clearance between the arm and the hub to the region downstream of the SSU.

The second stream flows through the space between two flanges with a relatively low velocity to the region downstream of the SSU.

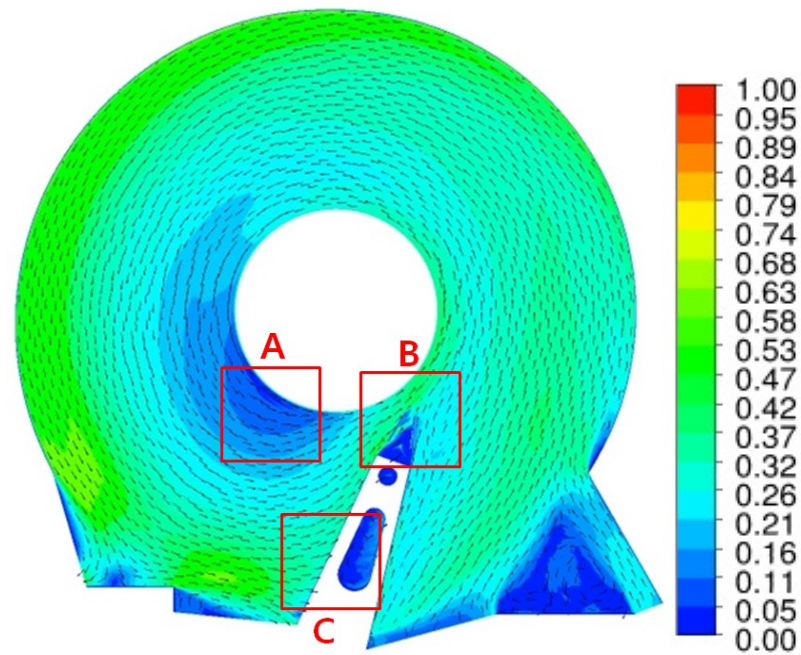


(a)

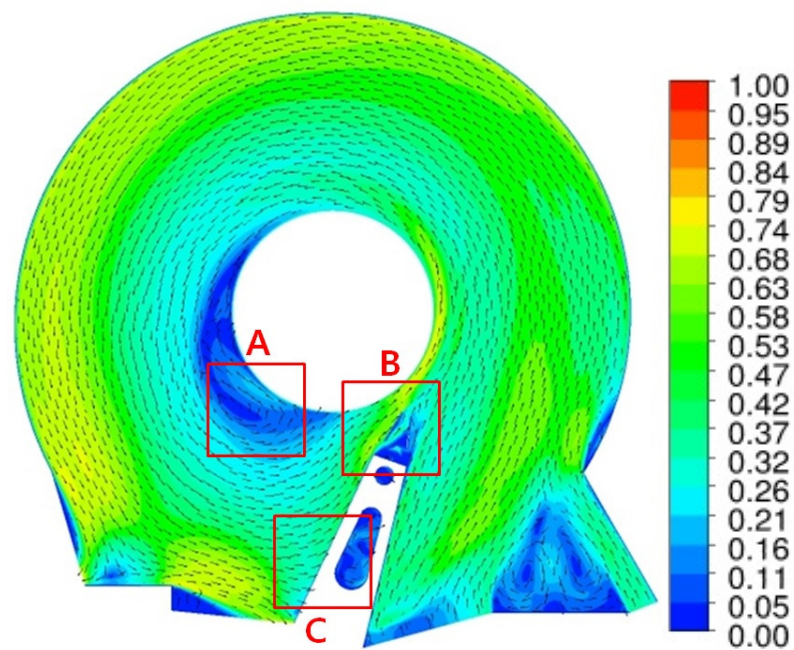


(b)

Figure 4.6: Contour plots of mean velocity of (a) air and (b) helium at the plane across the flanges ($z = 0.355$ mm) at 5400 rpm.



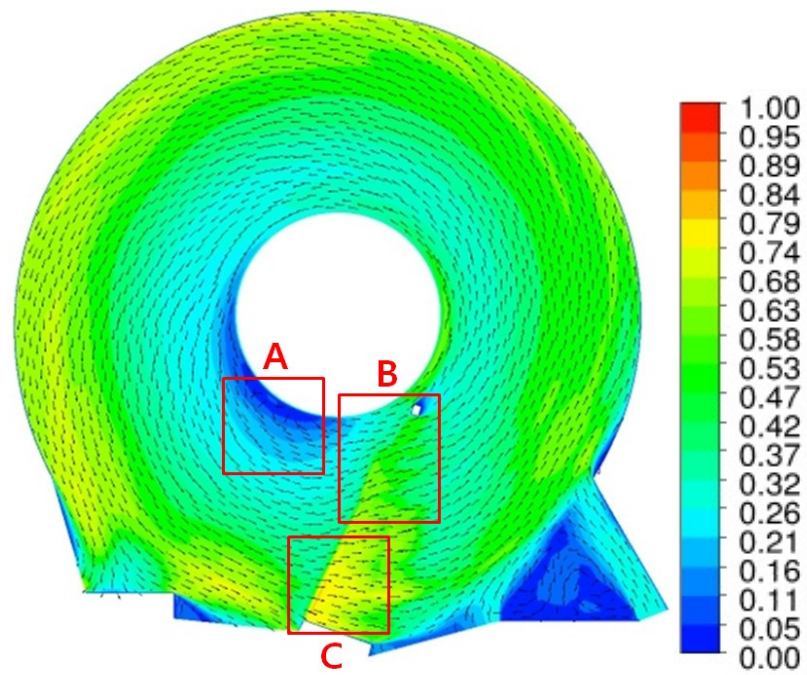
(a)



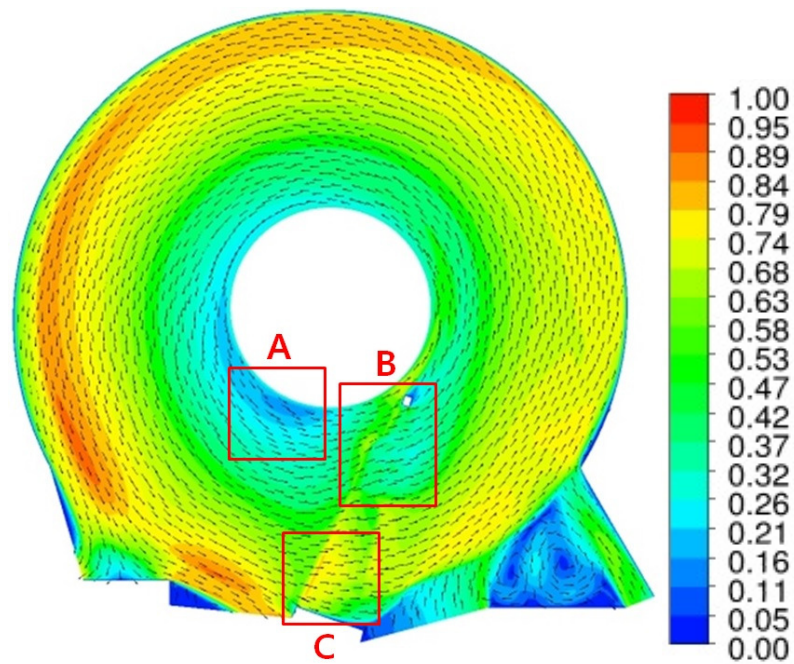
(b)

Figure 4.7: Contour plots of mean velocity of (a) air and (b) helium at the plane across the flanges ($z = 0.355$ mm) at 15000 rpm.

The contour plots at the mid-plane between the upper surface of the arm and the lower surface of the upper disk reveal that the flow field is almost in the circumferential direction (Figures 4.8 and 4.9). The three-dimensional inversed flow is no longer observed at this plane in either fluid at both 5400 and 15000 rpm (Box A in Figures 4.8 and 4.9). However, the stagnation point found at the inter-disk mid-plane is still valid, and the presences of the arm and the SSU still have an effect on this height due to Taylor–Proudman theorem. The flow above the arm is still divided into two streams by the stagnation point which is observed at the inter-disk mid-plane. The portion radially larger than the stagnation point travels over the arm, maintaining a relative constant radius. The flow at radii smaller than the stagnation point tends to be slightly redirected radially inward (Box B in Figures 4.8 and 4.9). Also, sudden velocity acceleration is induced in the space above the actuator arm. Since all the incoming flow has to pass across the clearance between the arm and the disks, the flow field needs to be accelerated. As a result, the higher magnitude of velocity is found between the arm and the disk (Box C in Figures 4.8 and 4.9).

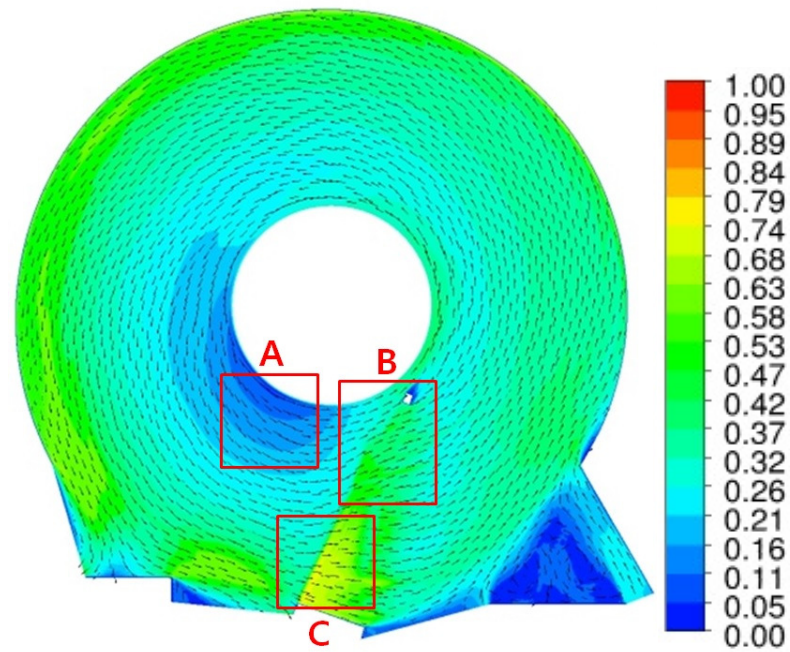


(a)

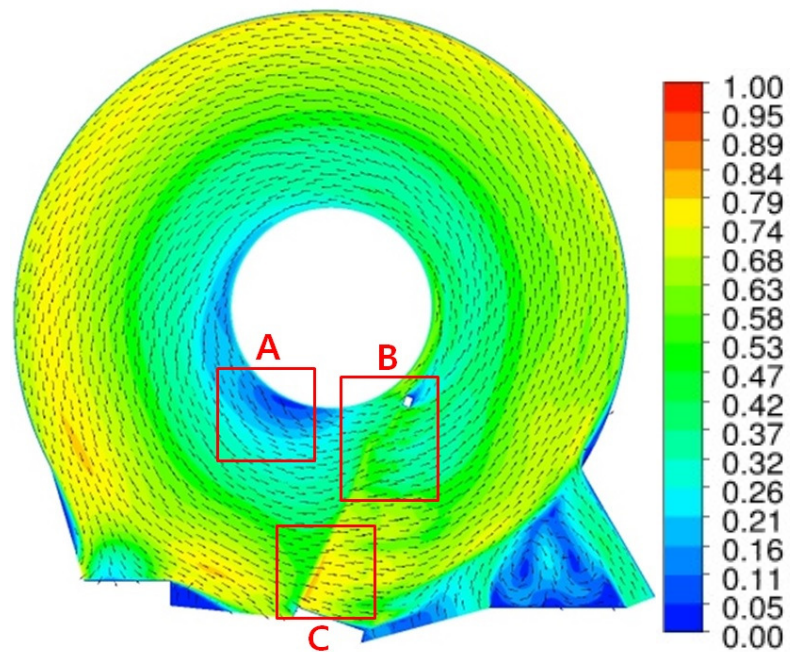


(b)

Figure 4.8: Contour plots of mean velocity of (a) air and (b) helium at the plane between the arm and the disk ($z = 0.8$ mm) at 5400 rpm.



(a)



(b)

Figure 4.9: Contour plots of mean velocity of (a) air and (b) helium at the plane between the arm and the disk ($z = 0.8$ mm) at 15000 rpm.

Figures 4.11, 4.12, 4.13 and 4.14 show contours and vectors of velocity in the three planes of Figure 4.2. The flow patterns on these planes clearly show that the air flow (Figures 4.11 and 4.13) induces more unsteadiness downstream of the SSU than the helium flow (Figures 4.12 and 4.14). The flow acceleration upstream of the SSU is also observed between the disks and the SSU's. In particular, since the clearance between the two SSU's is merely 0.353 mm, significant acceleration is found through the gap between the upper and the lower SSU where a highly sheared flow is estimated to exist. On the first plane near the arm, this accelerated flow occupies one quarter of the space between the leading and the trailing flanges due to the flow redirection of the incoming flow upstream of the arm at the leading edge in the air flow (Figure 4.10 (a)), and the helium flow shows more acceleration so that the high velocity region fills half of the space between two flanges (Figure 4.11 (a)) at 5400 rpm. On the second plane in the middle of the flanges, the flow acceleration gradually increases its area to a location of the elliptical weight-saving hole in the air flow (Figure 4.10 (b)) where the flow passes across the flanges with a relatively constant velocity in the helium flow (Figure 4.11(b)) at 5400 rpm. In the third plane at the end of the flanges, the accelerated flow completely fills the space inside the SSU in both air and helium and experiences another acceleration through the gap between the trailing flanges with a lower intensity than the velocity increase upstream of the SSU (Figure 4.10 (c) and 4.11 (c)). At 15000 rpm, due to the reduced flow rate, the accelerated flow loses its strength in both air and helium so that the extent of the high velocity region also decreases (Figures 4.12 and 4.13) across all the planes. The acceleration near the trailing flange tends to be maintained until the region downstream of the SSU in both air and helium. This leads to the shedding of a pair of

vortices by a sudden pressure imbalance created by the stiffening flanges. Since the higher kinematic viscosity of helium contributes to the generation of more steady flow than air, the vortex shedding downstream of the SSU in air seems to be more vigorous than that for the helium flow at both 5400 and 15000 rpm.

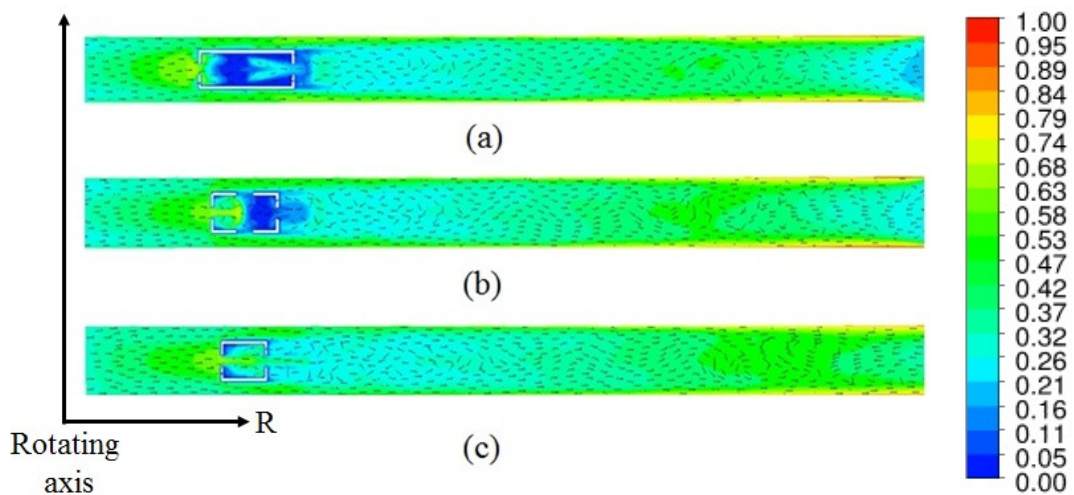


Figure 4.10: Contour plots of mean velocity on three planes across the stiffening; (a) near the arm. (b) middle of the flanges. (c) the end of the flanges in air at 5400 rpm.

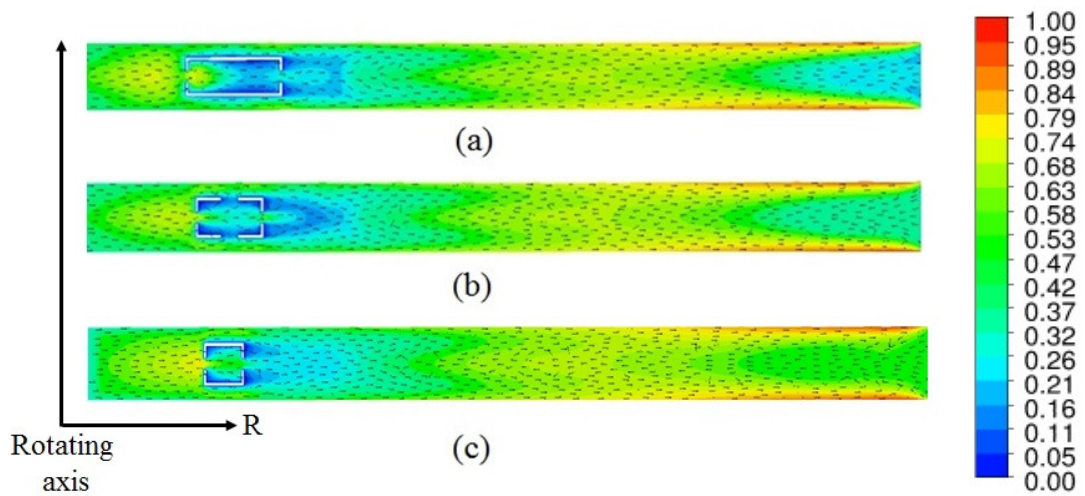


Figure 4.11: Contour plots of mean velocity on three planes across the stiffening; (a) near the arm. (b) middle of the flanges. (c) the end of the flanges in helium at 5400 rpm.

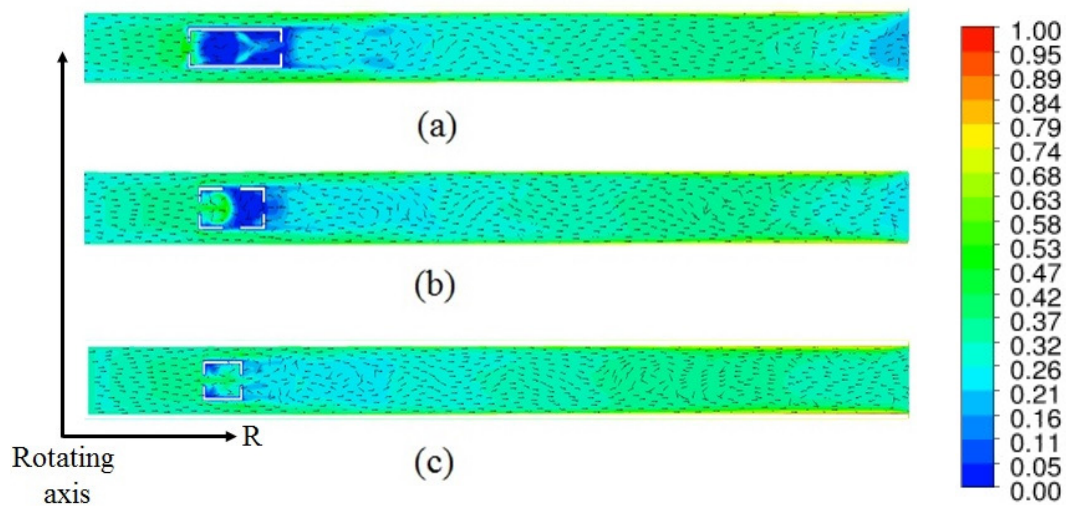


Figure 4.12: Contour plots of mean velocity on three planes across the stiffening; (a) near the arm. (b) middle of the flanges. (c) the end of the flanges in air at 15000 rpm.

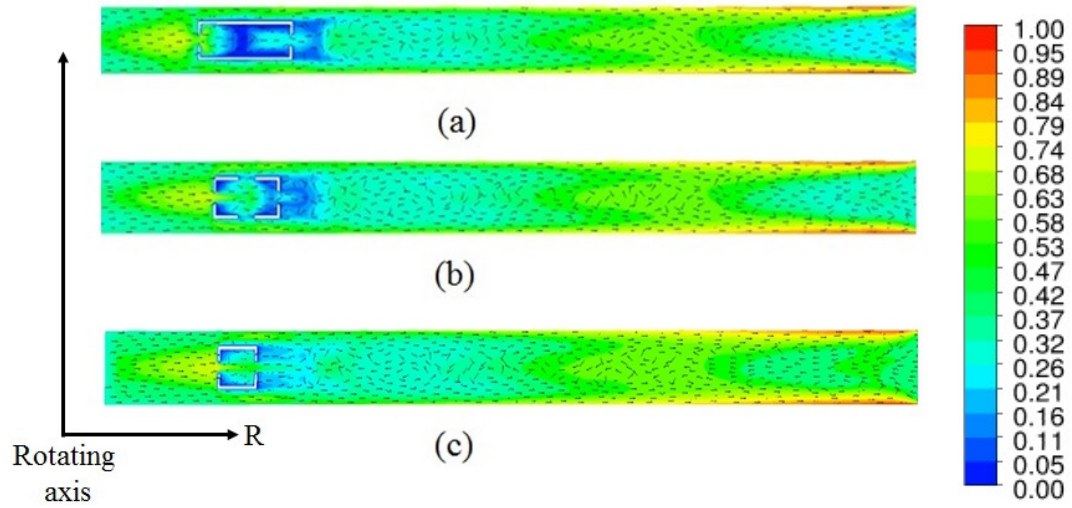


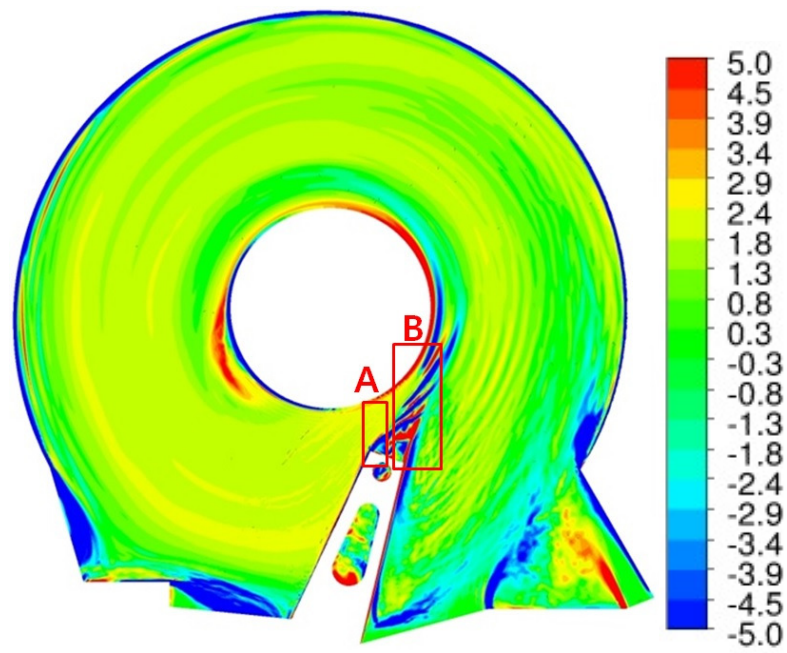
Figure 4.13: Contour plots of mean velocity on three planes across the stiffening; (a) near the arm. (b) middle of the flanges. (c) the end of the flanges in helium at 15000 rpm.

4.1.2 Vorticity

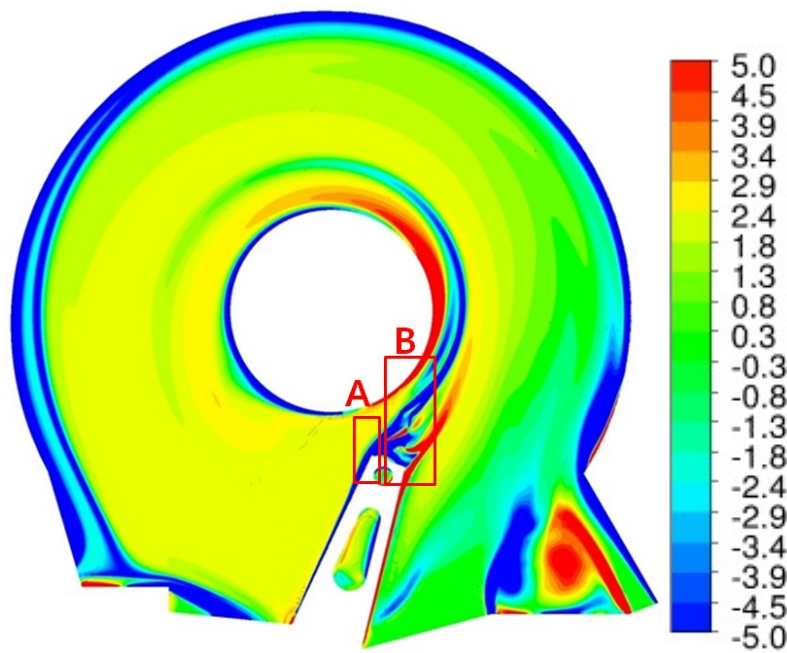
The contour plots of vorticity indicate that the flow field is highly sheared around the SSU (Figures 4.14, 4.15, 4.16, 4.17, 4.18 and 4.19). The incoming flow is redirected toward the SSU on the inside of the stagnation point. Through this redirection, the incoming flow induces a steep velocity gradient on the lateral surface of the arm due to the no-slip boundary condition. Then, this flow is vigorously sheared at the leading edge of the actuator arm where the accelerated flow induces a high velocity gradient by contacting a region with a low magnitude velocity (Box A in Figures 4.14 and 4.15). After the flow passes the leading edge, the complexity of the SSU contributes to the generation of vorticity streams while the flow travels across the SSU's. In particular, the stiffening flanges perturb the flow field further and create multiple velocity gradient regions at each corner of the edges in the flanges (Box B in Figures 4.14 and 4.15). Furthermore, the higher kinematic viscosity of helium contributes to the generation of the higher velocity magnitude than the air flow where the flow field is accelerated. Corresponding to the increased velocity, the flow field is more affected by the solid surfaces with the no-slip boundary condition. Thus, higher intensity vorticity streaks arise in the helium flow (Figures 4.14 (b), 4.15 (b), 4.16 (b), 4.17 (b), 4.18 (b) and 4.19 (b)) than in the air flow (Figures 4.14 (a), 4.15 (a), 4.16 (a), 4.17 (a), 4.18 (a) and 4.19 (a)) around the SSU. Due to the Taylor-Proudman theorem, the vorticity streaks tend to suppress the velocity gradient in the axial direction. The results observed at the inter-disk mid-plane are delivered to the plane across the flanges except the region between the leading and the trailing flanges. By the leading flange, the redirected flow is divided into two streams. The stream driven toward the space between the leading and the trailing

flanges is directly sheared by the surfaces of the SSU. Particularly, each corner of the flanges becomes a source of vorticity streaks at this height (Box A in Figures 4.16 and 4.17).

At the mid-plane between the arm and the upper disk, without any presence of the flow blockage except the small magnetic tip (Box A in Figures 4.18 and 4.19), the flow over the arm and the SSU induces vorticity streaks also due to the Taylor-Proudman theorem (Figures 4.18 and 4.19).

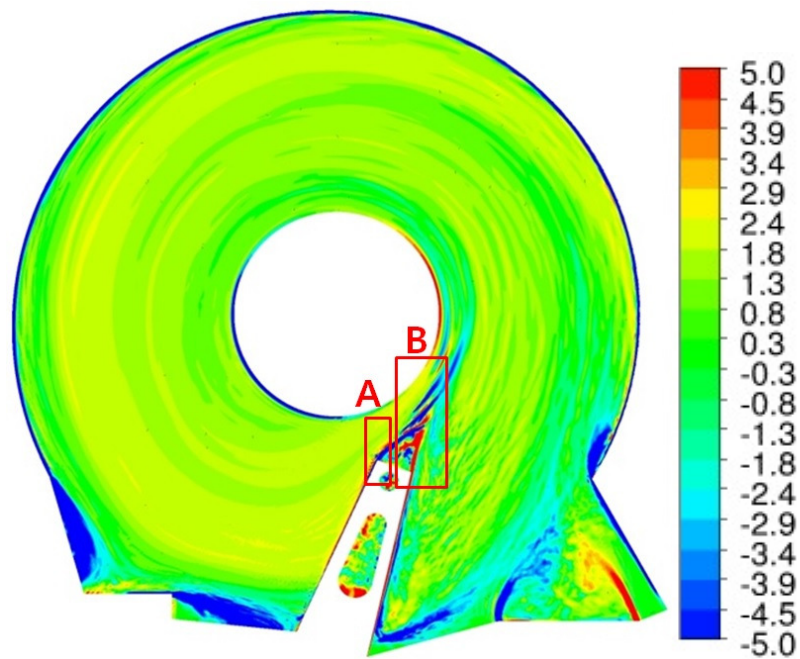


(a)

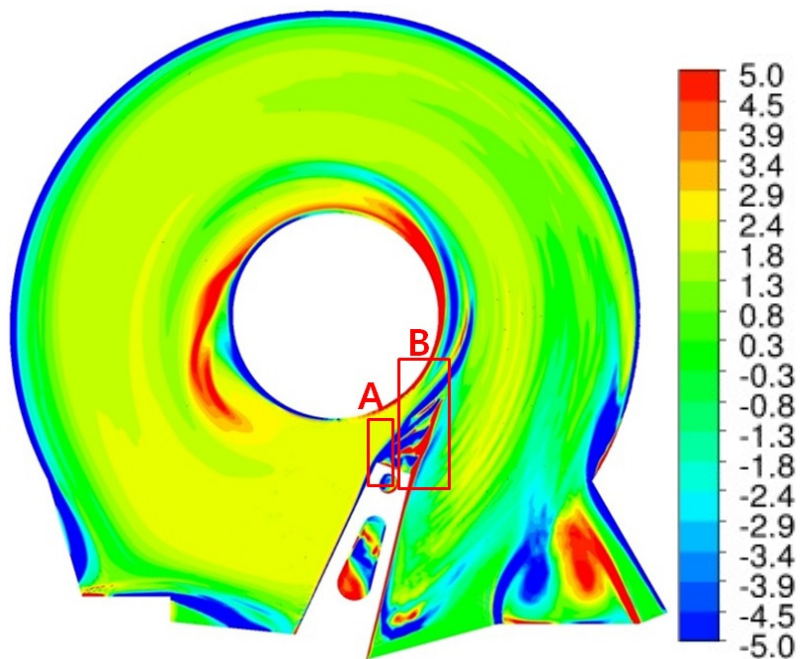


(b)

Figure 4.14: Contour plots of z - axial vorticity of (a) air and (b) helium at the inter-disk mid-plane ($z = 0$ mm) at 5400 rpm.

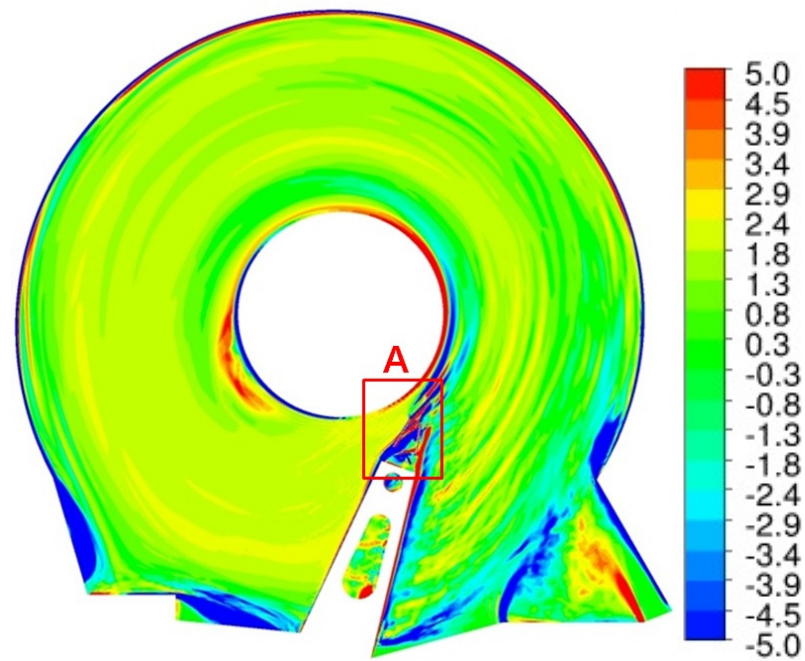


(a)

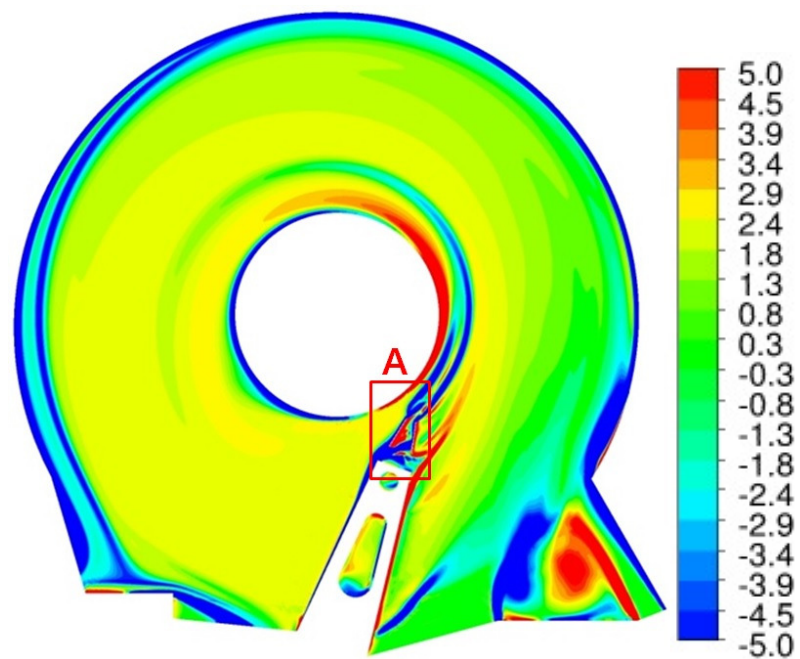


(b)

Figure 4.15: Contour plots of z - axial vorticity of (a) air and (b) helium at the inter-disk mid-plane ($z = 0$ mm) at 15000 rpm.

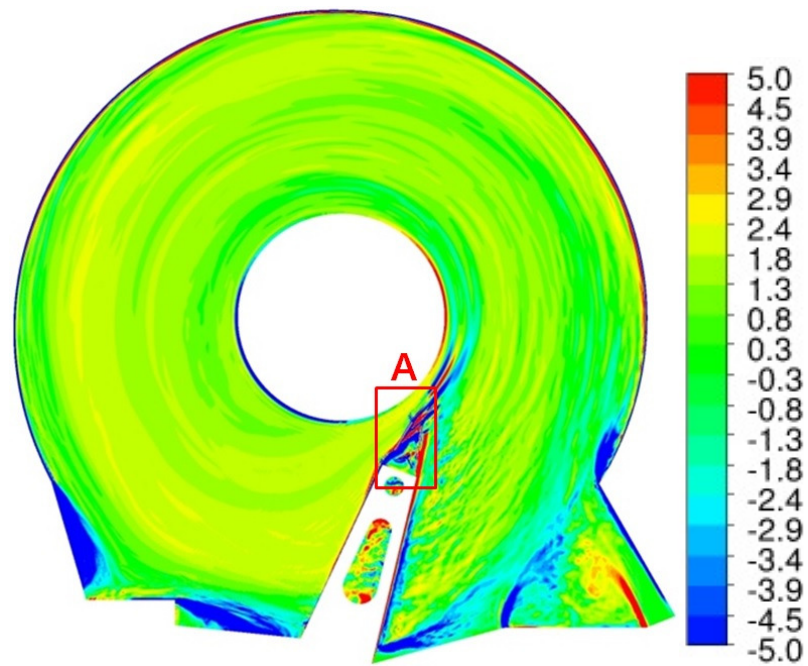


(a)

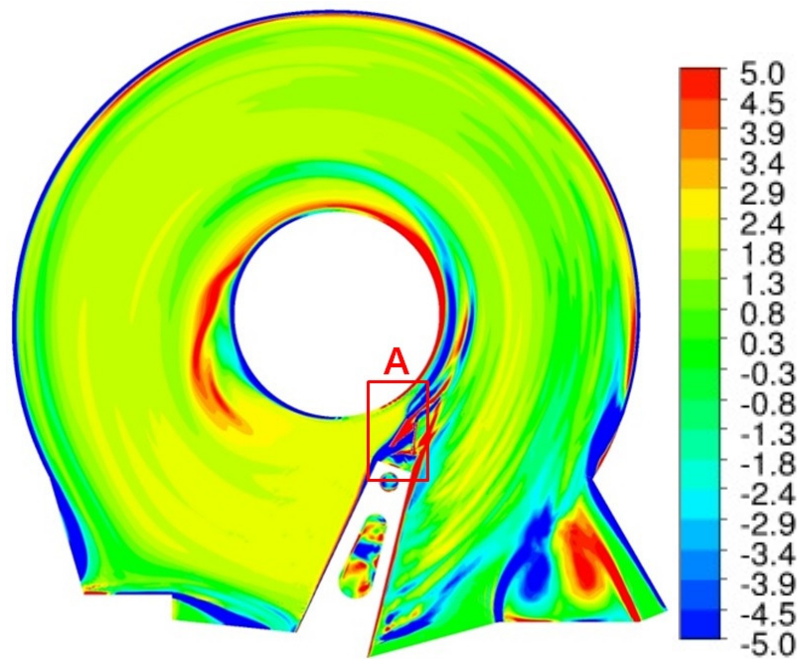


(b)

Figure 4.16: Contour plots of z - axial vorticity of of (a) air and (b) helium at the plane across the flanges ($z = 0.355$ mm) at 5400 rpm.

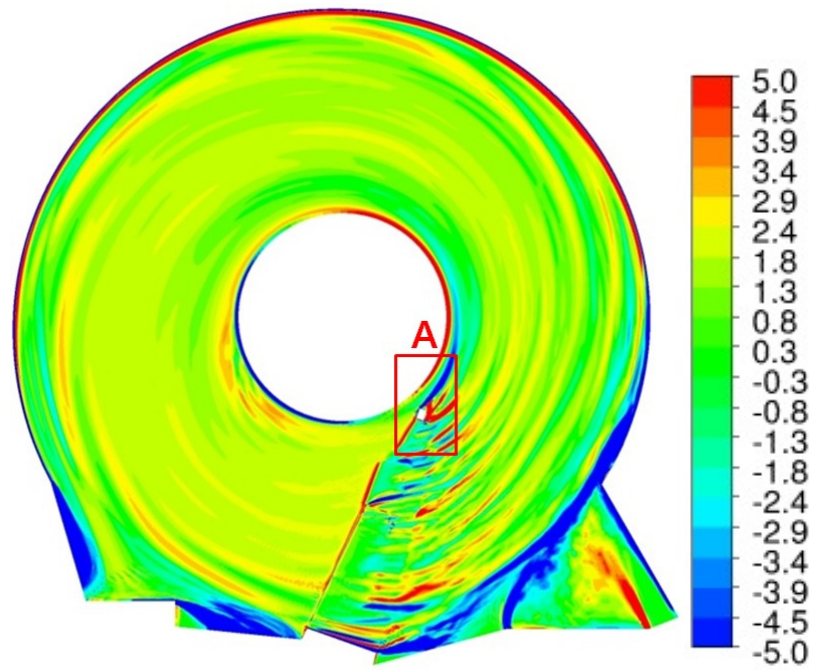


(a)

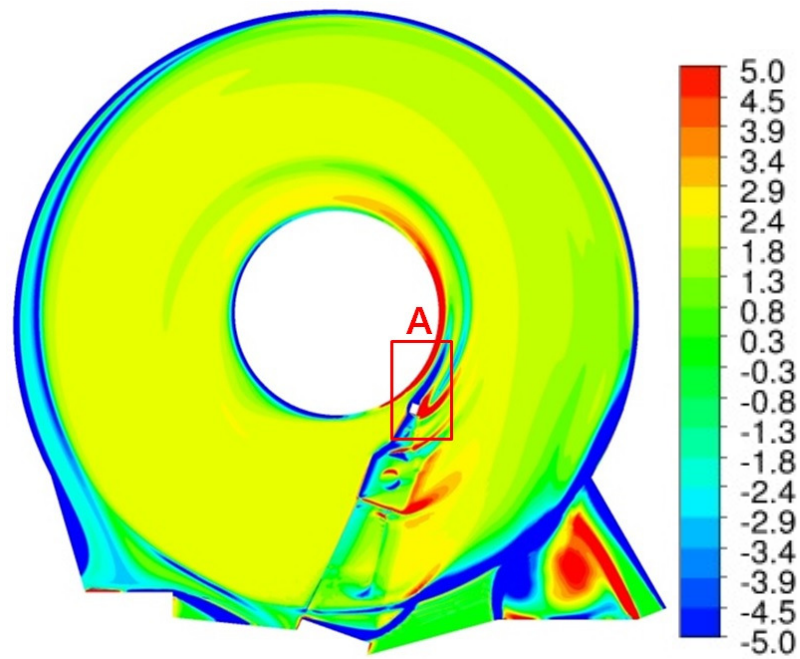


(b)

Figure 4.17: Contour plots of z - axial vorticity of of (a) air and (b) helium at the plane across the flanges ($z = 0.355$ mm) at 15000 rpm.



(a)



(b)

Figure 4.18: Contour plots of z - axial vorticity of (a) air and (b) helium at the plane between the arm and the disk ($z = 0.8$ mm) at 5400 rpm.

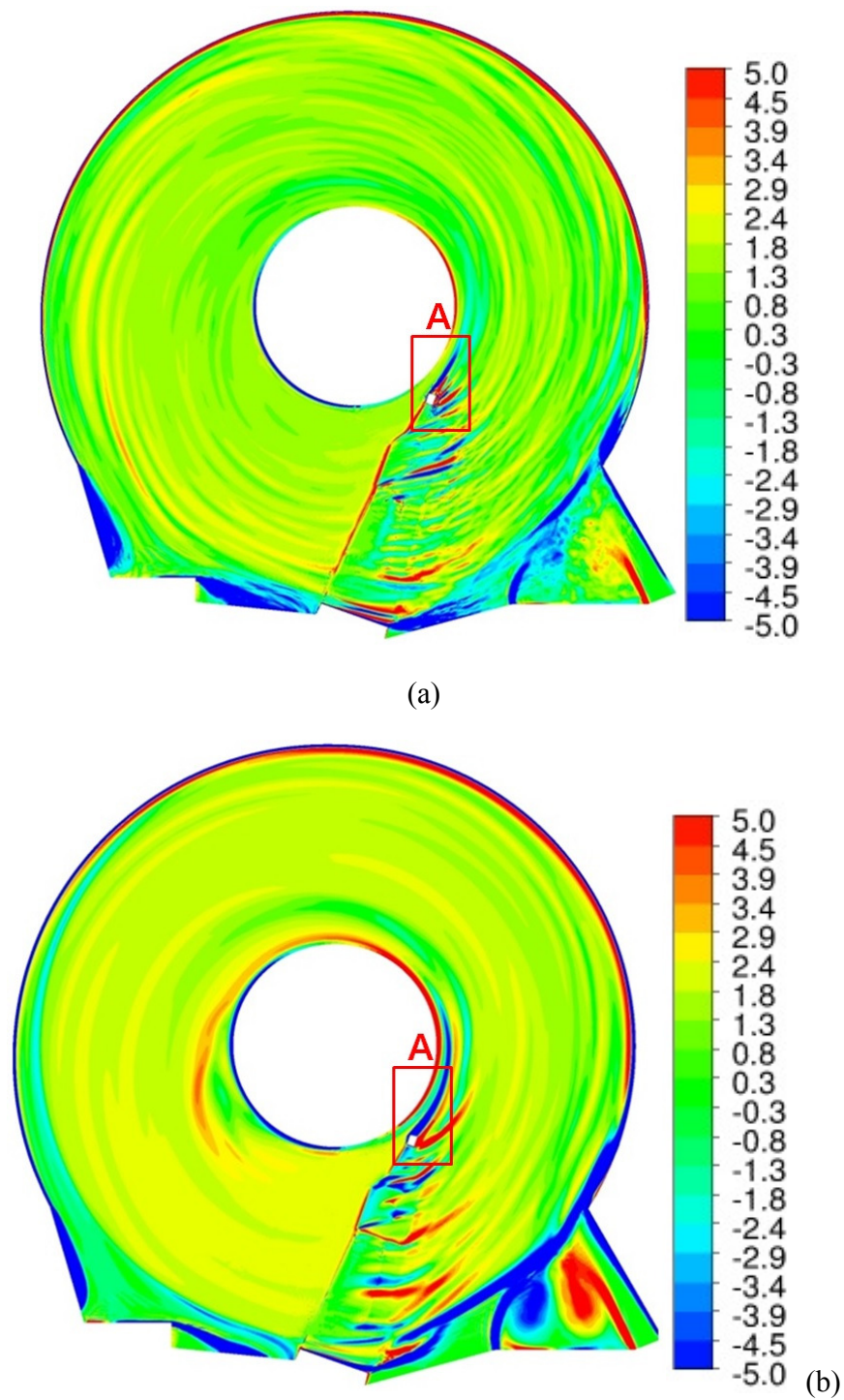


Figure 4.19: Contour plots of z - axial vorticity of of (a) air and (b) helium at the plane between the arm and the disk ($z = 0.8$ mm) at 15000 rpm.

The y – vorticity contour plots on the planes across the stiffening flanges (Figures 4.20, 4.21, 4.22 and 4.23) also show that the incoming flow is clearly sheared when it passes through the clearance between the SSU and the disks. As described in a previous chapter, the flow field needs to be accelerated around the SSU to satisfy the fluid continuity. As a result, the incoming flow is highly sheared where the flow acceleration takes place. In particular, the upper surface of the upper SSU and the lower surface of the lower SSU are main sources of shear layer generation separating the higher velocity region near the upper and the lower disks and a relatively low velocity region around the inter-disk mid-plane. Inside the stiffening flanges, a pair of vorticity streaks arise at each end of the flanges where pressure imbalance between the inside the SSU and the region downstream of the SSU leads to large accelerations. The y – vorticity tends to be intensified as the distance between the leading and the trailing flanges becomes narrower due to the higher magnitude of the flow acceleration. Similar with the contour plots of z – axial vorticity, helium causes longer and stronger vorticity streaks than air.

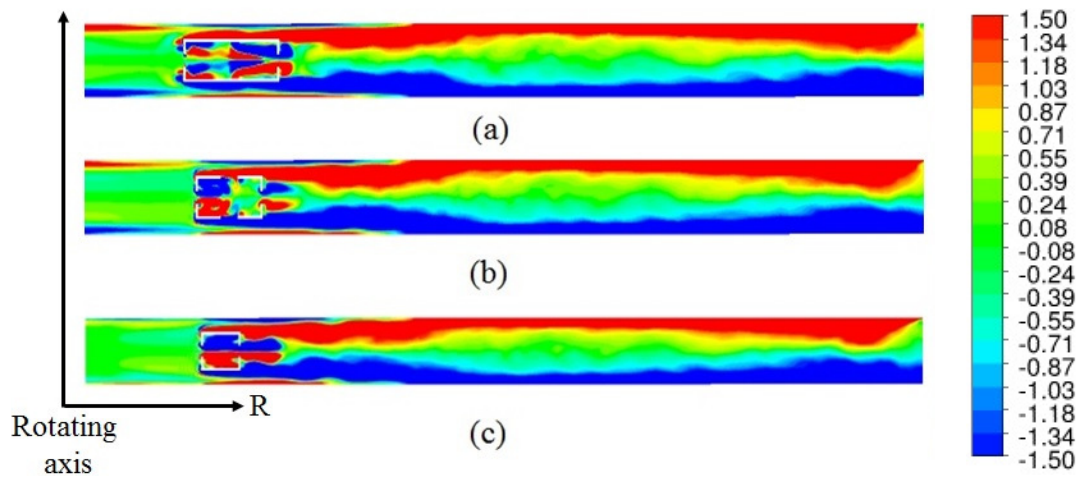


Figure 4.20: Contour plots of y - axial vorticity of on three planes across the stiffening; (a) near the arm. (b) middle of the flanges. (c) the end of the flanges in air at 5400 rpm.

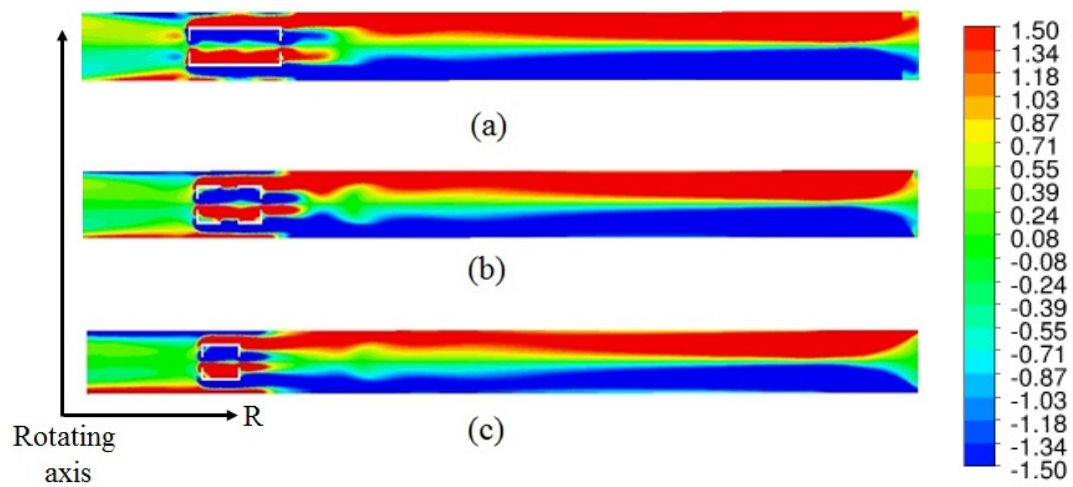


Figure 4.21: Contour plots of y - axial vorticity of on three planes across the stiffening; (a) near the arm. (b) middle of the flanges. (c) the end of the flanges in helium at 5400 rpm.

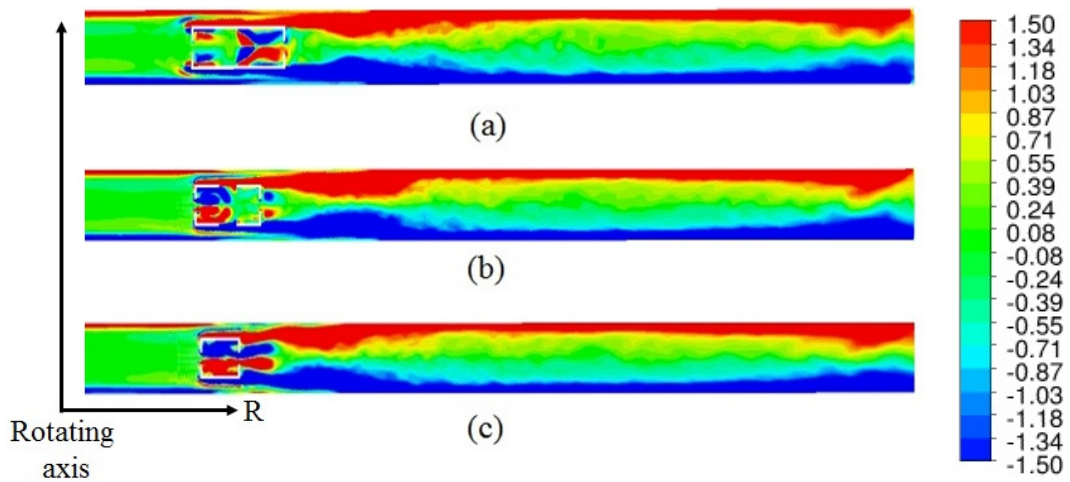


Figure 4.22: Contour plots of y - axial vorticity on three planes across the stiffening; (a) near the arm. (b) middle of the flanges. (c) the end of the flanges in air at 15000 rpm.

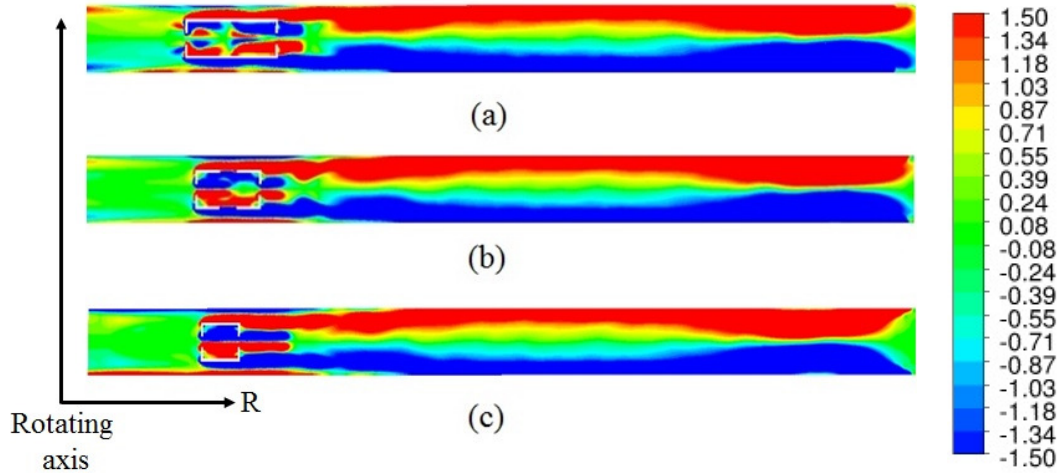


Figure 4.23: Contour plots of y - axial vorticity on three planes across the stiffening; (a) near the arm. (b) middle of the flanges. (c) the end of the flanges in helium at 15000 rpm.

4.1.3 Turbulence Intensity (TI)

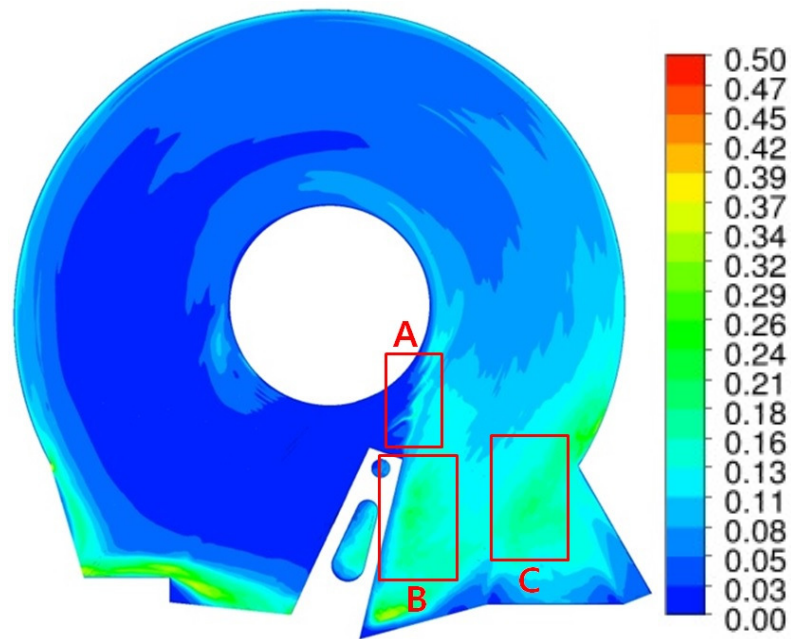
From contour plots of non-dimensional Turbulence Intensity (TI^*), it is found that a high magnitude of TI is concentrated in the regions downstream of the actuator arm and the SSU (Figures 4.24, 4.25, 4.26, 4.27, 4.28 and 4.29). This highly unsteady flow downstream of the arm arises due to the perturbations from the SSU and the weight-saving hole in the middle of the arm. The incoming flow upstream of the arm is divided into two streams by the stagnation point on the upstream lateral surface of the arm. The flow to the inside of the stagnation point is redirected toward the hub and accelerated into the clearance between the arm and the co-rotating hub. The redirected flow is highly sheared at the leading edge of the arm and generates a three-dimensional unsteady mixing layer with a low velocity region between the upper and the lower SSU (Box A in Figures 4.24 and 4.25). In addition, since the stiffening flanges are extruded in the axial direction which decreases the clearance between the upper and the lower disks, the flow field experiences a sudden pressure imbalance between the inside of the SSU domain and the region downstream of the SSU so that vortices with non-uniform frequency are induced. As a result, the flow field is perturbed severely twice by the leading edge of the arm and the stiffening flanges in the SSU's. Therefore, the intensified turbulence intensity starts arising between the upper and the lower SSU and is intensified downstream of the SSU. The other stream of the incoming flow at radii larger than the stagnation point impinges on the lateral surface of the arm and climbs up the arm. Similar to the pressure fluctuations across the stiffening flanges, the actuator arm also works as a source of pressure fluctuation between the region upstream and downstream of the arm (Box B in Figures 4.24 and 4.25). Vortices are generated downstream of the arm. Moreover, the

presence of the weight-saving hole further perturbs the flow so that intensified TI is observed downstream of the arm.

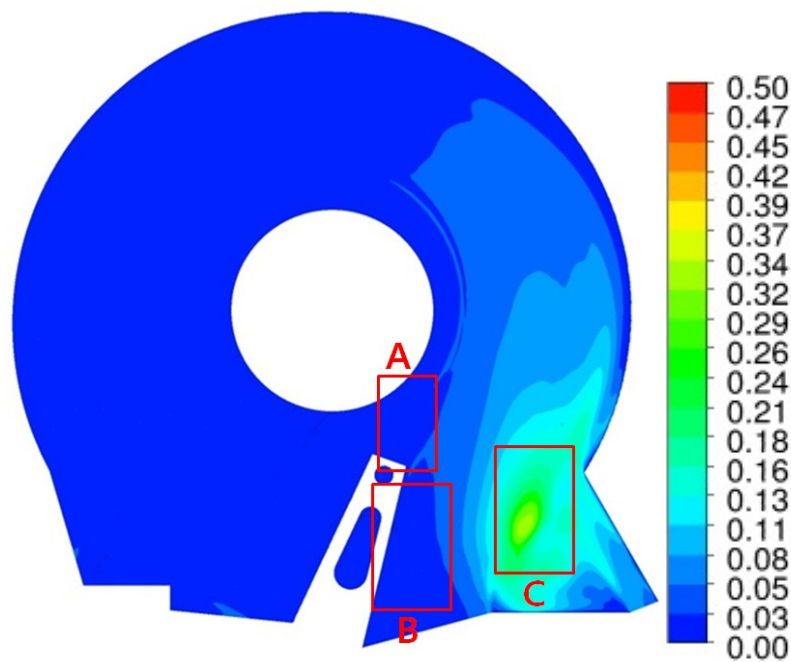
The contour plots in the air flow at the inter-disk mid-plane (Figure 4.24 (a) and 4.25 (a)) reveal that turbulent flow arises in the region downstream of the arm due to the presence of the weight-saving hole. However, the higher kinematic viscosity of helium (Figure 4.24 (b)) successfully reduces the magnitude of the TI downstream of the arm and the SSU. Since the stagnation point on the arm in the helium flow is observed to be further out radially, the vortex shedding induced by the arm is less intense than that of air. Also, the unsteady flow generated by the SSU is quickly stabilized in the helium flow. As a result, the only region that shows a high TI value is found to be where the fluid entrained from the outside of the rotating frame is sheared by the edge of the wall with the no-slip boundary condition and experiences a sudden acceleration by the rotation of the disk (Box C in Figures 4.24 and 4.25). On the contrary, the helium flow shows a quite intensified TI downstream of the weight-saving hole where also the region downstream of the SSU still shows a lower TI value at 15000 rpm than that at 5400 rpm (Figure 4.25 (b)). This abrupt increase of the TI is basically caused by the relocation of the stagnation point radially inward. The incoming flow at radii larger than the stagnation point is the source of the TI downstream of the arm. Between 5400 and 15000 rpm, the helium flow experiences larger movement of the stagnation point than that for the air flow, and the corresponding flow rate across the weight-saving hole grows. As a result, the increased flow rate over the arm strengthens the intensity of the vortex shedding downstream of the arm so that a higher magnitude of the TI is generated at 15000 rpm than that at 5400 rpm in the helium flow.

Figures 4.26 and 4.27 support that the turbulent mixing layer generated by the leading edge of the arm is completely three-dimensional. Also, this mixing layer is guided into the region between the leading and the trailing flanges with a high level of the TI and propagated to the region downstream of the SSU (Box A in Figures 4.26 and 4.27).

The figures captured at the mid-plane between the arm and the lower surface of the upper disk (Figures 4.28 and 4.29) clearly show that the weight-saving hole works as a main source of flow perturbation for the incoming flow. The flow over the arm is perturbed by the weight-saving hole area and becomes more turbulent in the region downstream of the actuator arm (Box A in Figures 4.28 and 4.29).

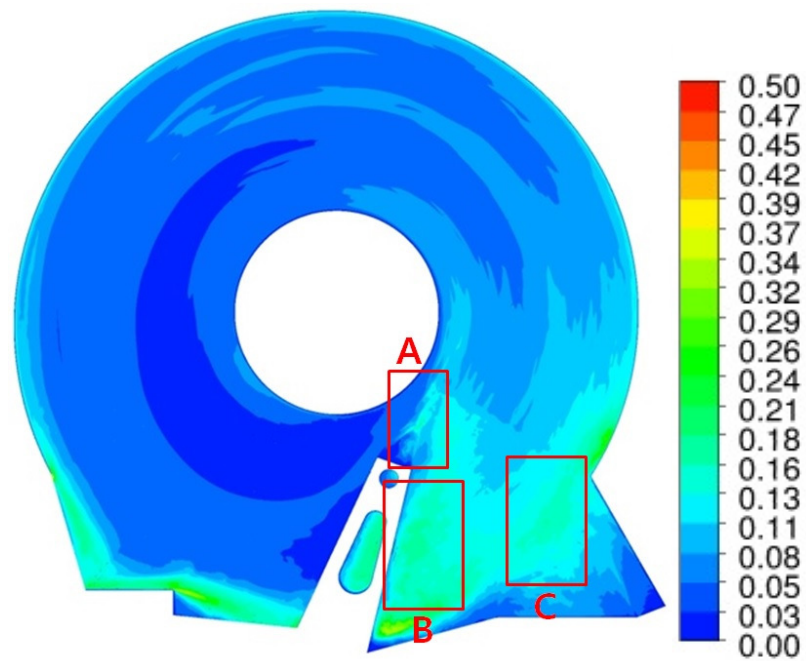


(a)

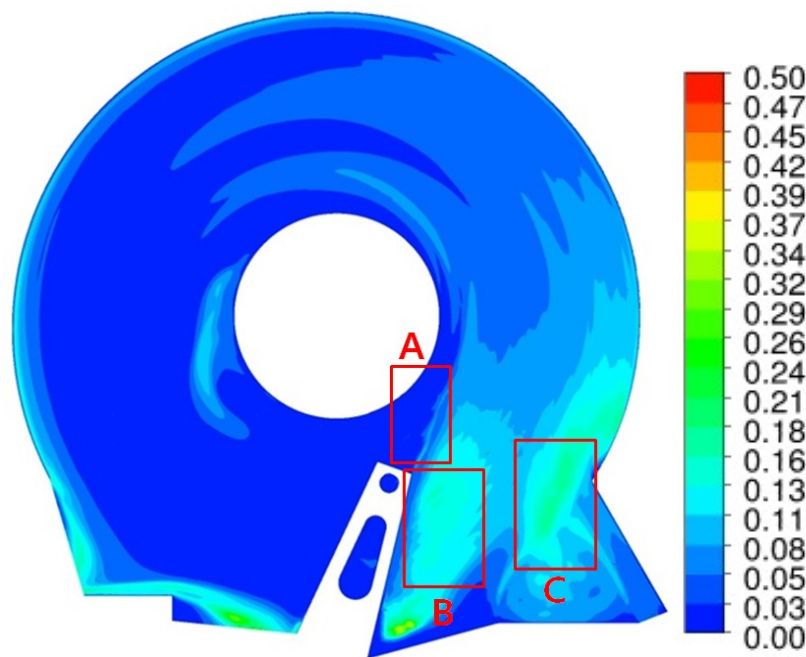


(b)

Figure 4.24: Contour plots of TI^* of (a) air and (b) helium at the inter-disk mid-plane ($z = 0$ mm) at 5400 rpm.

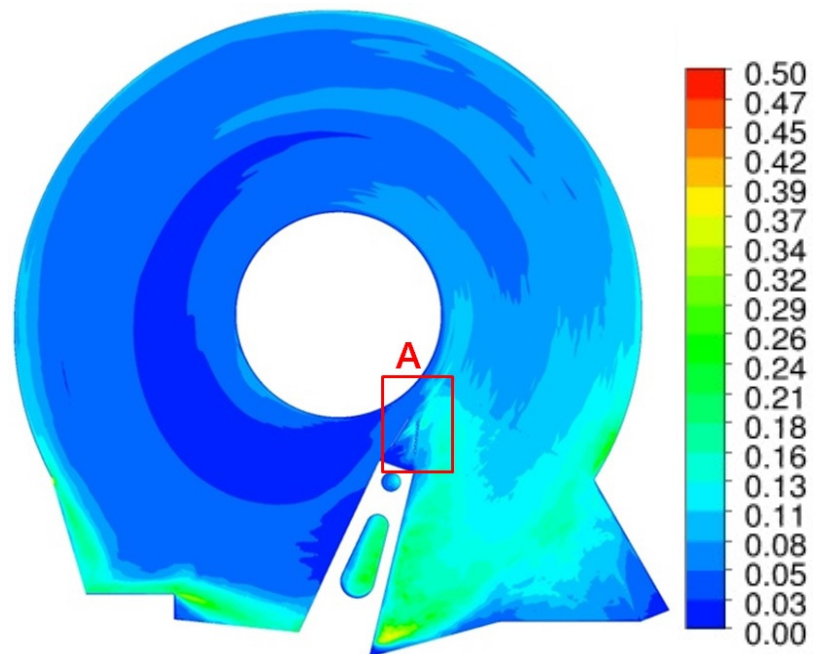


(a)

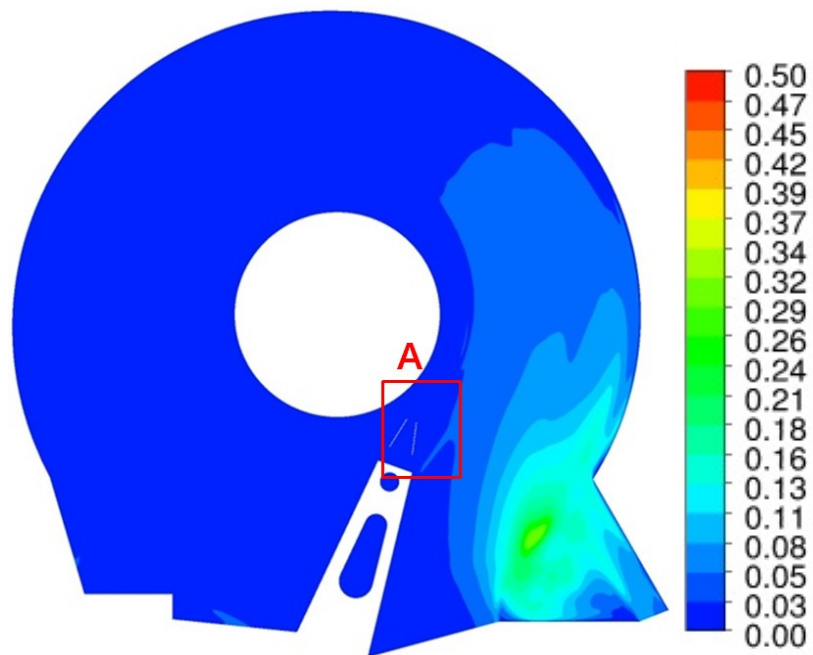


(b)

Figure 4.25: Contour plots of TI^* of (a) air and (b) helium at the inter-disk mid-plane ($z = 0$ mm) at 15000 rpm.

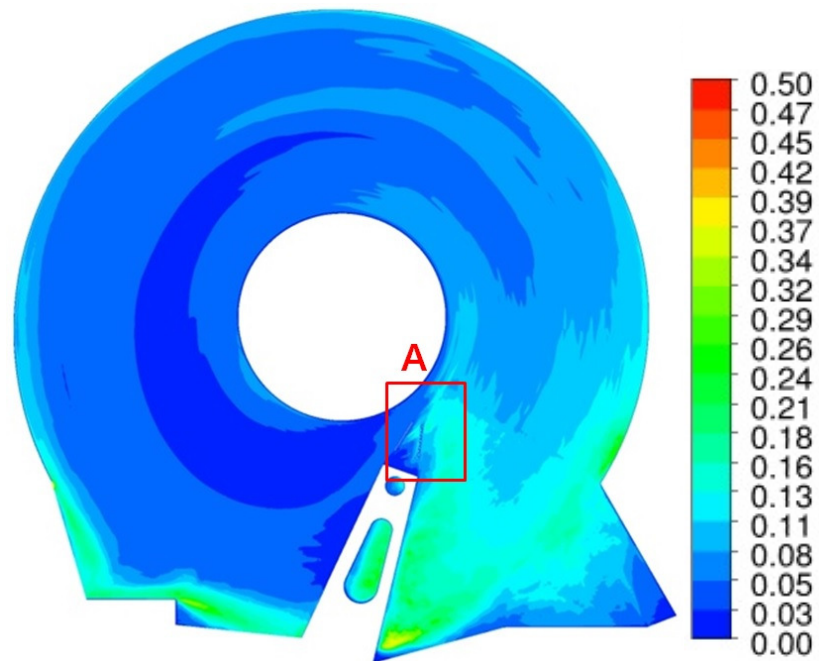


(a)

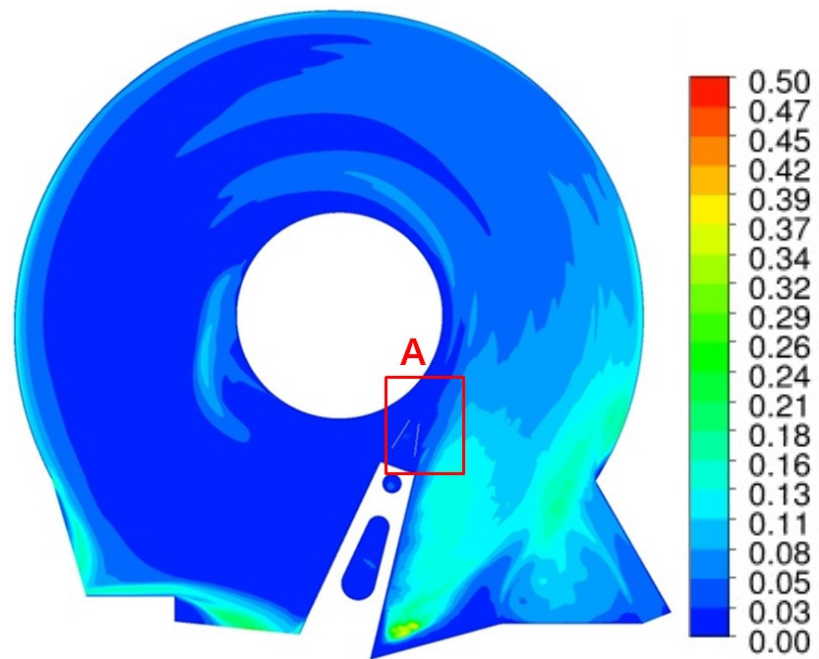


(b)

Figure 4.26: Contour plots of TI^* of (a) air and (b) helium at the plane across the flanges ($z = 0.355$ mm) at 5400 rpm.

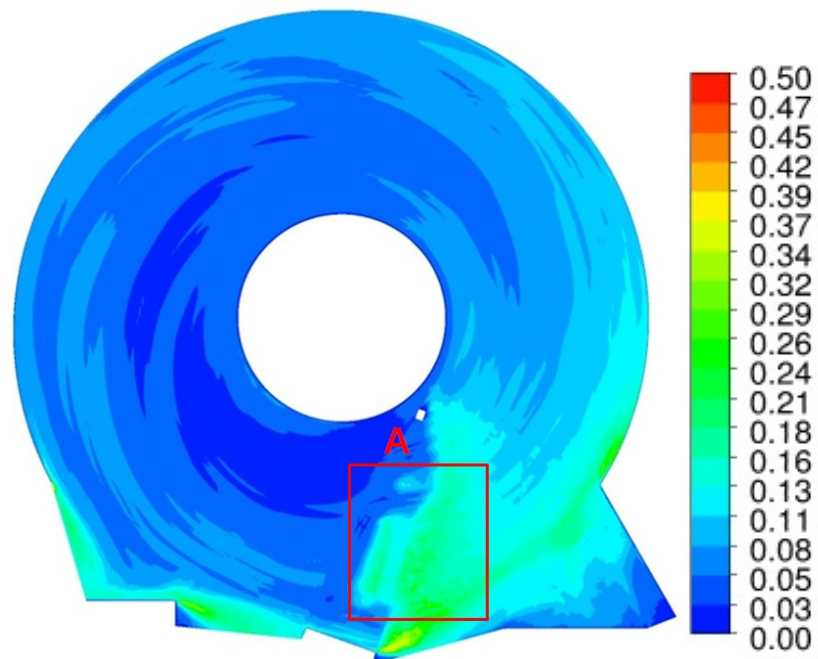


(a)

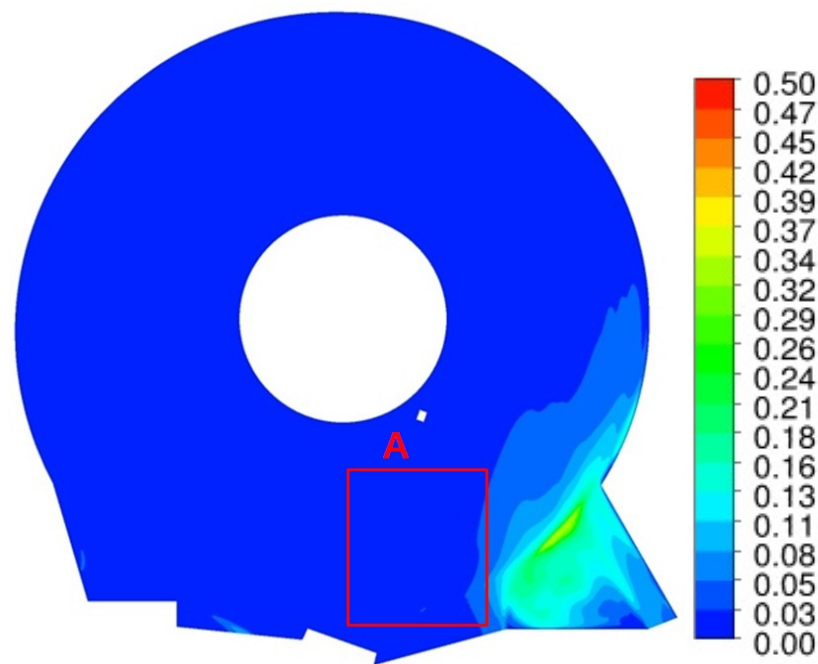


(b)

Figure 4.27: Contour plots of TI^* of (a) air and (b) helium at the plane across the flanges ($z = 0.355$ mm) at 15000 rpm.

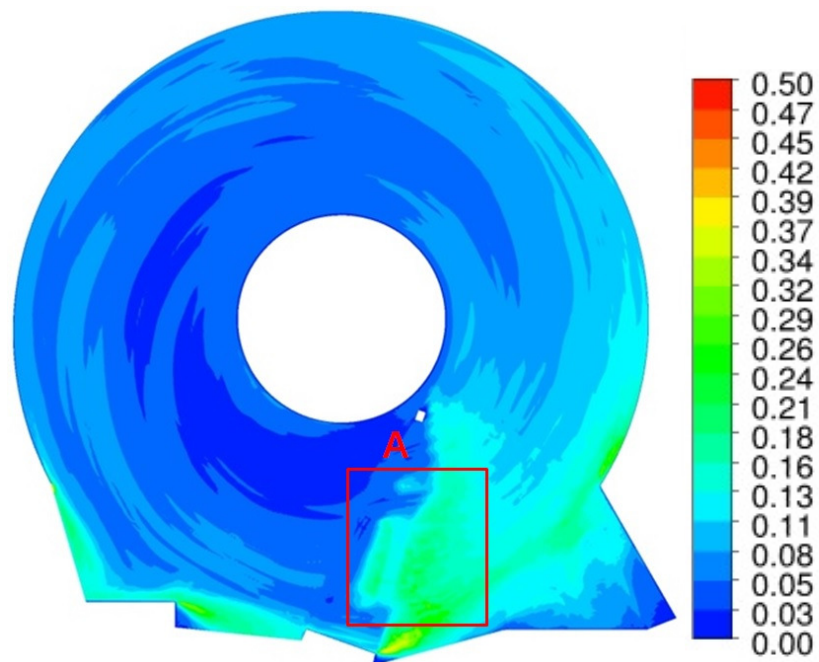


(a)

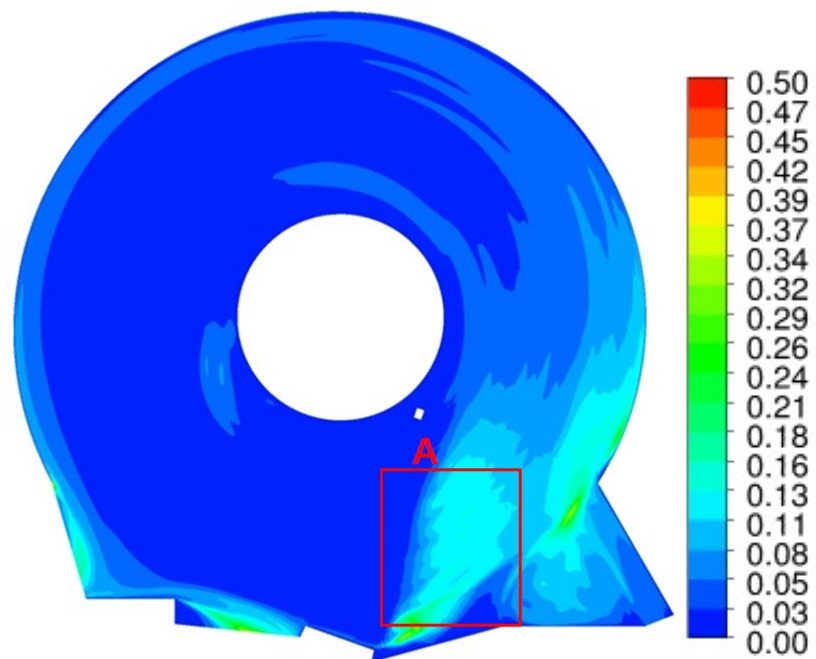


(b)

Figure 4.28: Contour plots of TI^* of (a) air and (b) helium at the plane between the arm and the disk ($z = 0.8$ mm) at 5400 rpm.



(a)



(b)

Figure 4.29: Contour plots of TI^* of (a) air and (b) helium at the plane between the arm and the disk ($z = 0.8$ mm) at 15000 rpm.

4.1.4 Vibration Analyses of the Slider Suspension Unit

Time-dependent displacements are measured at the center of the magnetic tip on the upper and the lower SSU. From Figures 4.30 to 4.32, the displacements in x, y, z – axis for both air and helium at 5400 rpm reveal that the magnitude of the displacements in all axes is lower in helium than that in air. The maximum peak-to-peak value of the flow induced displacement in the helium flow is approximately 51 % of the air flow. Moreover, the helium flow generates almost perfect symmetric and sinusoidal motions in all axes between the upper and the lower SSU; the displacements in air don't illustrate any distinctive stable patterns. The z – component (axial) of the motion induces the maximum oscillation in both fluids. In Figures 4.30 and 4.31, motions with a high frequency are detected in the early stage of the single-cycle simulation. This is due to initial conditions on the fluid and the solid domain. The calculation of the fluid domain starts from the fully developed condition by the process explained in Ch. 3 where the SSU is initially at rest and experiences abrupt aerodynamic forces at the beginning of the calculation. Therefore, a certain time period is required to adapt the solid domain for the fully coupled condition. At 15000 rpm (Figures 4.33, 4.34 and 4.35), the air flow illustrates a drastic increase in motions along all axes compared to the motions at 5400 rpm. In particular, the motion in the axial direction shows a ten-fold increase in the maximum peak between 5400 rpm and 15000 rpm. However, the helium flow doesn't cause any noticeable increase in the magnitude between those two different rotating speeds of the disk. This result can be attributed to two main factors. The first reason is the lower Reynolds number created by the lower density of helium than air. Since the momentum in the flow field is converted to the pressure on the structure surfaces as $1/2\rho u^2$, the force from the

flow is always smaller in helium than in air under the same boundary condition. Thus, the corresponding disturbance in the solid triggered by the fluid forces will be smaller. The second reason is the relocation of the stagnation point on the arm. The incoming flow at radii smaller than the stagnation point is redirected and accelerated around the SSU. However, the stagnation point at 15000 rpm is radially interior to that at 5400 rpm, and the corresponding flow rate toward the SSU is reduced so that the flow acceleration at 15000 rpm is not as intensified as that at 5400 rpm. As a result, the magnitude of the displacements between 5400 and 15000 rpm in helium doesn't show a comparatively large change similar to that in the air flow.

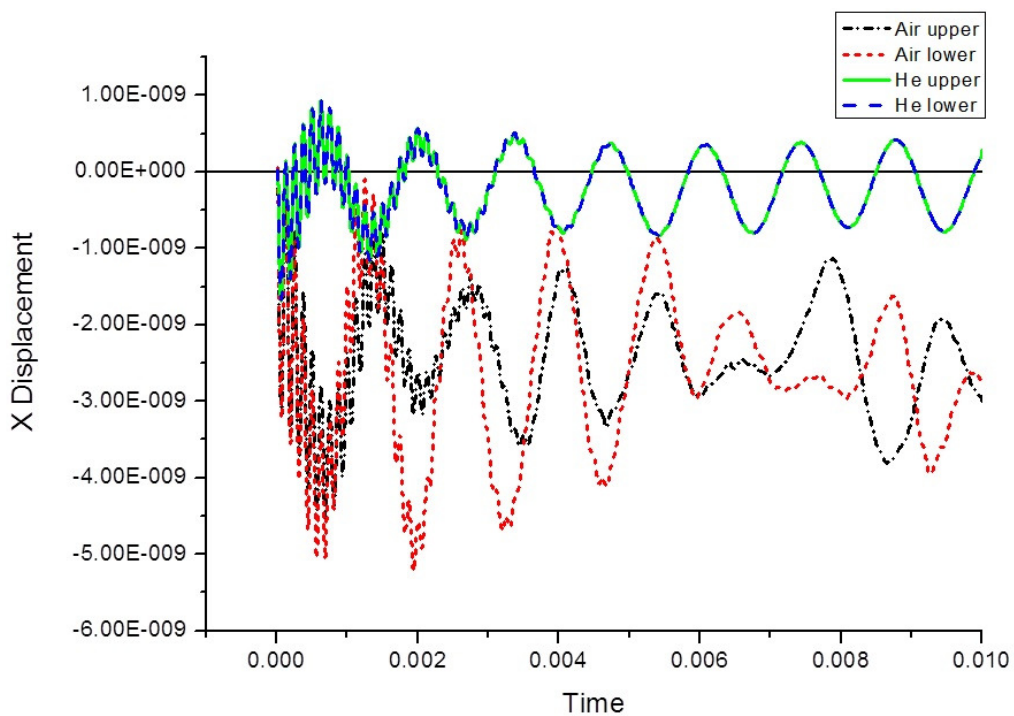


Figure 4.30: Displacement in x – axis on the center of the magnetic tips at 5400 rpm.

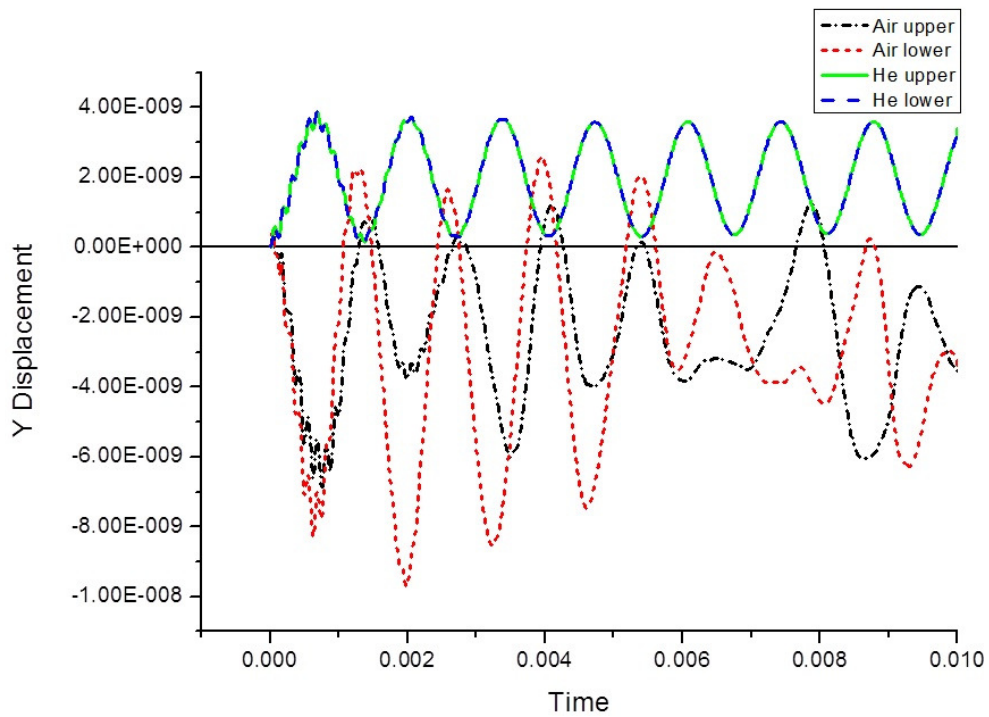


Figure 4.31: Displacement in y – axis on the center of the magnetic tips at 5400 rpm

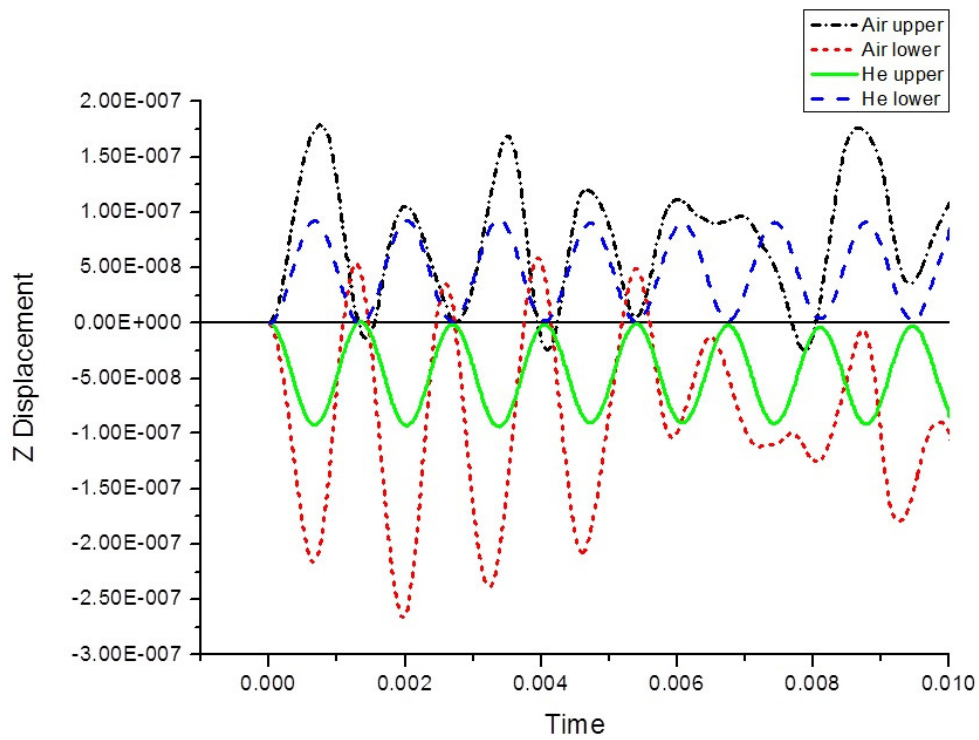


Figure 4.32: Displacement in z – axis on the center of the magnetic tips at 5400 rpm

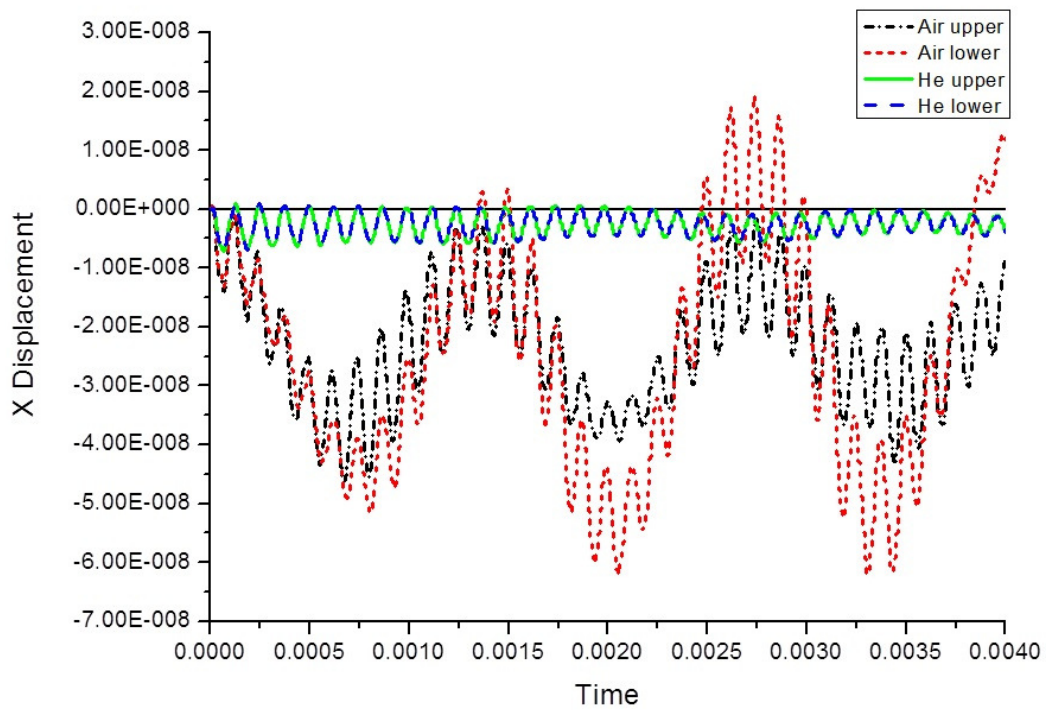


Figure 4.33: Displacement in x – axis on the center of the magnetic tips at 15000 rpm

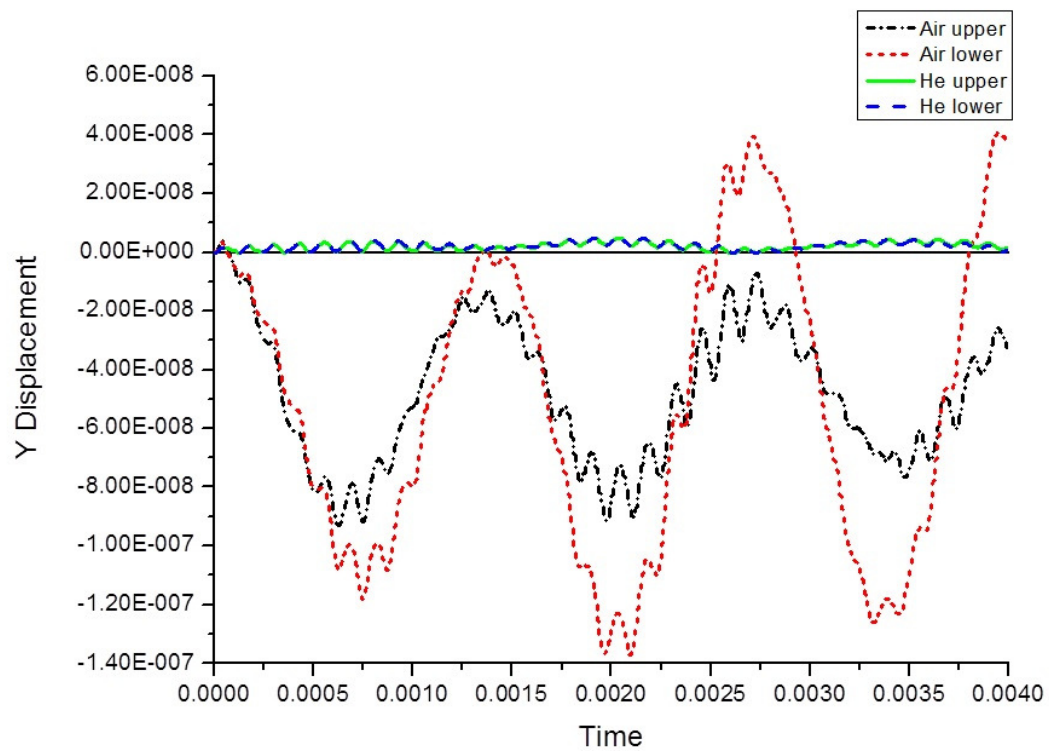


Figure 4.34: Displacement in y – axis on the center of the magnetic tips at 15000 rpm

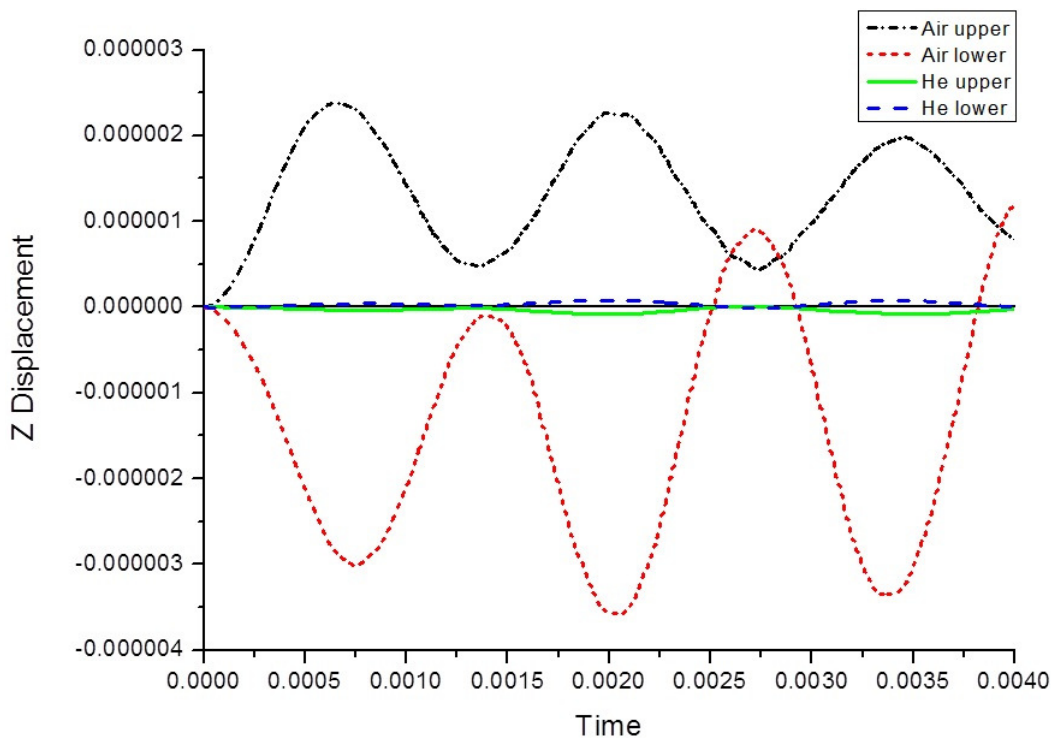


Figure 4.35: Displacement in z – axis on the center of the magnetic tips at 15000 rpm

A natural frequency test was performed by using ANSYS software with the same geometry, boundary conditions and the grid domain of the lower SSU. The surface where the SSU is mounted on the arm was imposed with a fixed boundary. Results from the analysis are shown in Table 4.1. The natural frequency is obtained from the first to tenth mode. In this table, plots are captured until the 6th mode. The plots reveal that the natural frequencies mainly depend on a bending and a torsional mode. The first, the second and the fourth mode show the bending while the all other frequencies are torsional.

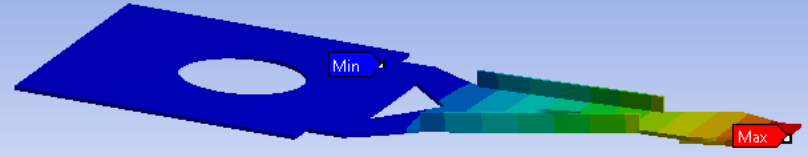
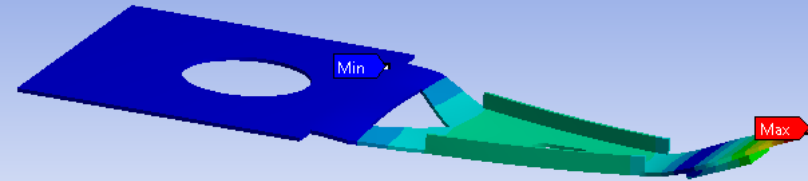
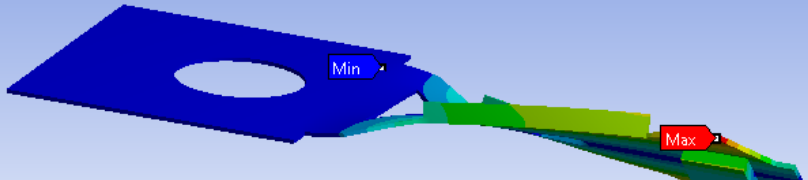
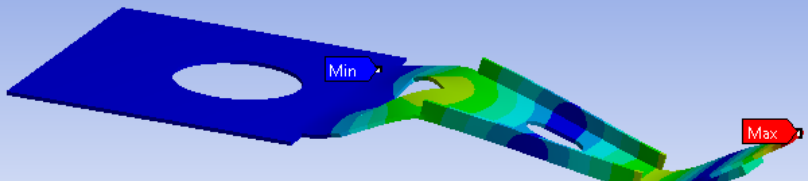
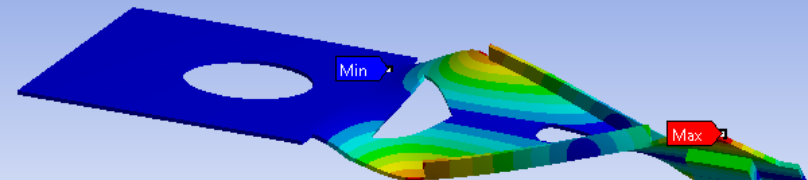
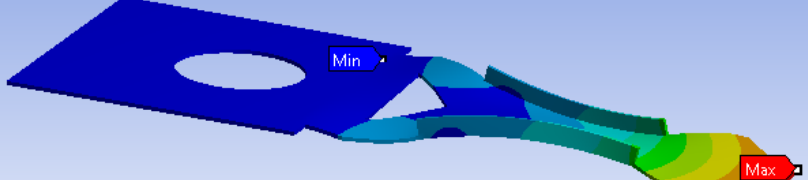
Mode	Figures	Frequency (Hz)
1 st		739.93 Bending
2 nd		7411.3 Bending
3 rd		8087.7 Torsion
4 th		14785 Bending
5 th		18160 Torsion
6 th		27402 Torsion

Table 4.1: Natural frequency of the lower Slider Suspension Unit.

From the result of the time-dependent displacement at the center of the magnetic tip, Power Spectral Density (PSD) over frequency ranges are computed by conducting a Fast Fourier Transform (FFT) for two different motions of the SSU; 1) An axial motion which is parallel to the rotating axis, 2) An in-plane motion which is parallel to the disk surface.

Figures 4.36 and 4.37 describe that, as observed in the transient displacements graphs, the air flow induces higher PSD than that of helium in both the in-plane and the axial displacements due to the higher fluid force and the flow oscillations by the higher density and the lower kinematic viscosity of air. However, those two gases with different material properties show the same dominant frequency containing the most energy at the frequency of 751 Hz. This frequency with the highest PSD is estimated to be induced by the unsteady flow downstream of the SSU. The PSD of the velocity fluctuation measured at a point with the most intense TI downstream of the SSU induces a noticeable peak at a frequency of 732 Hz which is quite close to the frequency with the highest PSD in the motions of the solid domain (Figure 4.38). However, the helium flow doesn't cause any distinctive frequency peaks with a high energy compared to the air flow due to the reason explained in the previous chapter. Another finding in the frequency domain is that the axial motion has a higher PSD than that of the in-plane motions. This can be interpreted with the natural frequency analyses in Table 4.1. Since the frequency with the high PSD is observed at 751 Hz which is relatively close to the first bending mode at 739.93 Hz, the SSU is more susceptible to windage perturbation in the axial direction. As a result, the PSD magnitude in the axial direction is approximately one thousand times higher than the in-plane direction.

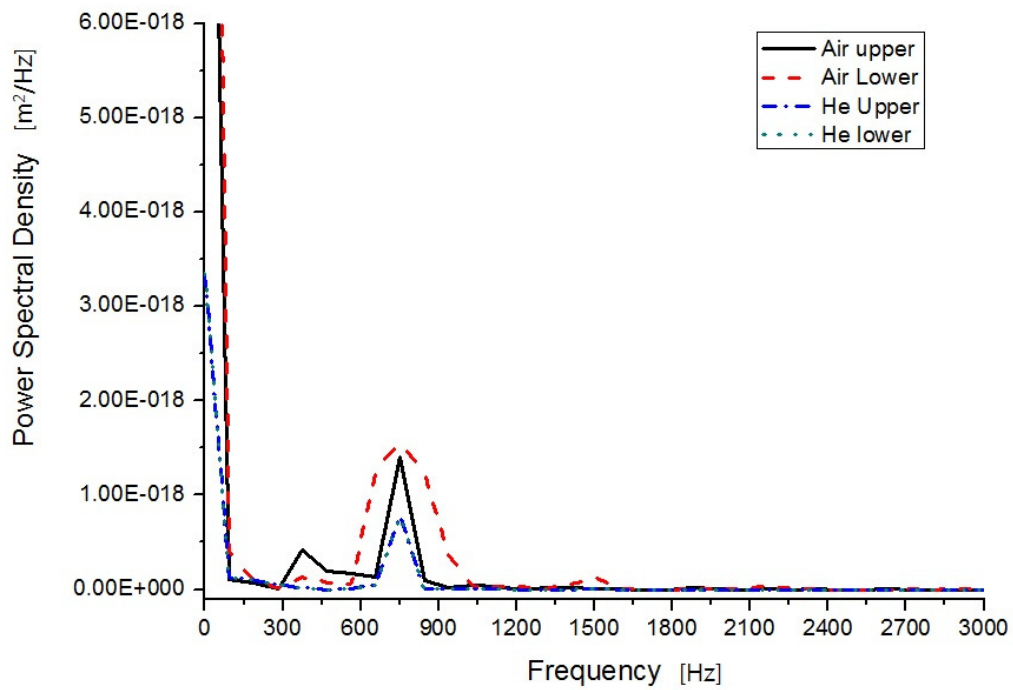


Figure 4.36: Power Spectral Density of the in-plane displacement at 5400 rpm.

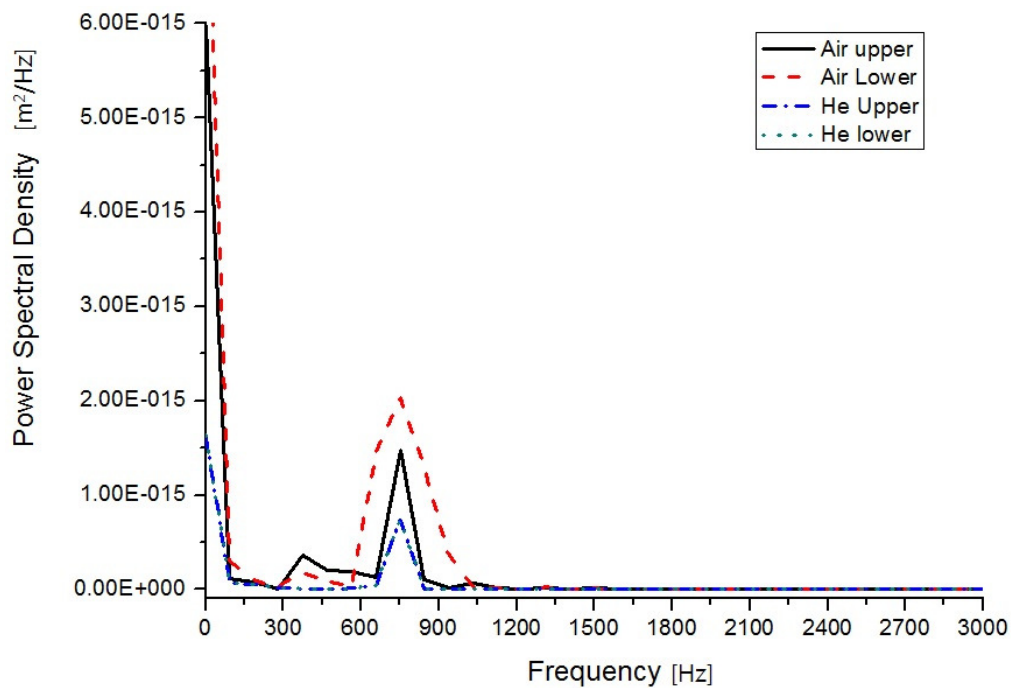


Figure 4.37: Power Spectral Density of the axial displacement at 5400 rpm.

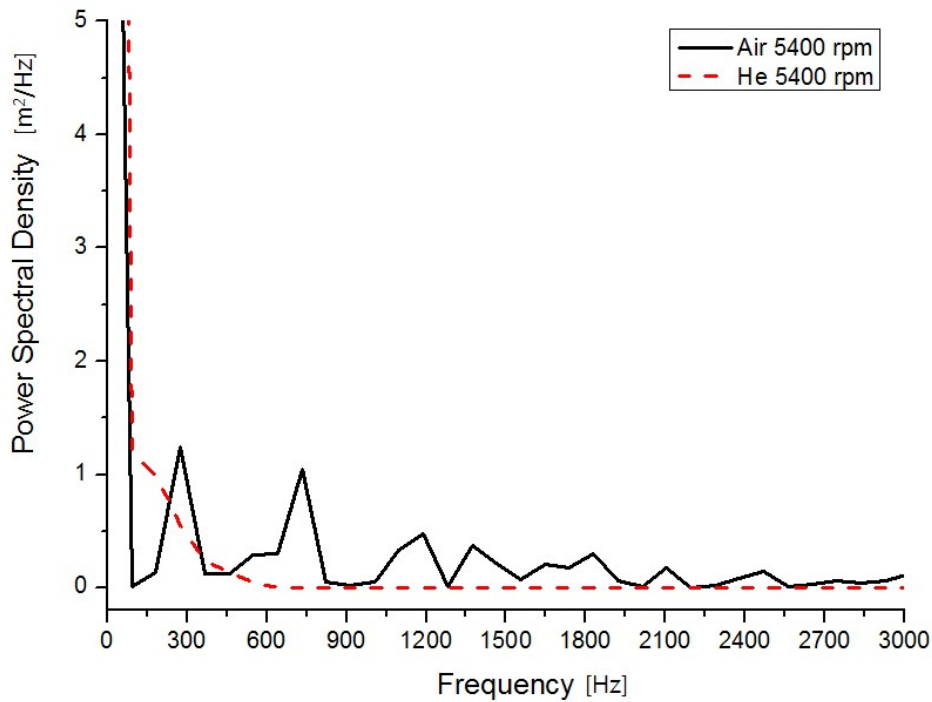


Figure 4.38: Power Spectral Density of the velocity fluctuation downstream of the SSU at 5400 rpm.

Results at 15000 rpm (Figures 4.39 and 4.40) also show a similar frequency peak as the results at 5400 rpm. A peak with the highest PSD is generated at 770 Hz in the axial and the in-plane motions of the air flow which is estimated to be caused by the flow fluctuation with the frequency of 760.6 Hz (Figure 4.41). Also, a trend that the axial motion induces a higher magnitude of the PSD than the in-plane motion is still valid. The values of both the in-plane and the axial PSD show significant increments corresponding to the increase of the rotating speed. However, the PSD of the helium flow doesn't show a clear peak across the frequency range due to the low magnitude of the displacements in the SSU due to the reduced flow rate and the more stable flow caused by the relocation of the stagnation point as well as the higher kinematic viscosity of helium.

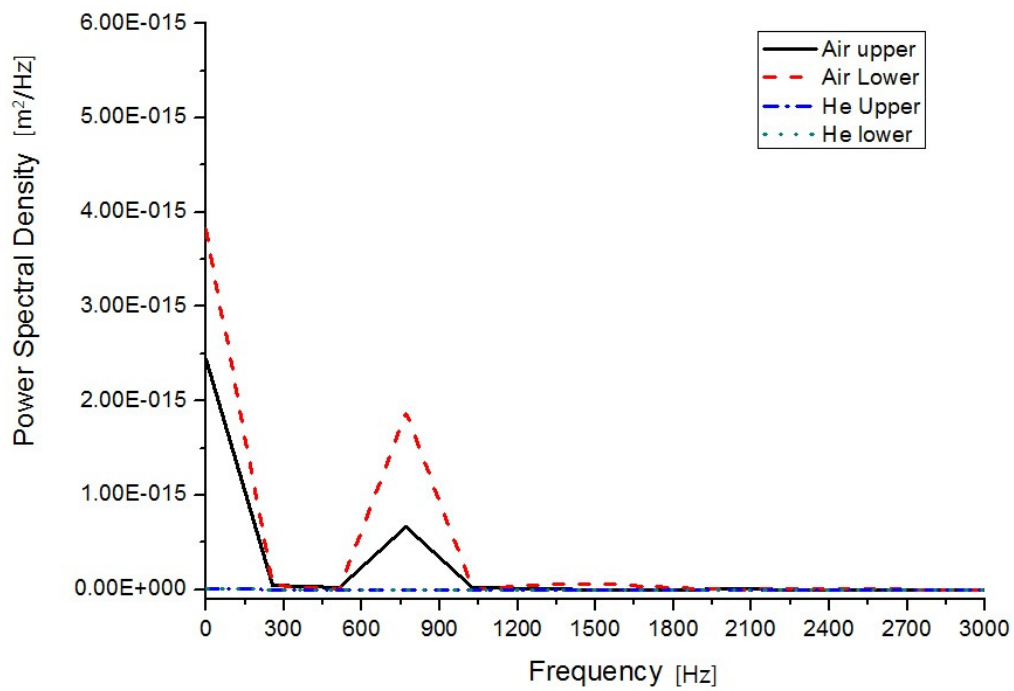


Figure 4.39: Power Spectral Density of the in-plane displacement at 15000 rpm.

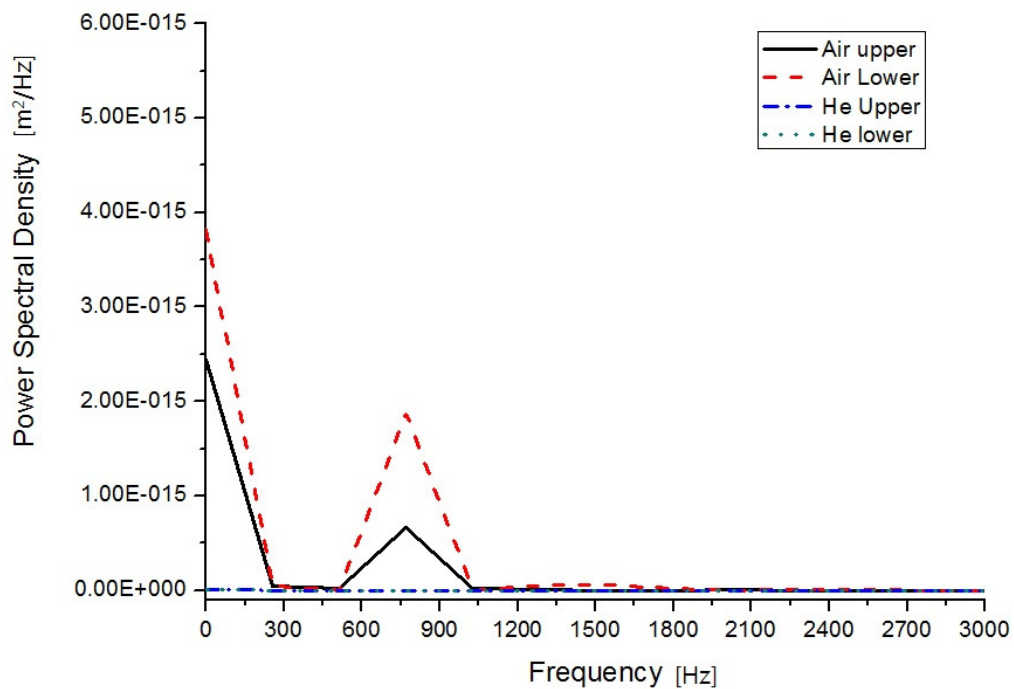


Figure 4.40: Power Spectral Density of the axial displacement at 15000 rpm.

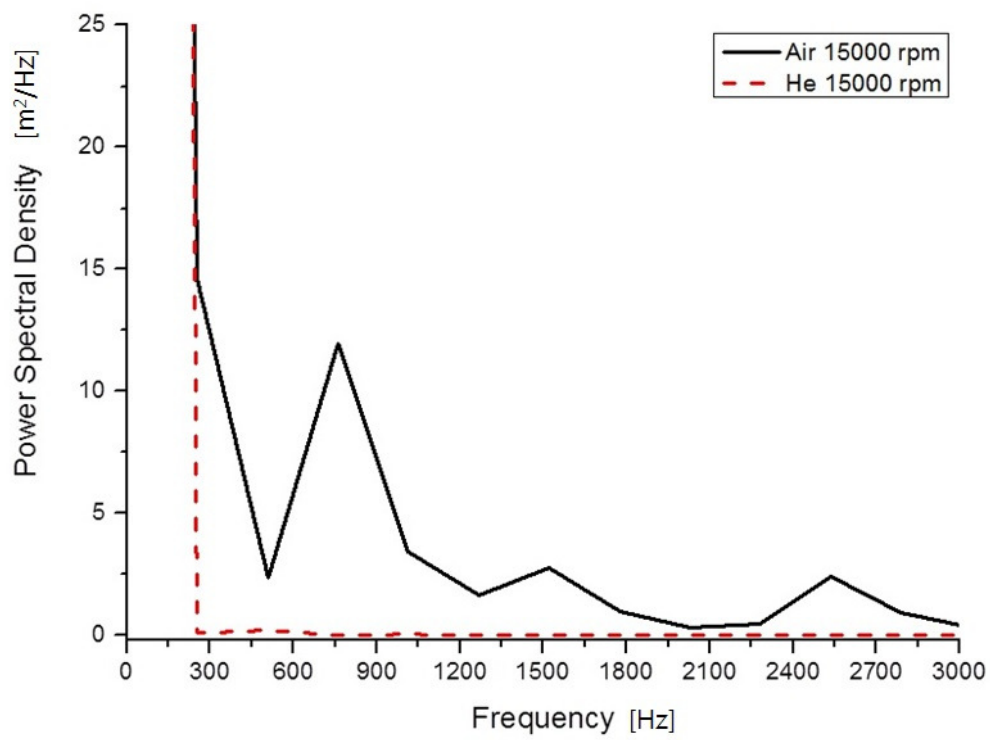


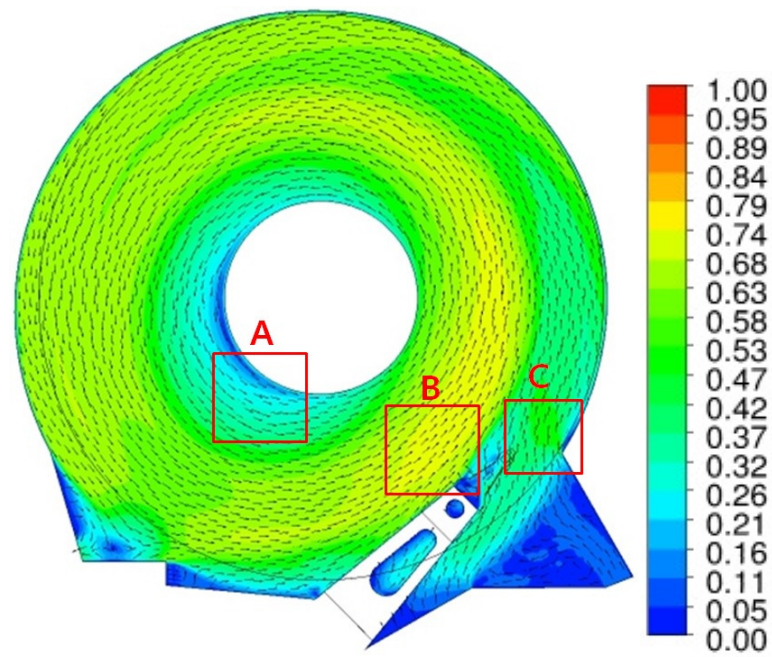
Figure 4.41: Power Spectral Density of the velocity fluctuation downstream of the SSU at 15000 rpm.

4.2 Outer configuration

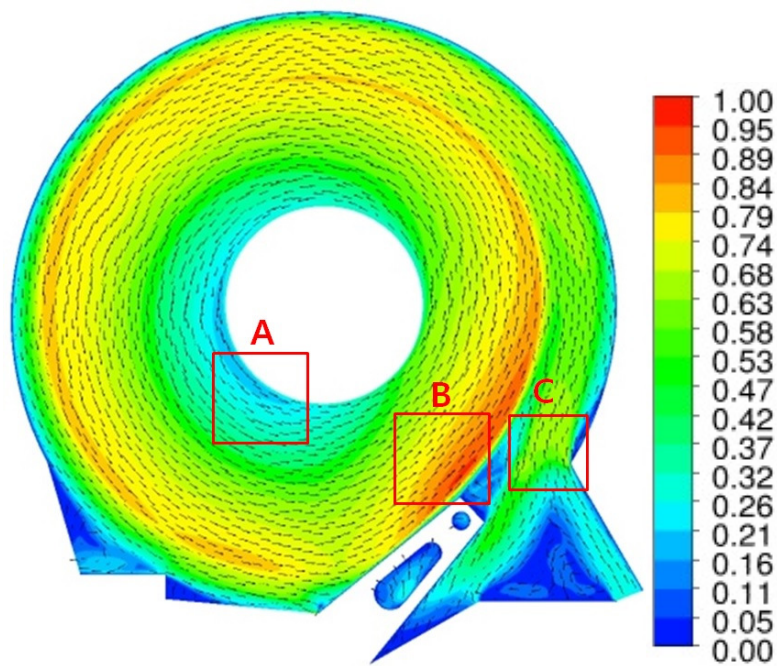
4.2.1 Velocity magnitude

The flow field for the Outer Configuration (OC) (Figure 4.2 (b)) shows quite different features compared to the results for the Inner Configuration (IC) at the inter-disk mid-plane (Figures 4.42 and 4.43). For the IC, as the incoming flow upstream of the arm approaches to the vicinity of the arm, a three-dimensional inversed flow developed to satisfy the fluid continuity near the co-rotating hub upstream of the arm. Since the Slider Suspension Unit (SSU) is located near the outer edge of the disk for the OC, the clearance between the actuator arm and the co-rotating hub is much wider than that for the IC. Therefore, the inversed flow upstream of the arm is not developed anymore (Box A in Figures 4.42 and 4.43), and the entire fluid domain is governed by the circumferential motion with the exception of the region around the SSU. However, the arm is blocking about a half of the space between the upper and the lower disk, the fluid acceleration which is observed near the SSU for the IC is also present upstream of the SSU for the OC. The incoming flow is smoothly redirected on the lateral surface of the arm toward the SSU and accelerated in the circumferential direction (Box B in Figures 4.42 and 4.43). Helium works more effectively as a momentum transport medium due to its higher kinematic viscosity than air. As a result, the magnitude of the flow acceleration upstream of the SSU is larger in the helium flow (Figures 4.42 (b) and 4.43 (b)) than in the air flow (figures 4.42 (a) and 4.43 (b)). This accelerated flow lasts for 180° downstream of the arm before it is dissipated completely. For the IC, the arm and the SSU significantly block the incoming flow. On the contrary, for the OC, the arm and the SSU are aligned with the flow, but pose blockage to the redirected flow from the outside

of the rotating disks. Therefore, the flow from the outside of the rotating frame needs to change its direction toward the clearance between the trailing edge of the arm and the enclosure wall. While this flow passes through the space between the arm and the enclosure, the flow field also tends to be dragged into the region between the upper and the lower SSU. However, the stiffening flanges in the SSU restrict the flow into the space between the flanges. As a result, most of the flow from outside the disk domain is redirected to the space between the arm and the enclosure and accelerated due to the decrease of the flow path area (Box C in Figures 4.42 and 4.43). But this acceleration is of a lower magnitude than that of the incoming flow upstream of the arm for the IC.

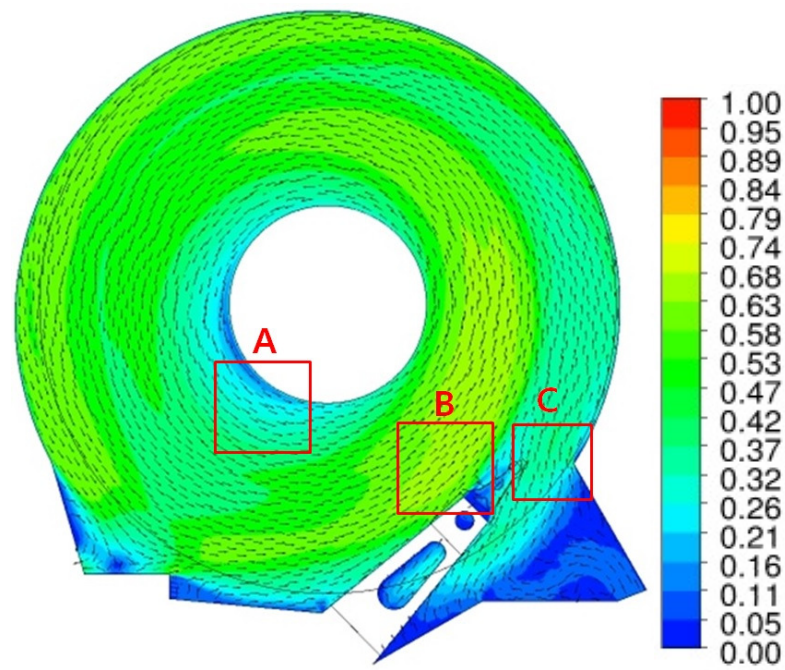


(a)

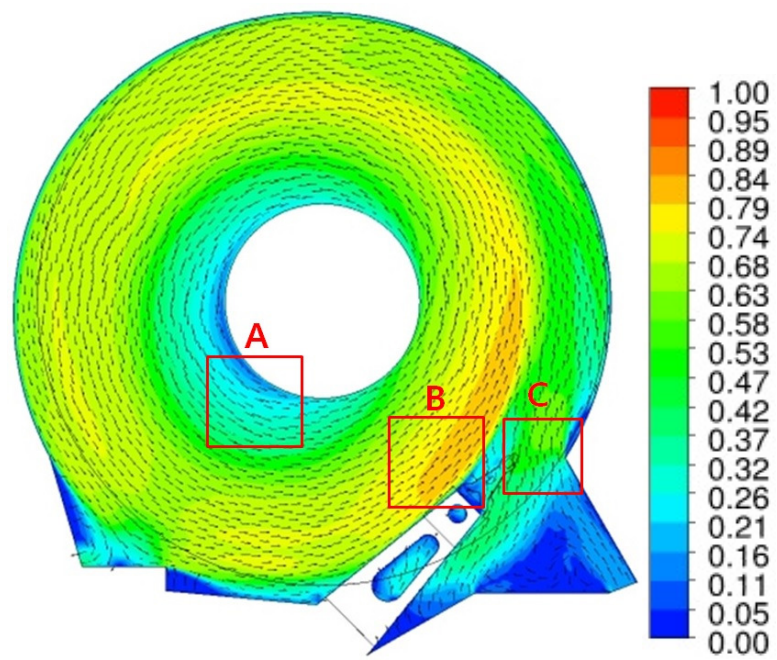


(b)

Figure 4.42: Contour plots of mean velocity of (a) air and (b) helium at the inter-disk mid-plane ($z = 0$ mm) at 5400 rpm.



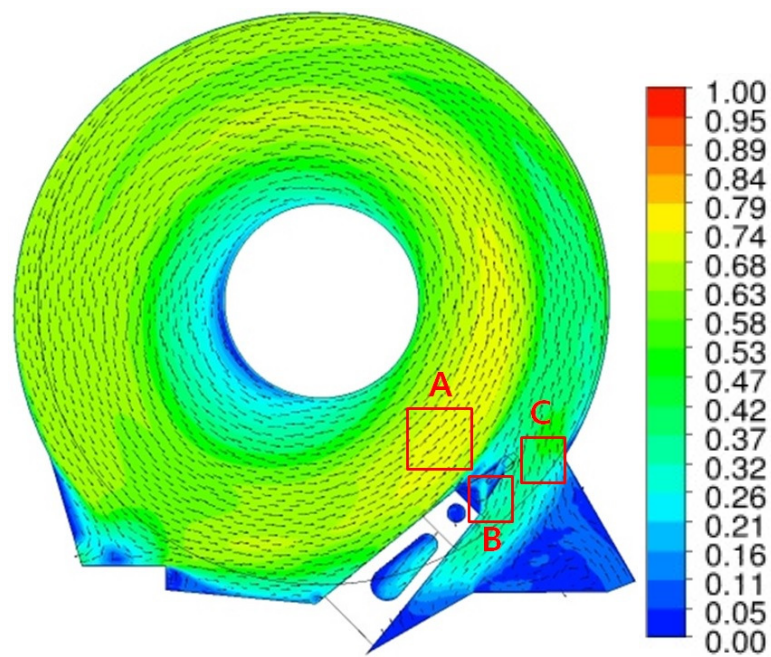
(a)



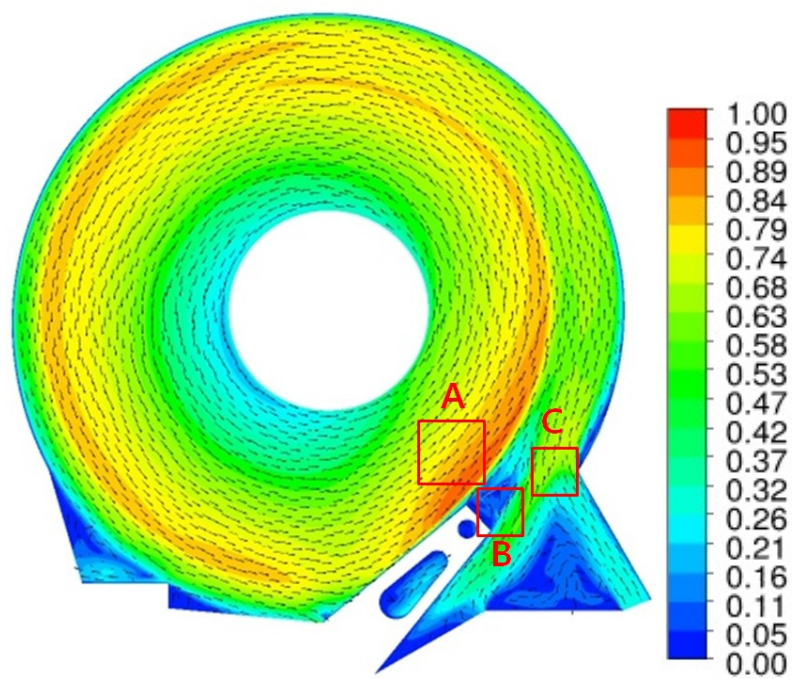
(b)

Figure 4.43: Contour plots of mean velocity of (a) air and (b) helium at the inter-disk mid-plane ($z = 0$ mm) at 15000 rpm.

The contour plots across the stiffening flanges (Figures 4.44 and 4.45) reveal that the region upstream of the SSU shows almost identical flow pattern of the inter-disk mid-plane. The incoming flow is smoothly redirected to the SSU and accelerated on the lateral surface of the arm (Box A in Figures 4.44 and 4.45). However, a different flow field is induced downstream of the SSU. The flow from the outside of the rotating frame is directly blocked by the stiffening flanges so that the domain between the upper and the lower SSU shows a lower magnitude of velocity than that at the inter-disk mid-plane. Since the air flow generates more severe pressure imbalance at the stationary domain between the upper and the lower SSU from the redirected flow than the helium flow, the flow redirected on the actuator arm is more driven toward the SSU domain and divided into two streams by the stiffening flanges in the air flow (Box B in Figure 4.44 (a)) at 5400 rpm where the helium flow induces relatively smooth flow redirection to the clearance between the SSU and the sharp edge in the enclosure wall (Box B in Figure 4.44 (b)). However, the increased rotating speed of the disk causes the split of the redirected flow from the outside of the disk domain by the stiffening flange in both gases (Box B in Figure 4.45 (a) and (b)). The dragged flow into the SSU domain undergoes a velocity reduction between the leading and the trailing flanges and is dissipated while the flow along the surface of the stiffening flanges is guided into the clearance and accelerated between the SSU and the enclosure wall (Box C in Figures 4.44 and 4.45).

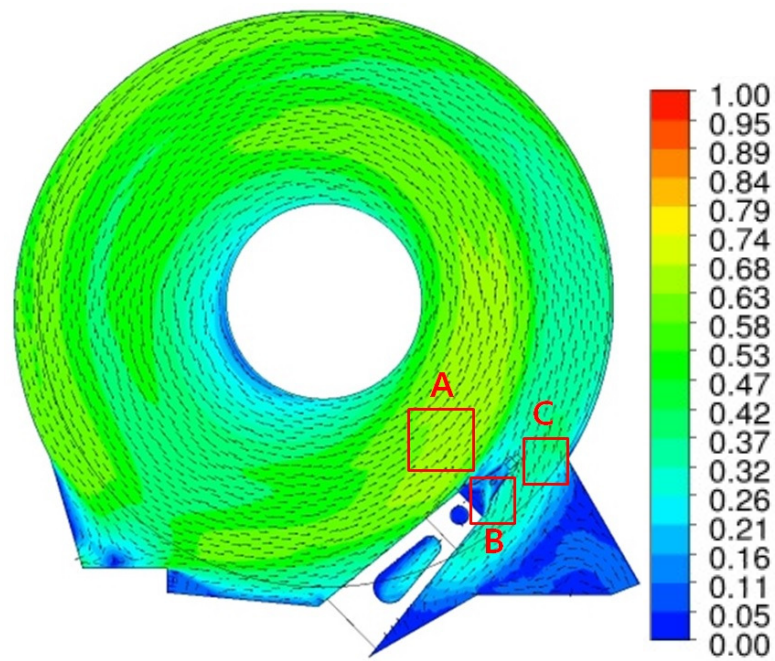


(a)

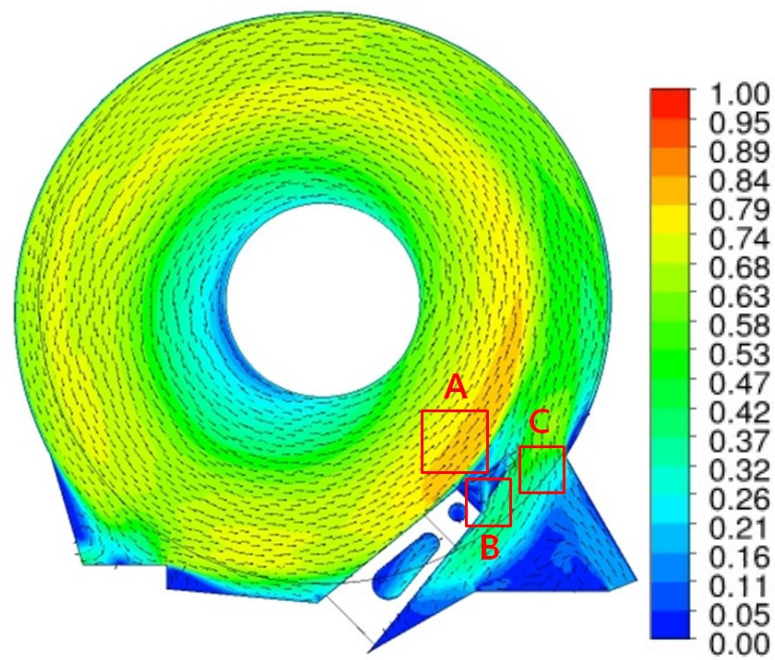


(b)

Figure 4.44: Contour plots of mean velocity of (a) air and (b) helium at the plane across the flanges ($z = 0.355$ mm) at 5400 rpm.



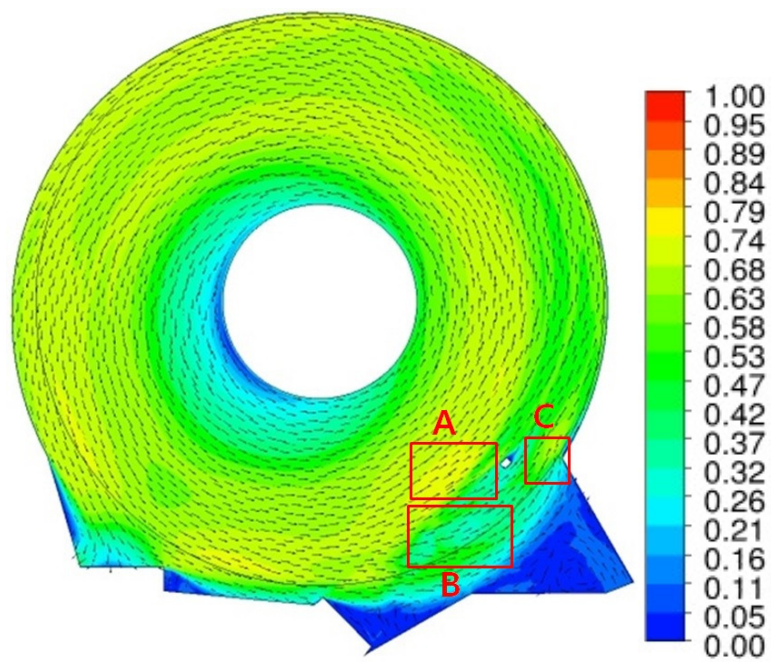
(a)



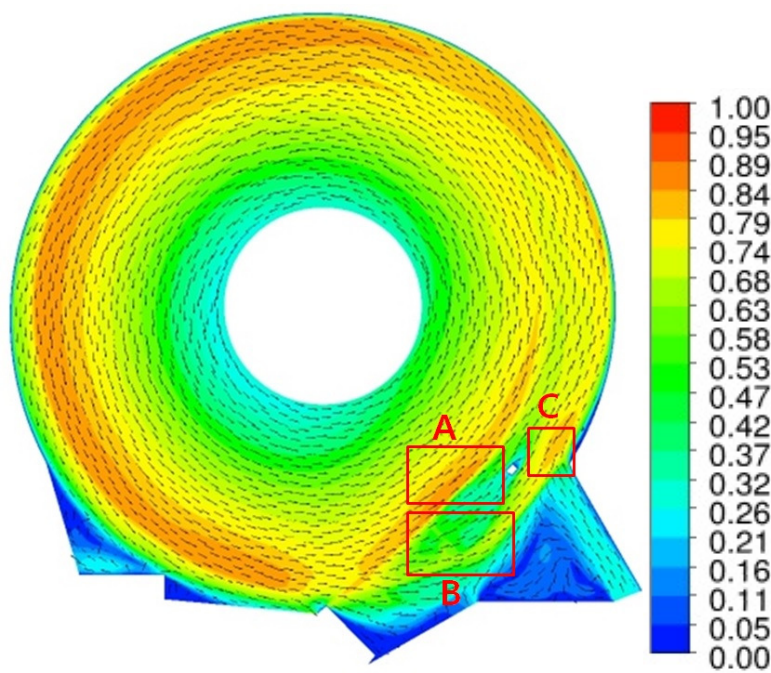
(b)

Figure 4.45: Contour plots of mean velocity of (a) air and (b) helium at the plane across the flanges ($z = 0.355$ mm) at 15000 rpm.

The mid-plane between the upper surface of the arm and the lower surface of the upper disk shows another instance of Taylor-Proudman theorem similar to the results for the IC (Figures 4.46 and 4.47). The only flow blockage is a small magnetic tip. However, the entire fluid domain still describes very similar flow field to the result at the inter-disk mid-plane. Without the presence of the arm obstruction, the incoming flow is still accelerated above the lateral surface of the arm where it experiences the same phenomenon (Box A in Figures 4.46 and 4.47). Right after this acceleration, a sudden reduction of the flow velocity is generated in the space between the arm and the lower surface of the upper disk across the length of the arm. At the same time, the flow over the arm is divided into two streams by the stagnation point on the lateral surface of the arm. The flow at radii smaller than the stagnation point shows a direction change toward the magnetic tip while the fluid outside the stagnation point travels over the arm with a relatively constant radius (Box B in Figures 4.46 and 4.47). These two streams are smoothly driven to the clearance between the magnetic tip and the sharp edge in the enclosure wall and accelerated with a lower magnitude than the acceleration observed in the region upstream of the SSU (Box C in Figures 4.46 and 4.47).

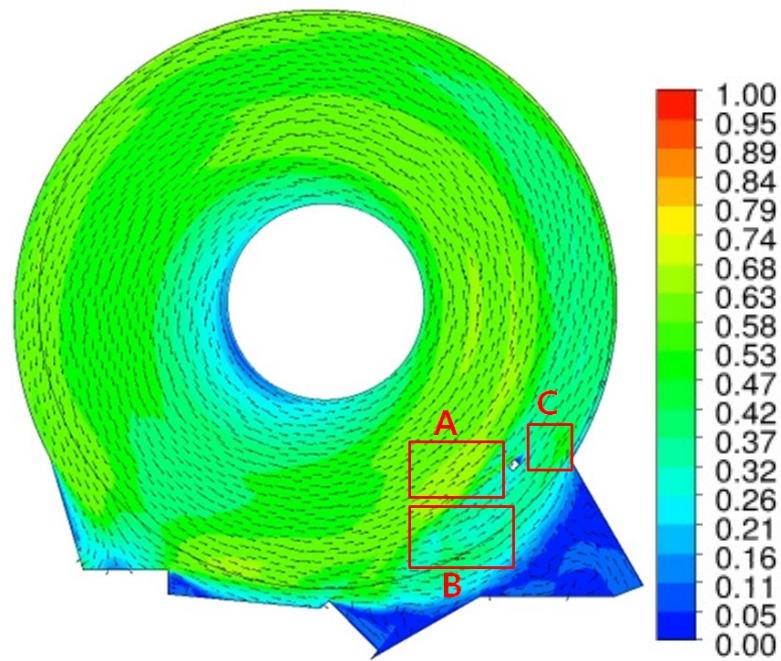


(a)

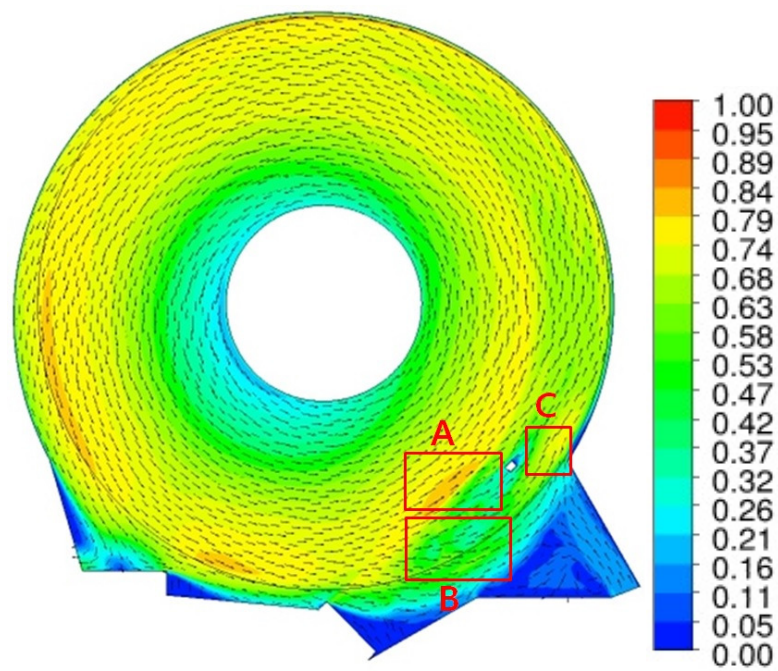


(b)

Figure 4.46: Contour plots of mean velocity of (a) air and (b) helium at the mid-plane between the arm and the upper disk ($z = 0.8$ mm) at 5400 rpm.



(a)



(b)

Figure 4.47: Contour plots of mean velocity of (a) air and (b) helium at the mid-plane between the arm and the upper disk ($z = 0.8$ mm) at 15000 rpm.

The contour plots with velocity vectors on the planes across the stiffening flanges (Figures 4.48, 4.49, 4.50 and 4.51) show that velocity magnitude around the stiffening flanges reduces due to the no-slip boundary conditions. Moreover, the presence of the stiffening flanges block the flow redirection from the outside of the rotating frame so that interactions between the region upstream and downstream of the SSU is quite limited except for the inter-disk mid-plane region. The flow upstream of the stiffening flanges illustrate that the location of the SSU near the outer edge of the disk changes the flow characters to the condition of the unobstructed flow represented by the presence of a pair of counter-rotating vortices with respect to the inter-disk mid-plane near the outer region. In Ch.2, it was shown that the flow between a pair of co-rotating disks experiences a transition from the solid body rotation to a pair of counter-rotating vortical structures in the outer radius region. As the space between the SSU and the co-rotating hub becomes wider, the incoming flow upstream of the arm doesn't need to undergo a steep direction change. Therefore, the flow between the arm and the hub is able to maintain features similar to the flow field between a pair of disks without the presence of the arm. The velocity near the disk surfaces becomes higher than the region around the inter-disk mid-plane due to the viscous effect from the SSU. Thus, the fluid near the disk surfaces is driven radially outward and divided into two streams. The first stream keeps its direction through a clearance between the SSU and the disk. Since the stiffening flange reduces the area of the flow field, the radial flow needs to be accelerated near the disk surface to satisfy the fluid continuity. The second stream is redirected to the axial direction on the surface of the stiffening flanges. Around the inter-disk mid-plane where the upper and the lower SSU allow a small clearance, there is a corresponding radially inward flow at the

inter-disk mid-plane to satisfy the fluid continuity. As a result, a pair of co-rotating vortices is completed in the region upstream of the SSU similar to the unobstructed flow. Since the radial momentum which is defined by $\rho r\Omega^2$ is always larger in air than helium due to its higher density, more fluid is driven radially outward and a larger size of vortices are generated in the air flow (Figures 4.48 and 4.50) than in the helium flow (Figures 4.49 and 4.51).

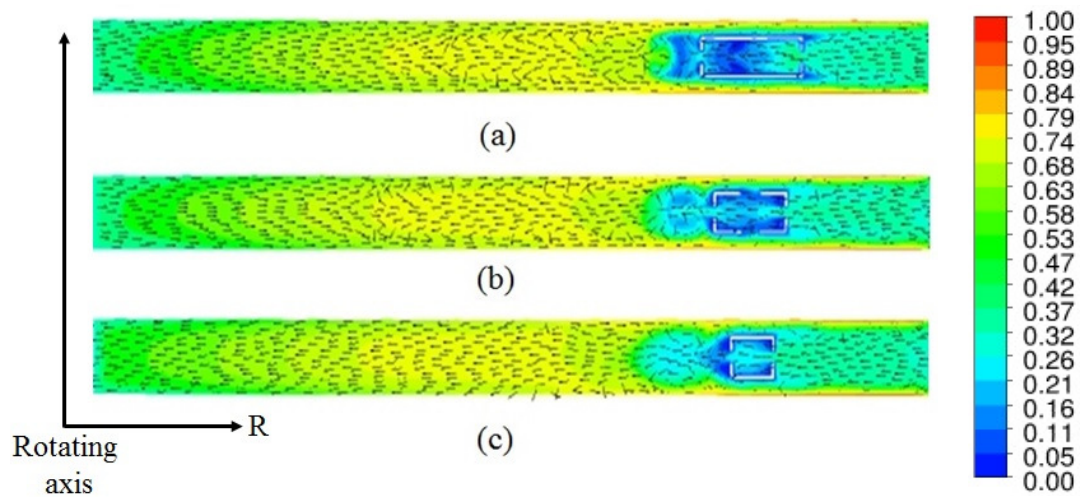


Figure 4.48: Contour plots of mean velocity on three planes across the stiffening flanges;
 (a) near the arm. (b) middle of the flanges. (c) the end of the flanges in air at
 5400 rpm.

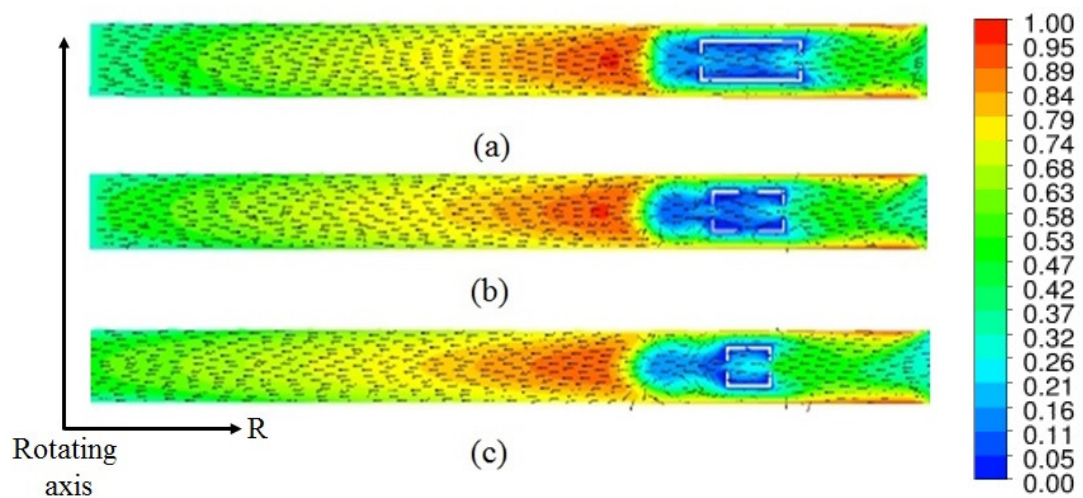


Figure 4.49: Contour plots of mean velocity on three planes across the stiffening flanges;
 (a) near the arm. (b) middle of the flanges. (c) the end of the flanges in
 helium at 5400 rpm.

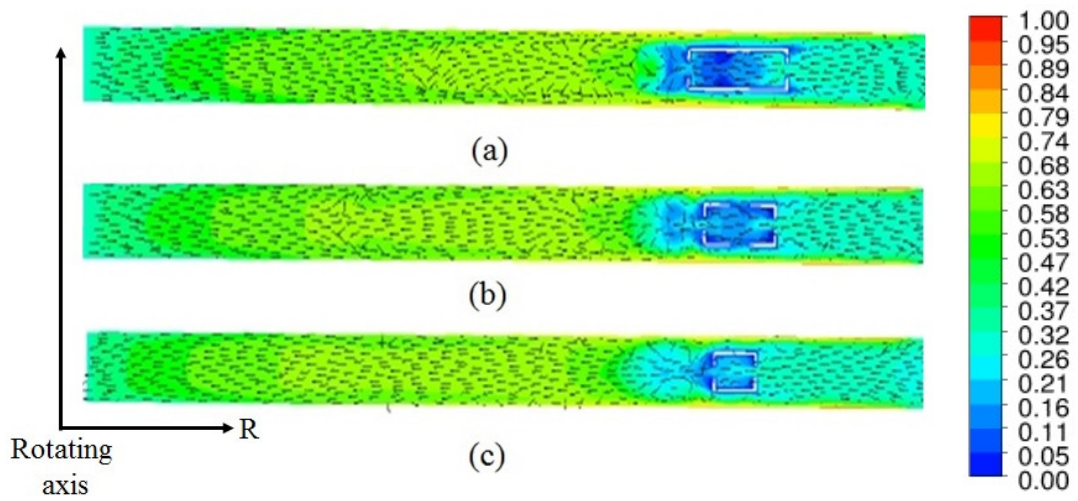


Figure 4.50: Contour plots of mean velocity on three planes across the stiffening flanges; (a) near the arm. (b) middle of the flanges. (c) the end of the flanges in air at 15000 rpm.

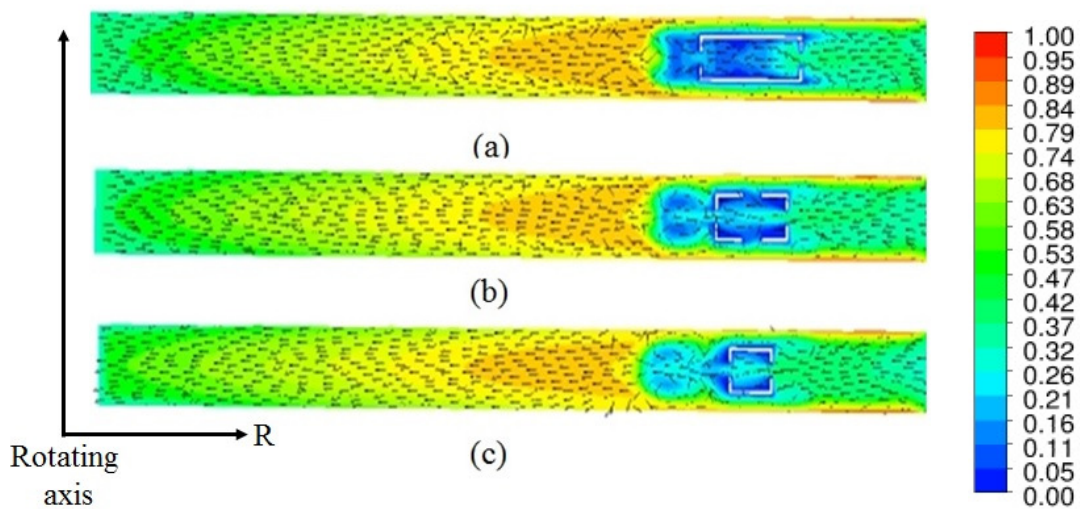


Figure 4.51: Contour plots of mean velocity on three planes across the stiffening flanges; (a) near the arm. (b) middle of the flanges. (c) the end of the flanges in helium at 15000 rpm.

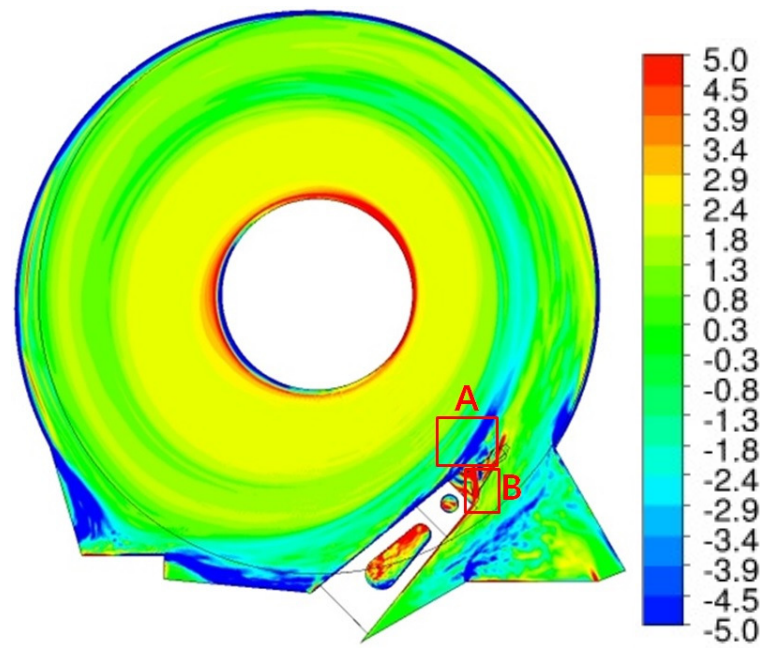
4.2.2 Axial vorticity

In the OC, the wider space between the arm and the co-rotating hub yields quite different vorticity streaks from the IC in the region around the SSU. At the inter-disk mid-plane (Figures 4.52 and 4.53), while the incoming flow is accelerated near the lateral surface of the actuator arm, the flow is highly sheared by the no-slip boundary condition imposed on the surfaces of the arm. At the leading edge of the actuator arm, the region created by the upper and the lower SSU has a low velocity magnitude and is able to generate a continuous shear layer along the circumferential direction (Box A in Figures 4.52 and 4.53). Therefore, the flow tends to maintain an intensified vorticity. In the region downstream of the SSU, the flow redirected from outside of the rotating frame is driven to the clearance between the trailing edge of the arm and the sharp edge in the enclosure wall. The redirected flow is also sheared due to the no-slip condition of the arm and divided into two streams at the trailing edge of the arm by the stiffening flange at the region downstream of the SSU. The first stream is guided into the SSU region and is dissipated near the stiffening flange at the upstream region. The other stream keeps being sheared on the surface of the flange and is extended to the region downstream of the SSU (Box B in Figures 4.52 and 4.53). As observed for the IC, the helium flow generates more vigorous vorticity streaks (Figures 4.52 (b) and 4.53(b)) than those in the air flow (Figures 4.52 (a) and 4.53 (a)) due to its higher kinematic viscosity than that of air.

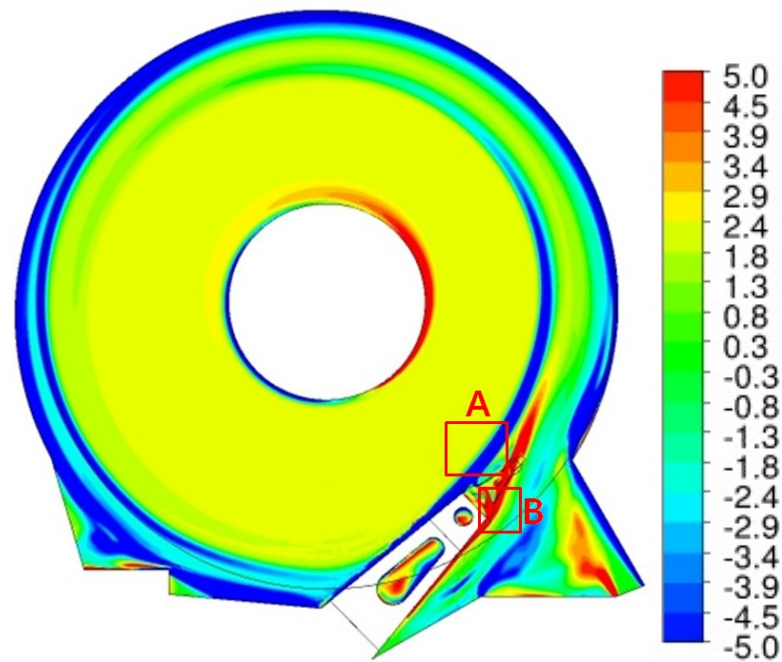
At $z = 0.355$ mm, it is clearly shown that the stiffening flanges work as a main source of vorticity streaks (Figures 4.54 and 4.55). Vorticity streaks induced by the lateral surface of the actuator arm (Box A in Figures 4.54 and 4.55) and the redirected flow from the outside of the rotating frame are observed at the inter-disk mid-plane. Similar to the IC

case, the redirected flow from outside of the disk domain is divided into two streams at the trailing edge of the arm downstream of the SSU in air at 5400 rpm (Box B in Figure 4.54 (a)). The first stream is driven into the SSU region and the second stream is guided along the flange surface while the helium flow induces a smooth flow redirection on the flange surface and propagates to the region downstream at 5400 rpm (Box B in Figure 4.54 (b)). However, at 15,000 rpm, both fluids show diverged vorticity streaks downstream of the SSU (Box B in Figure 4.55 (a) and (b)).

The contour plots at the mid-plane between the arm and the upper disk (Box A in Figures 4.56 and 4.57) also describe features induced at the inter-disk mid-plane by the Taylor-Proudman theorem. The only source of no-slip boundary condition is a small block which mimics the magnetic tip. However, all the vorticity streams observed at the inter-disk mid-plane and the plane across the stiffening flanges are still present with lower magnitude of the original vorticity streaks.

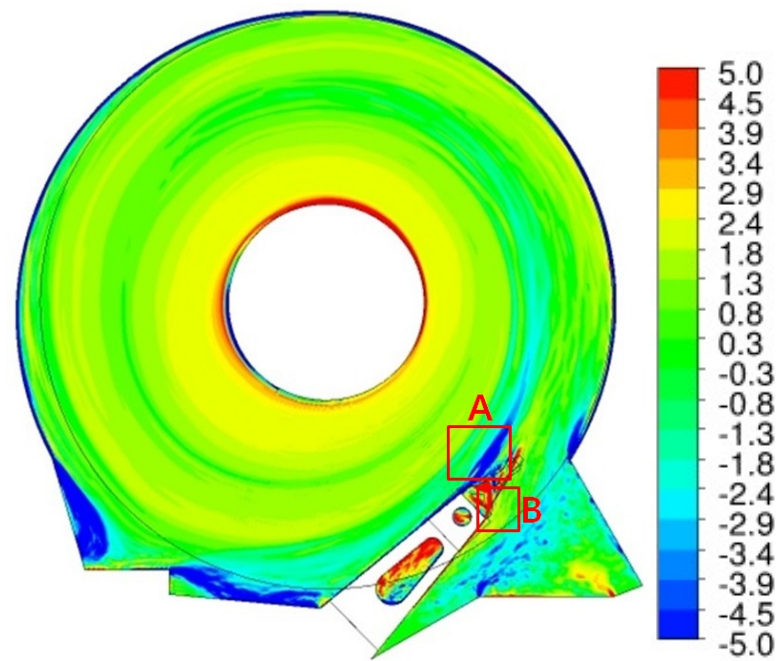


(a)

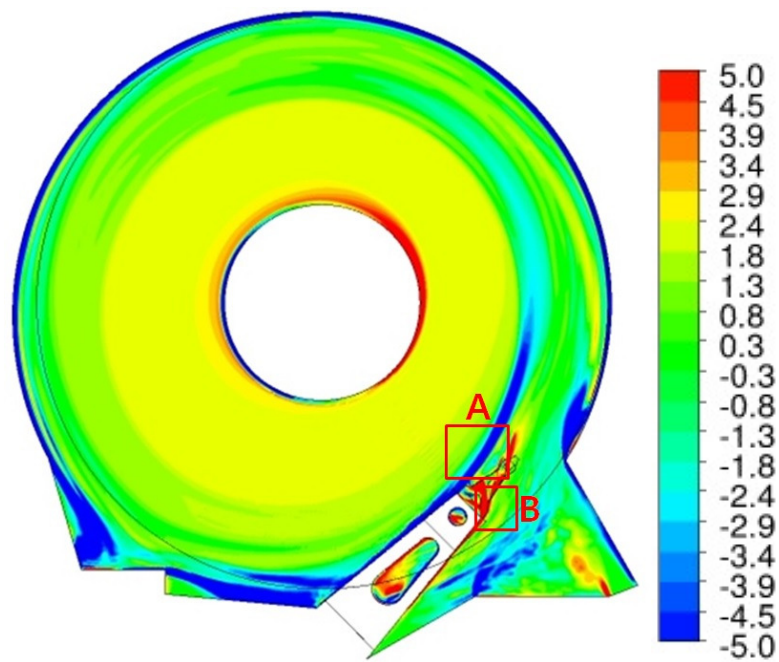


(b)

Figure 4.52: Contour plots of z - axial vorticity of (a) air and (b) helium at the inter-disk mid-plane ($z = 0$ mm) at 5400 rpm.

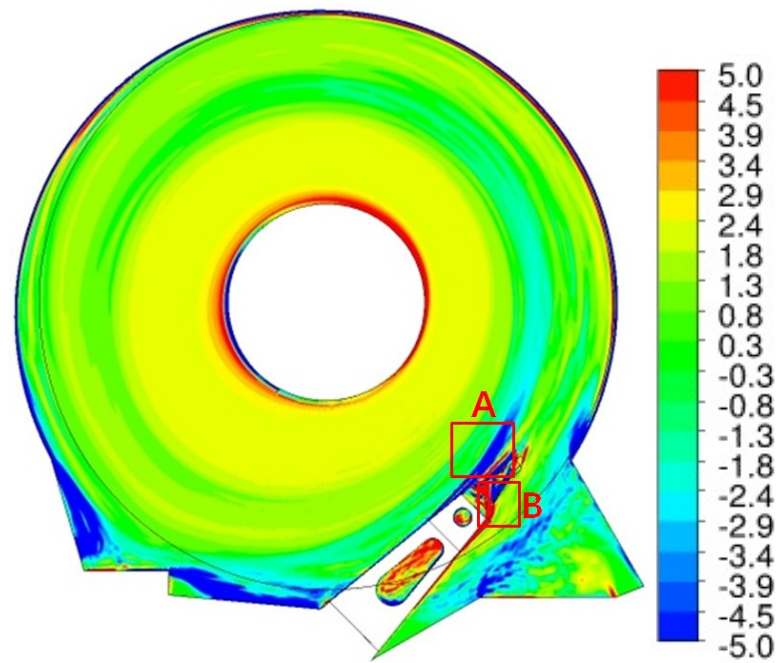


(a)

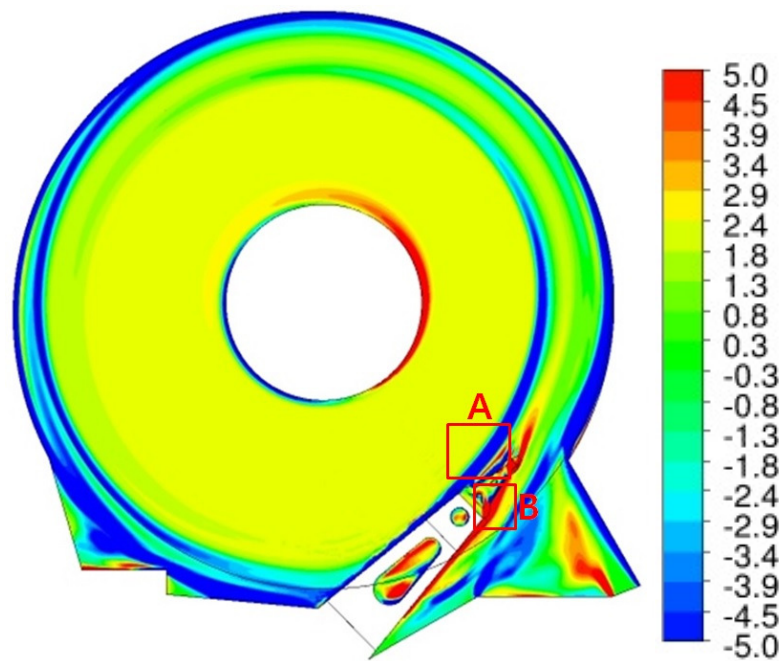


(b)

Figure 4.53: Contour plots of z - axial vorticity of (a) air and (b) helium at the inter-disk mid-plane ($z = 0$ mm) at 15000 rpm.

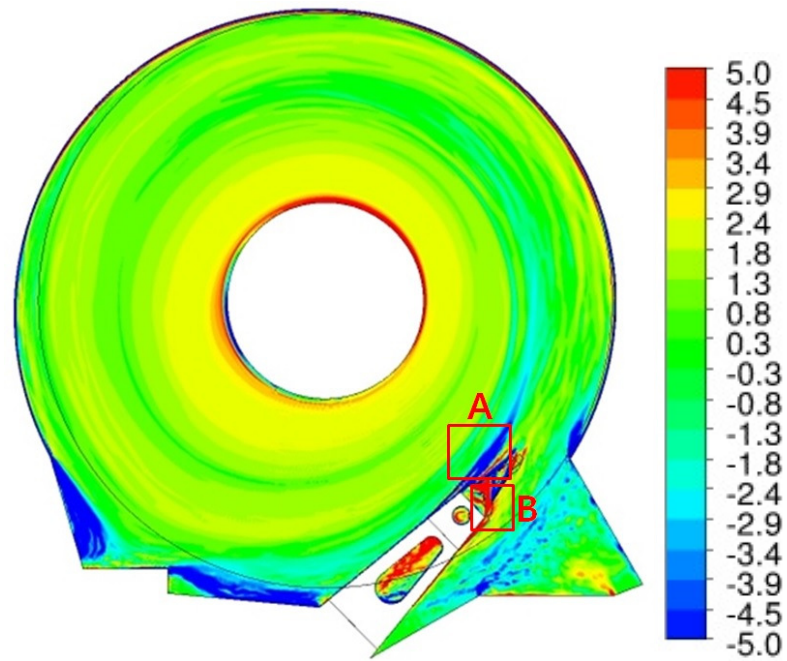


(a)

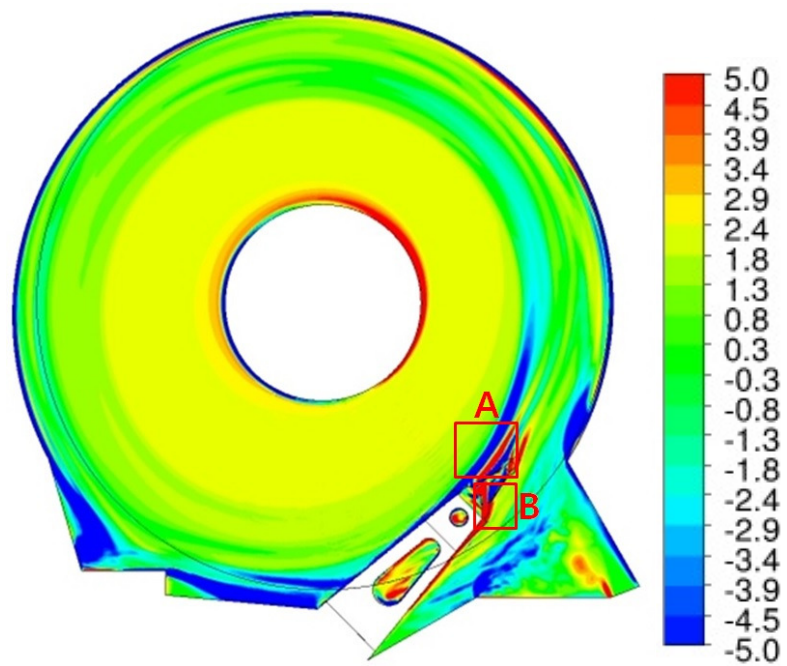


(b)

Figure 4.54: Contour plots of z - axial vorticity of (a) air and (b) helium at the plane across the flanges ($z = 0.355$ mm) at 5400 rpm.

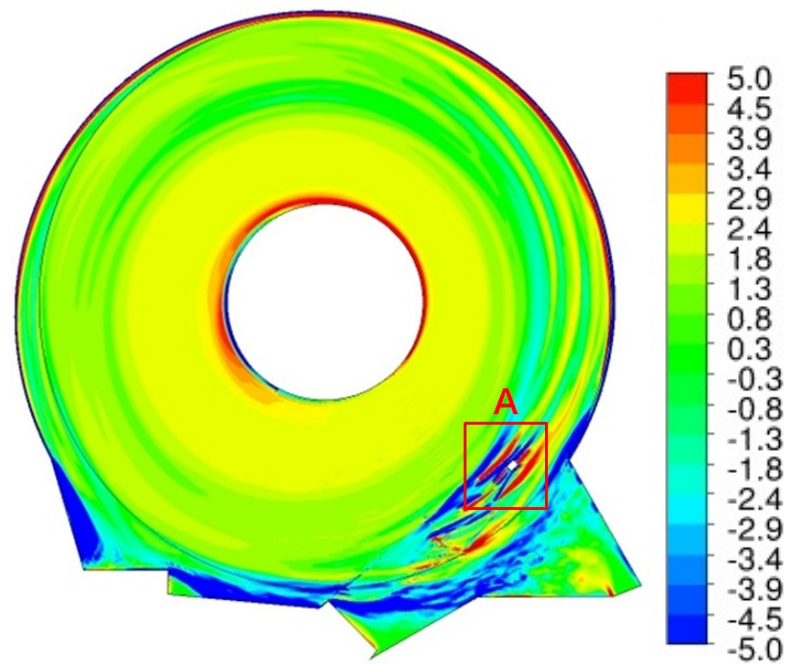


(a)

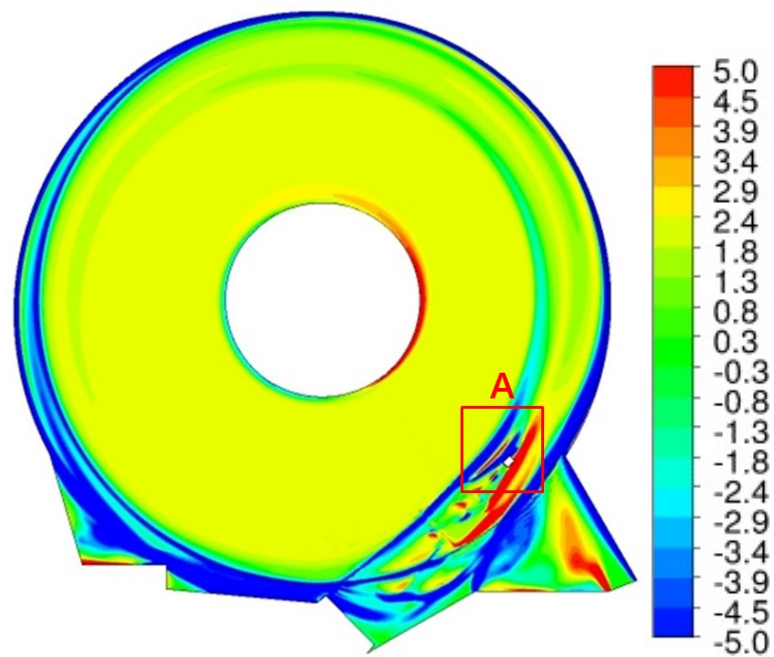


(b)

Figure 4.55: Contour plots of z - axial vorticity of (a) air and (b) helium at the plane across the flanges ($z = 0.355$ mm) at 15000 rpm.

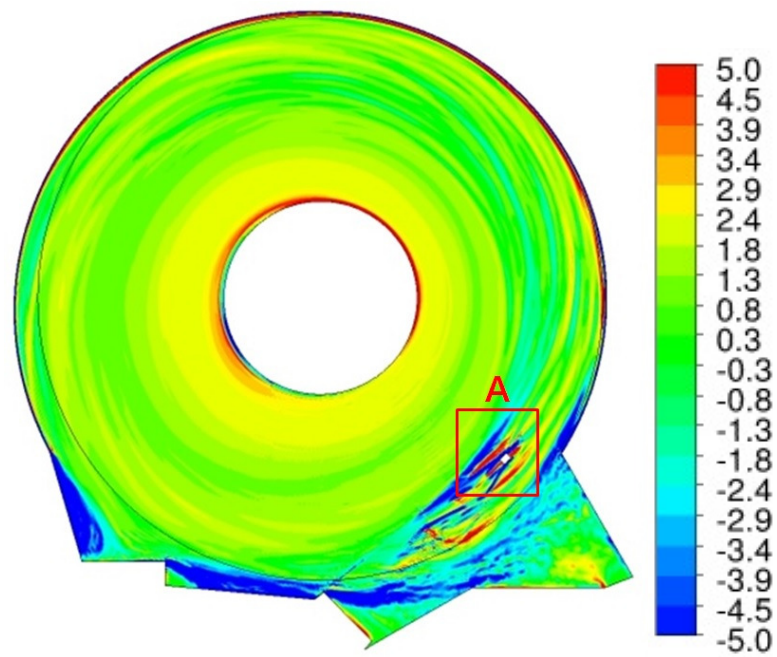


(a)

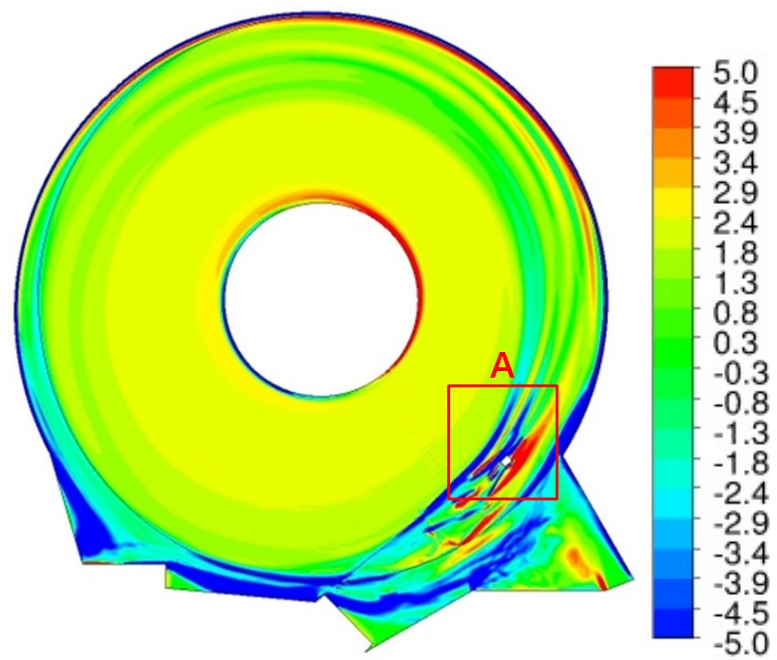


(b)

Figure 4.56: Contour plots of z - axial vorticity of of (a) air and (b) helium at the plane between the arm and the disk ($z = 0.8$ mm) at 5400 rpm.



(a)



(b)

Figure 4.57: Contour plots of z - axial vorticity of (a) air and (b) helium at the plane between the arm and the disk ($z = 0.8$ mm) at 15000 rpm.

On the planes across the stiffening flanges, highly sheared flows are observed between the SSU's and the disk surfaces. The radially outward driven flow is divided into two streams by the stiffening flanges. As explained in section 4.2.1, the first stream is driven radially outward near the disk surfaces. Due to the flow blockage by the stiffening flanges, the flow needs to be accelerated through the small clearance between the flanges and the disks. Corresponding to the increase of the flow velocity, intensified vorticity streaks are induced on the surface where the SSU's face the disk surface. The second stream is redirected toward the inter-disk mid-plane and conjoined with the radially inward flow through the gap between the upper and the lower flanges. Then, the inward flow is dragged near to the disk surface close to the boundary of the region of solid body rotation. By this process, a pair of counter-rotating vortices are completed in the region upstream of the SSU. In contour plots of Figures 4.58, 4.59, 4.60 and 4.61 (a), a pair of counter-rotating vortices exists where the vortices are created. Since the intensity of the radial momentum is related with the size of the vortices, a larger value of the vorticity is expected in the air flow compared with the helium flow due to its higher density. The contour plots at 5400 rpm show that the air flow causes a pair of counter-rotating vorticities where the flow is blocked by the stiffening flanges (Figure 4.58 (a)). However, the radial momentum is quite lower in the helium flow at 5400 rpm so that the magnitude of the vorticities are much smaller than those for the air flow (Figure 4.59 (a)). At 15000 rpm, the helium flow also induces a pair of vorticities by the increased rotation of the disk (Figure 4.60 (a)). Nevertheless, the higher density of air still generates stronger radial momentum so that more intense vortices exist than those of the helium flow (Figure 4.61 (a)).

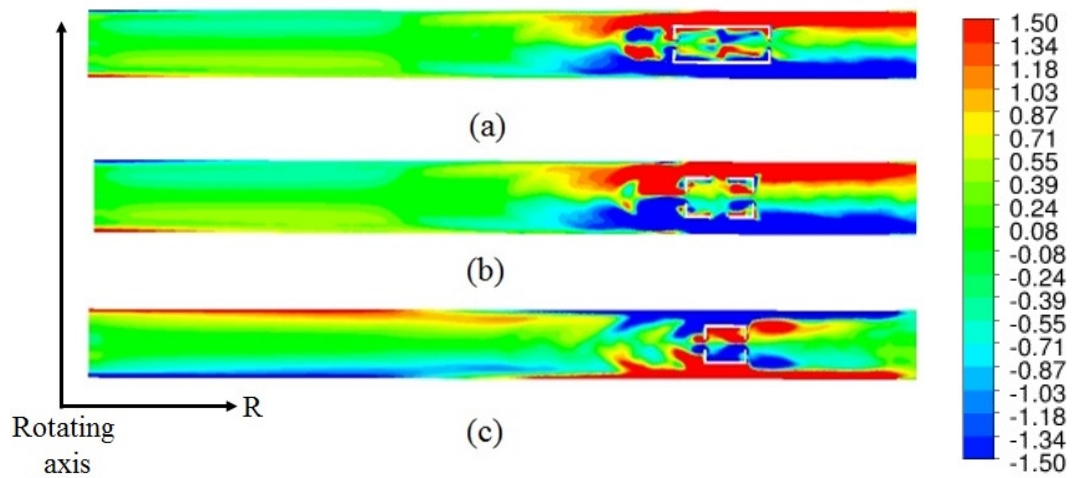


Figure 4.58: Contour plots of x - axial vorticity of on three planes across the stiffening flanges; (a) near the arm. (b) middle of the flanges. (c) the end of the flanges in air at 5400 rpm.

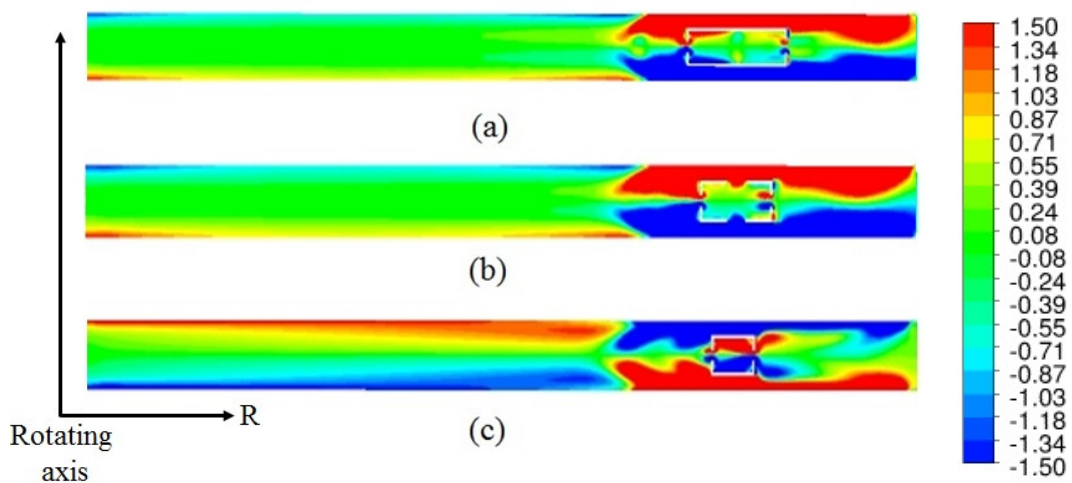


Figure 4.59: Contour plots of x - axial vorticity of on three planes across the stiffening flanges; (a) near the arm. (b) middle of the flanges. (c) the end of the flanges in helium at 5400 rpm.

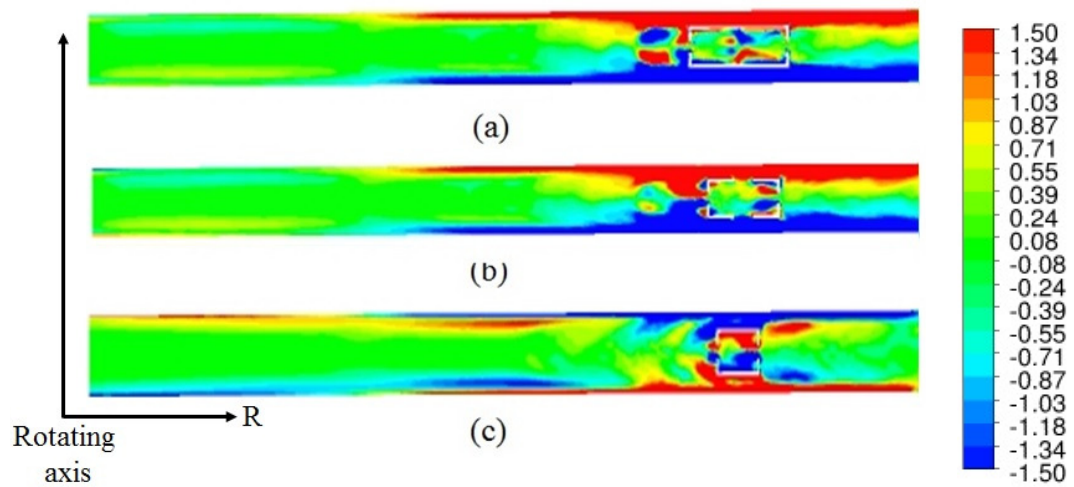


Figure 4.60: Contour plots of x - axial vorticity on three planes across the stiffening flanges; (a) near the arm. (b) middle of the flanges. (c) the end of the flanges in air at 15000 rpm.

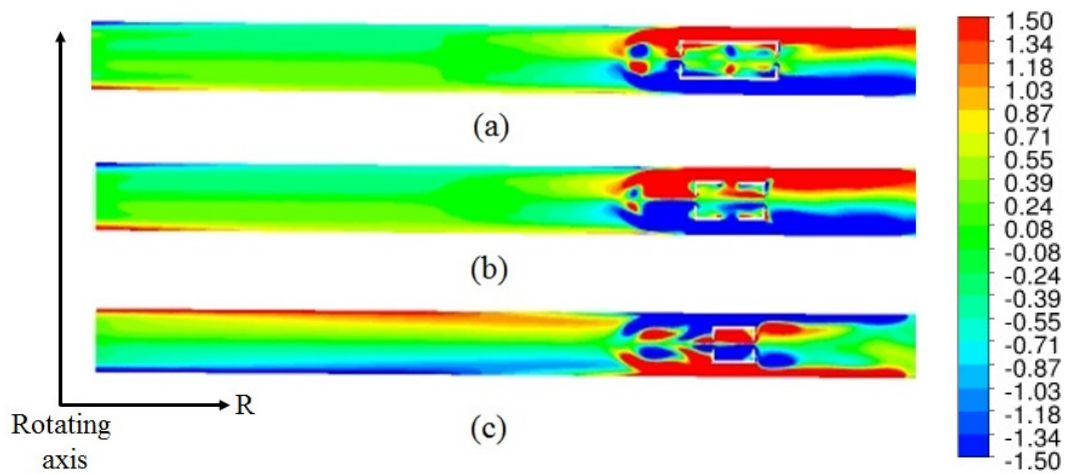


Figure 4.61: Contour plots of x - axial vorticity on three planes across the stiffening flanges; (a) near the arm. (b) middle of the flanges. (c) the end of the flanges in helium at 15000 rpm.

4.2.3 Turbulence Intensity (TI)

Contour plots of non-dimensionalized Turbulence Intensity (TI^*) describe that most of TI is concentrated in the region upstream of the SSU. While the incoming flow upstream of the arm is redirected and sheared on the lateral surface of the arm, the flow is accelerated to a high speed. At the same time, the actuator arm has no-slip boundary condition and the region between the upper and the lower SSU is almost unaffected by the rotation of the disk so that a low velocity region is generated. Therefore, the accelerated incoming flow experiences a drastic momentum imbalance by the lateral surface of the arm and the low velocity region inside the SSU domain. As a result, a Kelvin-Helmholtz instability type turbulent mixing layer develops in the region of the SSU along the stiffening flanges. Moreover, a pair of counter-rotating vortices on the plane perpendicular to the disk surface collide and give rise to velocity oscillations with respect to the inter-disk mid-plane and lead to an increase of the TI intensity (Box A in Figures 4.63 and 4.64). Similar to the IC, the higher kinematic viscosity of helium successfully reduces the unsteady flow upstream of the SSU. In addition, the radial momentum in the helium flow is always smaller than the air flow due to its lower density, and the corresponding counter-rotating vortices are smaller and weaker so that velocity fluctuation is decreased. As a result, lower TI is created upstream of the SSU in helium than in air (Figure 4.63 (a) and (b)) at 5400 rpm. At 15000 rpm, the increased rotating speed of the disk intensifies the TI in both air and helium. Nevertheless, the intensity of TI in the helium flow is still quite lower than that in the air flow (Figure 4.64 (a) and (b)).

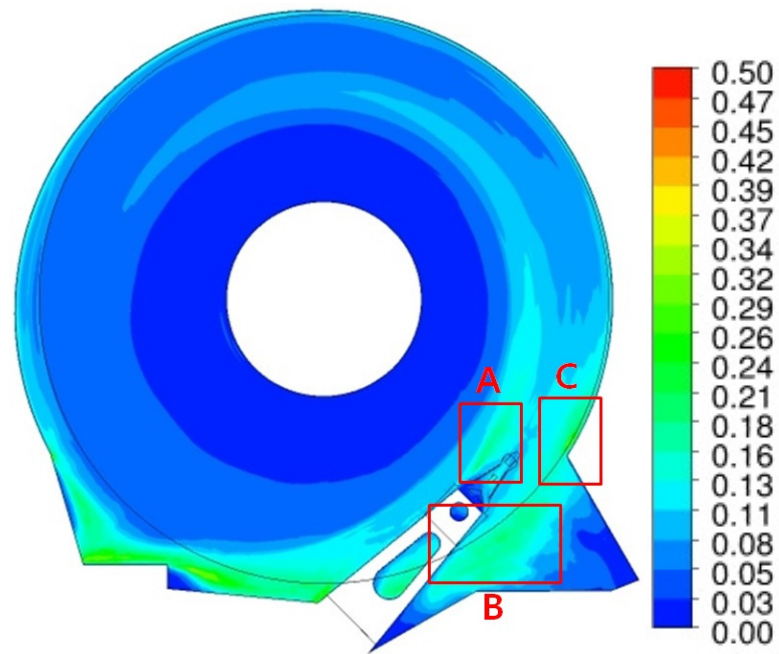
In the region downstream of the arm, another region of turbulent flow is found. The incoming flow over the arm is perturbed by the weight-saving hole. Therefore, vortex

shedding with non-uniform frequency is induced in the region downstream of the arm similar to the IC (Box B in Figures 4.63 and 4.64). Additionally, the redirected flow from outside of the rotating frame is driven to the reduced space between the trailing edge of the arm and the sharp edge in the enclosure wall. To satisfy fluid continuity, the flow field needs to be accelerated. After it passes through the gap, the sharp edge of the enclosure works as a source of another unsteady flow (Box C in Figures 4.63 and 4.64).. As a result, the turbulent flow induced by the sharp edge of the wall becomes more vigorous than that for the IC.

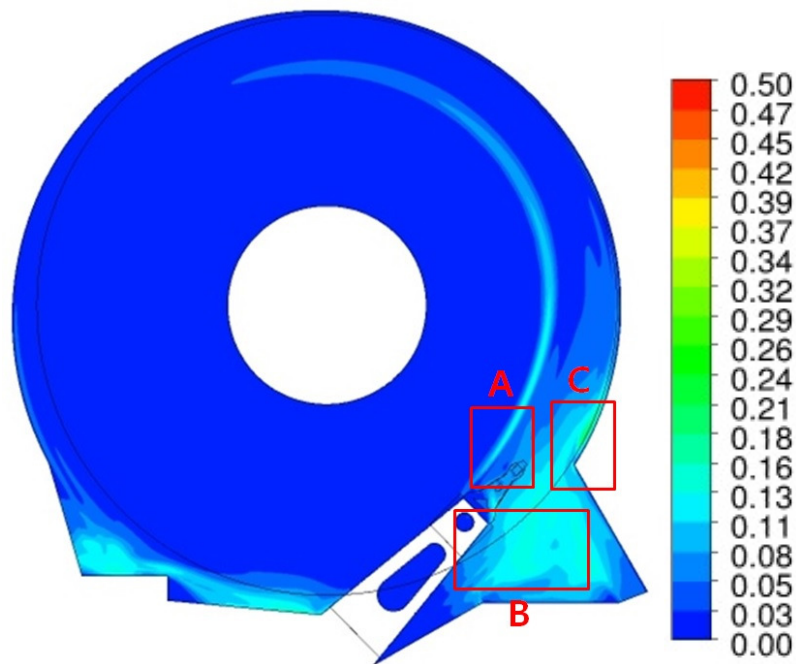
The contour plots in Figures 4.64 and 4.65 show almost similar features to the results at the inter-disk mid-plane. All the flow blockages are located at the same places at the inter-disk mid-plane except for the SSU domain with the flanges. At the inter-disk mid-plane, the stiffening flanges allow a clearance between them. However, the distance between the upper and the lower flange is merely 0.353 mm which is 16.5 % of the disk-to-disk space so that most of the redirected flow from outside of the rotating frame lose momentum and are quickly dissipated inside the SSU region. Therefore, the magnitude of the TI is quite low in this region. At the plane across the stiffening flanges, the flow is directly blocked by the arm and the flanges. As a result, the contour plot of the TI* seem to be quite identical to the inter-disk mid-plane (Box A, B and C in Figures 4.64 and 4.65).

At the mid-plane between the arm and the upper disk (Figures 4.66 and 4.67), results show evidence of Taylor-Proudman theorem. The three main sources of the unsteady flow found at the inter-disk mid-plane; i) turbulent mixing layer upstream of the arm (Box A in Figures 4.66 and 4.67), ii) unsteady vortex shedding downstream of the

weight-saving hole (Box B in Figures 4.66 and 4.67), iii) unsteady flow induced by the sharp edge in the enclosure wall (Box C in Figures 4.66 and 4.67), are also generated at this height. Moreover, the perturbation of the weight-saving hole on the flow field is clearly seen. At 5400 rpm, the air flow (Figure 4.66 (a)) creates a high magnitude of the TI above the weight-saving hole where the helium flow (Figure 4.66 (b)) reduces the unsteady flow. However, both the air and the helium flow cause turbulent flow in the space over the weight saving hole (Figure 4.67 (a) and (b)) due to the relocation of the stagnation point on the lateral surface of the arm.

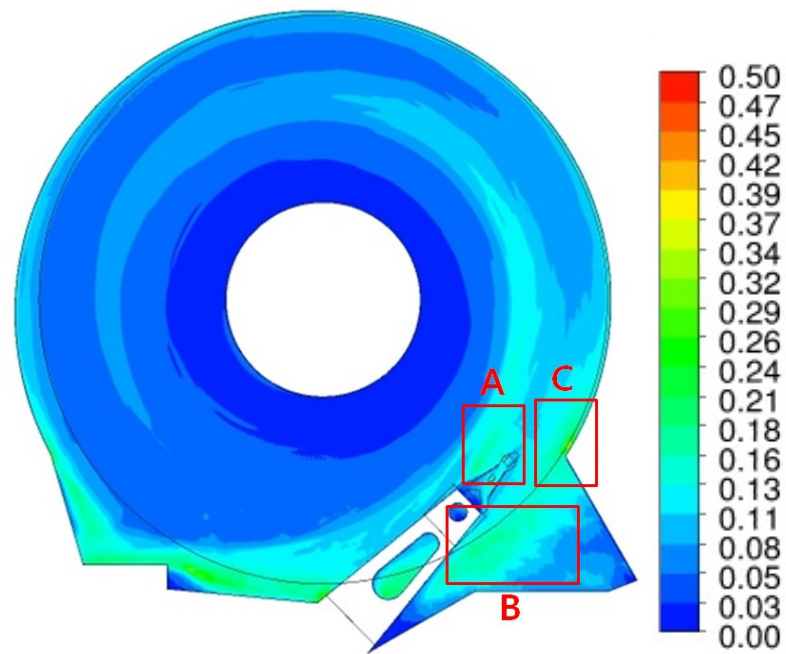


(a)

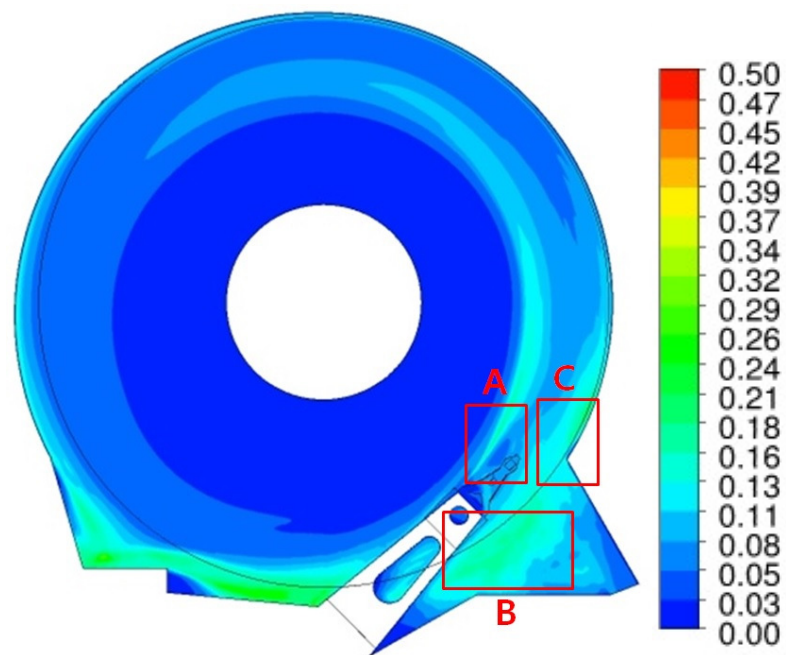


(b)

Figure 4.62: Contour plots of TI^* of (a) air and (b) helium at the inter-disk mid-plane ($z = 0$ mm) at 5400 rpm.

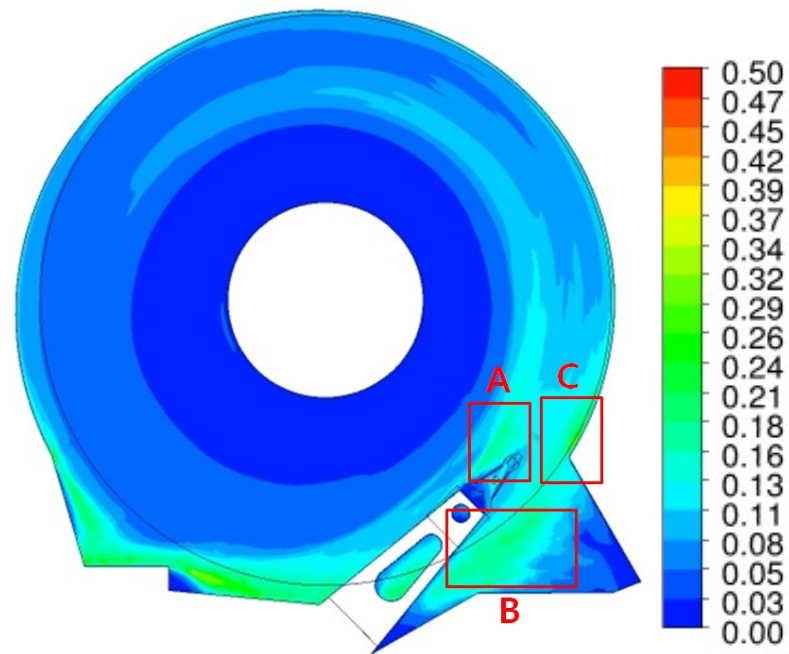


(a)

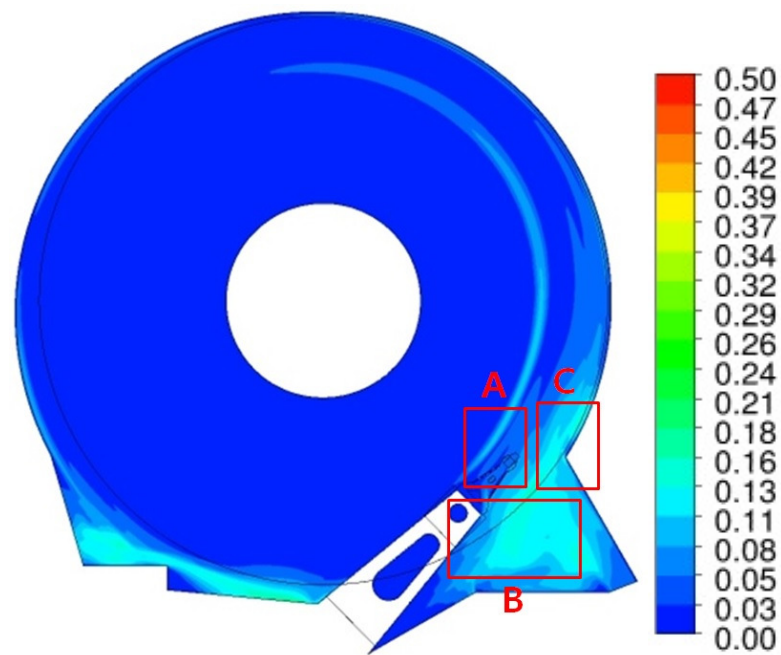


(b)

Figure 4.63: Contour plots of TI^* of (a) air and (b) helium at the inter-disk mid-plane ($z = 0$ mm) at 15000 rpm.

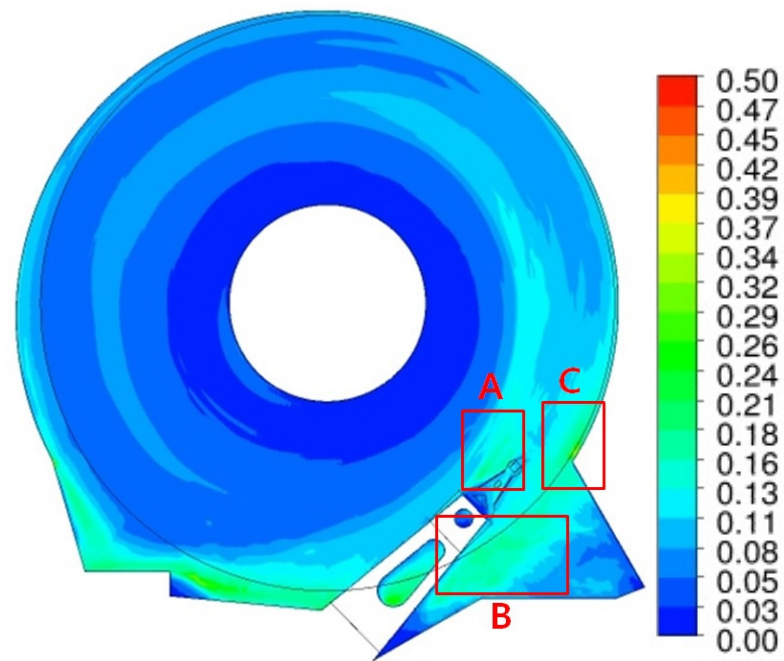


(a)

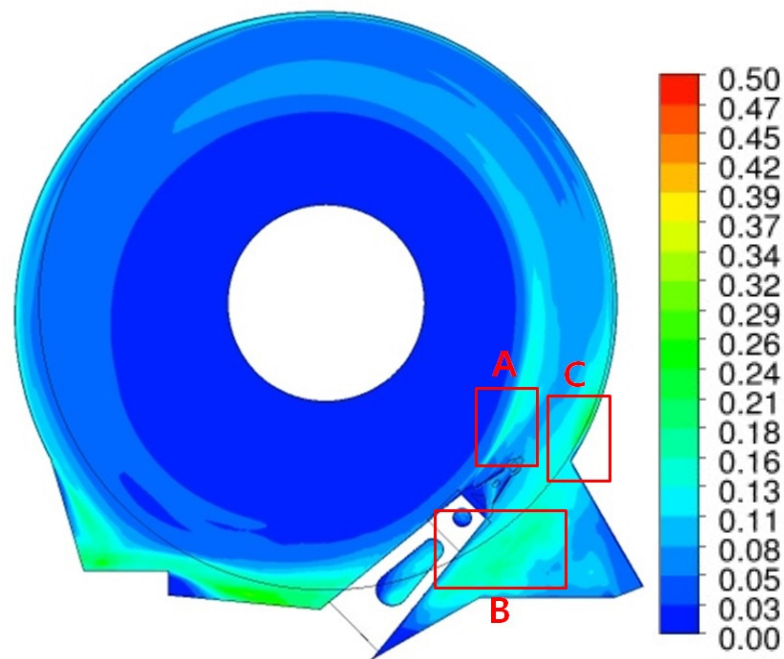


(b)

Figure 4.64: Contour plots of TI^* of (a) air and (b) helium at the plane across the flanges ($z = 0.355$ mm) at 5400 rpm.

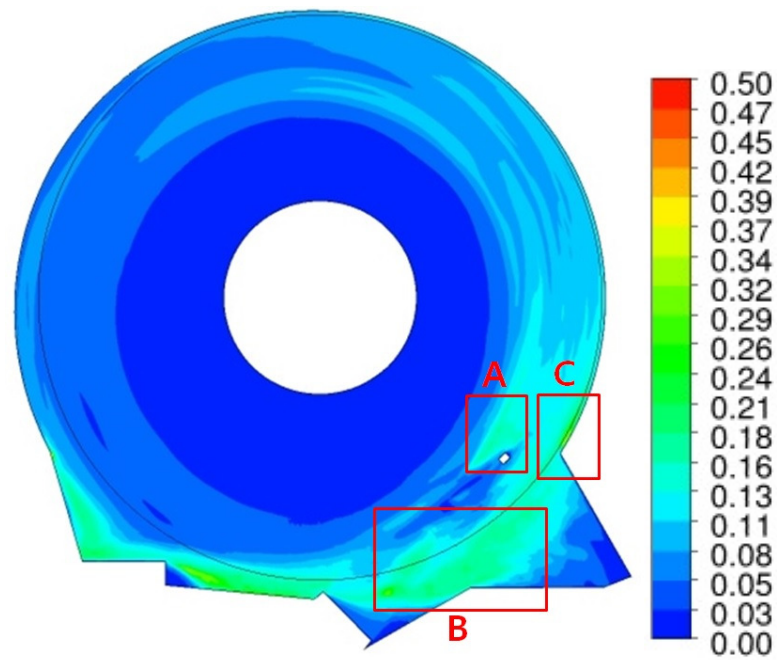


(a)

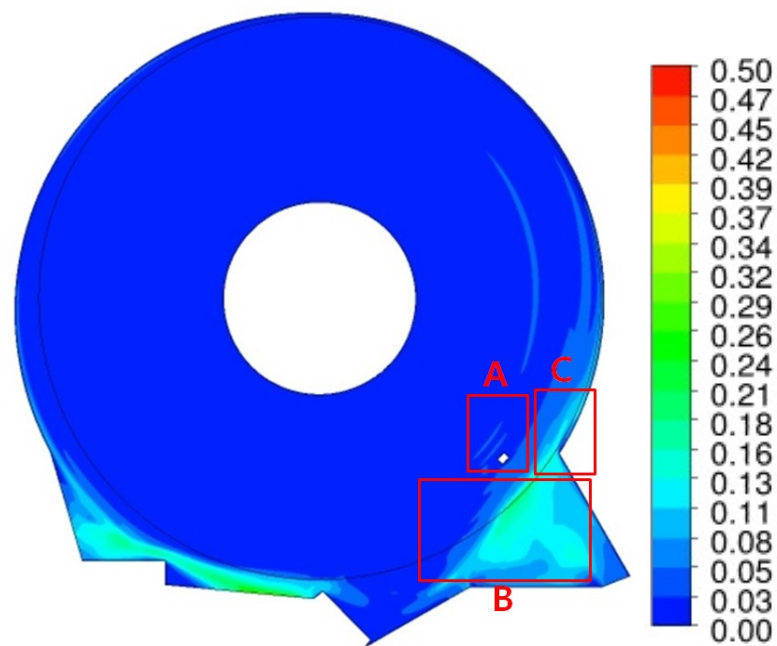


(b)

Figure 4.65: Contour plots of TI^* of (a) air and (b) helium at the plane across the flanges ($z = 0.355$ mm) at 15000 rpm.

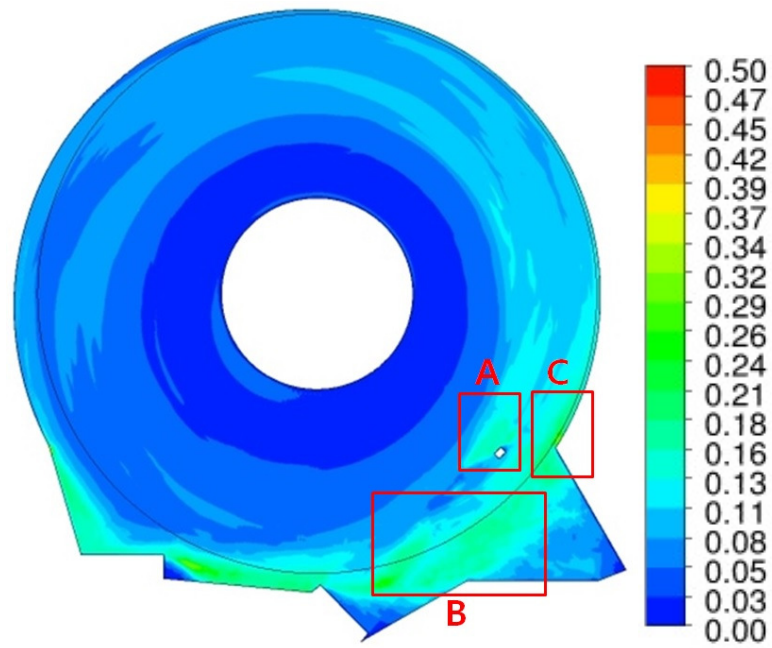


(a)

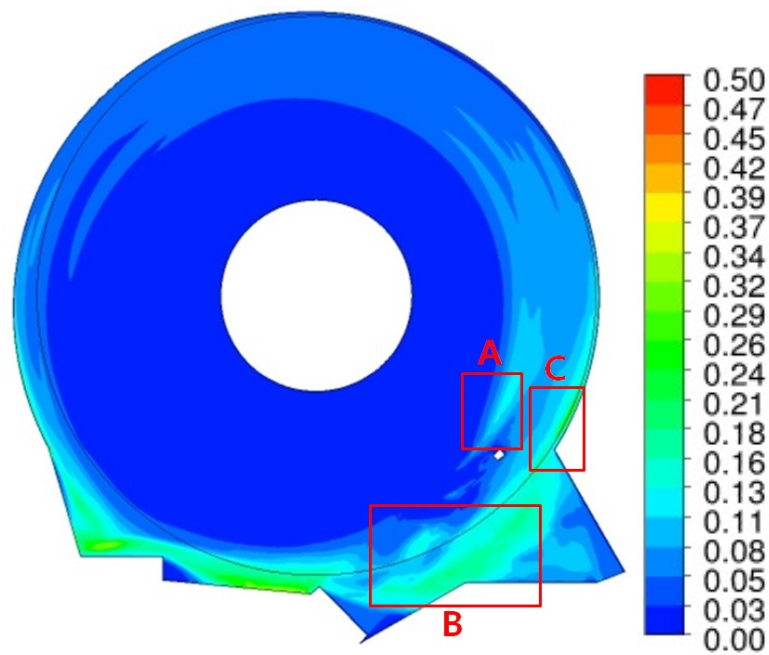


(b)

Figure 4.66: Contour plots of TI^* of (a) air and (b) helium at the plane between the arm and the disk ($z = 0.8$ mm) at 5400 rpm.



(a)



(b)

Figure 4.67: Contour plots of TI^* of (a) air and (b) helium at the plane between the arm and the disk ($z = 0.8$ mm) at 15000 rpm.

4.2.4 Displacement and Frequency Analysis of Slider Suspension Unit

For the OC, the time-dependent displacement is again smaller in helium than in air as expected. The helium flow generates a smooth and sinusoidal displacement whereas the air flow creates a displacement without any distinctive patterns at either rotating speeds of the disk. In particular, the helium flow induces much reduced magnitude of the displacements along all axes at 5400 rpm (Figure 4.68, 4.69 and 4.70). As noted, the displacement in the helium flow is approximately 51 % of that for the air flow in the z – axis for the IC. However, for the OC, the maximum displacement in the helium flow is merely 7% of that for the air flow at 5400 rpm. For the IC, the unsteady flow arises between the upper and the lower SSU as the incoming flow upstream of the arm is sheared by the leading edge of the actuator arm. Then, this unsteady flow is perturbed once more by the stiffening flanges. Therefore, the turbulent flow is observed right downstream of the flanges and the SSU's are vibrated directly by the flow oscillations. However, the source of TI for the OC is the turbulent mixing layer due to the momentum imbalance between the accelerated flow on the lateral surface of the actuator arm and the low velocity region between the upper and the lower SSU. This unsteady flow propagates along the circumferential direction so that the magnetic tip has a greater distance to the turbulent flow and the flow field is allowed to undergo more flow stabilization before the unsteady flow reaches the SSU. As a result, a low displacement is observed in helium for the OC than that for the IC.

At 15000 rpm, the time-dependent displacements in both air and helium show similarity with the displacements for the IC (Figures 4.71, 4.72 and 4.73). The maximum displacement in helium is only approximately 10 % of the maximum value in air.

Consequently, the expectation that the kinematic viscosity of helium will be more effective at lowering the vibrations at higher rotating speeds is supported again from the results for the OC at 15000 rpm.

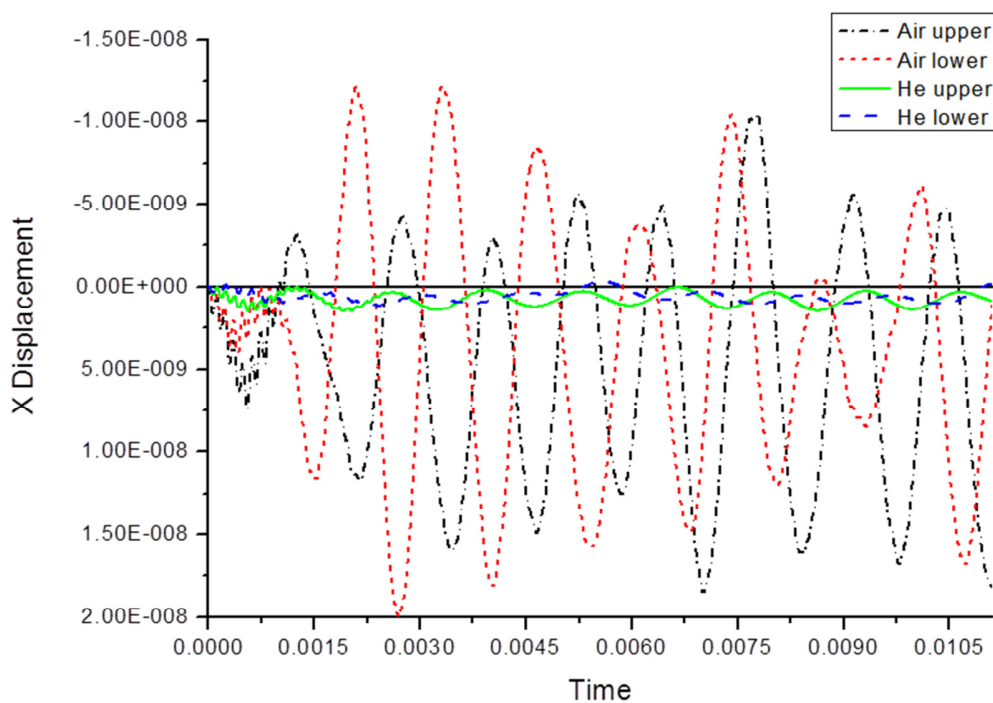


Figure 4.68: Displacement in x – axis on the center of the magnetic tips at 5400 rpm.

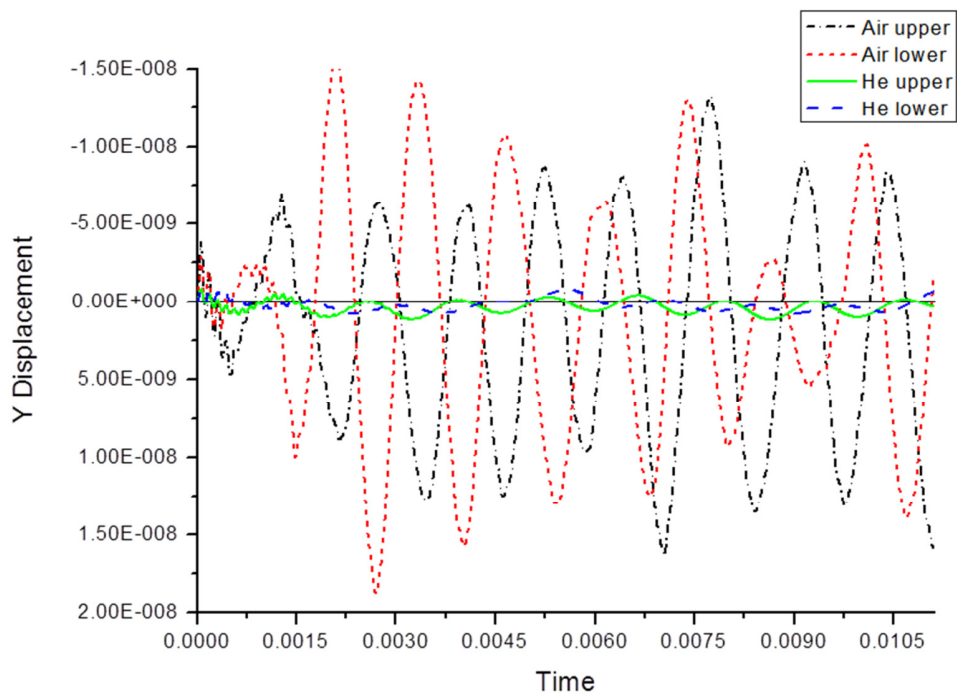


Figure 4.69: Displacement in y – axis on the center of the magnetic tips at 5400 rpm.

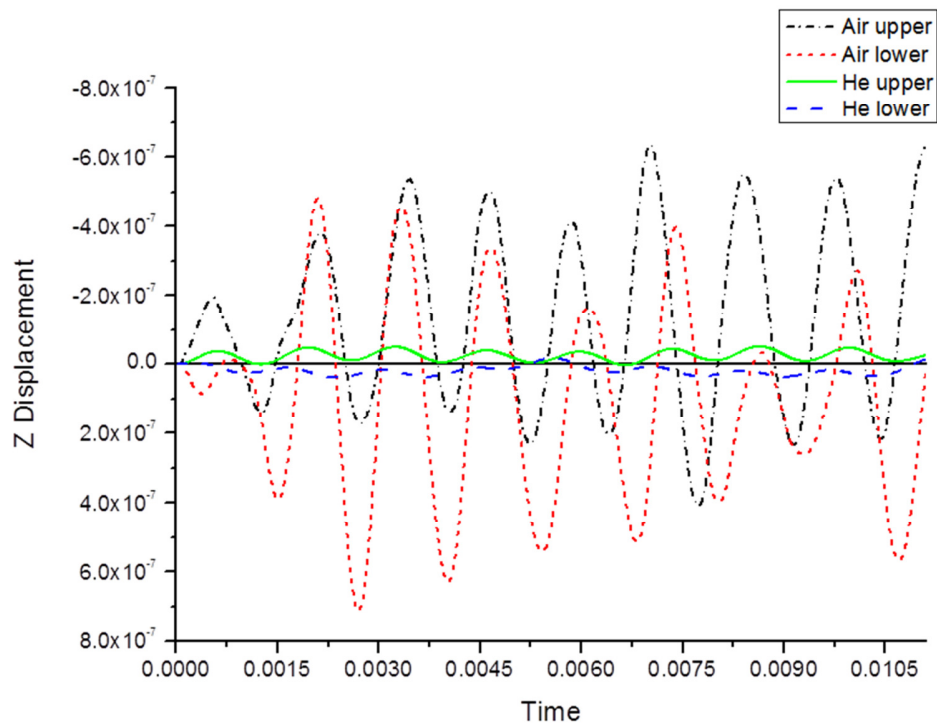


Figure 4.70: Displacement in z – axis on the center of the magnetic tips at 5400 rpm.

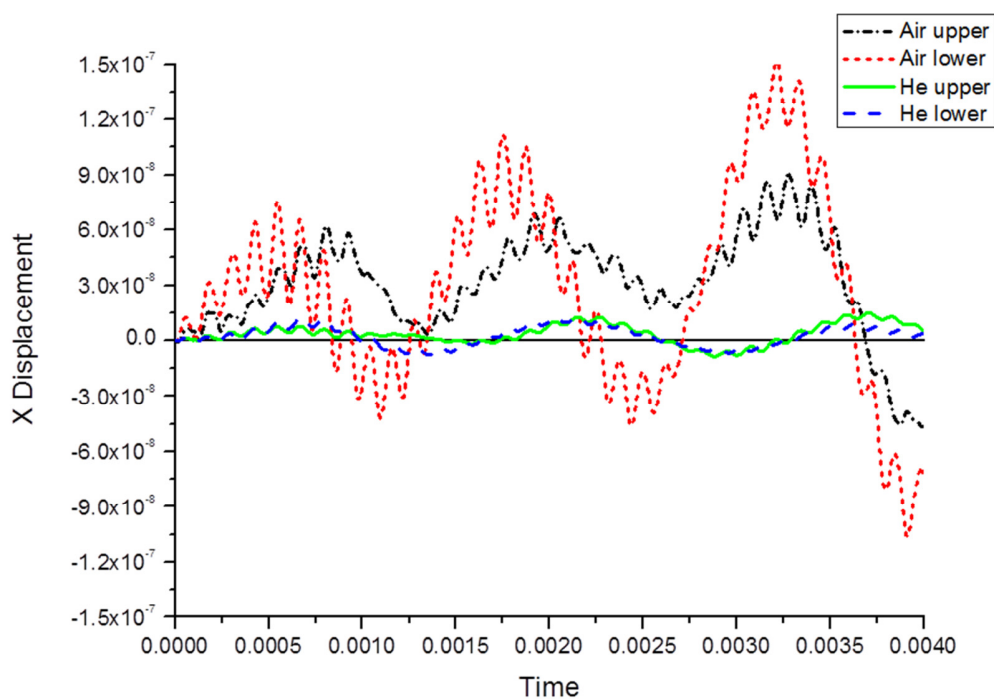


Figure 4.71: Displacement in x – axis on the center of the magnetic tips at 15000 rpm

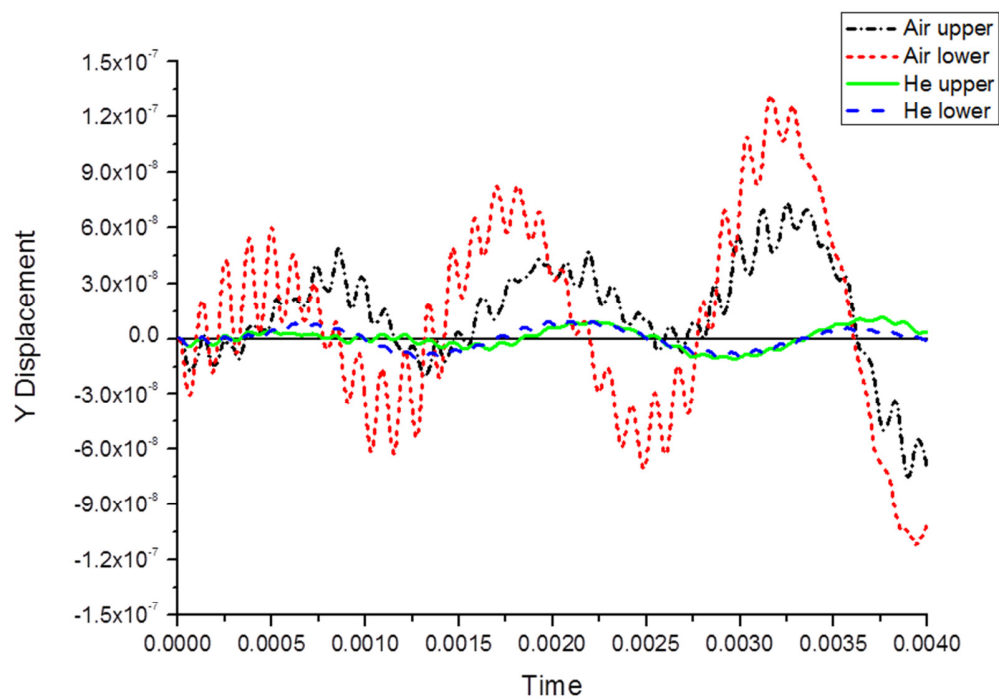


Figure 4.72: Displacement in y – axis on the center of the magnetic tips at 15000 rpm

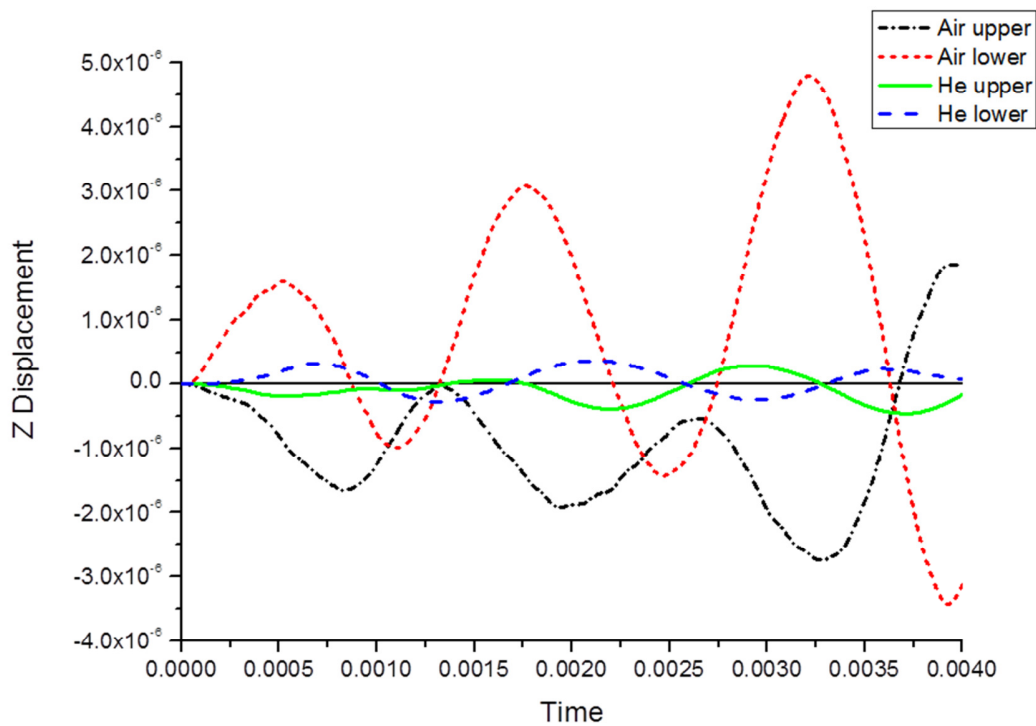


Figure 4.73: Displacement in z – axis on the center of the magnetic tips at 15000 rpm.

Power Spectral Density (PSD) is computed from the time-dependent displacement history over a frequency range. Two different motions are considered, similar to the IC; i) in-plane motion and ii) axial motion. In Figures 4.74 and 4.75, the air flow exhibits a higher PSD than the helium flow. In particular, distinctive peaks are found at 751.2 Hz at the upper and the lower SSU in the air flow which is quite close to the first bending mode at 739.93 Hz. One more peak is generated around 1500 Hz in the in-plane motion for the air flow. This is triggered by the high frequency motion of the SSU due to a sudden transition from a stationary state to a fully coupled one, it is estimated not to be present after several cycles of the disk. Similar to the IC, the magnitude of PSD shows the higher value for the axial motion than the in-plane. This vibration is estimated to be induced by

the turbulent mixing layer upstream of the SSU. PSD of the velocity field is measured at the point where the most intense TI is observed in air and helium (Figure 4.76). The graph shows that the PSD for the air flow has several peaks. Among them, a peak at 823.8 Hz is estimated to contribute to the vibration close to the first bending mode, and the PSD of the helium flow is comparatively smooth without a dominant frequency

PSD of the air flow at 15000 rpm induces a peak at 770 Hz in both the in-plane and the axial motions whereas the PSD of helium is almost negligible compared to the results of air (Figures 4.77 and 4.78). Corresponding PSD of the velocity fluctuation upstream of the SSU indicates that multiple peaks exist across the frequency range due to an increased level of turbulence. One of those peaks is found at 760.6 Hz which is also quite close to the first bending mode of the SSU (Figure 4.79). In addition, the helium flow also shows a dominant peak for 15000 rpm. A sudden increase of the PSD is observed at 507 Hz. However, this frequency is relatively away from the natural frequencies so that the flow fluctuation fails to create a noticeable vibration on the SSU motion.

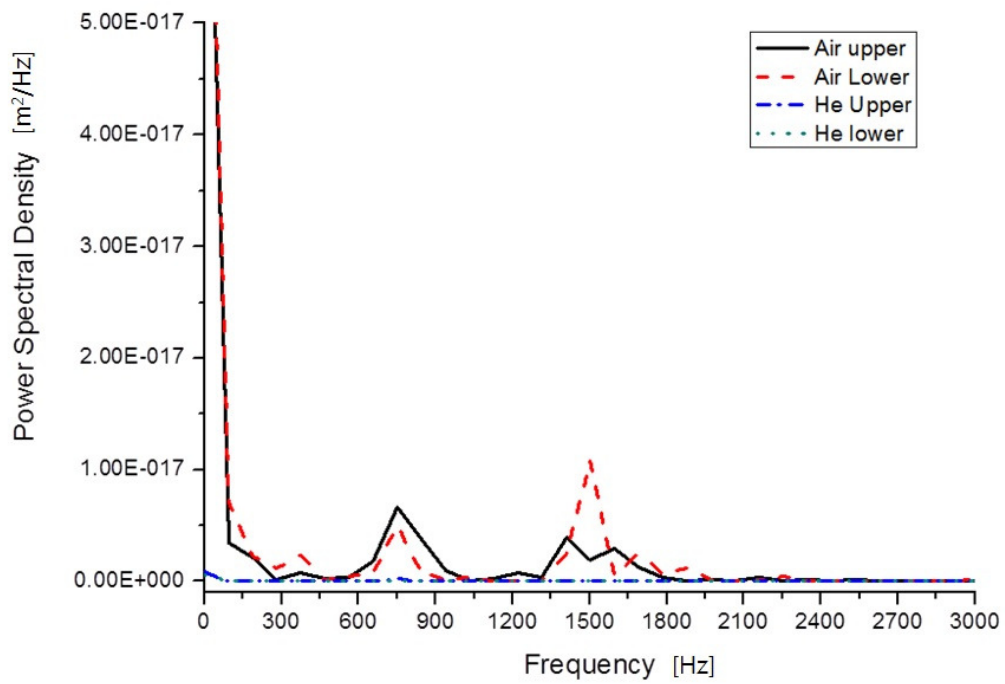


Figure 4.74: Power Spectral Density of the in-plane displacement at 5400 rpm.

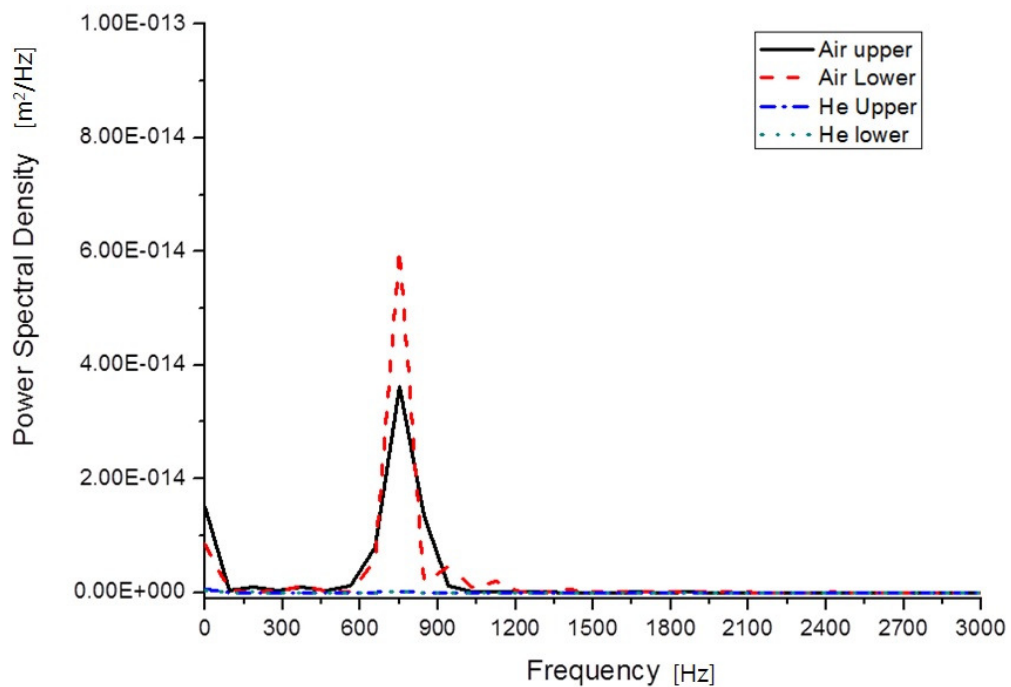


Figure 4.75: Power Spectral Density of the axial displacement at 5400 rpm.

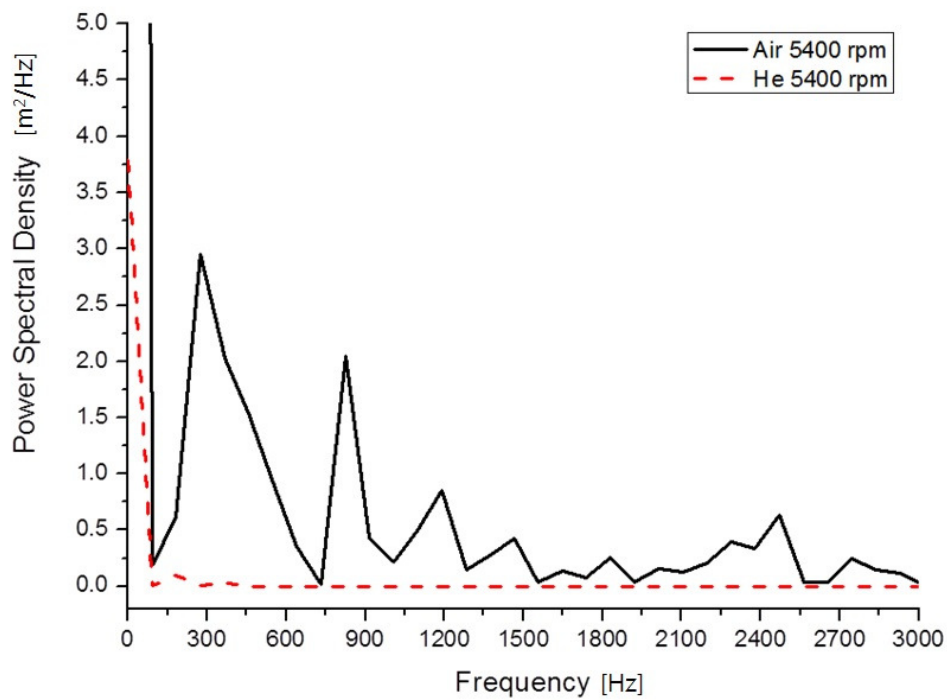


Figure 4.76: Power Spectral Density of the velocity fluctuation downstream of the SSU at 5400 rpm.

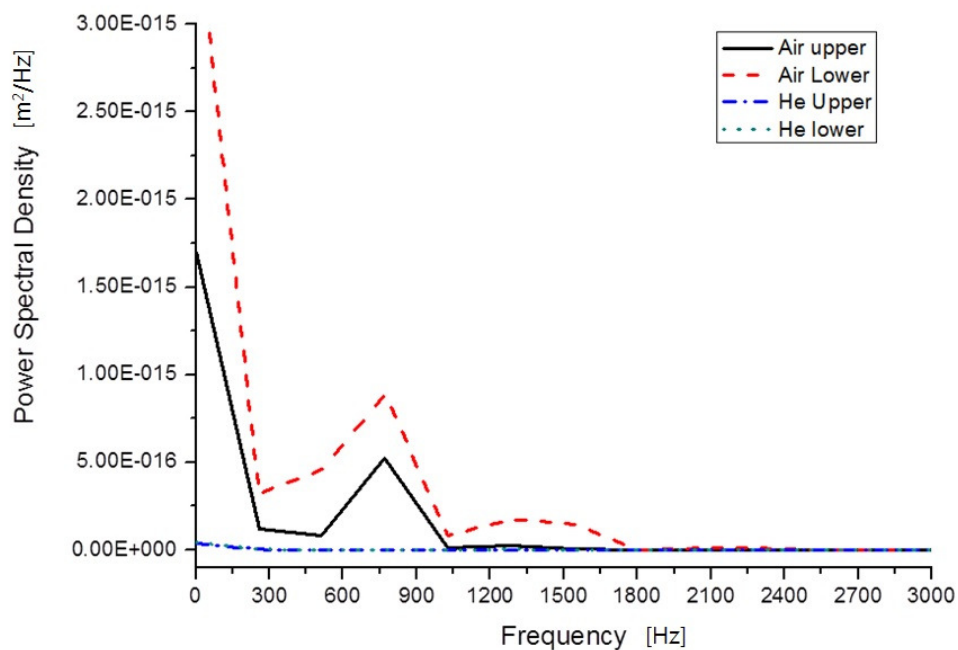


Figure 4.77: Power Spectral Density of the in-plane displacement at 15000 rpm.

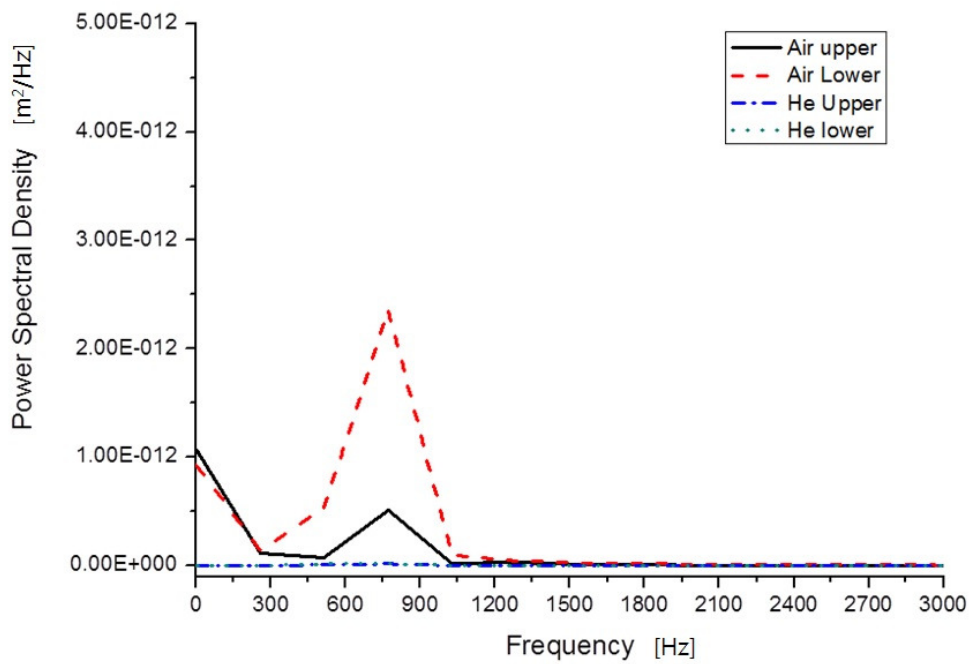


Figure 4.78: Power Spectral Density of the axial displacement at 15000 rpm.

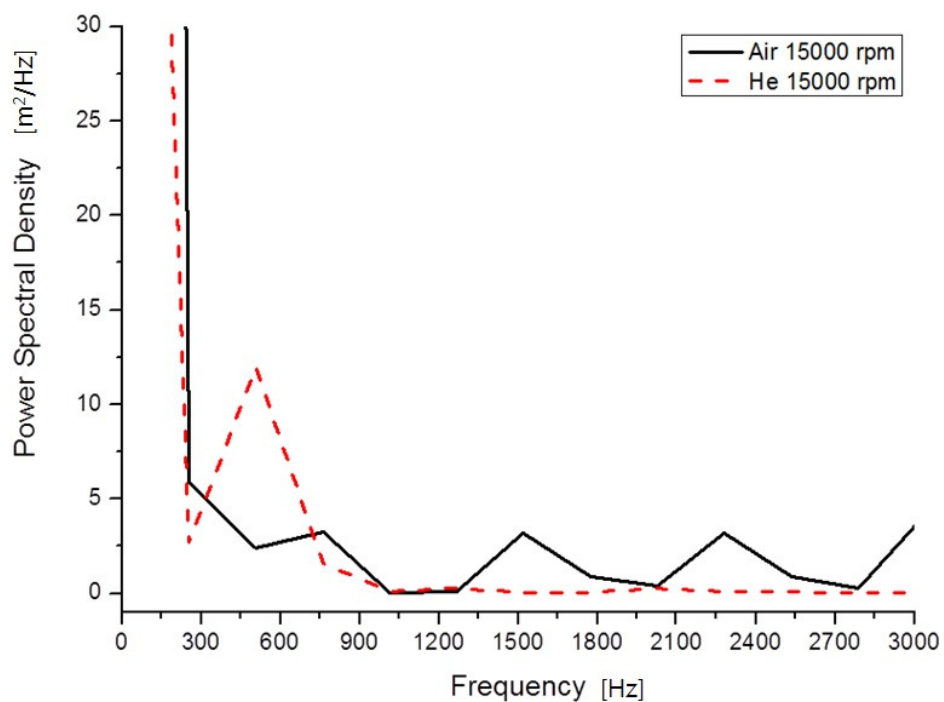


Figure 4.79: Power Spectral Density of the velocity fluctuation downstream of the SSU at 15000 rpm.

Chapter 5

Conclusions and future work

1. Conclusions

1.1 Findings for the fluid domain

Based on the results of the numerical analyses, the flow fields of air and helium can be characterized as follows:

- The flow field is dominated by motion in the circumferential direction except for the region around the actuator arm and the SSU in both air and helium.
- The components outside the rotating frame contribute to the redirection of the incoming flow upstream of the arm to the disk domain.
- The incoming flow upstream of the arm induces a stagnation point on the lateral surface of the arm.
- The flow at radii smaller than the stagnation point is redirected to the space between the co-rotating hub and the actuator arm and accelerated in the azimuthal direction.

- The flow at radii larger than the stagnation point impinges on the arm and travels across the weight-saving hole and generates vortex shedding downstream of the actuator arm.
- For the Inner Configuration (IC), there is a three-dimensional inversed flow located in the region upstream of the SSU near the co-rotating hub. This inversed flow region occupies an amount of the axial space comparable to the blockage by the arm and the SSU.
- Since the stagnation point in the helium flow is located radially further out than that for the air flow, more fluid is redirected toward the SSU. Therefore, the helium flow needs to be accelerated more in the clearance between the arm and the hub and the size of the inversed flow has to become larger than the air flow.
- The flow acceleration induces a highly sheared layer where the Turbulence Intensity (TI) becomes high between the upper and the lower SSU's. The stiffening flanges perturb the sheared flow once more so that a higher intensity of the TI is created around the SSU.
- Helium causes increased level of TI downstream of the arm at 15000 rpm. The stagnation point is moved toward the SSU so that the portion of the incoming flow over the arm becomes larger and the corresponding intensity of the vortex shedding grows.
- In the region downstream of the arm, a large amount of the flow is redirected from outside of the rotating frame into the disk domain. This redirected flow experiences a sudden acceleration near the edge of the disk which leads to the generation of more turbulent flow.
- For the Outer Configuration (OC), the space between the arm and the hub is wider than that for the IC. As a result, the three-dimensional inverse flow is no longer observed.
- The incoming flow is highly accelerated on the lateral surface of the arm.
- This accelerated flow forms the turbulent mixing layer in the region upstream of the SSU due to the momentum imbalance with the low velocity region between the upper and the lower SSU's.

-
- A pair of counter-rotating vortices is induced on the plane perpendicular to the disk surface by the flow redirection into the axial direction from the presence of the SSU and the stiffening flanges. These vortices collide with each other and contribute to the increase of the TI magnitude upstream of the SSU.
 - In the region downstream of the arm, the fluid is entrained from outside of the rotating frame similar to the IC. Because of the decreased clearance between the arm and the enclosure wall due to the location of the SSU, the flow needs to be accelerated through this gap.
 - Helium successfully stabilizes the unsteady flow downstream of the arm and the SSU by its higher kinematic viscosity so that the TI magnitude in helium is always lower than that of air.
 - In both gases, evidence of Taylor-Proudman theorem is clearly present. The flow pattern at the inter-disk mid-plane tends to be maintained along the rotating axis.

1.2 Findings for the solid domain

The time-dependent displacements and the Power Spectral Density (PSD) across the frequency range during one cycle of the disk rotation can be summarized as follow

- At both 5400 and 15000 rpm, the displacements of the helium flow along all axes are smaller than the air flow.
- Helium flow induces sinusoidal and symmetric displacements in all directions for the upper and the lower SSU; air flow does not.
- For the IC, the maximum displacement value for helium is approximately 51 % of the maximum value in air.
- For the OC, the maximum displacement value for helium is approximately 10 % of the maximum value in air.
- The higher kinematic viscosity of helium stabilizes the flow field. At 15000 rpm, the ratio of the displacements in helium to that in air is lower than that at 5400 rpm.

- The natural frequencies of the SSU show that the bending and the torsion modes are dominant up to the sixth mode.
- The corresponding PSD's are significantly lower in helium than those in the air flow.
- Among the displacements in all axes, the axial motion exhibits the highest value in all conditions.
- Flow oscillations are found around the first bending mode which is at 793.93 Hz. Due to this proximity, the SSU shows the higher PSD for the axial vibration than the in-plane vibration.

2. Future work

The present research investigated a method for the reduction of disturbances by flow fluctuations around the SSU. The results revealed that the flow oscillation frequency is quite close to the first bending frequency of the SSU and the magnitude of the SSU displacements becomes larger at the higher rotating speeds. Helium successfully decreases the windage-disturbance so that improved positioning accuracy of the SSU can be achieved without any geometric modifications in the middle of the flow field. Nevertheless, further studies are necessary to make helium the working medium inside the commercial disk drive. Those unsolved problems are;

- What is the best method to seal helium inside the disk drive?
- How do flow stabilizers (i.e. flow diverter, flow spoiler, air damper, etc.) change the flow field for the helium flow?
- Can the higher thermal conductivity contribute to more effective cooling for the disk drive?

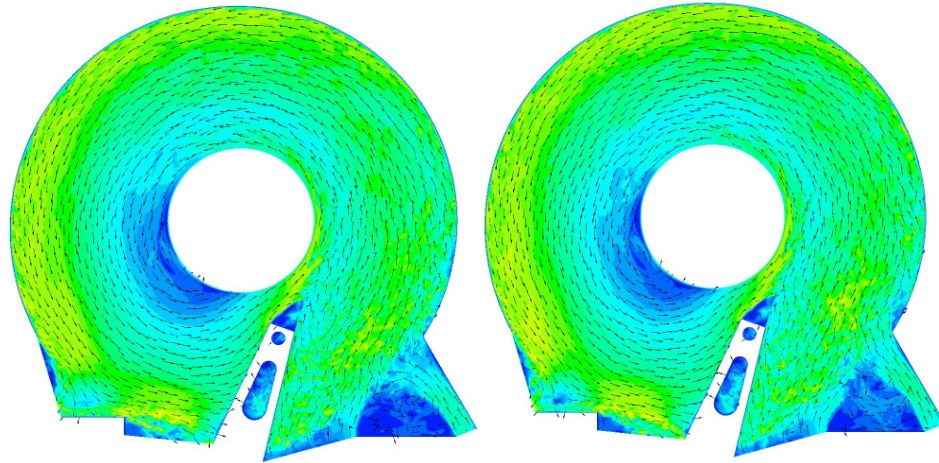
- What improved results can be expected by performing calculations for a longer duration?
- What effect will inclusion of the actuator arm in the coupled FSI have?
- How does the Ekman pumping change with the presence of the blockage in the middle of the flow field?
- What other dynamic characteristics are present during the stroke of the actuator arm and the SSU over the disk surface?
- How will the frequency of the flow fluctuation change by the dimension change of the stiffening flanges?

Appendix A

Contour plots at the inter-disk mid-plane for the inner configuration

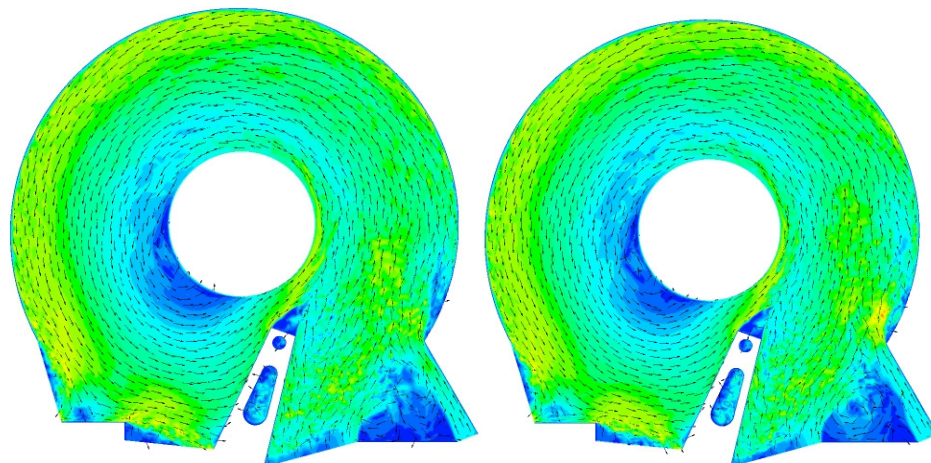
In appendix A, contour plots are captured at ten time steps equally spaced over one cycle of the disk rotation on the inter-disk mid-plane. An instantaneous time, t^* , was non-dimensionalized by the duration of one cycle for the disk rotation. The contour plots reveal that velocity fluctuations and intensified vorticity streaks induced by the actuator arm and the SSU.

A.1 Velocity with vectors
A.1.1 Air flow at 5400 rpm



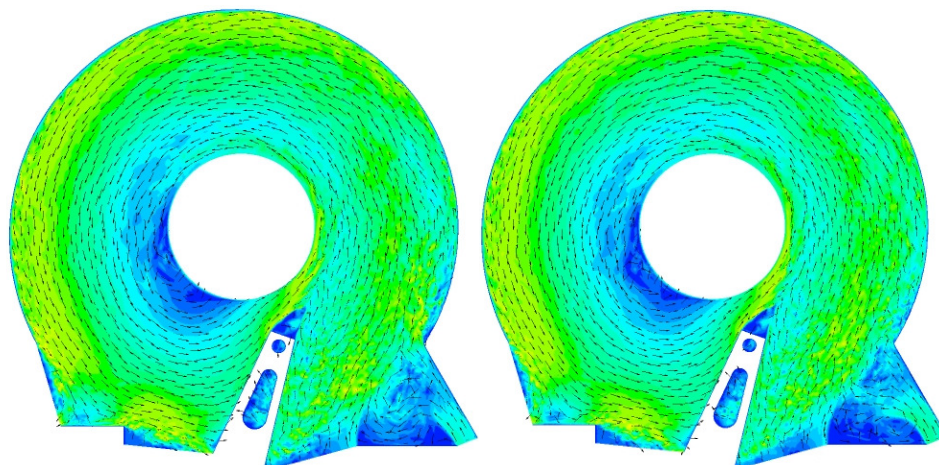
(a) $t^* = 0$

(b) $t^* = 0.1$



(c) $t^* = 0.2$

(d) $t^* = 0.3$



(e) $t^* = 0.4$

(f) $t^* = 0.5$

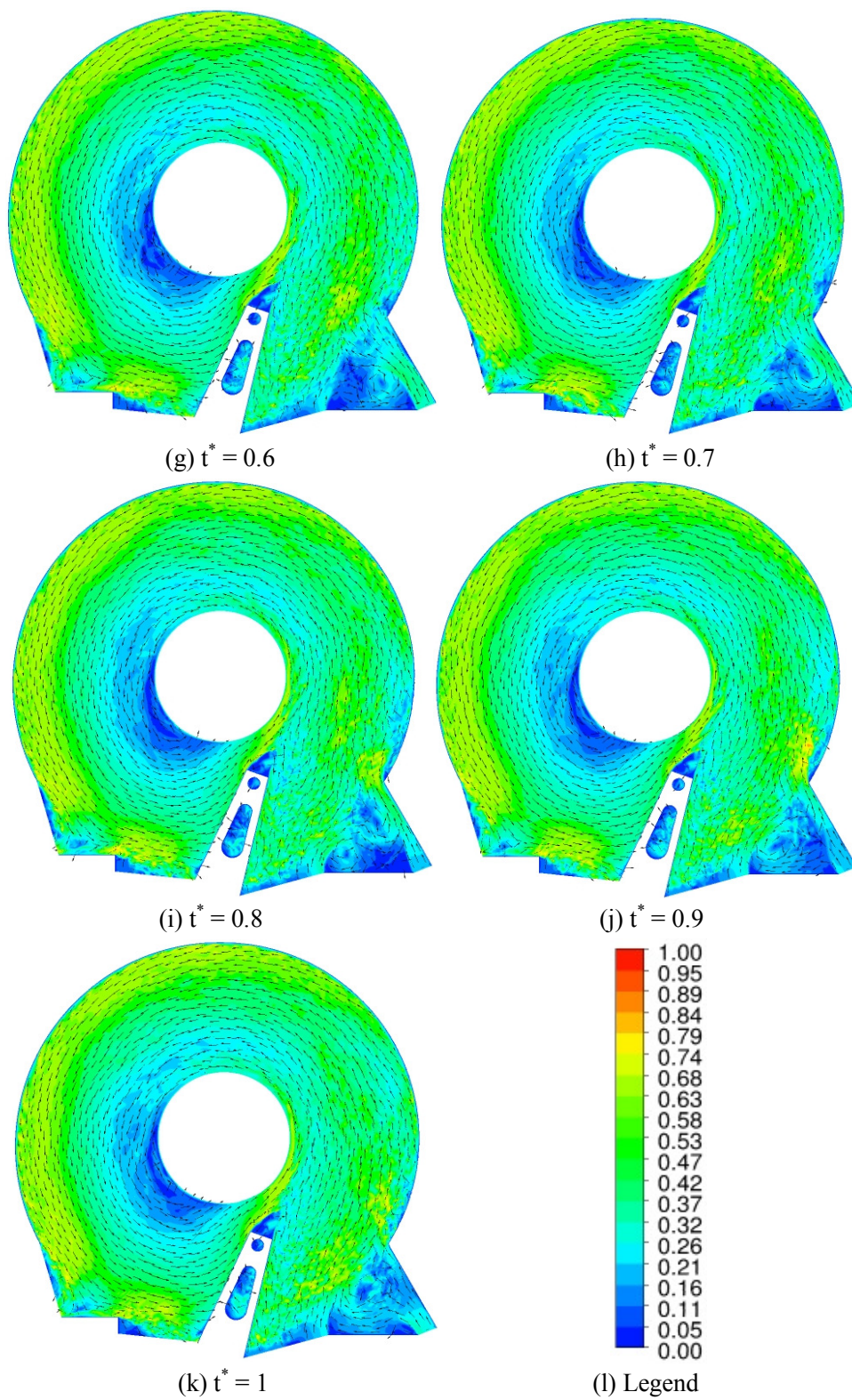
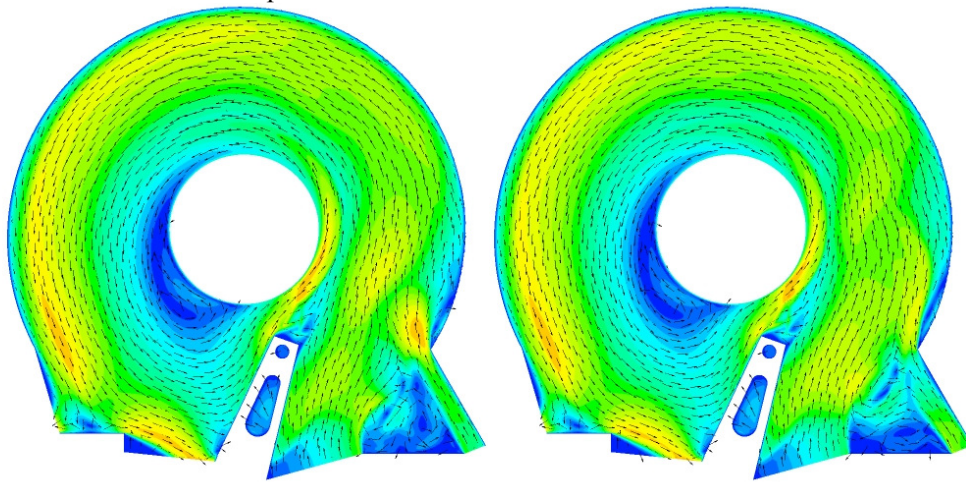
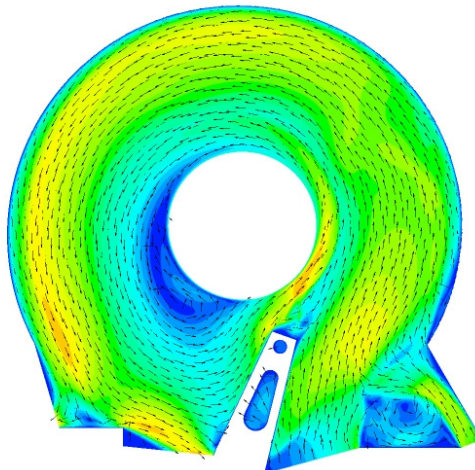
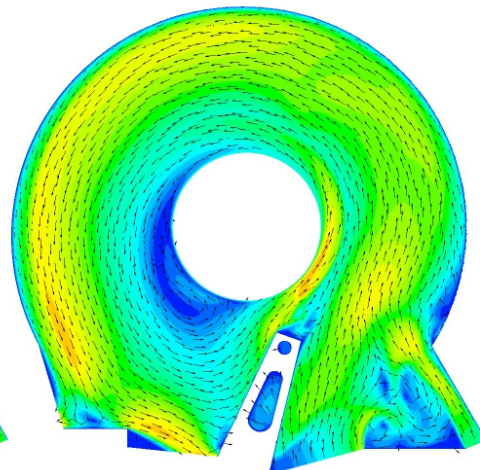
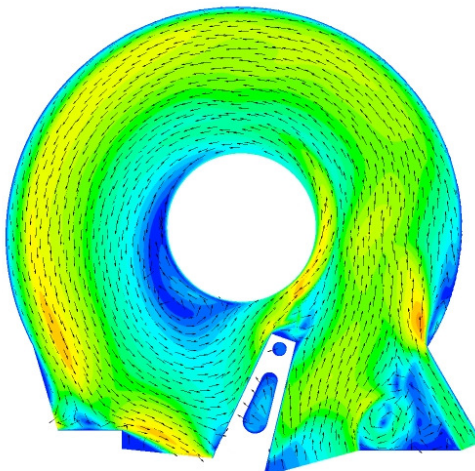
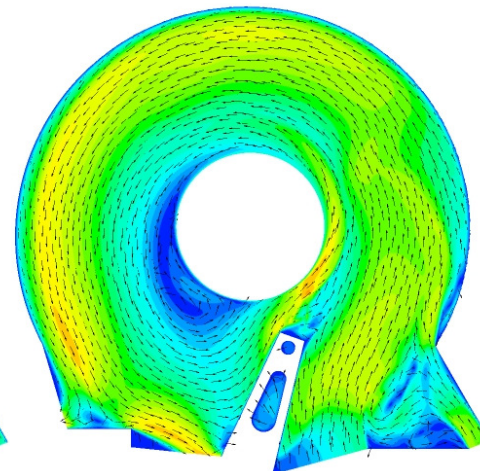


Figure A.1: Contour plot of velocity with vectors of air at 5400 rpm

A.1.2 Helium flow at 5400 rpm

(a) $t^* = 0$ (b) $t^* = 0.1$ (c) $t^* = 0.2$ (d) $t^* = 0.3$ (e) $t^* = 0.4$ (f) $t^* = 0.5$

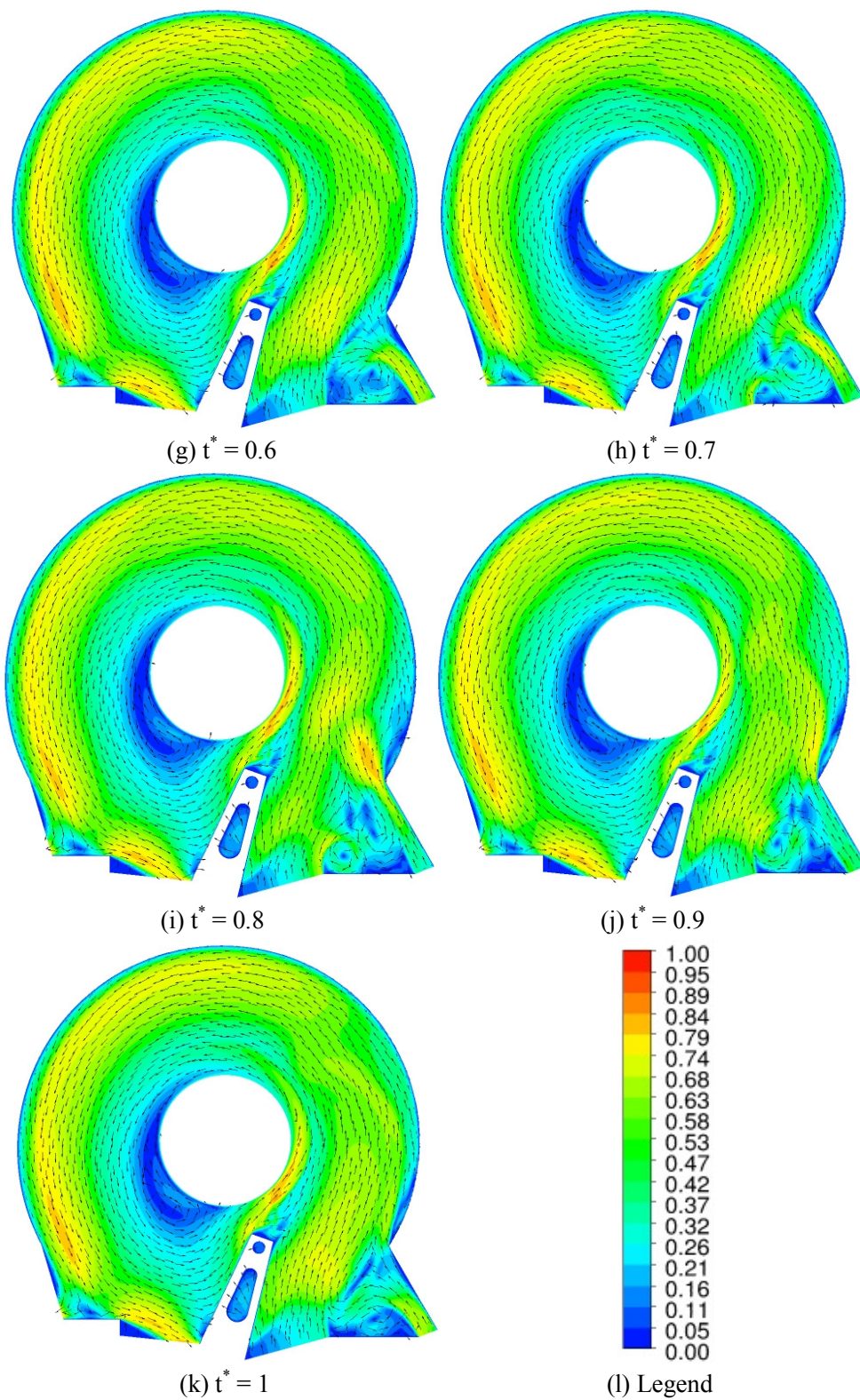
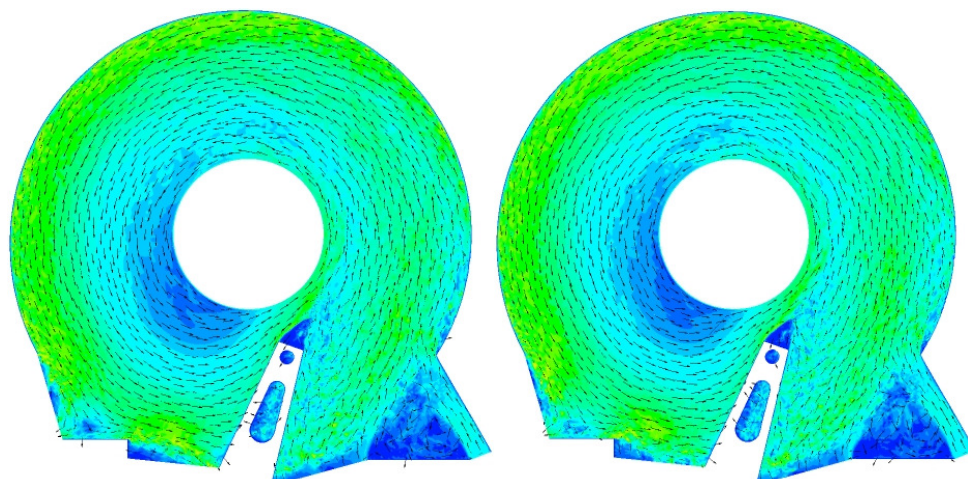
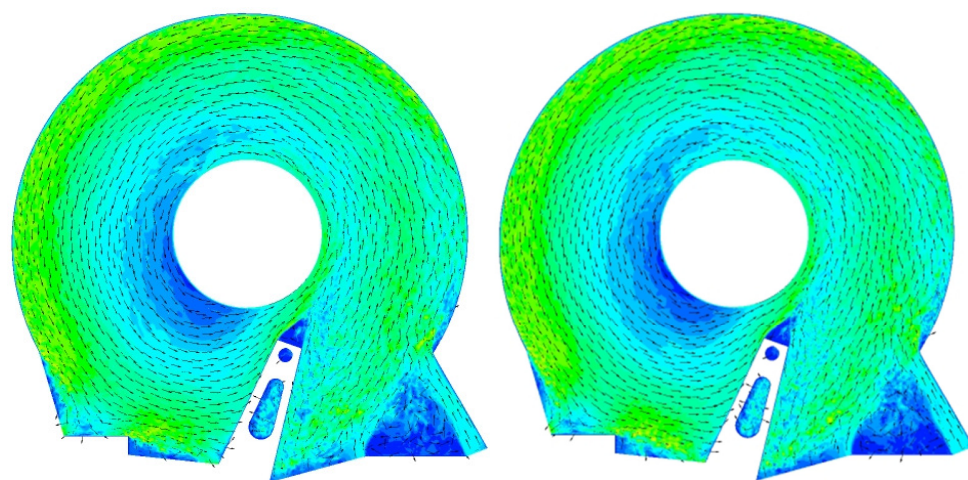
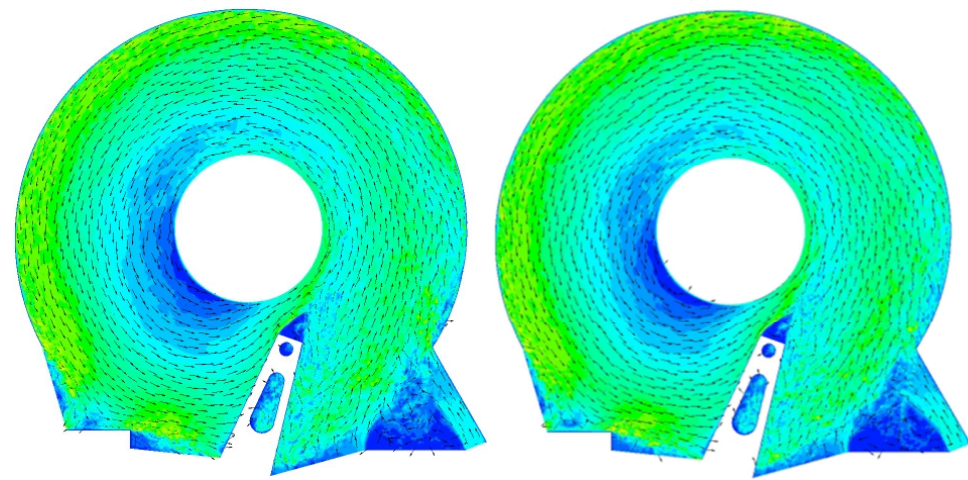


Figure A.2: Contour plot of velocity with vectors of helium at 5400 rpm

A.1.3 Air flow at 15000 rpm

(a) $t^* = 0$ (b) $t^* = 0.1$ (c) $t^* = 0.2$ (d) $t^* = 0.3$ (e) $t^* = 0.4$ (f) $t^* = 0.5$

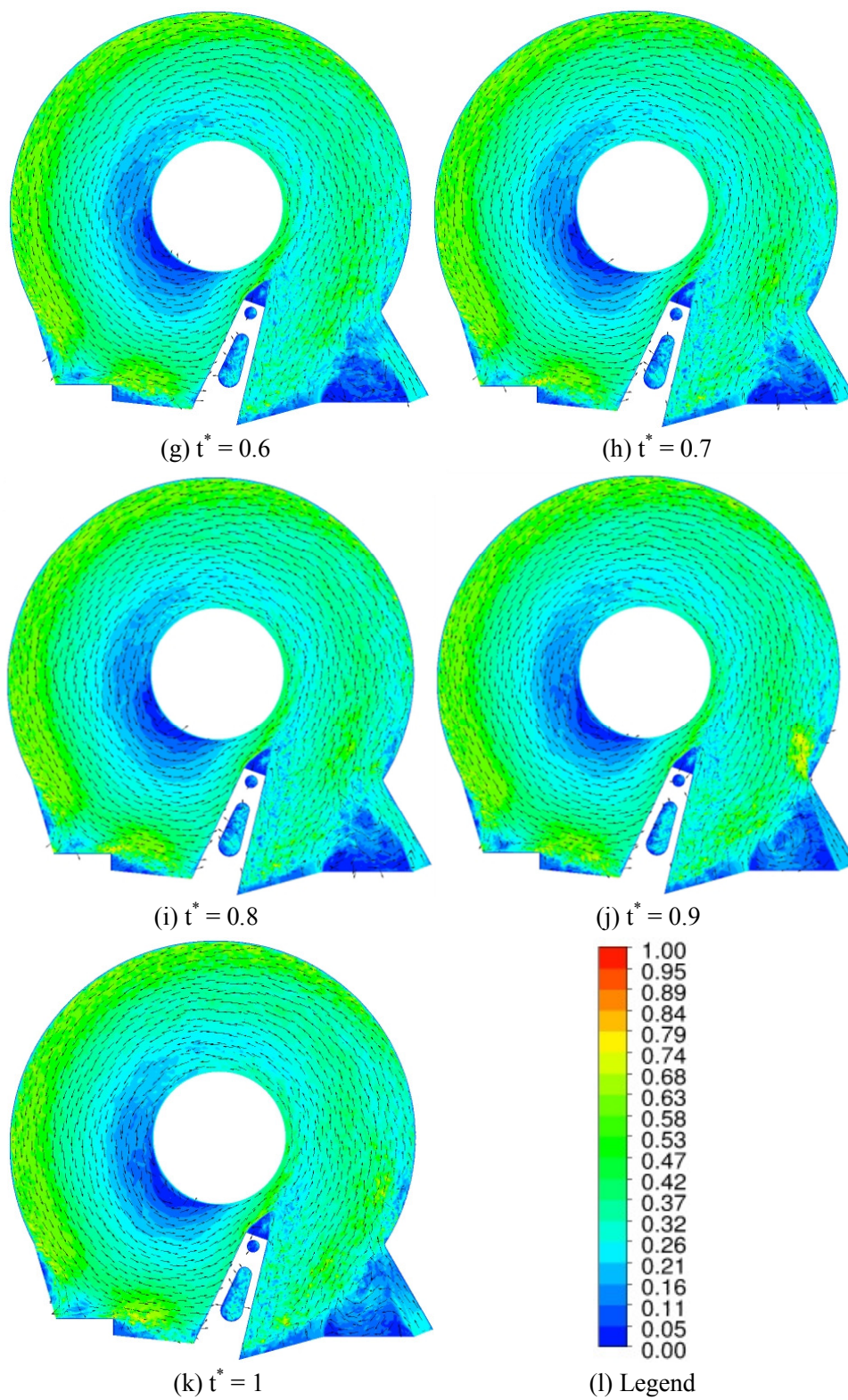
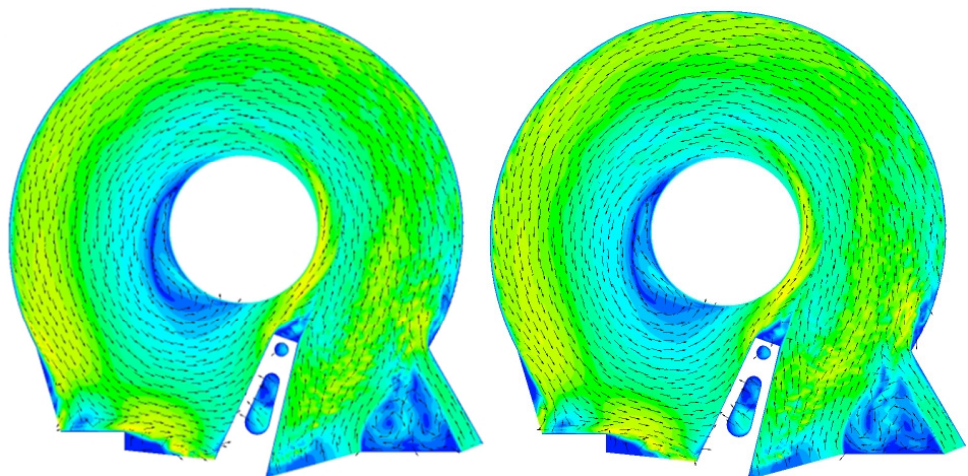
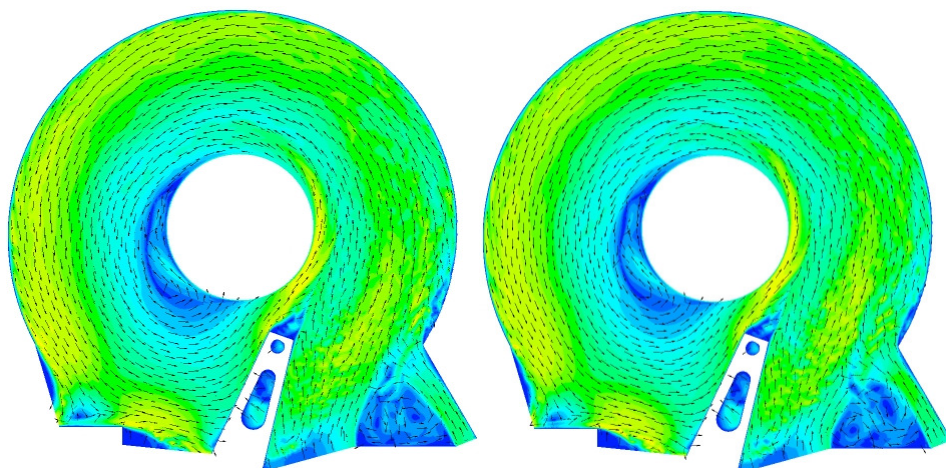
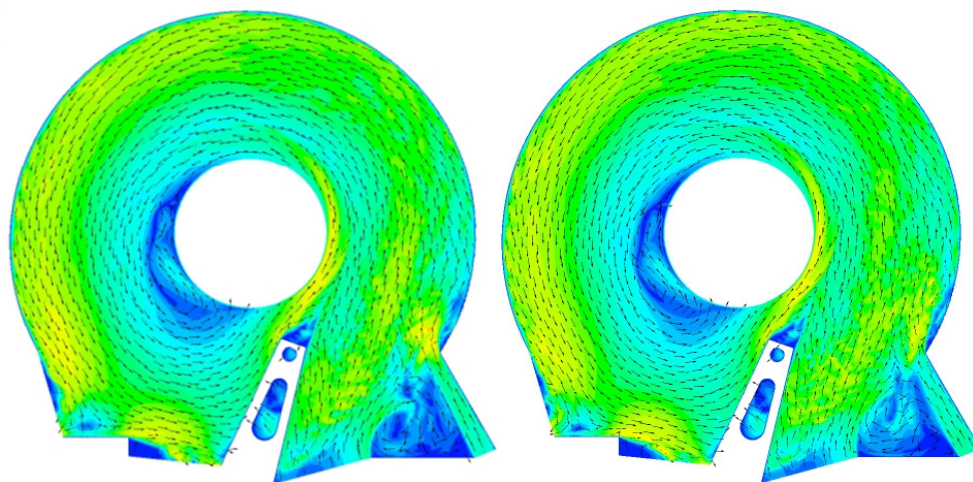


Figure A.3: Contour plot of velocity with vectors of air at 15000 rpm

A.1.4 Helium flow at 15000 rpm

(a) $t^* = 0$ (b) $t^* = 0.1$ (c) $t^* = 0.2$ (d) $t^* = 0.3$ (e) $t^* = 0.4$ (f) $t^* = 0.5$

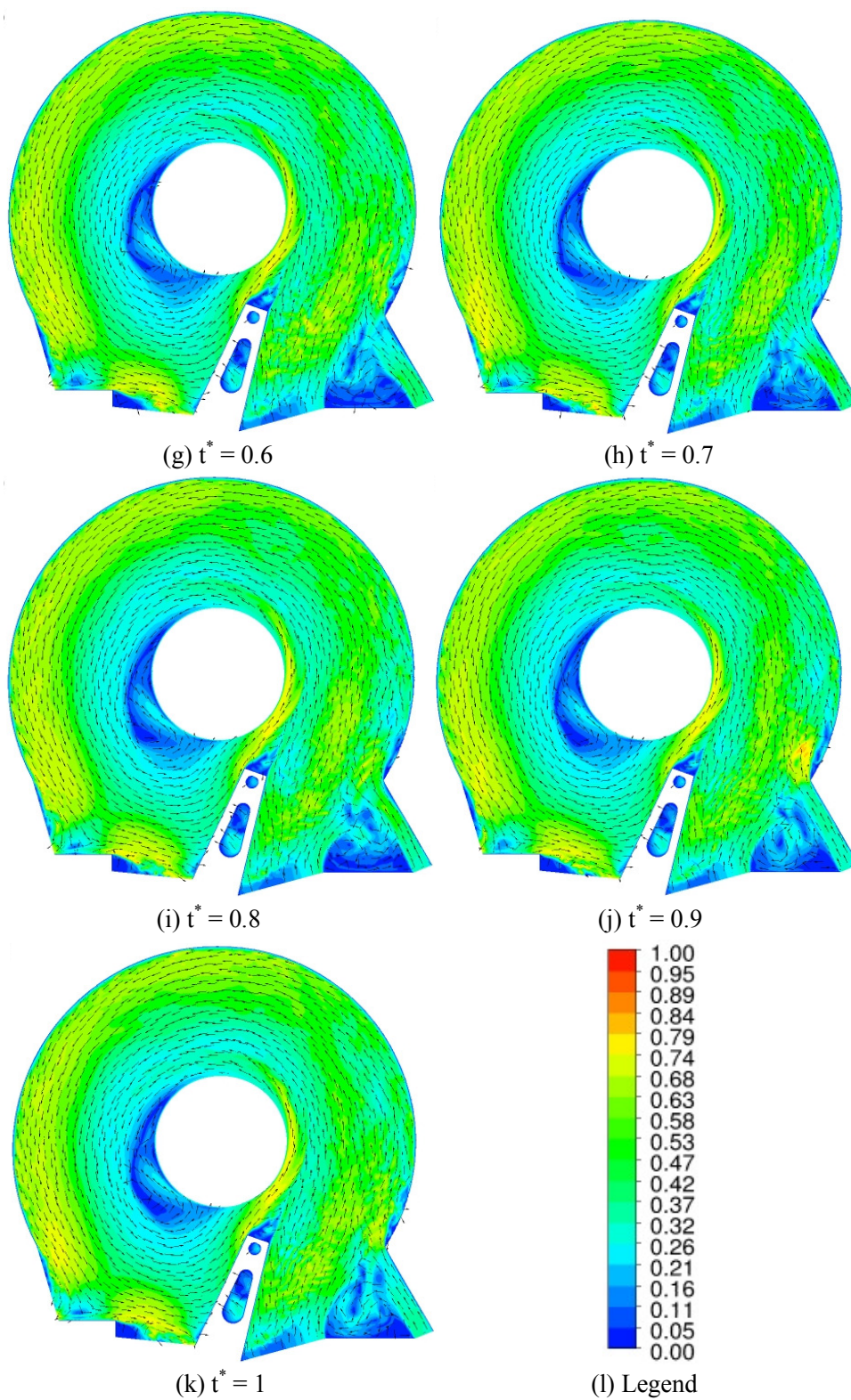
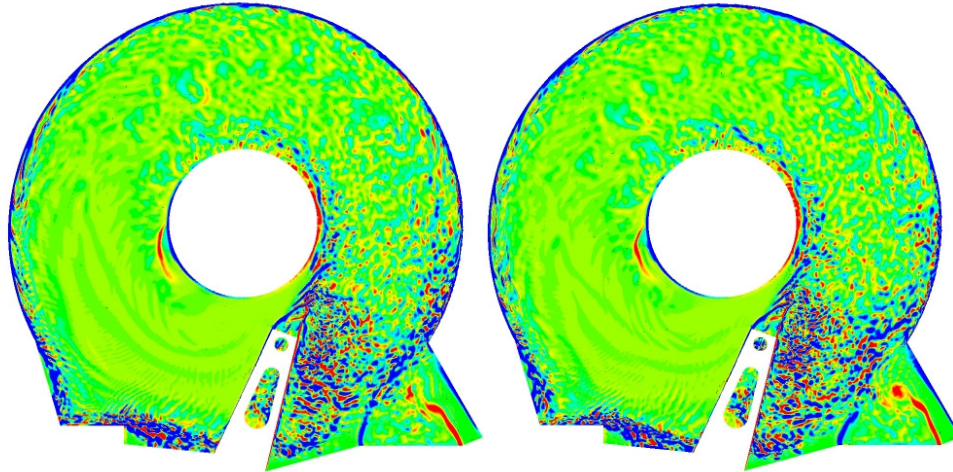
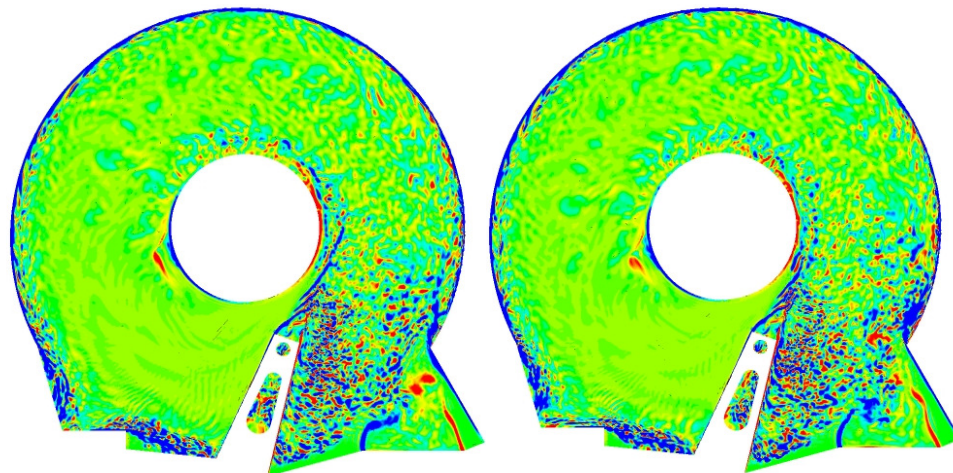
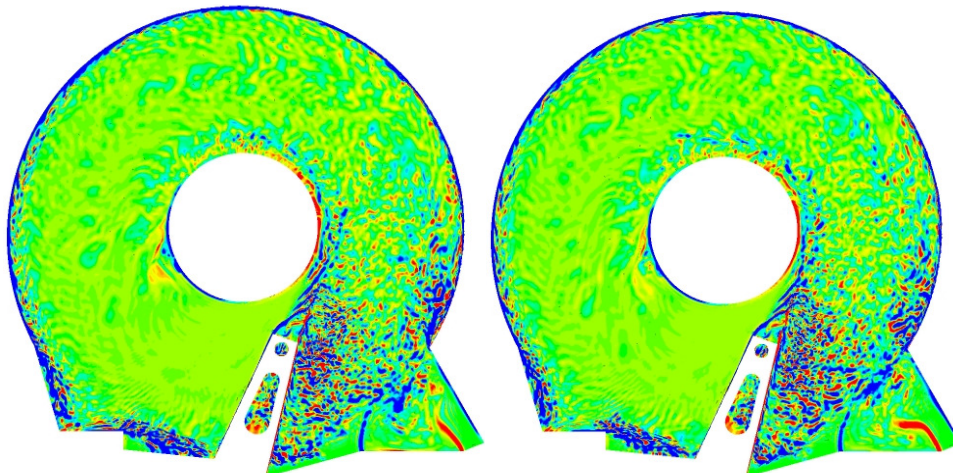


Figure A.4: Contour plot of velocity with vectors of helium at 15000 rpm

A.2 Z-axis vorticity

A.2.1 Air flow at 5400 rpm

(a) $t^* = 0$ (b) $t^* = 0.1$ (c) $t^* = 0.2$ (d) $t^* = 0.3$ (e) $t^* = 0.4$ (f) $t^* = 0.5$

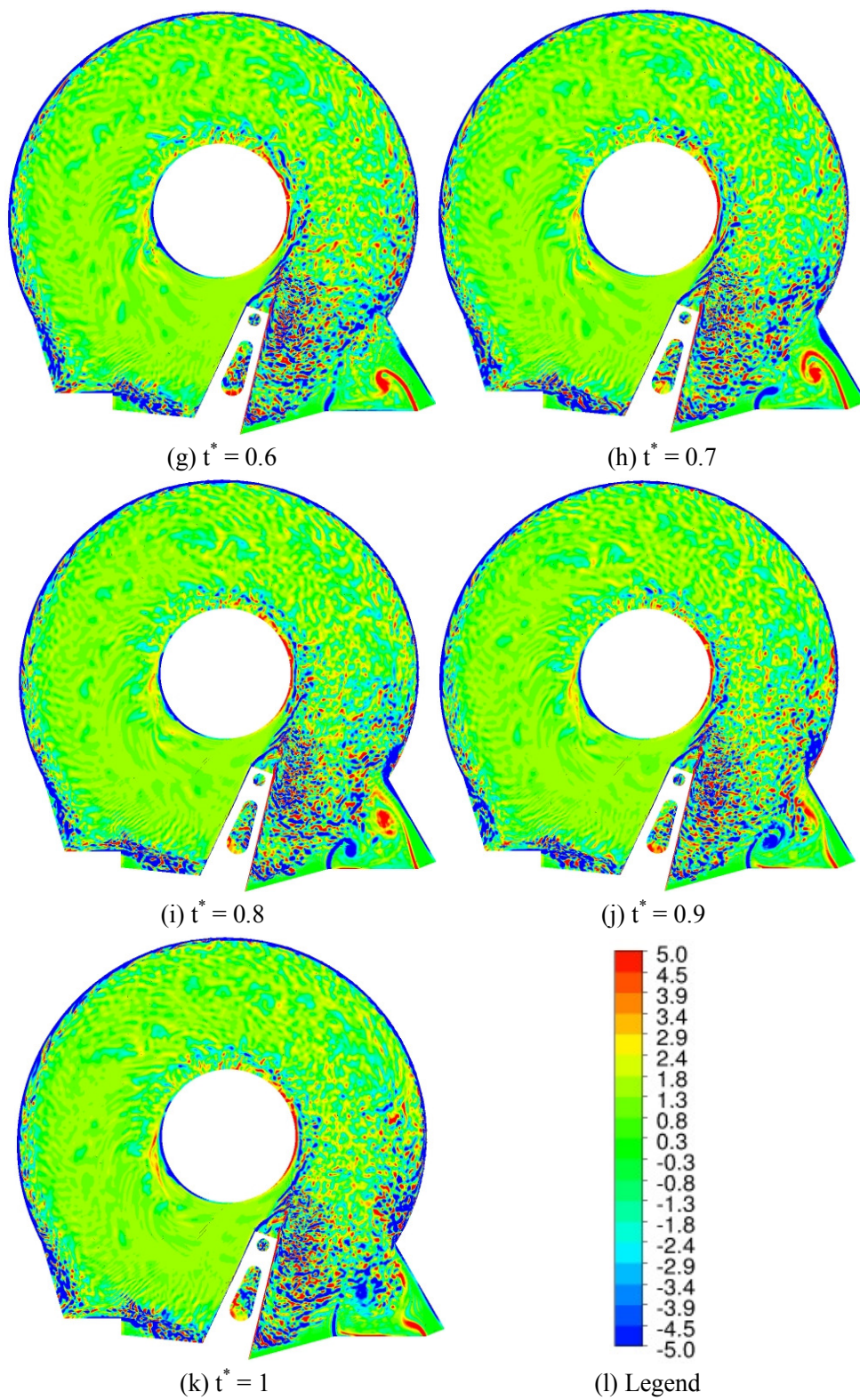
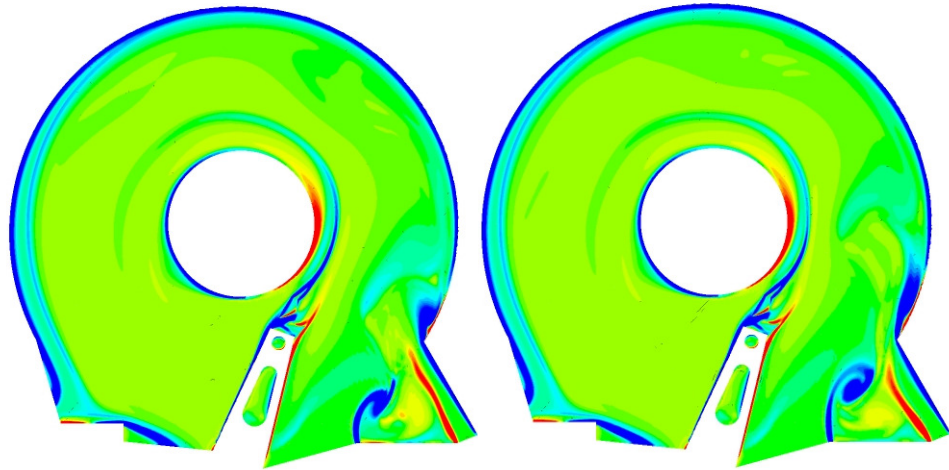
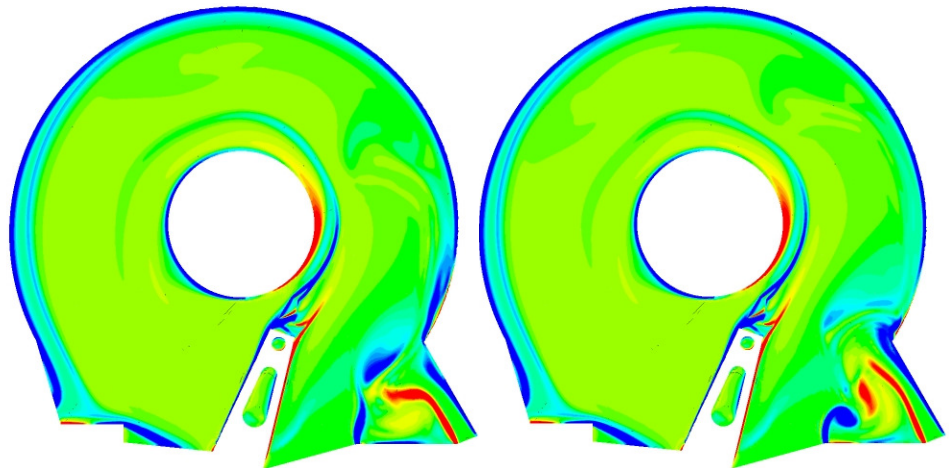
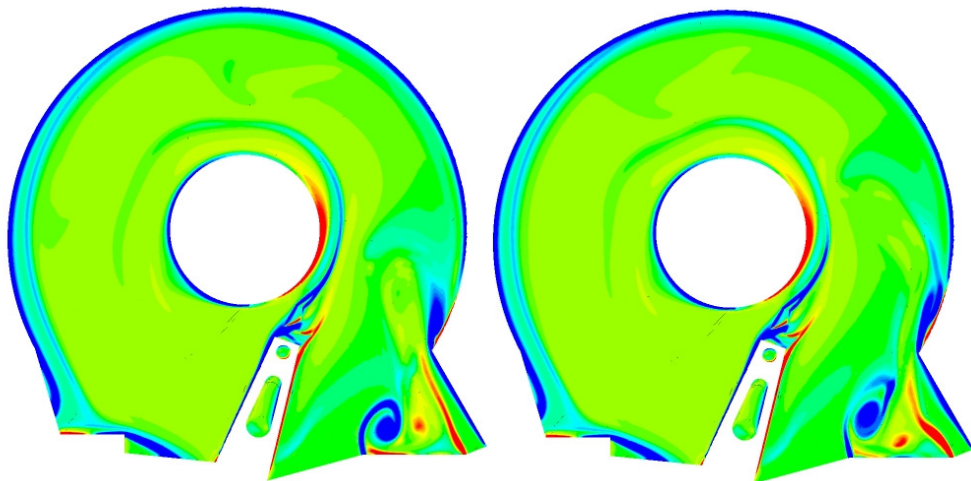


Figure A.5: Contour plot of Z-axis vorticity for the air flow at 5400 rpm

A.2.2 Helium flow at 5400 rpm

(a) $t^* = 0$ (b) $t^* = 0.1$ (c) $t^* = 0.2$ (d) $t^* = 0.3$ (e) $t^* = 0.4$ (f) $t^* = 0.5$

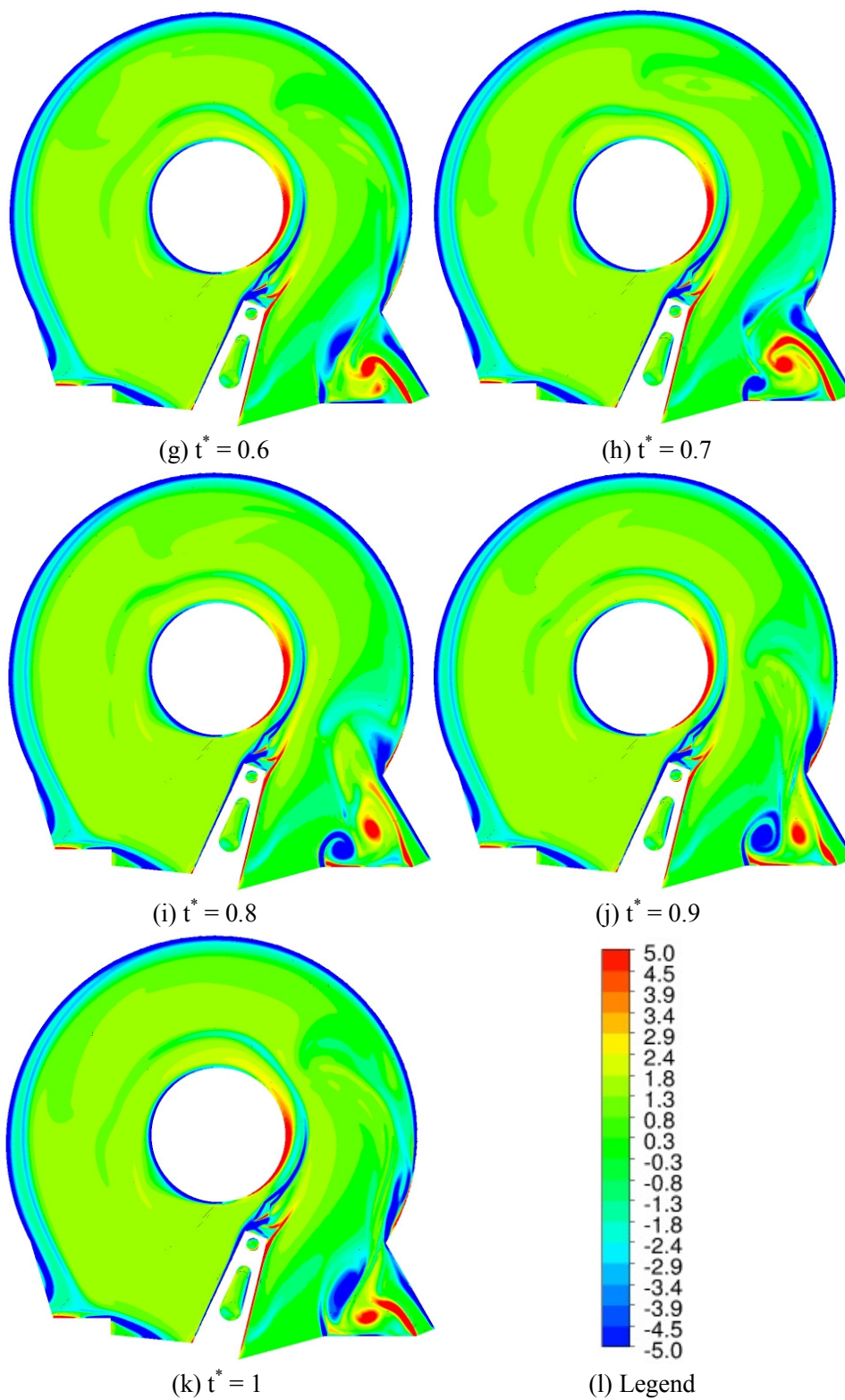
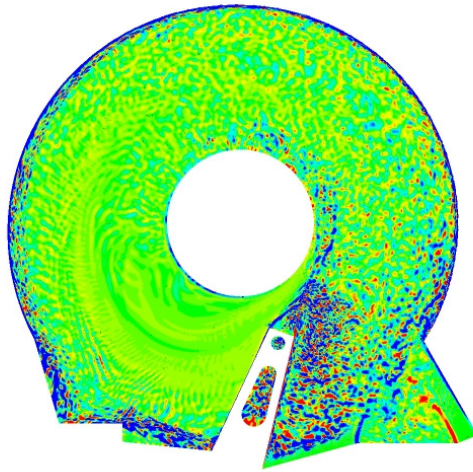
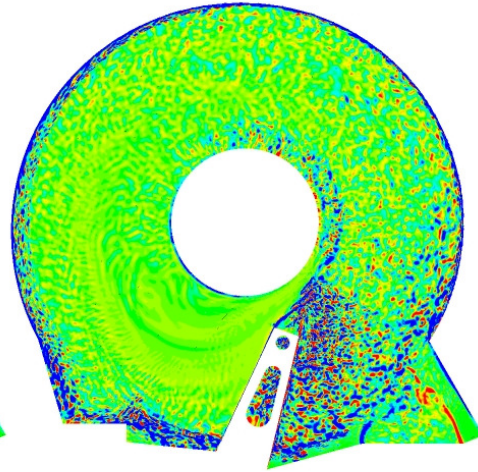
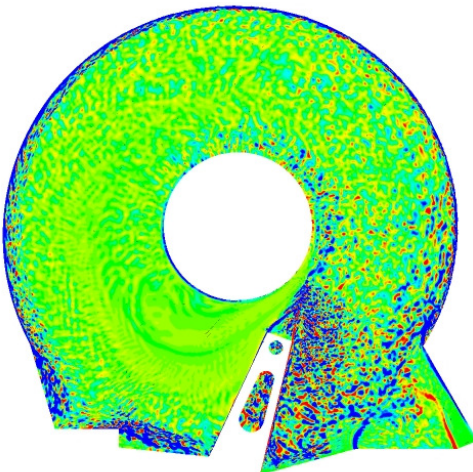
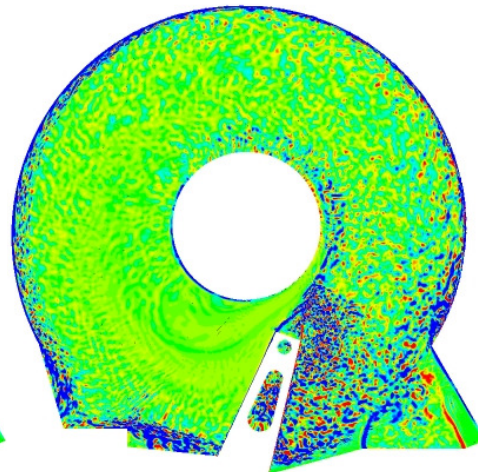
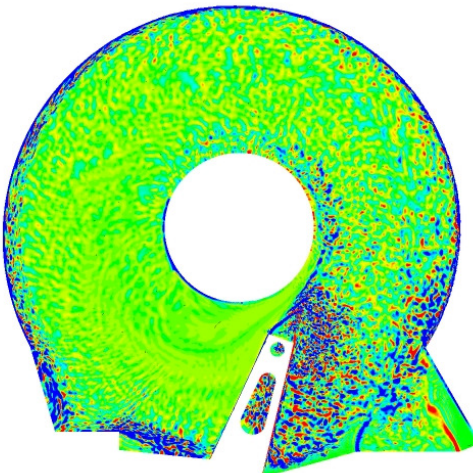
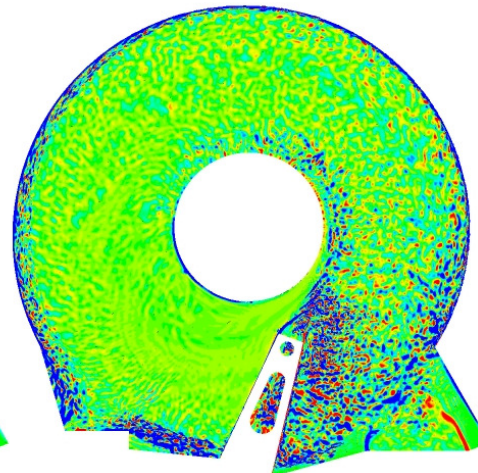


Figure A.6: Contour plot of Z-axis vorticity for the helium flow at 5400 rpm

A.2.3 Air flow at 15000 rpm

(a) $t^* = 0$ (b) $t^* = 0.1$ (c) $t^* = 0.2$ (d) $t^* = 0.3$ (e) $t^* = 0.4$ (f) $t^* = 0.5$

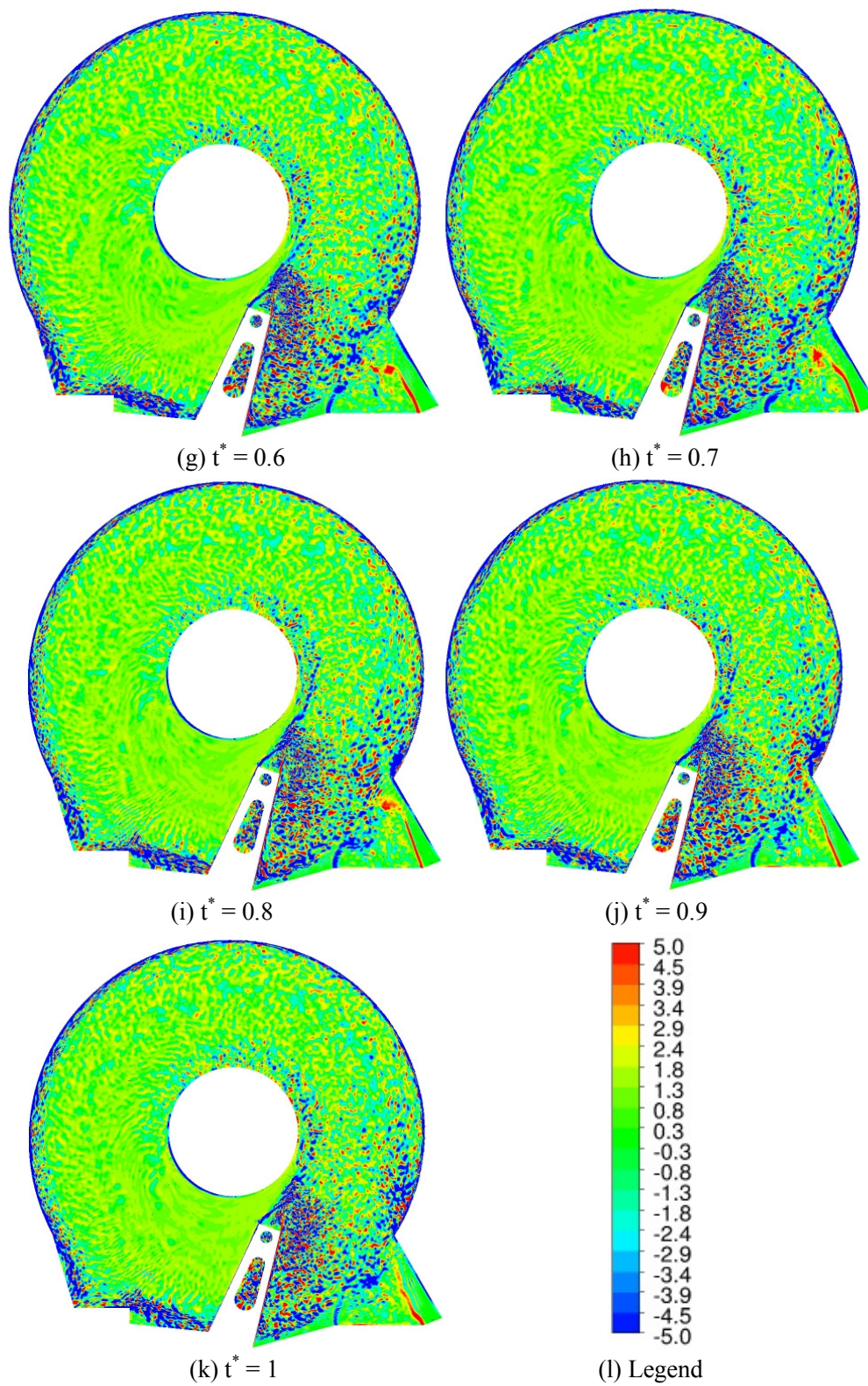
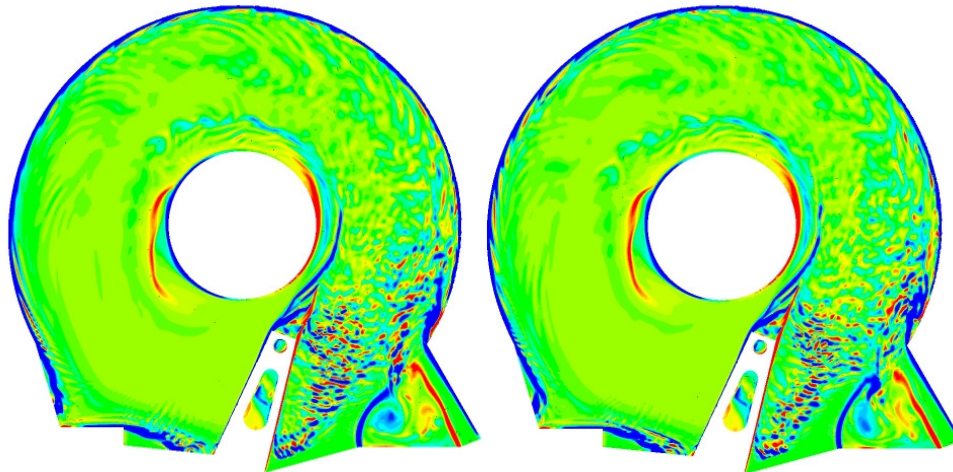
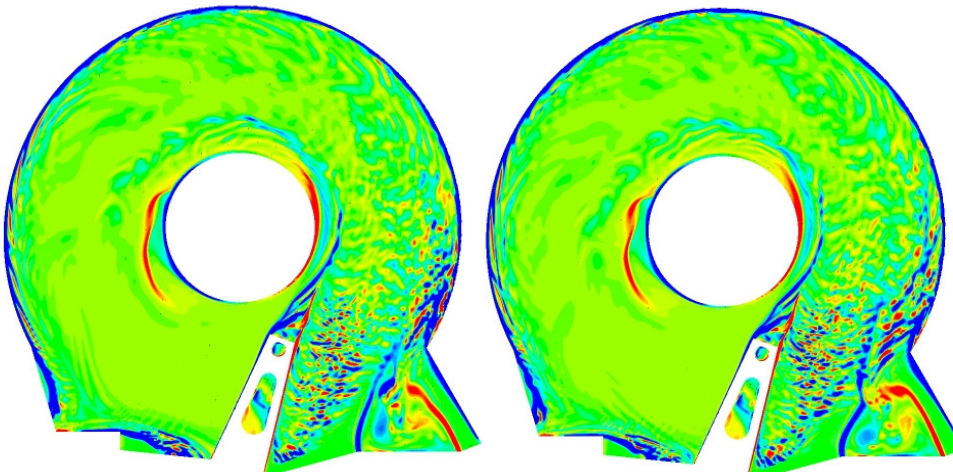
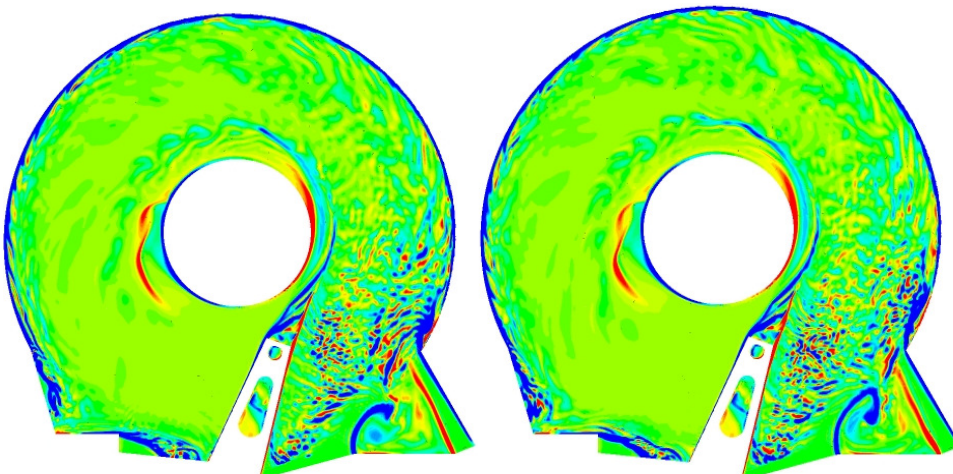


Figure A.7: Contour plot of Z-axis vorticity for the air flow at 15000 rpm

A.2.4 Helium flow at 15000 rpm

(a) $t^* = 0$ (b) $t^* = 0.1$ (c) $t^* = 0.2$ (d) $t^* = 0.3$ (e) $t^* = 0.4$ (f) $t^* = 0.5$

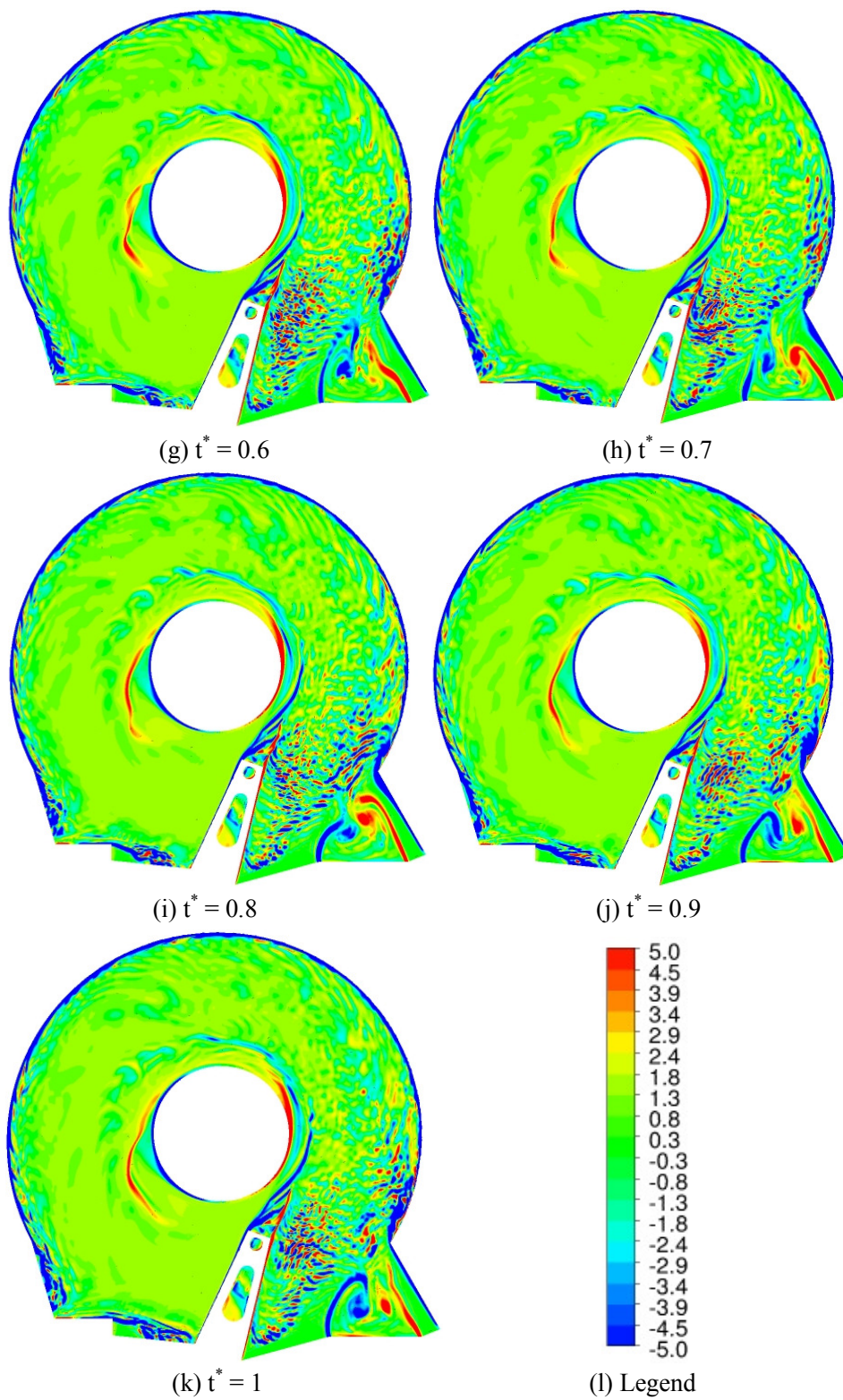


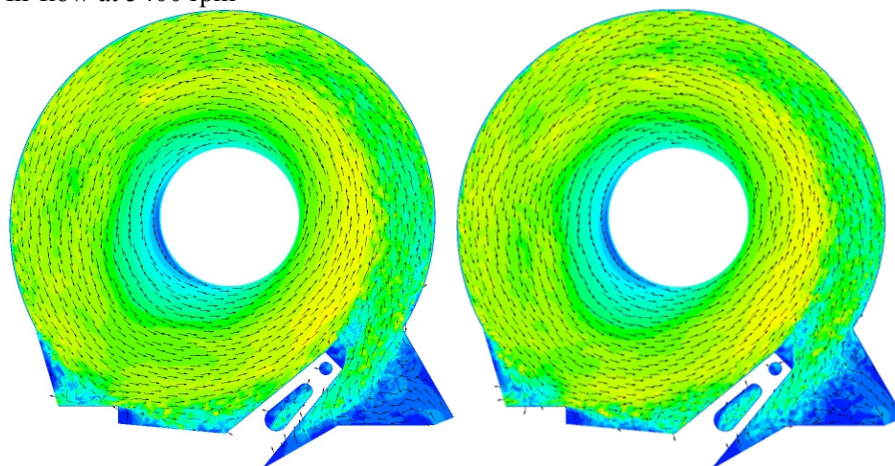
Figure A.8: Contour plot of Z-axis vorticity for the helium flow at 15000 rpm

Appendix B

Contour plots of velocity at the inter-disk mid-plane for the outer configuration

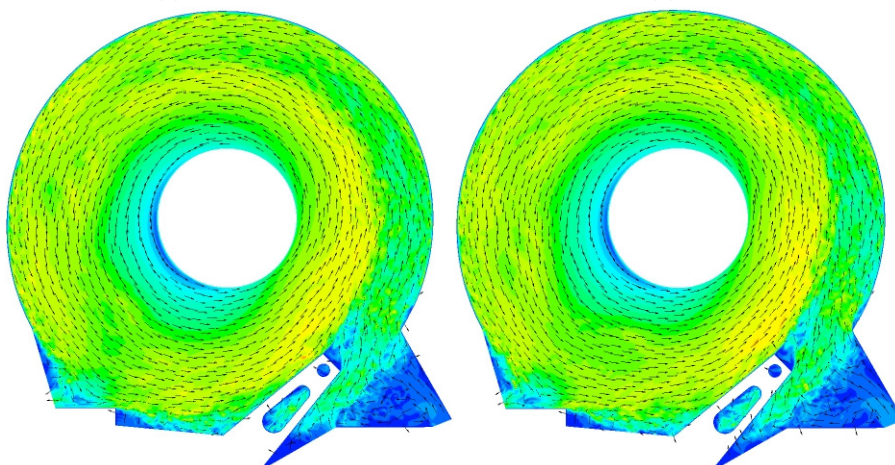
In appendix B, contour plots are captured at the same time steps as those for the inner configuration. The contour plots clearly describe that the source of velocity fluctuations and intensified vorticity streaks are the presence of the actuator arm and the SSU.

B.1 Velocity with vectors
B.1.1 Air flow at 5400 rpm



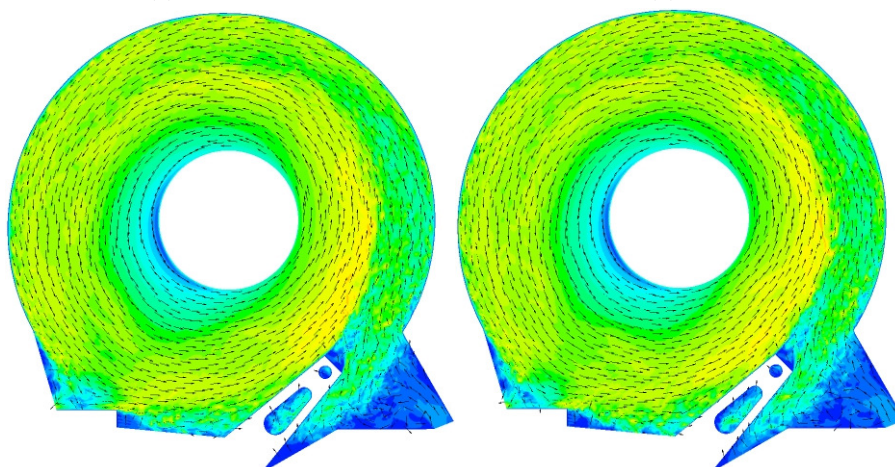
(a) $t^* = 0$

(b) $t^* = 0.1$



(c) $t^* = 0.2$

(d) $t^* = 0.3$



(e) $t^* = 0.4$

(f) $t^* = 0.5$

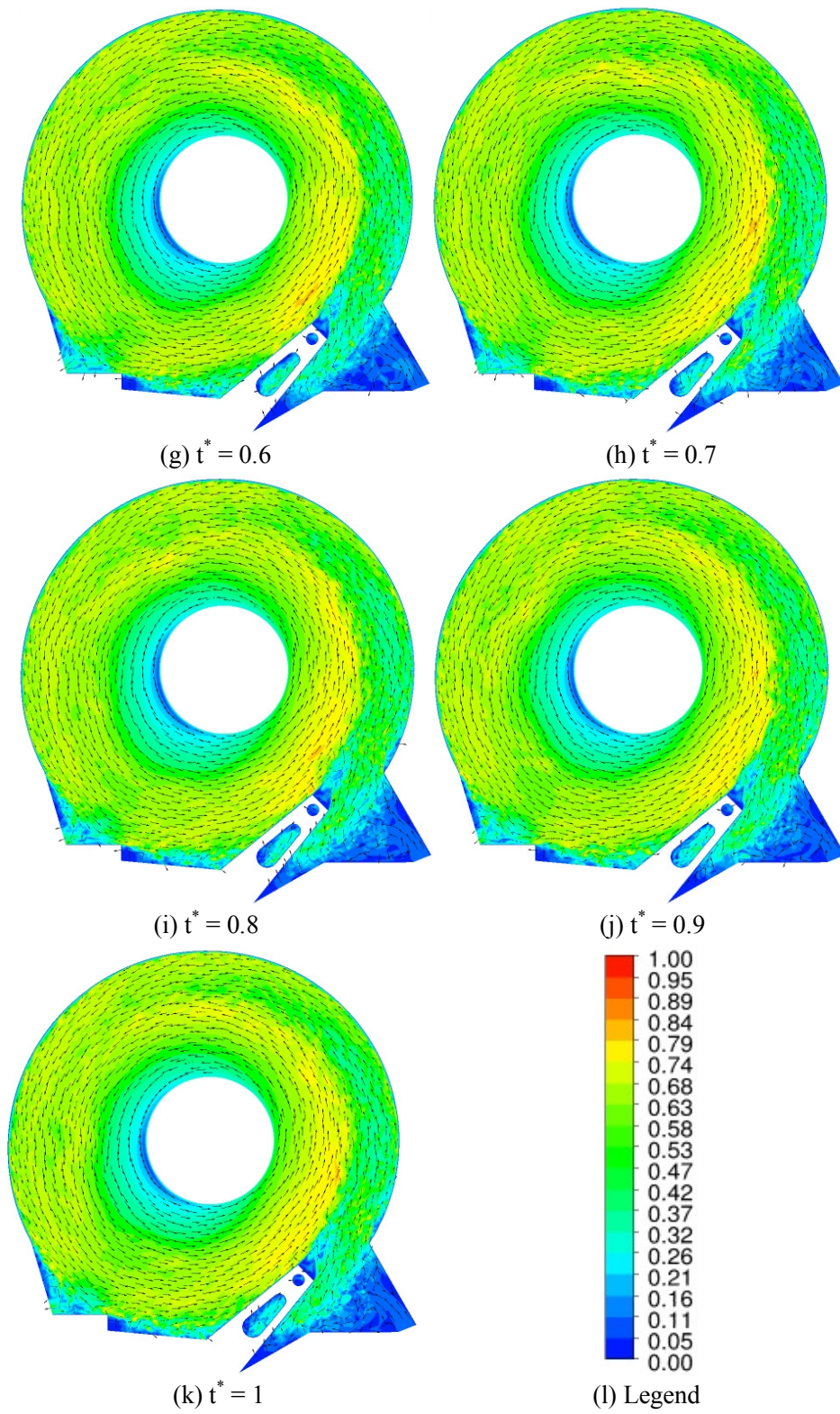
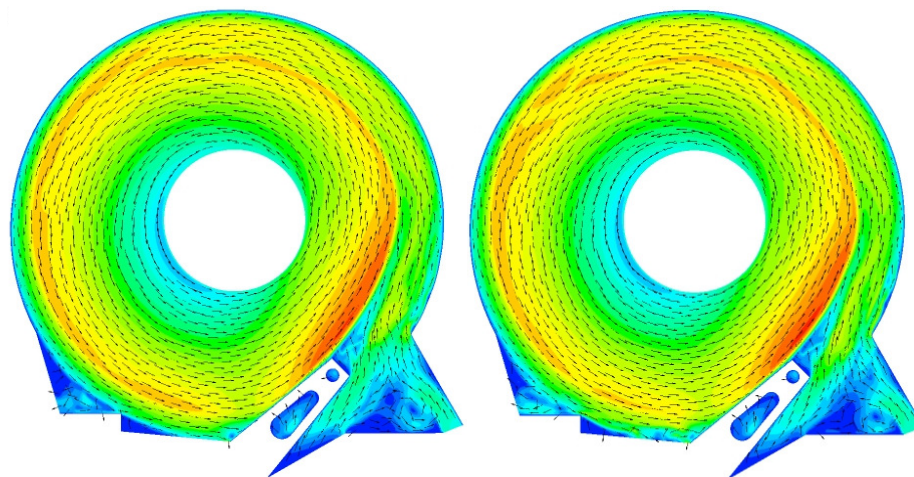
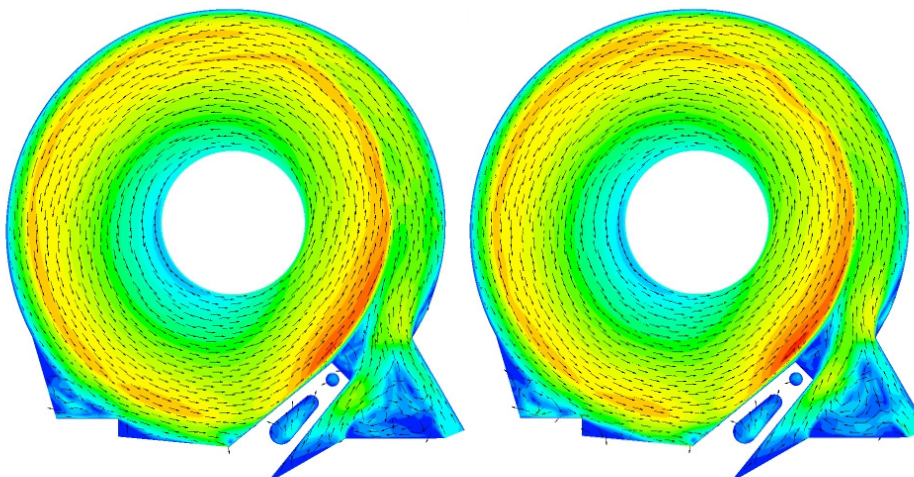
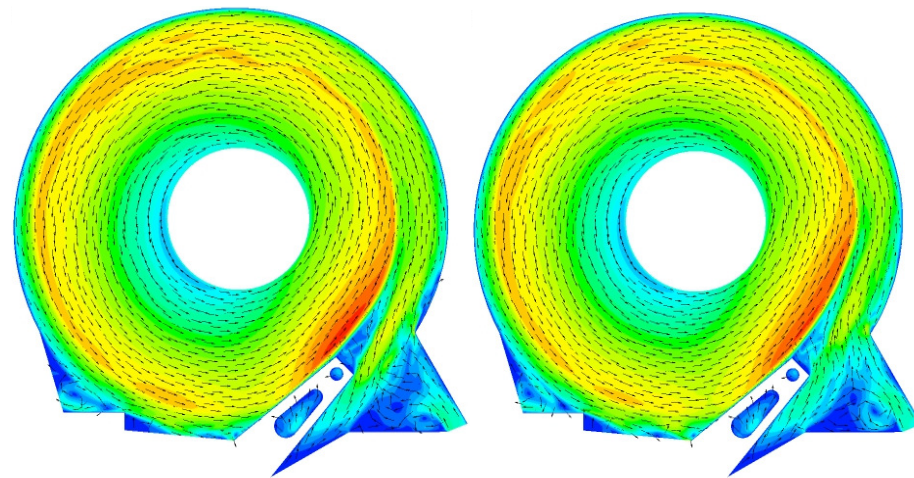


Figure B.1: Contour plot of velocity with vectors of air at 5400 rpm

B.1.2 Helium flow at 5400 rpm

(a) $t^* = 0$ (b) $t^* = 0.1$ (c) $t^* = 0.2$ (d) $t^* = 0.3$ (e) $t^* = 0.4$ (f) $t^* = 0.5$

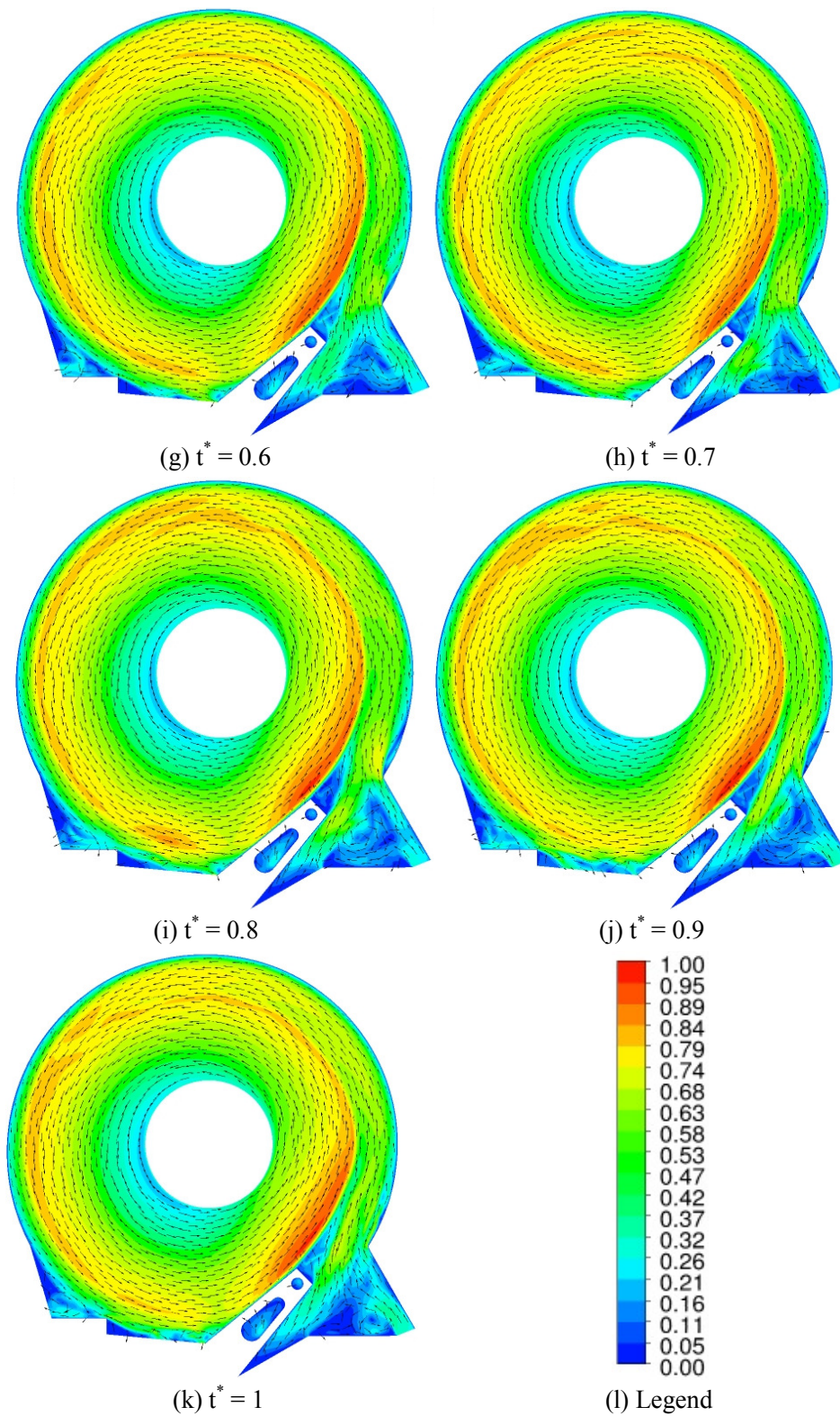
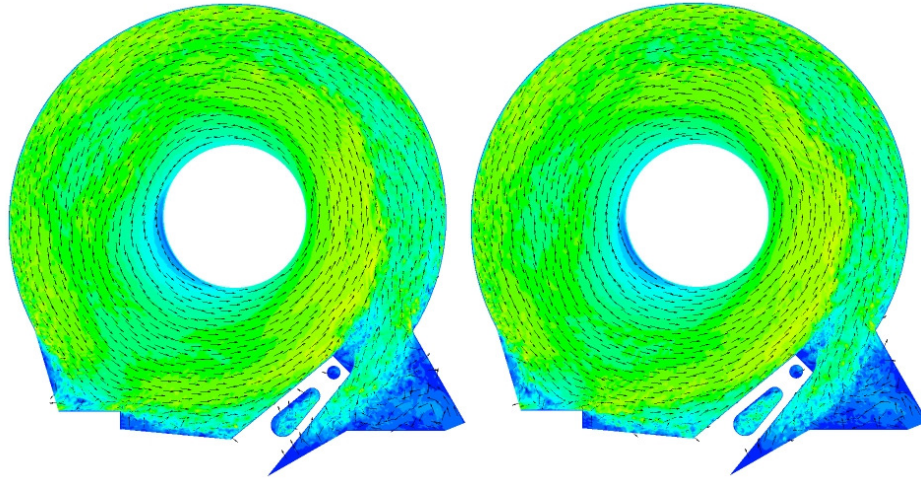
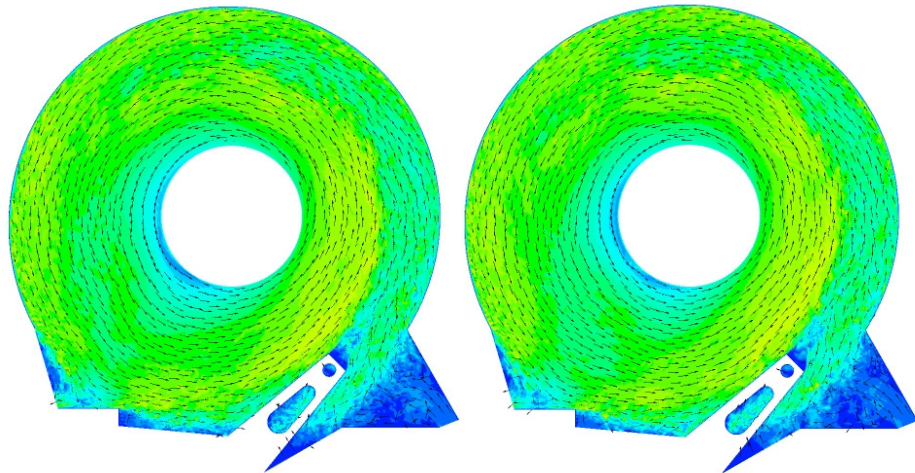
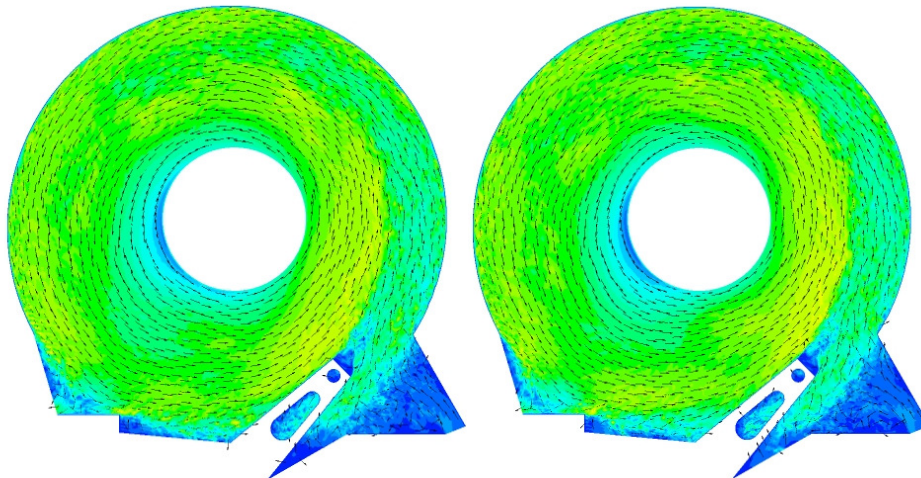


Figure B.2: Contour plot of velocity with vectors of helium at 5400 rpm

B.1.3 Air flow at 15000 rpm

(a) $t^* = 0$ (b) $t^* = 0.1$ (c) $t^* = 0.2$ (d) $t^* = 0.3$ (e) $t^* = 0.4$ (f) $t^* = 0.5$

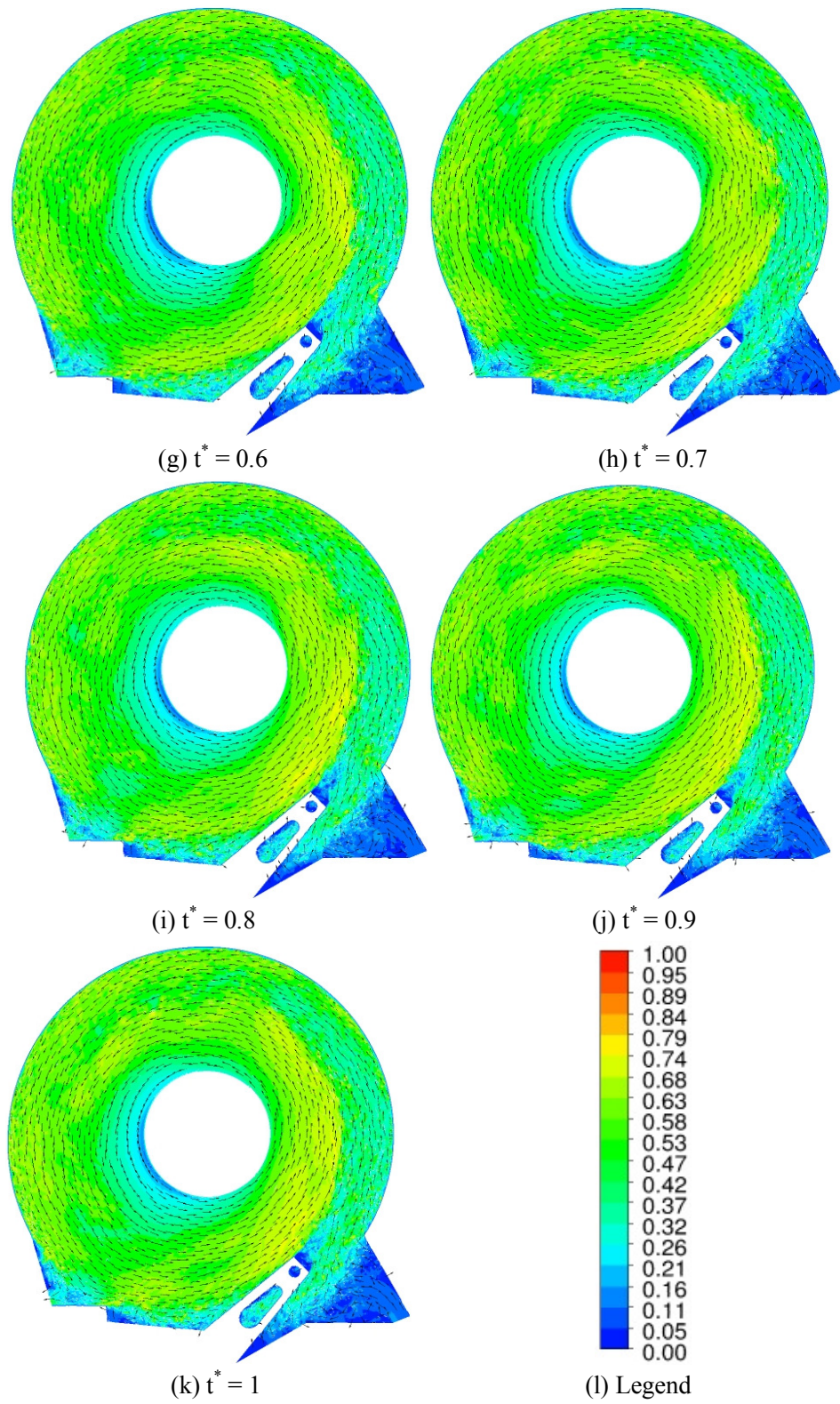
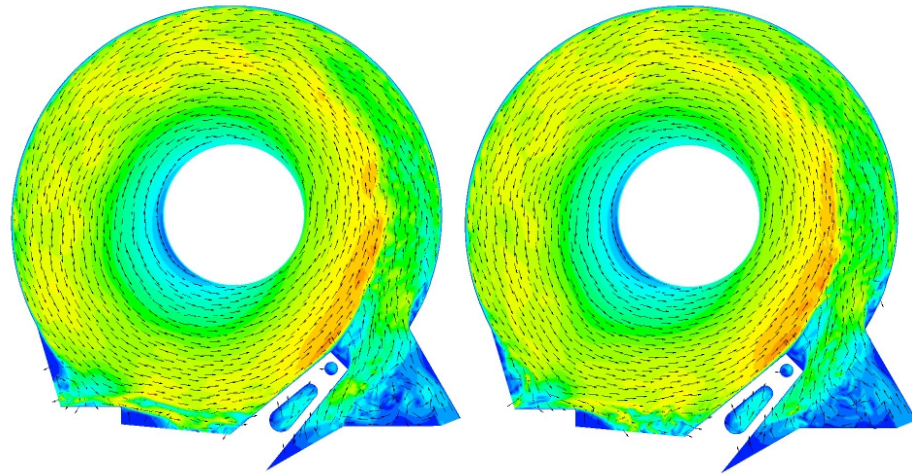
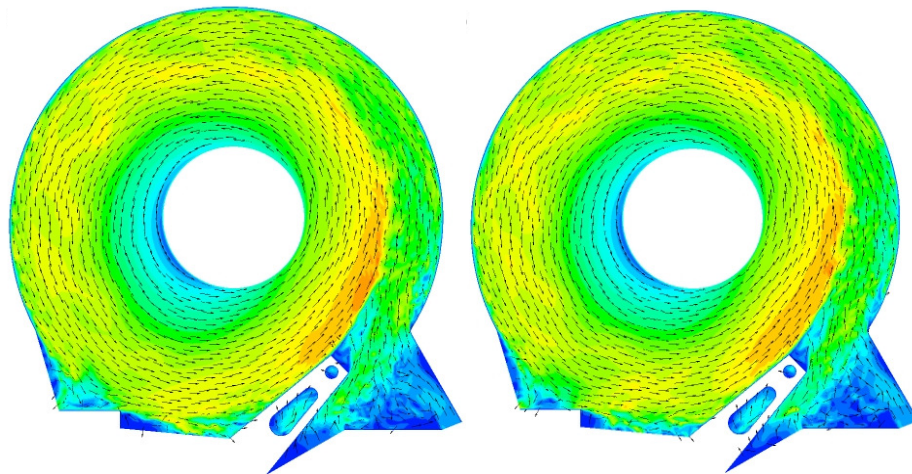
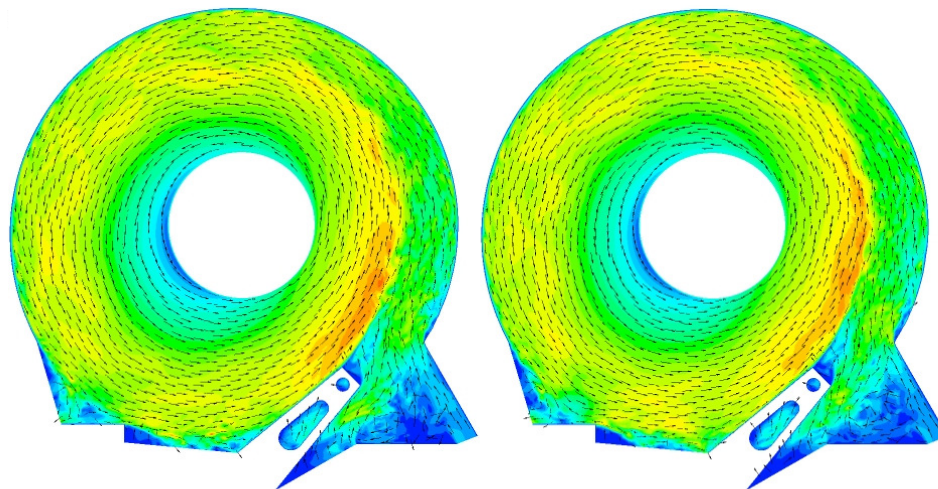


Figure B.3: Contour plot of velocity with vectors of air at 15000 rpm

B.1.4 Helium flow at 15000 rpm

(a) $t^* = 0$ (b) $t^* = 0.1$ (c) $t^* = 0.2$ (d) $t^* = 0.3$ (e) $t^* = 0.4$ (f) $t^* = 0.5$

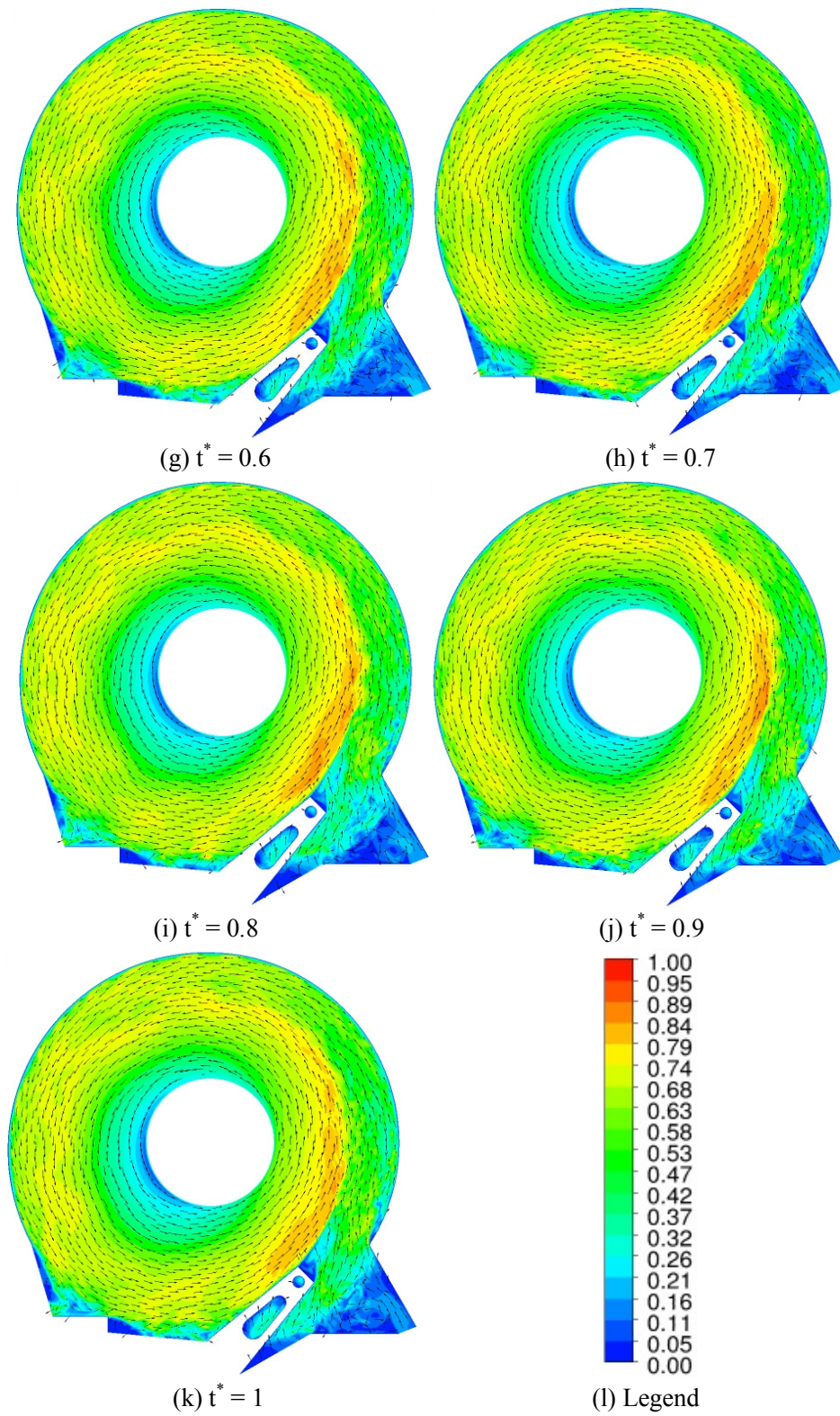
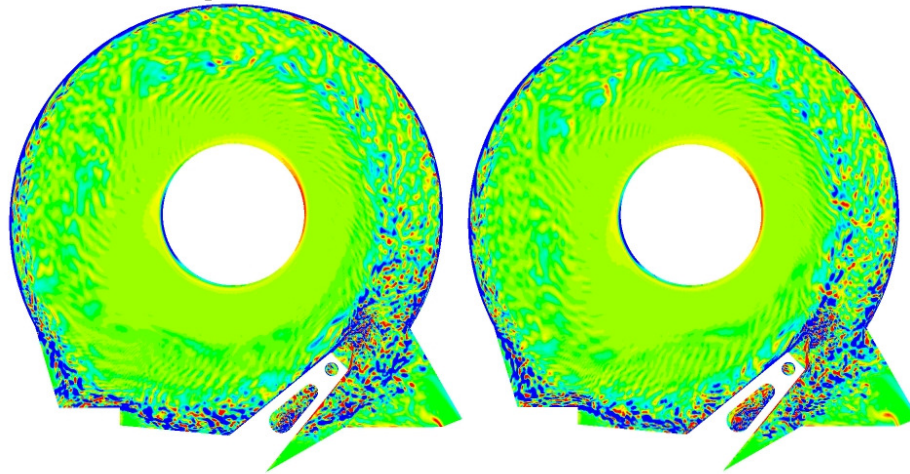


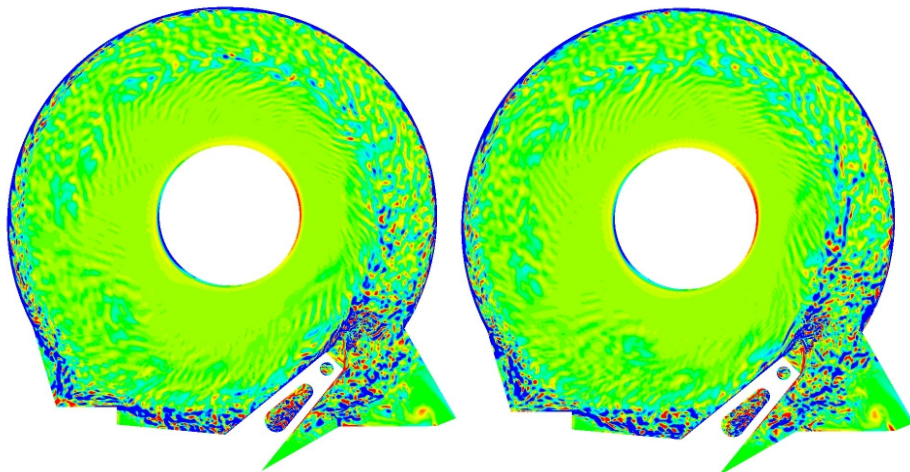
Figure B.4: Contour plot of velocity with vectors of helium at 15000 rpm

B.2 Z-axis vorticity
B.2.1 Air flow at 5400 rpm



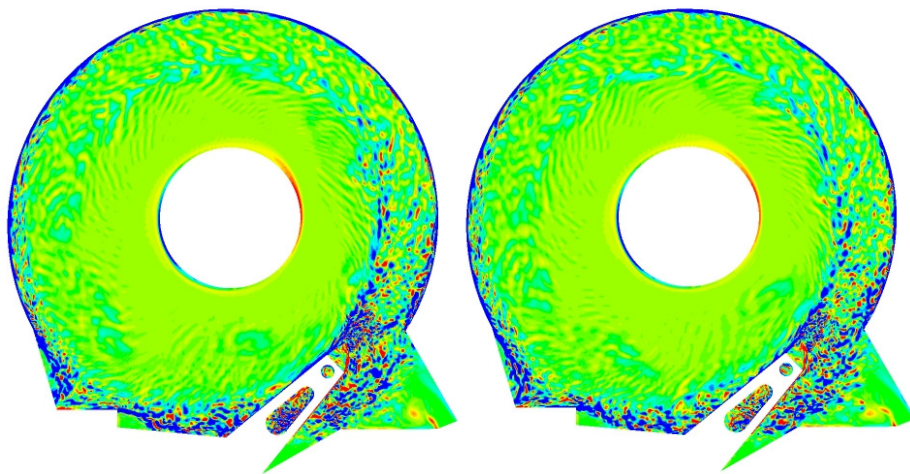
(a) $t^* = 0$

(b) $t^* = 0.1$



(c) $t^* = 0.2$

(d) $t^* = 0.3$



(e) $t^* = 0.4$

(f) $t^* = 0.5$

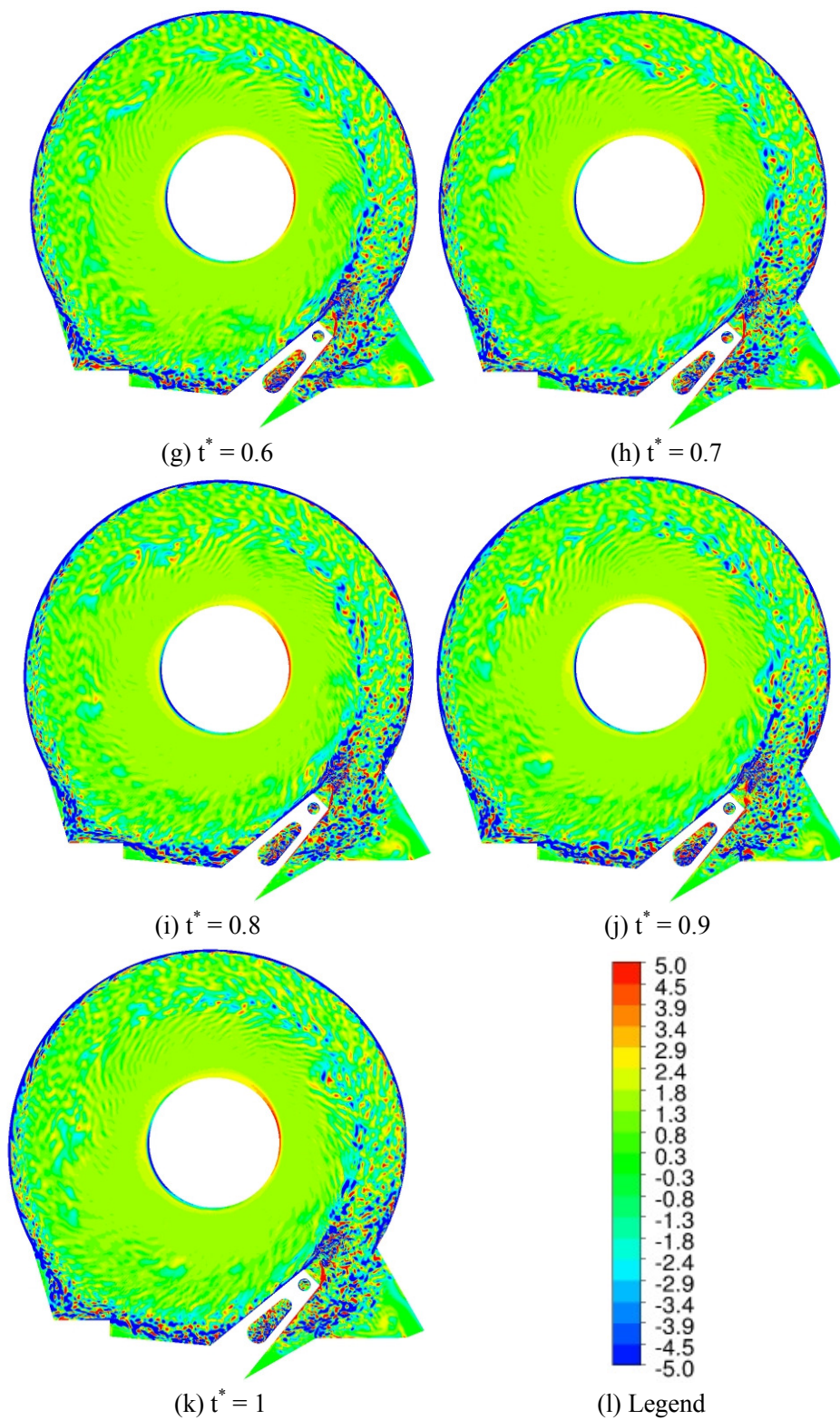
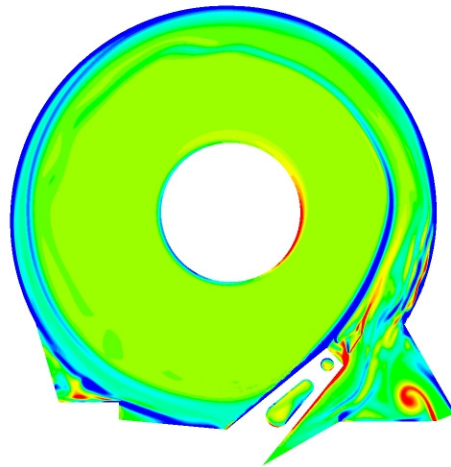
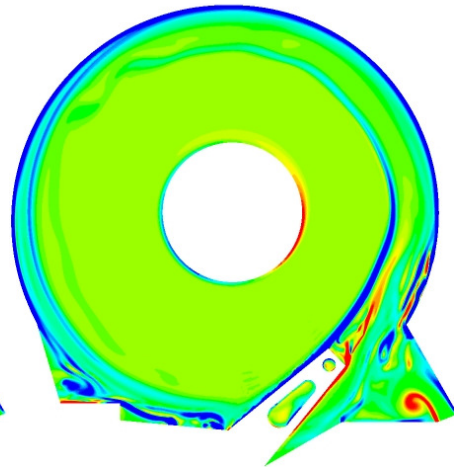
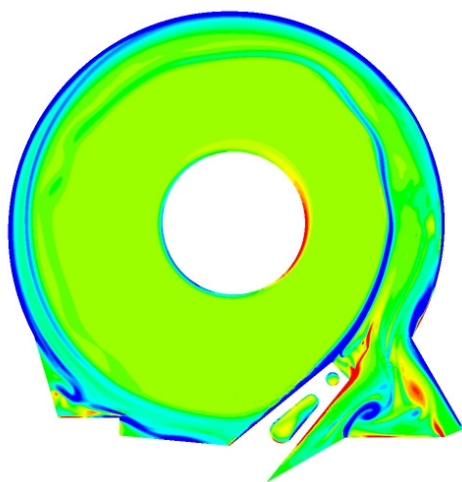
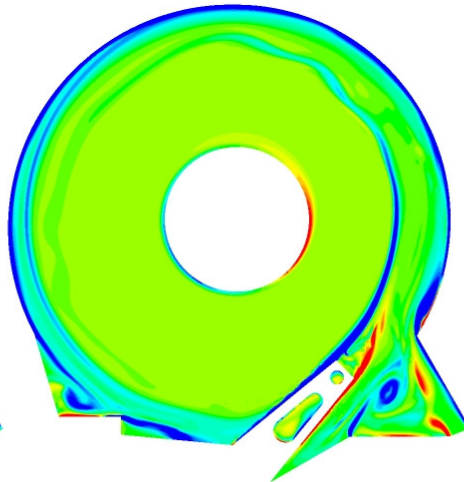
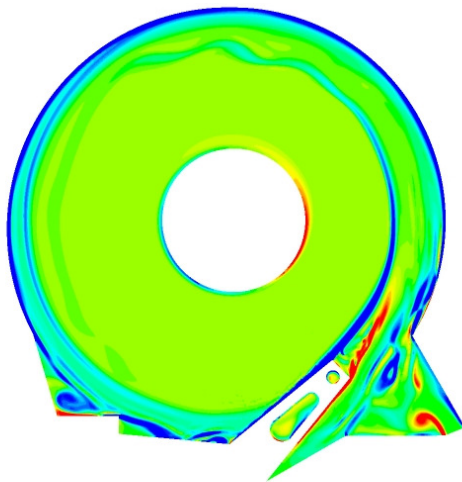
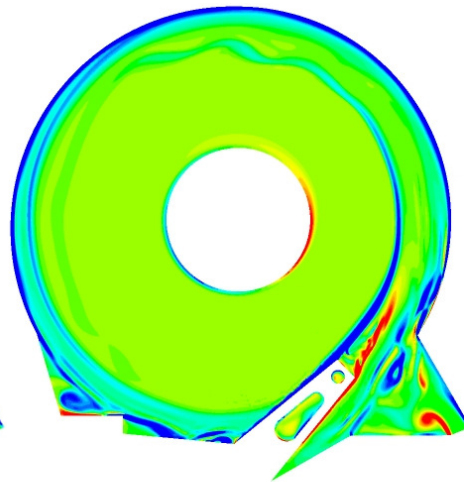


Figure B.5: Contour plot of Z-axis vorticity for the air flow at 5400 rpm

B.2.2 Helium flow at 5400 rpm

(a) $t^* = 0$ (b) $t^* = 0.1$ (c) $t^* = 0.2$ (d) $t^* = 0.3$ (e) $t^* = 0.4$ (f) $t^* = 0.5$

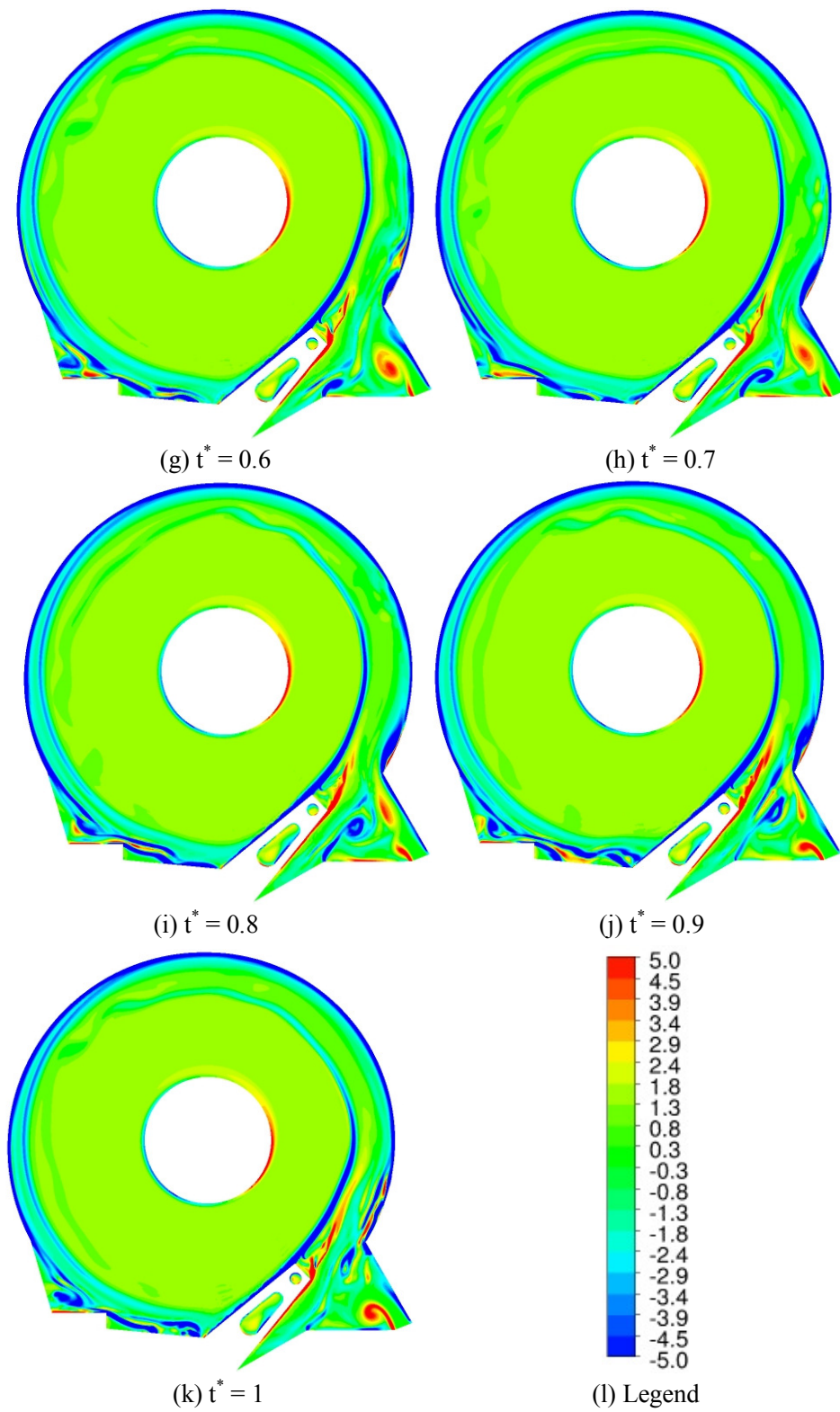
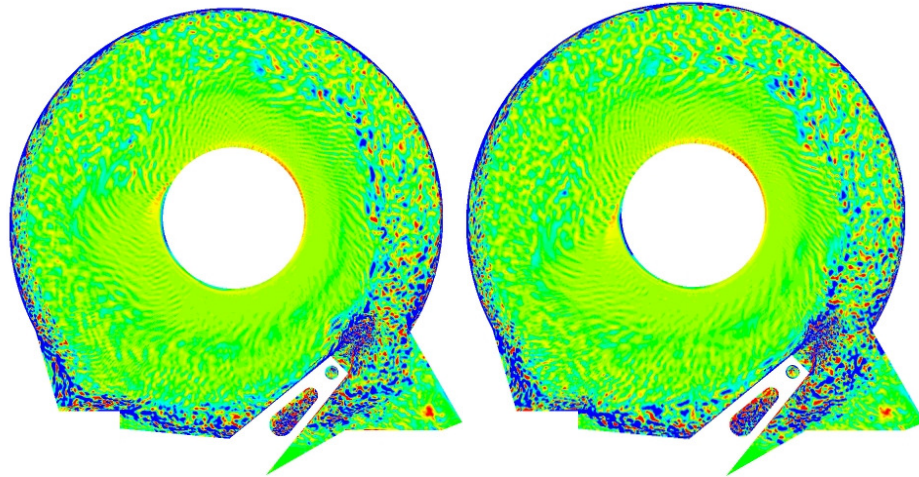
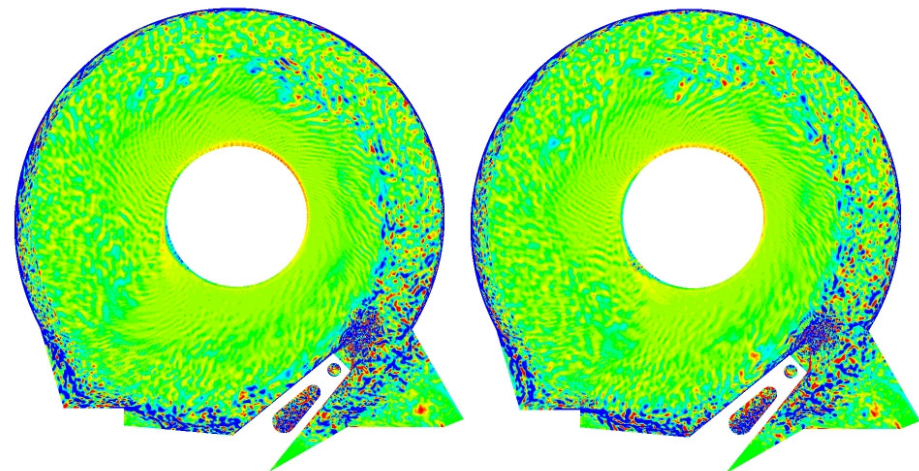
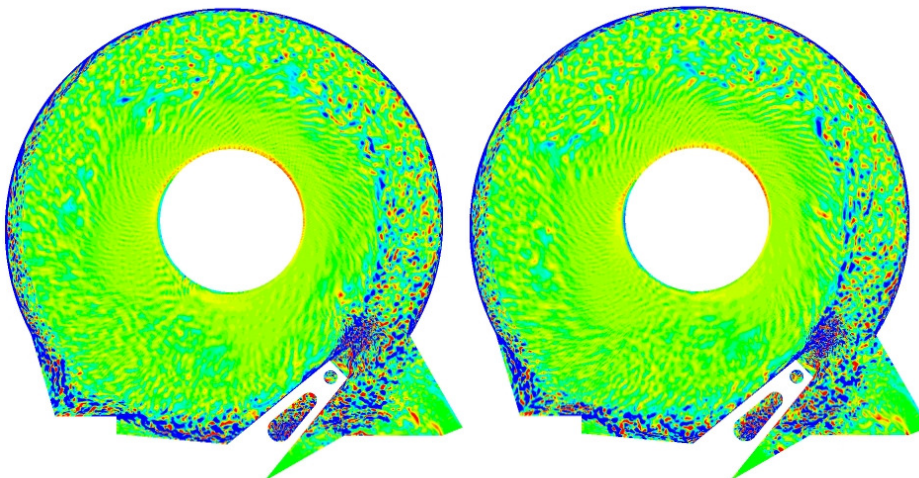


Figure B.6: Contour plot of Z-axis vorticity for the helium flow at 5400 rpm

B.2.3 Air flow at 15000 rpm

(a) $t^* = 0$ (b) $t^* = 0.1$ (c) $t^* = 0.2$ (d) $t^* = 0.3$ (e) $t^* = 0.4$ (f) $t^* = 0.5$

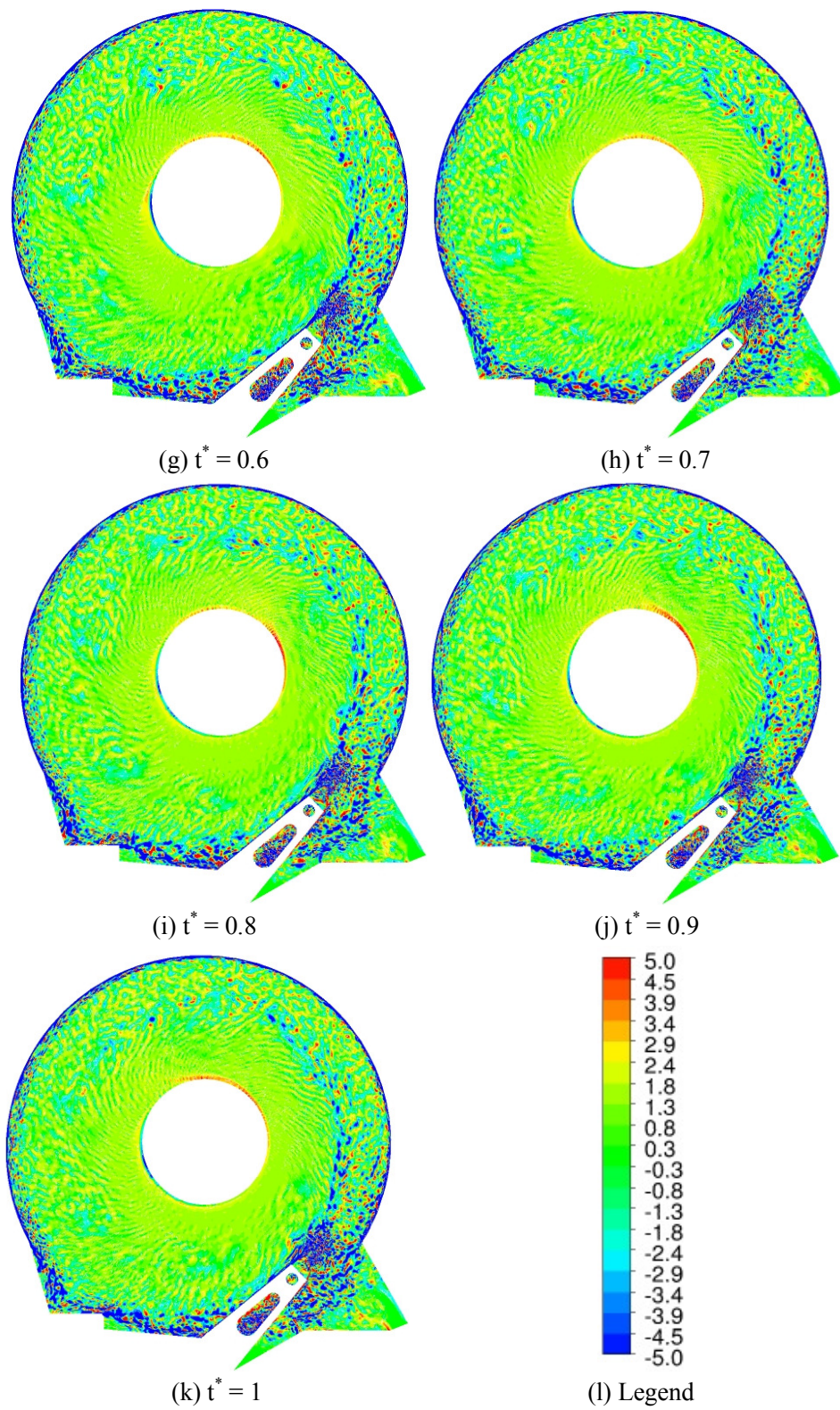
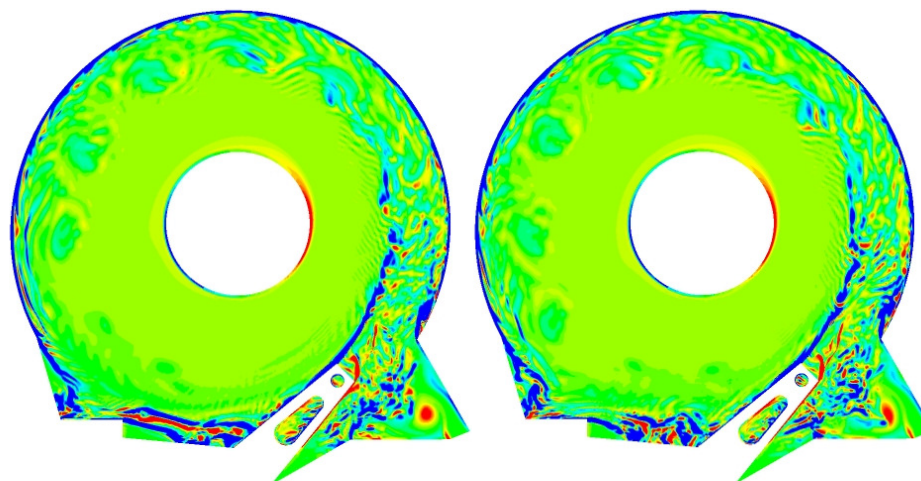
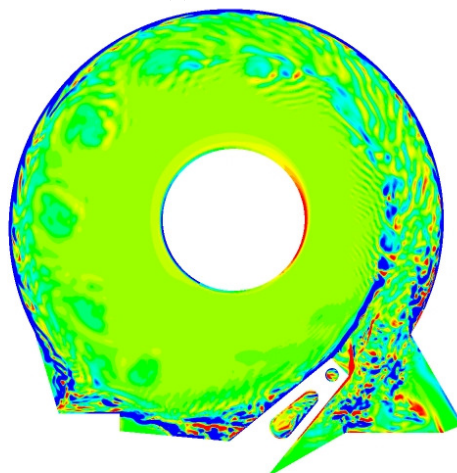
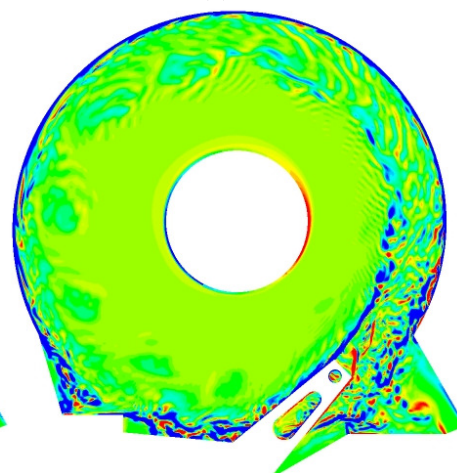
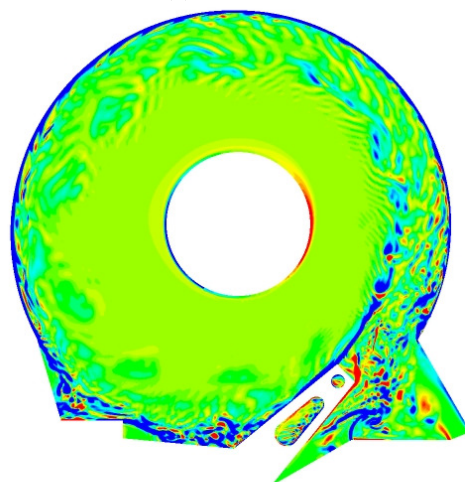
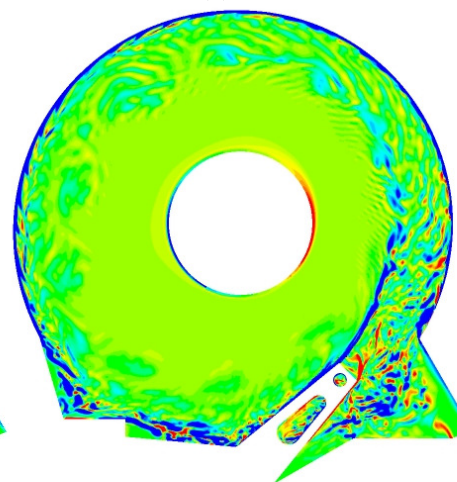


Figure B.7: Contour plot of Z-axis vorticity for the air flow at 15000 rpm

B.2.4 Helium flow at 15000 rpm

(a) $t^* = 0$ (b) $t^* = 0.1$ (c) $t^* = 0.2$ (d) $t^* = 0.3$ (e) $t^* = 0.4$ (f) $t^* = 0.5$

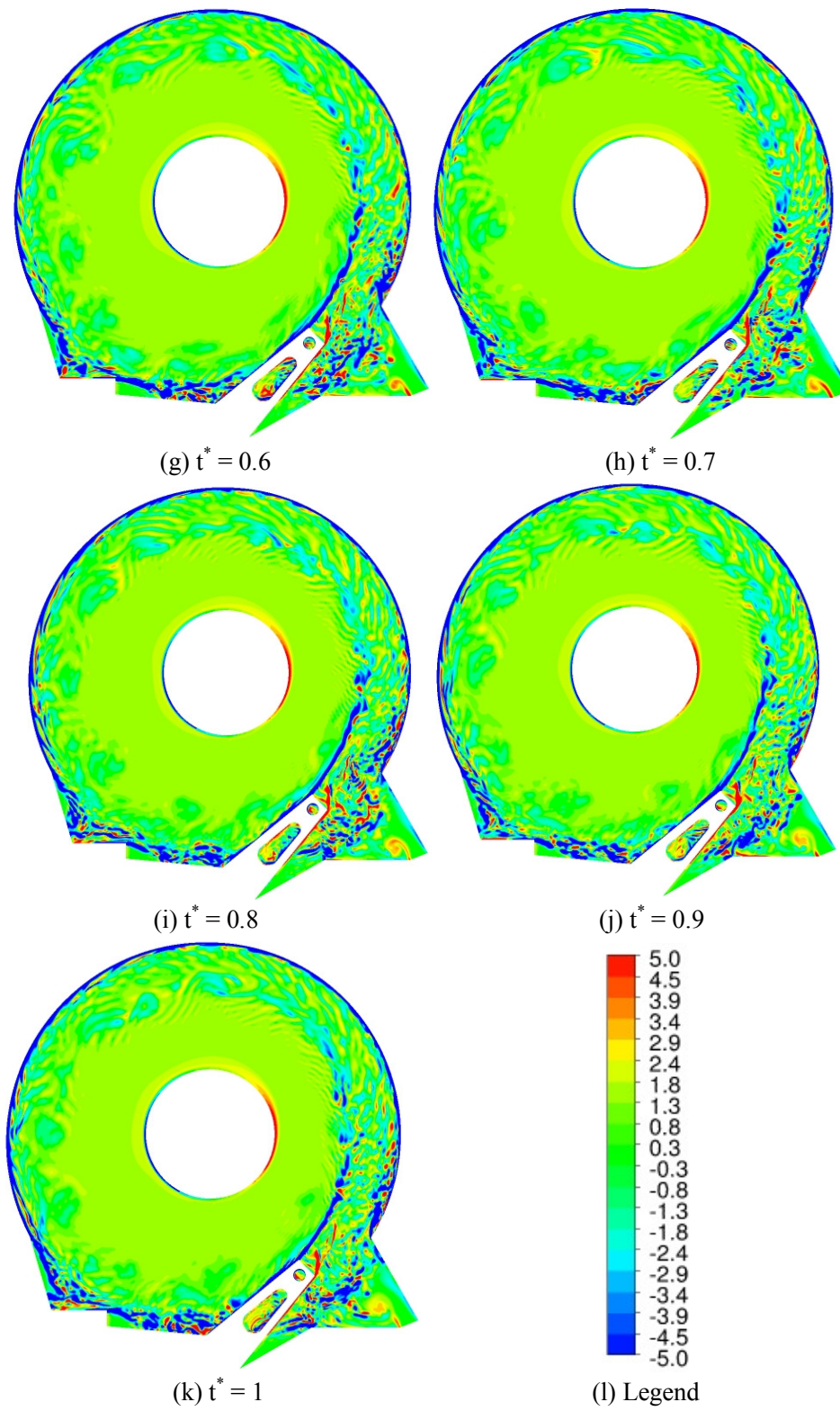


Figure B.8: Contour plot of Z-axis vorticity for the helium flow at 15000 rpm

Appendix C

Derivation of Taylor-Proudman theorem

In appendix C, Mathematical derivation of Taylor-Proudman theorem is provided.

Navier-Stokes equation in the rotating frame is given by

$$\frac{\partial \mathbf{U}}{\partial t} + (\mathbf{U} \cdot \nabla \mathbf{U}) + \Omega \times (\Omega \times \mathbf{x}) = -\frac{1}{\rho} \nabla p + \nu \nabla^2 \mathbf{U} \quad (\text{C.1})$$

where \mathbf{U} indicates the velocity vector. $(\mathbf{U} \cdot \nabla \mathbf{U})$ is Coriolis force term and $\Omega \times (\Omega \times \mathbf{x})$ is centripetal force term. These two terms can be merged to $-\nabla[1/2(\Omega \times \mathbf{x})^2]$. By defining a new variable $P_R = p - \nabla[1/2(\Omega \times \mathbf{x})^2]$, Coriolis and centripetal force terms can be absorbed by the pressure gradient term. Then, the equation (C.1) can be simplified by

$$\frac{\partial \mathbf{U}}{\partial t} + 2\Omega \times \mathbf{x} = -\frac{1}{\rho} \nabla P_R + \nu \nabla^2 \mathbf{U} \quad (\text{C.2})$$

With assumptions of steady and inviscid flows, the time-dependent term and the viscosity term can be canceled out in the equation (C.2). Therefore, a simplified equation can be defined

$$2\Omega \times \mathbf{x} = -\frac{1}{\rho} \nabla P_R \quad (\text{C. 3})$$

By taking the curl on the both sides,

$$\nabla \times (2\Omega \times \mathbf{x}) = -\frac{1}{\rho} \nabla \times (\nabla P_R) \quad (\text{C. 3})$$

The right hand side is simply zero, and the left hand side can be rewritten by.

$$2\Omega \cdot \nabla \mathbf{U} = 0 \quad (\text{C. 4})$$

As a result, a velocity gradient in z – axis is zero.

Appendix D

Introduction of Taylor microscale

Taylor microscale is widely used method to measure the smallest eddy size in turbulent flow with Kolmogorov microscale. In this chapter, brief physical explanation of Taylor microscale is specified. In 1935, Taylor successfully found an expression of Taylor microscale with an assumption of isotropic turbulence [40]. The viscous dissipation can be defined by

$$\varepsilon = 2\nu\overline{S_{ij}S_{ij}} \quad (\text{D. 1})$$

$$S_{ij} = \frac{1}{2}\left(\frac{\partial\overline{U}_i}{\partial x_j} + \frac{\partial\overline{U}_j}{\partial x_i}\right) \quad (\text{D. 2})$$

Equation (D.1) can be rewritten by

$$\varepsilon = 2\nu(\overline{S_{11}^2} + \overline{S_{22}^2} + \overline{S_{33}^2} + 2(\overline{S_{12}^2} + \overline{S_{13}^2} + \overline{S_{23}^2})) \quad (\text{D. 3})$$

The smaller the eddy size gets, the more isotropic flow field becomes. Therefore, following relations can be made in the isotropic flow

$$\overline{\left(\frac{\partial U}{\partial x}\right)^2} = \overline{\left(\frac{\partial V}{\partial y}\right)^2} = \overline{\left(\frac{\partial W}{\partial z}\right)^2} \quad (\text{D.4})$$

$$\overline{\left(\frac{\partial U}{\partial y}\right)^2} = \overline{\left(\frac{\partial U}{\partial z}\right)^2} = \overline{\left(\frac{\partial V}{\partial x}\right)^2} = \overline{\left(\frac{\partial V}{\partial z}\right)^2} = \overline{\left(\frac{\partial W}{\partial x}\right)^2} = \overline{\left(\frac{\partial W}{\partial y}\right)^2} \quad (\text{D.5})$$

$$\frac{\overline{\partial U \partial V}}{\partial y \partial x} = \frac{\overline{\partial W \partial V}}{\partial y \partial z} = \frac{\overline{\partial U \partial W}}{\partial z \partial x} \quad (\text{D.6})$$

With these relations, equation (D.3) becomes

$$\varepsilon = 6\nu \left(\overline{\left(\frac{\partial U}{\partial x}\right)^2} + \overline{\left(\frac{\partial U}{\partial y}\right)^2} + \frac{\overline{\partial V \partial U}}{\partial x \partial y} \right) \quad (\text{D.7})$$

Adding to this, the condition of continuity yields

$$\frac{\overline{\partial U}}{\partial x} + \frac{\overline{\partial V}}{\partial y} + \frac{\overline{\partial W}}{\partial z} = 0 \quad (\text{D.8})$$

$$\overline{\left(\frac{\partial U}{\partial x}\right)^2} + \overline{\left(\frac{\partial V}{\partial y}\right)^2} + \overline{\left(\frac{\partial W}{\partial z}\right)^2} = -2 \left(\frac{\overline{\partial U \partial V}}{\partial x \partial y} + \frac{\overline{\partial W \partial V}}{\partial z \partial y} + \frac{\overline{\partial U \partial W}}{\partial x \partial z} \right) \quad (\text{D.9})$$

In the beginning of this derivation, the statistically isotropic turbulence was made.

Therefore, equation (D.9) can be summarized by

$$\overline{\left(\frac{\partial U}{\partial x}\right)^2} = -2 \frac{\overline{\partial U \partial V}}{\partial x \partial y} \quad (\text{D.10})$$

The assumption of statistical isotropic condition also allows a rotating transformation of coordinate axes by 45° about z axis. This transformation yields a new relation.

$$\overline{\left(\frac{\partial U}{\partial x}\right)^2} - \overline{\left(\frac{\partial U}{\partial y}\right)^2} - \frac{\partial U}{\partial x} \frac{\partial \bar{V}}{\partial y} - \frac{\partial U}{\partial y} \frac{\partial \bar{V}}{\partial x} = 0 \quad (\text{D. 11})$$

The relation (D.10) yields

$$\overline{\left(\frac{\partial U}{\partial y}\right)^2} + \frac{\partial U}{\partial y} \frac{\partial \bar{V}}{\partial x} = -3 \frac{\partial U}{\partial x} \frac{\partial \bar{V}}{\partial y} \quad (\text{D. 12})$$

The continuity equation (D.7) with the relation of equation (D.12) and equation (D.10) becomes

$$\varepsilon = 6\nu \left(\overline{\left(\frac{\partial U}{\partial x}\right)^2} - 3 \frac{\partial U}{\partial x} \frac{\partial \bar{V}}{\partial y} \right) \quad (\text{D. 13})$$

$$\varepsilon = 15\nu \left(\frac{\partial \bar{U}}{\partial x}\right)^2 = 15\nu \left(\frac{\bar{U}}{\lambda}\right)^2 \quad (\text{D. 14})$$

This λ is called ‘‘Taylor microscale’’ which can estimate an average length scale by the dissipation of turbulent eddies. This result can be substituted into the velocity correlation function between two points in the flow field. The velocity correlation function and the shear strain correlation are expressed mathematically [36]

$$Q_{ij}(r) = \overline{U_i(x)U_j(x+r)}, Q_{xx}(re_x) = U^2 f(r), Q_{yy}(re_x) = U^2 g(r) \quad (D.15 \text{ (a), (b), (c)})$$

$$w_i(x) = \nabla \times U = \varepsilon_{ijk} \frac{\partial U_k(x)}{\partial x_j} \quad (D.16)$$

$$\begin{aligned} \overline{w_i(x)w_j(x+r)} &= \varepsilon_{ilm}\varepsilon_{jpn} \frac{\partial U_m(x)}{\partial x_l} \frac{\partial U_q(x+r)}{\partial (x+r)_p} \\ &= -(\delta_{ij}\delta_{lp}\delta_{mq} + \delta_{ip}\delta_{lq}\delta_{mj} + \delta_{iq}\delta_{lj}\delta_{mp} - \delta_{ij}\delta_{lq}\delta_{mp} - \delta_{ip}\delta_{lj}\delta_{mq} \\ &\quad - \delta_{iq}\delta_{lp}\delta_{mj}) \frac{\partial^2 Q_{mq}(r)}{\partial r_l \partial r_p} \\ &= \nabla^2 Q_{ij} + \frac{\partial Q_{ll}}{\partial r_i \partial r_j} - (\nabla^2 Q_{ll})\delta_{ij} \end{aligned} \quad (D.17)$$

To obtain the relation between $g(r)$ and $f(r)$, a general form of the second order isotropic tensor has to be defined [41]

$$Q_{ij}(r) = Ar_i r_j + B\delta_{ij} \quad (D.18)$$

where A and B are arbitrary functions related to $f(r)$ and $g(r)$. From the equation (D.15),

A and B can be calculated by

$$A = \frac{U^2(f(r) - g(r))}{r^2}, B = U^2 g(r) \quad (D.19)$$

$$Q_{ij}(r) = \frac{U^2(f(r) - g(r))}{r^2} r_i r_j + U^2 g(r)\delta_{ij} \quad (D.20)$$

By taking a derivative with respect to r_j , equation (D.18) becomes

$$\frac{\partial Q_{ij}}{\partial r_j} = r_i(4A(r) + r \frac{\partial A(r)}{\partial r} + \frac{1}{r} \frac{\partial B(r)}{\partial r}) \quad (\text{D. 21})$$

With the condition of continuity, equation (D.21) has to be zero. Therefore, all terms in the parenthesis sum to zero.

$$4A(r) + r \frac{\partial A(r)}{\partial r} + \frac{1}{r} \frac{\partial B(r)}{\partial r} = 0 \quad (\text{D. 22})$$

By substituting equation (D.19), the following relation between $g(r)$ and $f(r)$ can be obtained

$$g(r) = f(r) + \frac{r}{2} \frac{\partial f(r)}{\partial r} \quad (\text{D. 23})$$

Using the relation (D.16), Q_{ij} and its trace Q_{ii} can be rewritten by

$$Q_{ij}(r) = \frac{U^2}{2r} \left[\frac{\partial}{\partial r} (r^2 f) \delta_{ij} - \frac{\partial f(r)}{\partial r} r_i r_j \right] \quad (\text{D. 24})$$

$$Q_{ii}(r) = \frac{U^2}{r^2} \frac{\partial}{\partial r} (r^3 f(r)) \quad (\text{D. 25})$$

With the condition of continuity, equation (D.17) can be simplified by

$$\overline{w_1(x)w_1(x+r)} = -\nabla^2 Q_{jj}(r) = -\frac{U^2}{r^2} \frac{\partial}{\partial r} \left[r^2 \frac{\partial}{\partial r} \frac{1}{r^2} \frac{\partial}{\partial r} (r^3 f(r)) \right] \quad (\text{D. 26})$$

The function, f , is symmetric in r , and $f(0) = 1$. Therefore, the velocity correlation function, f , can be expressed using Maclaurin series

$$f(r) = 1 + \frac{r^2}{2} \frac{\partial^2 f}{\partial r^2} \Big|_{r=0} + \text{Higher order terms} \quad (\text{D. 26})$$

The higher order terms are negligible, and the second order term is identified as Taylor microscale.

$$\frac{\partial^2 f}{\partial r^2} \Big|_{r=0} = -\frac{1}{\lambda^2} \quad (\text{D. 27})$$

$$f(r) = 1 - \frac{r^2}{2\lambda^2} \quad (\text{D. 28})$$

Substituting equation (D.28) into equation (D.26) yields

$$\overline{w_1(x)w_1(x+r)} = \frac{30U^2}{2\lambda^2} \quad (\text{D. 29})$$

From equation (D.1)

$$\varepsilon = \overline{vw_1(x)w_1(x+r)} = \frac{15\nu U^2}{\lambda^2} \quad (\text{D. 30})$$

The viscous dissipation also has another expression [36]:

$$\varepsilon = \frac{U^3}{l} = \frac{15\nu U^2}{\lambda^2} \quad (\text{D. 31})$$

With the definition of Reynolds number ($\text{Re} = Ul/\nu$), Taylor microscale can be related to Reynolds number by

$$\frac{\lambda}{l} = \sqrt{15}\text{Re}^{-1/2} \quad (\text{D. 32})$$

References

- [1] Roger W. Future hard disk drive systems, *Journal of Magnetism and Magnetic materials*, 321: 555-561. 2009.
- [2] Zvonimir Z.B., Randall H.V., *Advances in Magnetic Data Storage Technologies*, *Proceedings of the IEEE*, 96(10): 1749-1753, 2005.
- [3] Coughlin. T.M., *High Density Hard Disk Drive Trends in the USA*, *Journal of Magnetic Society of Japan*, 25(3), 2001.
- [4] Lennemann E. *Aerodynamics Aspect of Disk files*. *IBM Journal of Research and Development*, 480-488, 1974.
- [5] Mochizuki S. and Yang W.J., *Self-sustained radial oscillating flows between parallel disks*, *Journal of Fluid Mechanics*, 154: 377-397, 1985.
- [6] Abrahamson S. D., Koga Dennis J and Eaton J.K., *The flow between shrouded co-rotating disks*, *Phys. Fluids*, 1(2): 241-251, 1989.
- [7] Schuler C.A., Usry W., Weber B., Humphrey J.A.C. and Greif R. *On the flow in the unobstructed space Between shrouded co-rotating disks*, *Phys. Fluid* , 2(10): 1760-1770, 1990.
- [8] Tzeng H.M. and Humphrey J.A.C., *Co-rotating disk flow in an axi- symmetric enclosure with and without bluffing body*, *Int. J. Heat and Fluid Flow*, 12(3): 194-201, 1991.
- [9] Tsai Y.S., Chang Y.M., Chang Y.J. and Chen Y.M., *Phase-resolved PIV measurements of the flow between a pair of corotating disks in a cylindrical enclosure*, *Journal of Fluids and Structures*, 23: 191-206, 2007

-
- [10] Dijkstra D. and Van Heijst G.J.F., The flow between two finite rotating disks enclosed by a cylinder., *Journal of fluid mechanics.*, 128: 123-154, 1983.
- [11] Humphrey J.A.C., Schuler C.A. and Webster D.R., Unsteady laminar flow between a pair of disks co-rotating in a fixed cylindrical enclosure., *Physics of Fluids.*, 7:1225-1240. 1995.
- [12] Iglesias I. and Humphrey J.A.C., Two and Three-Dimensional laminar flows between disks co-rotating in a fixed cylindrical enclosure. *International journal for numerical methods in fluid.*, 26: 581-603, 1998.
- [13] Herrero J., Giralt F. and Humphrey J.A.C., Influence of the geometry on the structure of the flow between a pair of co-rotating disks., *Physics of fluids.*, 11(1): 88-96, 1999.
- [14] Tatewaki M., Tuada N. and Maruyama T., An analysis of disk flutter in hard disk Drives in aerodynamic simulations., *IEEE transaction on magnetic.*, 37(2):842-846, 2001.
- [15] Soong C.Y., Wu C.C., Liu T.P. and Liu T.P., Flow structure between two co-axial disks rotating independently, *Experimental Thermal and Fluid Science*, 27: 295-311, 2003.
- [16] Hendriks F., On Taylor vortices and Ekman layers in flow-induced vibration of hard disk drives., *Microsystem Technologies.*, 16:93-101, 2010.
- [17] Abrahamson S.D., Chiang C. and Eaton J.K., Flow Structure in Head-Disk Assemblies and Implications for Design., *Adv. Info. Storage Syst.*, 1:111-132, 1991.
- [18] Tzeng H.M. and Chang C.J., Obstructed flow between shrouded corotating disks., *Phys. Fluids A.*, 3(3): 484-486, 1991.

-
- [19] Usry W.R., Humphrey J.A.C. and Greif R., Unsteady Flow in the Obstructed Space Between Disks Corotating in a Cylindrical Enclosure., *Journal of Fluid Engineering.*, 115:620-626, 1993.
- [20] Girard J., Abrahamson S. and Uznanski K., The Effect of Rotary Arms on Corotating Disk Flow., *Journal of Fluid Engineering.*, 117:259-262, 1995.
- [21] Barbier C., Humphrey J.A.C. and Maslen E., Experimental study of the flow in a simulated Hard Disk Drive, *Journal of Fluid Engineering.*, 128: 1-11, 2006.
- [22] Aruga K., Suwa M., Shimizu K. and Watanabe T., A study on positioning error caused by flow induced vibration using helium-filled disk drives., *IEEE transactions on magnetic.*, 43(9): 3750-3755, 2007.
- [23] Kaneko S., Nishihara T. and Watanabe T., Aerodynamics characteristics of carriage arm equipped on hard magnetic disks., *Microsyst. Technol.* 13: 1297–1306, 2007.
- [24] Kil S.W., Humphrey J.A.C. and Haj-Hariri H., Experimental study of the flow-structure interactions in an air or helium filled Hard Disk Drive Geometry., *Microsyst. Technol.*, 18: 43–56, 2012.
- [25] Hayato S., Mikio T., Satomitsu I., Shigeo N. and Kazuo S., Study of aerodynamic characteristics in hard disk drives by numerical simulation., *IEEE transactions on magnetic.*, 37(2): 831-836, 2001.
- [26] Kubotera H., Tsuda N., Tatewaki M. and Maruyama T., Aerodynamic vibration mechanism of HDD arms predicted by unsteady numerical simulations., *IEEE transaction on magnetic.*, 38(5): 2201-2203, 2002.
- [27] Kirpekar S. and Bogy D.B., A study of the efficacy of flow mitigation devices in hard disk drives., *IEEE transactions on magnetic.*, 42(6): 1716-1729, 2006.

-
- [28] Kazemi M., Numerical analysis of off-track vibration of head gimbal assembly in hard disk drive caused by the airflow., *Microsyst. Technol.*, 13:1201-1209, 2007.
- [29] Zhang Q.D., Tan C.S., Sundaravadivelu K., Suriadi M.A., Chin G.L., Yip T.H., Ong E.H. and Liu N.Y., Mitigation of flow induced vibration of head gimbal assembly., *Microsyst Technol.*, 16:213-219, 2010
- [30] Liu N., Zhang Q. and Sundaravadivelu K., A New Fluid Structure Coupling Approach for High Frequency/Small Deformation Engineering Application., *IEEE TRANSACTIONS ON MAGNETICS*, 47(7): 1886-1889, 2011
- [31] Kil S.W., Humphrey J.A.C. and Haj-Hariri H., Numerical study of the flow-structure interactions in an air- or helium-filled simulated hard disk drive., *Microsyst. Technol.*, 18:57–75, 2012
- [32] Kil S.W., Humphrey J.A.C. and Haj-Hariri H., Turbulence intensity inversion induced by the mass-reducing hole in an air or helium filled hard disk drive., *Microsyst. Technol.*, 19:31-42, 2013.
- [33] Sundaravadivelu K., Zhang Q. and Liu N., Air Flow Analyses in an Ultra-Thin Hard Disk Drive., *IEEE TRANSACTIONS ON MAGNETICS*, 49(6): 2473-2476,2013.
- [34] ANSYS CFX Solver Modeling Guide.
- [35] Pope S.B., *Turbulent Flows*. Cambridge University Press., Cambridge, 2000.
- [36] Davidson P.A., *Turbulence. An introduction for scientists and engineers.*, Oxford, 2004.
- [37] Kundu P.K., Cohen I.M., *Fluid Mechanics third edition.*, Elsevier academic press., 2004.

- [38] Milton J.S. and Arnold J.C., Introduction to probability and statistics. Fourth edition, McGraw Hill, 2007.
- [39] Vanyo J.P., Rotating fluids in Engineering and Science. Butterworth-Heinemann, 1993.
- [40] Taylor G.I., Statistical Theory of Turbulence., Proceedings of the Royal Society of London. Series A, Mathematical and Physical Sciences, 151(873): 421-444.
- [41] Batchelor G.K., The Theory of Homogeneous Turbulence. Cambridge University Press, 1959.